SANDIA REPORT
SAND2012-9664
Unlimited Release
Printed November 2012

Selective Stress-Based Microcantilever Sensors for Enhanced Surveillance

Mark D. Allendorf, Louise J. Criscenti, Hakan Demir, Matthew C. Dixon, T. R. Guilinger, I. Ellern, Jeffery A. Greathouse, Peter J. Hesketh, Aaron M. Katzenmeyer, Jin-Hwan Lee, Nathan W. Ockwig, Phil Pohl, Alex L. Robinson, David S. Sholl, Vitalie Stavila, Steve M. Thornberg, Timothy Van Heest, Anandram Venkatasubramanian, Joanne Volponi, Michael I. White, Todd R. Zeitler

Prepared by
Sandia National Laboratories
Albuquerque, New Mexico 87185 and Livermore, California 94550

Sandia National Laboratories is a multi-program laboratory managed and operated by Sandia Corporation, a wholly owned subsidiary of Lockheed Martin Corporation, for the U.S. Department of Energy's National Nuclear Security Administration under contract DE-AC04-94AL85000.

Issued by Sandia National Laboratories, operated for the United States Department of Energy by Sandia Corporation.

Available to DOE and DOE contractors from
U.S. Department of Energy
Office of Scientific and Technical Information
P.O. Box 62
Oak Ridge, TN 37831

Telephone: (865) 576-8401
Facsimile: (865) 576-5728
E-Mail: reports@adonis.osti.gov
Online ordering: http://www.osti.gov/bridge

Available to the public from
U.S. Department of Commerce
National Technical Information Service
5285 Port Royal Rd.
Springfield, VA 22161

Telephone: (800) 553-6847
Facsimile: (703) 605-6900
E-Mail: orders@ntis.fedworld.gov
Online order: http://www.ntis.gov/help/ordermethods.asp?loc=7-4-0#online

SAND2012-9664
Unlimited Release
Printed November 2012

Selective Stress-Based Microcantilever Sensors for Enhanced Surveillance

Mark D. Allendorf, Aaron M. Katzenmeyer, Vitalie Stavila, Joanne Volponi
Sandia National Laboratories, Livermore, California

Louise J. Criscenti, Jeffery A. Greathouse, T. R. Guilinger, Nathan W. Ockwig, Phil Pohl, Alex L. Robinson, Steve M. Thornberg, Michael I. White,
Todd R. Zeitler
Sandia National Laboratories, Albuquerque, New Mexico

Matthew C. Dixon
Biolin Scientific, Inc., Linthicum Heights, MD, 21090

Jin-Hwan Lee
Intel Corporation, Rio Ranch, NM, 87124

Hakan Demir, David S. Sholl, Timothy Van Heest
School of Chemical & Biomolecular Engineering, Georgia Institute of Technology
311 Ferst Drive, Atlanta, GA 30332-0100

I. Ellern, Peter J. Hesketh, Anandram Venkatasubramanian
G.W. Woodruff School of Mechanical Engineering, Georgia Institute of Technology
Atlanta, GA, 30332

Abstract

Assessment of component aging and degradation in weapon systems remains a considerable challenge for the Integrated Stockpile Evaluation program. Analysis of weapon atmospheres can provide degradation signatures and indicate the presence of corrosive vapors. However, a critical need exists for compatible in-situ sensors to detect moisture and other gases over stockpile lifetimes. This inhibits development of both “self-aware weapons” and fully instrumented weapon test platforms that could provide in-situ data to validate high-fidelity models for gases within weapons. We developed platforms for on-demand weapon atmosphere surveillance based on static microcantilevers (SMC) and surface accoustic wave (SAW) devices coated with nanoporous metal organic frameworks (MOFs) to provide selectivity. SMC detect analytes via adsorbate-induced stress and are up to 100X more sensitive than resonant

beam designs. They are also low-power, highly compact devices that can be manufactured using CMOS technologies. SAW devices are low cost, compact, and easily functionalized to impart selectivity. MOFs have ultrahigh surface areas (up to 6000 m2/g), are extremely radiation resistant, and have a hybrid inorganic-organic structure providing much more flexibility to tailor pores for selective adsorption than any other nanoporous material. We created MOF-based recognition chemistries for H_2O, solvents, and other volatile organics. In particular, we demonstrated a humidity sensor composed of the MOF HKUST-1 coated on the surface of a SAW device that detects sub-ppm water vapor concentrations. We also used computational simulations to identify potential MOFs for detecting CH_4 and O_2. A novel MCL design incorporating reference cantilevers and integrated temperature measurement for in-situ self-calibration was fabricated. Long-term device performance (drift, calibration, noise, and cross sensitivity) was quantified. The results demonstrate conclusively that MOFs can impart high sensitivity and selectivity when used as chemical recognition layers on MEMS-based detection devices.

ACKNOWLEDGMENTS

This work was supported by the Sandia Laboratory Directed Research and Development Program. Sandia National Laboratories is a multi-program laboratory managed and operated by Sandia Corporation, a wholly owned subsidiary of Lockheed Martin Corporation, for the U.S. Department ofEnergy's National Nuclear Security Administration under contract DE-AC04-94AL85000

[Blank page following section.]

CONTENTS

FIGURES

TABLES

[Blank page following section.]

1. INTRODUCTION

1.1. Executive Summary

Age-related degradation of components is an important concern for the enduring stockpile. Despite the careful selection of materials, such issues continue to emerge. These occurrences are largely due the presence of latent manufacturing defects and/or the existence of localized microenvironments that evolve during the lifetime of a system. The local environment around a material can reduce its life by initiating or accelerating aging processes, such as corrosion, oxidation, or hydrolysis. Through the Integrated Stockpile Evaluation (ISE) program Sandia has sought to provide advanced diagnostics to identify when and where aging occurs. Ultimately, this will ensure that aging does not adversely impact system performance. Unfortunately, it is extremely difficult to create in-situ sensors compatible with the unique constraints of the weapon environment. These include extremely small size (distributed sensing near critical components), very low power consumption (minimal energy for safety), long-term stability, low cross-sensitivity, and the ability for in-situ self-calibration (an "Achilles heel" of many potential sensor systems). This inhibits not only development of a "self-aware weapon," but also of fully instrumented weapon test platforms that could provide in-situ data to validate high-fidelity composition and transport models for gases within weapons.

The objective of this project was to surmount these challenges by developing MEMS (Micro-Electro-Mechanical Systems) devices, in particular static microcantilevers (SMC), as platforms for on-demand weapon atmosphere surveillance. A new class of crystalline nanoporous materials known as metal-organic frameworks (MOFs) would be used to provide both selectivity and high sensitivity. SMC are extremely compact, high resonant-frequency, low-power devices in which the transduction mechanism is the stress at the cantilever surface induced by analyte adsorption. SMC are up to 100 times more sensitive than resonant-beam designs and can be made using standard CMOS technologies. MOFs are structurally flexible materials with ultrahigh surface areas (up to 7000 m^2/g), high radiation resistance, and synthetic tailorability that allow their pores to be optimized for selective adsorption. In research prior to the onset of this project, we demonstrated a MOF-coated SMC that could detect absolute humidity at frost points as low as -60 degrees °C (20 ppm) and could also selectively detect CO_2. Thus, practical MOF-based multigas sensors appear to be within reach. In this LDRD project, our overall goal was to prove the SMC+MOF sensor technology concept for stockpile application.

1.2. Research Plan

This project was comprised of three tasks. In Task 1, we created MOF-based recognition chemistries that maximize selectivity. Synthesis was guided by computational modeling, using previously validated atomistic modeling tools. In Task 2, new device designs were developed and assessed, with the objective of improving long-term durability and stability, and enabling systems combining multiple sensors with parallel reference devices to be assembled. Task 3 focused on testing MOF-coated devices in simulated weapon atmospheres and assessing long-term device performance to quantify drift, noise, and cross-sensitivity. The project leveraged an

ongoing collaboration with Prof. Peter Hesketh of the Georgia Tech Woodruff School of Mechanical Engineering (GT) to develop SMC devices, fabrication methods, and data collection strategies. We leveraged existing test bed facilities from the Advanced and Exploratory Systems Dept. and Sandia's existing surface acoustic wave (SAW) devices, which provided an economical platform for developing MOF coatings while design and fabrication of SMC devices was in progress. The objectives in project year 1 (PY1) were to achieve a fully functional moisture sensor based on both SMC and SAW devices and simulate the uptake of H_2O and other analytes using atomistic modeling tools. In PY2, the major objectives were to assess the possibility of detecting very weakly interacting gases such as methane (CH_4), show that volatile organic compounds (VOCs) could be detected, and modify the original SMC design developed at GT to improve sensitivity and mechanical robustness. In the final project year (PY3), the objectives were to further expand the suite of detectable VOCs to include many common solvents, assess the potential for detecting O_2 using computational modeling to simulate its adsorption within MOF pores, and fabricate SMC using the modified GT designed developed in PY2. The resulting achievements are summarized below.

1.3. Summary of Accomplishments

This project succeeded in a multiplicity of ways, as demonstrated by achieving the nearly all project goals, but also by publishing a substantial number of articles in reviewed journals, obtaining a patent related to the intellectual property developed here, and substantially raising the visibility of Sandia's research program in the field of MOFs for chemical sensing. The most significant accomplishments are summarized briefly below. Many of these are discussed in greater detail in subsequent chapters of this report, which are comprised of the text from various journal and conference proceedings papers that we published. We note that, as of the writing of this report, several manuscripts are in preparation that will likely be submitted during the Fall of 2012.

- A MOF-coated SAW device was developed that detects water vapor at temperatures as low as 280 ppbv (-85 °C frost point) and as high as 14,800 ppmv (+10 °C frost point). This performance is competitive with state-of-the-art humidity sensors in commercial use today (Chap. 2).
- Durable, repeatable performance of a MOF-coated device was demonstrated by a MOF-coated SMC, which operated continuously for ten months with no degradation of performance (Chap. 3).
- Detection of VOCs of various types (alcohols, alkanes, acetone, and chlorinated hydrocarbons) was demonstrated, using both SAW and SMC devices (Chap. 3).
- New methods of depositing MOFs on oxide surfaces were developed, resulting in a suite of nine coating materials. Because several of these MOFs are representative examples of a larger series of frameworks having the same topology, the actual number of possible coatings is much larger.
- The growth of MOF bilayers comprised of two different MOFs was demonstrated. This is significant because it allows the properties of the top layer to be used as a way of preventing interfering species from interacting with the lower layer adjacent to the substrate, which performs the actual sensing.

- A series of 100 MOFs representing the major structural classes was computationally screened to identify materials favorable for CH_4 (Chap. 4) and O_2 (Chap. 5) detection.
- A computational investigation of the uptake of several classes of large organic molecules by MOFs showed that selective detection of closely related molecules should be feasible (Chap. 6).
- The basic science of MOF coating formation was determined in a detailed investigation of the growth of the MOF used in the humidity sensing device. (Chap. 7) The results of this study show for the first time how reactant concentration and growth temperature can be used to control film thickness.
- The effects of MOF film thickness and elastic properties were modeled to identify optimal device structures incorporating these materials (Chap. 8).
- A modified SMC design was developed and fabricated. Relative to the original Georgia Tech design, this one should be more robust and exhibit higher sensitivity. As the date of this report these devices were undergoing testing.
- 7 journal articles, 1 book chapter, and 3 conference proceedings were published
- 10 invited lectures and 17 contributed papers were presented at major scientific conferences
- A U.S. patent was awarded on strain-based detection of water vapor
- A Technical Advance was filed concerning detection of volatile organic compounds

The results demonstrate conclusively that MOFs can impart high sensitivity and selectivity when used as chemical recognition layers on MEMS-based detection devices. In general, it is clear that MEMS-based diagnostics, functionalized with MOF coatings, possess great potential for applications in enhanced surveillance where knowledge of gas composition would be of value. In particular, detection of gases that are signatures of aging and corrosion would enable much more accurate assessments of the condition of systems, components, and materials.

[Blank page following section.]

2. ULTRA-SENSITIVE DETECTION OF WATER VAPOR[1]

2.1. Introduction

Metal-organic frameworks (MOFs) are a recently developed class of nanoporous, supramolecular materials with tunable properties that make them very attractive for chemical sensing. MOFs are crystalline coordination polymers in which metal cations are connected by organic, electron-donating "linker" groups. These serve as rigid struts, allowing the material to maintain its porosity when guest solvent molecules are removed. Very high surface areas can be achieved; Langmuir values as high as 10,000 m^2/g have been reported.[1] Moreover, the presence of an organic component within the structure creates many opportunities to synthetically modify the pore environment with respect to both size and chemical properties. Previous experiments and modeling demonstrate that selective gas uptake and separation are achievable,[2] although most of these results were obtained under high-pressure conditions that bear little resemblance to the conditions typically encountered by chemical sensors. Recent atomistic modeling we performed suggests that selective detection of a wide range of molecular species should be feasible. A number of MOFs have been reported that exhibit the ability to adsorb various classes of molecules including volatile organic compounds, polyaromatic hydrocarbons, explosives,[3-6] nerve agents,[7] and methane.[8] An additional advantage of MOFs for sensing purposes is that they are very stable thermally. Most display decomposition temperatures in the range of 350 – 400°C, with a few decomposing above 500°C (e.g., the UiO MOFs[9]). These features, combined with their highly uniform pore structure, make them superior in many ways to other high-surface-area nanoporous materials, such as anodized aluminum oxide (AAO), porous carbons, and aerogels, as well as organic polymers used to provide sensor selectivity.[10] Proof-of-concept experiments demonstrate that chemical detection based on several MOF-enabled transduction mechanisms is feasible.[11] For example, sensors based on impedance,[12] colorimetry,[13-15] interferometry,[16] plasmonics,[17] and luminescence[18] have been described; this work was recently reviewed.[19,20] In most cases, however, the bench-scale experiments performed on a specific material do not involve full integration of the MOF into a self-contained sensing device. Responses to analytes are demonstrated, but detection limits are left undetermined.

Among the many sensing applications of industrial importance, MOFs appear to be particularly well suited for humidity detection. Although a number of MOFs react with water (the IRMOFs are well known for this[21,22]), some are only stable at low humidity levels, notably MIL and ZIF structures.[23] The prevalence of oxygen-containing linkers (typically carboxylates) provides a high density of sites capable of forming hydrogen bonds, and exchangeable coordination sites allow even stronger binding. Biemmi et al. first suggested the possibility of using a MOF for humidity sensing. They functionalized a quartz-crystal microbalance with a film of the MOF Cu_3(benzenetricarboxylate)$_2$ (abbreviated $Cu_3(BTC)_2$ or Cu-BTC; also known as HKUST-1) to determine the water adsorption isotherm.[24] This MOF has a very high water adsorption capacity (as high as 40% g/g[25]) and although it reacts with liquid water, experiments by Kusgens et al.

[1] A. L. Robinson, V. Stavila, M. I. White, S. M. Thornberg, T. R. Zeitler, J. A. Greathouse, M. D. Allendorf "Ultra-sensitive Humidity Detection Using MOF-Coated Microsensors," *Anal. Chem.* ***84*** (2012), 7043.

suggest that its structure should be stable in low relative humidity (RH) environments.[23] In another report, Achmann et al. described an impedance sensor that can detect water vapor at concentrations as low as 0.25 vol%.[12]

Recently, Allendorf et al. demonstrated the first integration of a MOF thin film (Cu-BTC in this case) with a micro-electro-mechanical system (MEMS), a microcantilever (MCL) equipped with a built-in piezoresistor.[26] In that device, the transduction mechanism is adsorption-induced stress at the interface between the MOF film and the sensor surface, enabled by the structural flexibility inherent in MOFs,[27,28] a characteristic that is largely absent in inorganic porous materials such as zeolites. This device is sensitive to water vapor and alcohols, with no cross-sensitivity to light gases such as N_2, O_2, and CH_4. Sensitivity to CO_2 is possible if physisorbed water in the pores is first removed by moderate heating. Rapid and reversible detection of these gases was demonstrated and no degradation of the response was observed over repeated cycles, indicating that the MOF film is stable. The lowest water vapor concentration detected was 500 ppm, but the observed signal-to-noise ratio suggested a detection limit of ~20 ppm. More recently, Venkatasubramanian et al. explored optimization of MOF coating properties and microcantilever design to optimize this sensing platform.[29]

Here, we show that a thin film of Cu-BTC grown on a surface acoustic wave (SAW) sensor can be used to detect water vapor at sub-ppmv concentrations, demonstrating that functionalizing devices with MOF materials can enable highly sensitive gas detection. SAWs have been used as mass sensors for many years. First introduced as sensors by Henry Wohltjen and Raymond Dessy in 1979,[30-32] there are excellent reviews[33-35] and books [36,37] on the topic, covering both theory and practical applications. Specifically, SAWs have previously been used as chilled mirror hygrometers with attached Peltier coolers [38,39] or high surface area coatings.[40,41] Peltier-cooled SAWs have similar sensitivity to Cu-BTC coated SAWs, while experimental equipment in the other papers was inadequate to compare below -20°C frost point. Our MOF-coated SAWs exhibit a rapid and reversible response to water vapor concentrations, spanning 4 orders of magnitude from –85°C to +10°C frost point (0.28 – 14,800 ppm at local elevation). Response time is comparable to other sensors. Though precision and accuracy are reduced compared to these methods (Table 1), our device is quite simple and without the added complexity of attached Peltier coolers and precision ancillary hardware. No cross-sensitivity to N_2, O_2, CO_2, Ar, or methane was observed. We accomplished this by covalently binding Cu-BTC to surface hydroxyl groups on the quartz surface. This provided a much stronger mechanical coupling than was possible with the self-assembled monolayers (SAM) of our earlier MCL devices. In addition to describing the sensor performance, we discuss the relationship between film thickness and device response, demonstrating that an optimum value exists, above which little additional sensitivity is gained. Because of their low cost, robustness, and the relative ease of coating (compared with MEMS devices such as microcantilevers), SAWs are a convenient platform for evaluating MOF coatings for gas sensing, and are suited for practical use as well.

Table 1. Metrics of high performance humidity sensors for different classes.

Type	Range	Precision	Accuracy	Response Time	Stability
analog dial hygrometer	1 to 100%	1%	±3% RH	minutes	high
solid state sensor	0 to 100%	analog voltage	±2 to 4% RH	5 to 30 sec	±0.25% RH per year
chilled mirror instrument	-95 to +20°C frost point	±0.05°C frost point	±0.1°C frost point	< 2.5 hrs	±0.05°C dew/frost point
porous coating SAWs	-90°C frost point to 100% RH	±4°C frost point	±4°C frost point	minutes	±4°C frost point over 1 week
MOF coated SAWs	-85°C to +10°C frost point demonstrated	±4°C dew/frost point	±10°C dew/frost point	minutes	±10°C dew/frost point

2.2. Experimental Methods

2.2.1. SAW Sensors

The results described here were obtained using 97 MHz ST-cut quartz SAWs (Figure 1, left), fabricated in-house by the MESA facility at Sandia National Laboratories (Albuquerque, NM). Devices have two pairs of interdigitated electrodes (IDE), each consisting of 100 fingers, 7 microns wide by 1.5 mm long, with 14 micron pitch (Figure 1, right). The delay line (sensing area) is 1.5 mm wide by 5.8 mm long. Experimental results show sensitivities near the theoretical value of 1.2 ng/cm^2, which is approximately 200 times more sensitive than a 5 MHz QCM (quartz crystal microbalance). Research using this basic SAW design has resulted in a number of scientific articles and patents on gas and vapor sensing using coating including polymers, sol-gels, zeolites, nanoporous carbon, high surface-area anodized metals, and even uncoated[40-48] to obtain sense many analyte classes. This design continues to serve as a versatile test platform. For signal transduction, we used the phase and amplitude detection method described by Cernosek et al.[47] All data is reported as phase shift in radians of the SAW sensor relative to an uncoated reference SAW. Operation in this manner, minimizes common mode influences (e.g. temperature drift, flow rate, and electronic noise), and results in a signal primarily proportional to the chemical environment. Voltage signals were digitized by a 16-bit NI USB-6216 data acquisition module (National Instruments, Austin, TX) controlled with LabVIEW® software. Each recorded value was the average of 1000 measurements sampled at 50,000 kS/sec, saved once per minute.

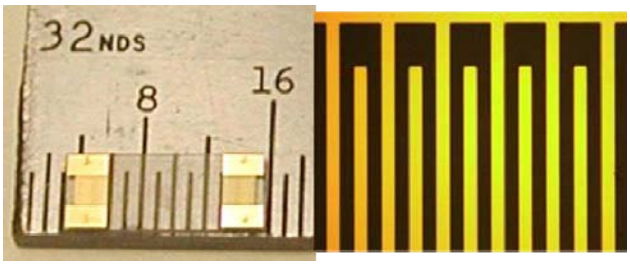

Figure 1. Left: 97 MHz quartz SAW on inch-scale ruler. Right: Magnified section showing interdigitated electrode pattern.

2.2.2. Cu-BTC Coatings

Deposition of Cu-BTC films on SAW devices was performed using a layer-by-layer (LBL) growth procedure first proposed by Wöll et al.[49,50] In a typical procedure, three SAW devices were treated with 30 mL of sequential, alternating ethanolic solutions of 1.0 mM copper acetate ($Cu(OAc)_2$), and 0.1 mM trimesic acid (1,3,5-benzenetricarboxylic acid, H_3BTC) for 20 minutes each at 50°C in a static reaction vessel. Two 10 minute ethanol rinses followed each growth step to remove excess reagent from the surface. In the process, the initial layer covalently attaches to the quartz surface, and each subsequent cycle grows the Cu-BTC thickness by a controlled increment. A ligand exchange reaction takes place whereby newly introduced solvated metal ions coordinate to ligands already bound to the previous MOF layer. Exposure time, temperature, and solution concentration were controlled to establish a constant growth rate. Sets of SAWs were machine-coated with 10, 20, 30, 40, 50, 60, and 100 cycles of film growth. A vector network analyzer was used to measure impedance spectra of each SAW device before and after coating to quantitate shifts in resonant frequency and insertion loss due to film growth. A limited number of SAWs were also coated using a manual procedure. These devices were first treated in saturated methanolic KOH solution, rinsed with ethanol, and dried in a stream of dry nitrogen. The SAWs were then hand-dipped in separate ethanolic solutions of 1.0 mM $Cu(OAc)_2$ and 0.2 mM H_3BTC for 10 and 20 minutes, respectively, and rinsed by immersion in EtOH between cycles.

Grazing Incidence X-Ray Diffraction (GIXRD) studies of the deposited Cu-BTC thin films were performed on a PANalytical (Westborough, MA) Empyrean diffractometer equipped with a PIXcel3D detector. A 5 mm mask was used to limit the size of the X-ray beam to irradiate the desired area of the SAW device. The data collection software automatically subtracts the offset angle (chosen grazing incidence angle) and provides data in terms of intensity versus 2θ. Therefore, GIXRD patterns can be interpreted simply by application of the standard Bragg condition. Processing of the powder diffraction results and phase identification was accomplished using HighScore Plus®. The morphology of the as-prepared $Cu_3(BTC)_2@SiO_2$ thin films was also imaged by scanning electron microscopy (SEM; Hitachi S-4500) (Figure 2).

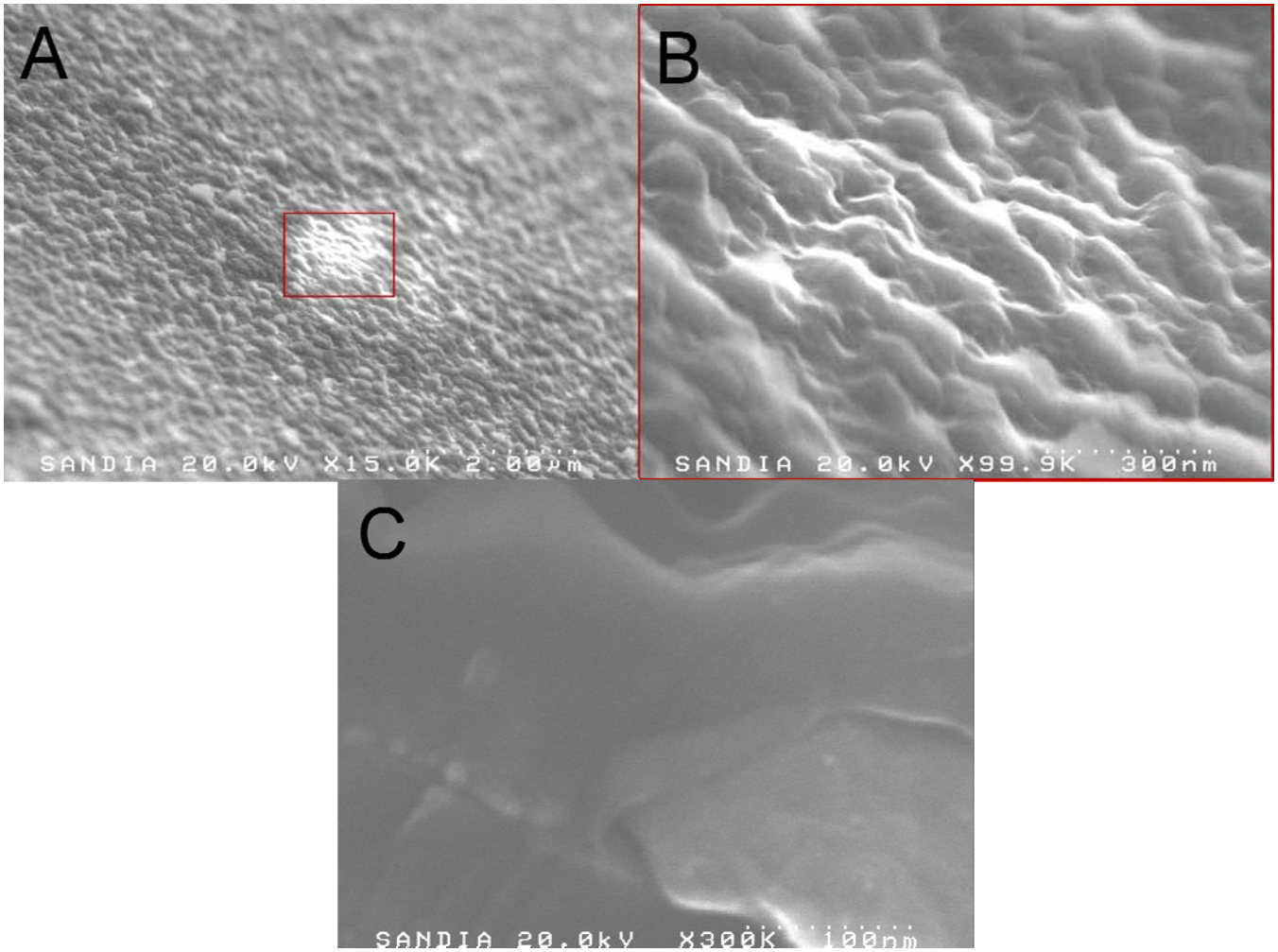

Figure 2. A) SEM image of a Cu-BTC film deposited on the surface of a SAW sensor for 40 cycles of LBL growth. B) High-magnification view, showing typical coating morphology. C) Image showing conformal growth from the silica surface over the interdigitated gold electrodes.

2.2.3. Gas Testing

SAWs in two parallel flow cells were exposed to H_2O vapors from a humidity generator. Each flow cell held one SAW sensor and one uncoated reference SAW. In each flow cell, vapors passed over both SAWs in series, crossing the reference SAW first. The flow cells were fabricated of stainless steel and passivated with Sulfinert® treatment (Restek Corp., Bellefonte, PA). The only non-steel parts were Viton O-ring seals and PEEK fittings to interface stainless steel tubing with the humidity generator. This minimized the release of retained moisture during the driest conditions. The resulting signal sensitivity (phase shift of sensor relative to reference SAW) was sub-milliradian, and short-term drift was approximately 2 milliradians. Long-term drift was less than 10 milliradians, which limited run-to-run reproducibility of results. A preliminary experiment comparing two bare SAWs with only one in the vapor stream demonstrated the lack of moisture sensitivity by an uncoated reference SAW. Attached to each lid of the fixture was a low voltage Kapton-encased heater operated at 2 Watts, and a feed-back thermocouple. The program activated the heater for two hours during the regeneration stage of the humidity generator to aid drying of the MOF coating between cycles. It has been shown that 70°C is sufficient to regenerate Cu-BTC in thermostatted isotherm experiments.[23] Our heaters only achieved 55-60°C, but signal hysteresis from incomplete sensor drying was minimal. Hysteresis proved to be significant without the regenerative heating step, as described later.

Precise humidity levels were generated with a Model 3900 Low Humidity Generator (Thunder Scientific, Albuquerque, NM), and verified with a Model 373S3 Dew Point Mirror (RH Systems, Albuquerque, NM). The Model 3900 is capable of generating relative humidities between -95 and +10°C frost point with an uncertainty of ±0.1°C (below -70°C frost point, the uncertainty is ±0.2°C). Corresponding values in ppmv and percent relative humidity for local pressure (632 mmHg) are given in Table 2. During an experiment, the generator purged its lines to regenerate the flow path with dry nitrogen gas from a liquid nitrogen tank. Humidity steps were controlled at the various setpoints for 4 hours, with an additional 2 hours given to steps when the generator's ice block temperature changed. A nine step sequence repeated in duplicate took 4 days to complete. While sensors typically responded quickly to humidity changes, extended stabilization times were required to ensure vapor equilibrium was achieved with all materials along the flow path. A schematic of the experimental setup is shown in Figure 3.

Table 2. Equivalent expressions of water vapor concentration at 12.23 PSI (632 Torr) and 23.5°C.

Frost Point (°C)	PPM(v/v)	%RH
-95.0	0.12	0.0003
-85.0	0.28	0.001
-80.0	0.65	0.002
-75.0	1.5	.004
-70.0	3.1	0.009
-65.0	6.5	0.019
-60.0	13	0.037
-50.0	47	0.14
-40.0	153	0.44
-35.0	266	0.77
-30.0	453	1.3
-20.0	1230	3.6
-10.0	3102	9.0
-5.0	4807	13.9
0.0	7325	21.2
10.0	14,830	42.5

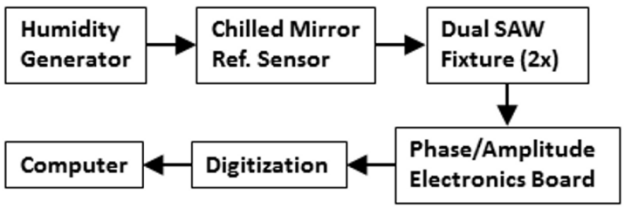

Figure 3. Schematic of experimental configuration.

2.2.4. GCMC Simulation

Uptake of water by Cu-BTC was modeled using Grand Canonical Monte Carlo simulation for comparison to experimental results. Framework atoms remained fixed at their crystallographic coordinates with a cubic cell of length 26.343Å, and water molecules were treated as rigid bodies. The conditions considered were constant H_2O chemical potential μ, volume V, temperature T at 298K. At each chemical potential, 10^7 simulation steps were used as an equilibration period, while data was collected over an additional 10^7 steps. GCMC move probabilities were employed as follows: insertion/deletion (40%); translation (15%); intrabox reinsertion (15%); rotation (15%); growth (15%). Water vapor pressure was calculated from chemical potential by performing "empty box" GCMC simulations, as in our previous work.[8,51] The input structure was taken from published XRD data.[52] Removal of H_2O molecules coordinated to Cu-centers resulted in an "activated" framework. All simulations were performed with the Towhee program[53] using procedures as outlined in our previous work.[8]

The universal force field (UFF[54]) was used to calculate short-range van der Waals energy contributions (parameters are presented in Table 3). The SPC/E model[55] was used for H_2O, and water-MOF interactions were calculated using Lorentz-Berthelot mixing rules.[56] The SPC/E model and UFF have been previously used together.[8] Long-range electrostatic energy contributions were calculated using an Ewald summation with a real-space cutoff of 12.5 Å. Atomic charges for framework atoms were calculated using the CBAC method[57] and are presented in Table 4.

Table 3. Potential parameters for water[1] and framework atoms.[2,a]

Atom	σ (Å)	ε/k_B (K)
C	3.43	52.8
H	2.57	22.1
O	3.12	30.2
Cu	3.11	2.5
OW[b]	3.17	78.2
HW	0.00	0.0

[a]For nonbonded energy $E_{ij} = 4\varepsilon_{ij}[(\sigma_{ij}/r)^{12} - [(\sigma_{ij}/r)^6]$ between H_2O molecules and framework atoms separated by a distance *r*.
[b]The H_2O model is made up of a central OW atom bonded to two HW atoms at a distance of 1.0 Å, forming an angle of 109.47°.

Table 4. Atomic charges (in *e*) for framework atoms and H2O.[a]

Zhong[3] Atom Type	Bonding Connectivity	Cu-BTC
C1	C, O, O	0.786
C2	C, C, C	0.040
C3	C, C, H	-0.141
Cu	O, O, O, O	1.050
H1	C	0.098
O3	C, Cu	-0.654

[a]Atomic charges (in H_2O model) for OW and HW are -0.8476*e* and 0.4238*e*, respectively.

2.3. Results and Discussion

2.3.1. Cu-BTC MOF Coatings

The composition of the deposited MOF coatings was verified by grazing-incidence XRD. GIXRD is a surface-sensitive technique that enhances the diffracted signals from polycrystalline thin films, allowing structural variations to be probed as a function of depth by precisely controlling penetration depth using the incident angle of X-rays. The GIXRD pattern of the 40-

cycle SAW device coated with Cu-BTC is seen in Figure 4. The pattern unequivocally reveals the presence of Cu-BTC diffraction peaks, as well as some peaks from the crystalline ST-cut quartz substrate. The as-deposited MOF is polycrystalline; however, a significant preferred orientation along the (*hhh*) crystallographic direction is observed. This is consistent with a previous report of Cu-BTC thin films deposited by the LBL procedure on OH-terminated SAMs.[58] In contrast, deposition on COOH-terminated SAMs results in films highly oriented along the (*h00*) direction.[58] The reason for the different film textures lies in the enhanced interactions of the COOH surface groups with the paddle-wheel Cu_2 dimeric units in the [100] plane. In contrast, OH groups exhibit preferential binding to the apical position of the Cu^{2+} ions situated in the [111] lattice plane. The surface of freshly cleaved quartz hydrolyzes and adducts ambient water, resulting in the formation of surface silanol groups.[59] These have a high polarity and most likely interact with the water molecules in the $[Cu_2(-CO_2)_4(H_2O)_2]$- paddle-wheel secondary building units (SBUs) during crystal growth.

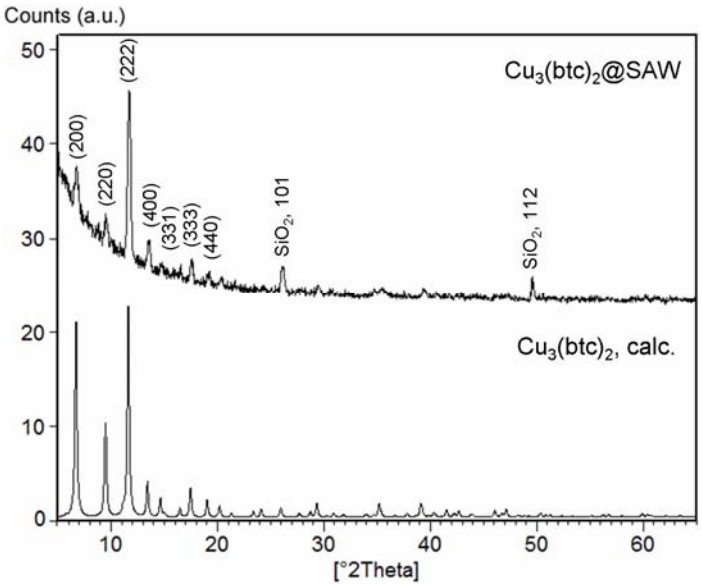

Figure 4. GIXRD diffraction pattern at ω = 0.3° for a Cu-BTC film deposited on the quartz surface of a SAW device with 40 cycles of step-by-step growth (top trace), and simulated pattern calculated for same thickness (bottom trace). For clarity, only selected *hkl* reflections are labeled.

SEM imaging of Cu-BTC-coated SAW devices reveals homogenous coverage of the quartz surface with MOF (Figure 2A and 2B). The film morphology consists of inter-grown grains of random shapes evenly distributed across the sample with diameters ranging from tens to hundreds of nm. No cracks were observed on the surface, indicating uniform film-growth kinetics and relatively low layer stress. Higher magnification SEM images reveal that the faces of the Cu-BTC grains are not smooth, but coarse and irregular in shape with numerous pores, voids, and other nanoscale surface features that we expect are beneficial for gas uptake as a result of increased surface area and improved gas transport into the film. Although chemical attachment of the film presumably occurs only on the silicon oxide portion of the device surface, the growth becomes conformal and covers the interdigitated gold electrodes as well (Figure 2C). This observation is somewhat unexpected, since no SAM was used that would encourage Cu-

BTC growth on the gold. Although deposition on the electrodes has no effect on SAW device performance, it may be problematic for other device types. Potentially, this could be avoided by employing the route described by Hermes et al., who showed that MOF-5 growth on a Au(111) surface can be prevented by patterning the gold with a SAM composed of 1*H*,1*H*,2*H*,2*H*-perfluorododecane thiol, from which the MOF will not nucleate.[60]

2.3.2. Sensor Electrical Characterization

Following application of the MOF coating, the electrical performance of each sensor was examined using the S12 mode of a vector network analyzer (VNA). Measurements were made at room temperature immediately after heating a device to 100°C on a hotplate to ensure minimal contribution from adsorbed atmospheric water. The results of these impedance scans are shown in Figure 5 as a function of the number of LBL coating cycles. In a separate investigation into the kinetics of Cu-BTC LBL growth,[61] we determined that growth on quartz or silica surfaces is essentially linear with the number of coating cycles and that 30 cycles yields a coating approximately 100 nm thick. As seen in the figure, the peak of the main resonance shifts to lower frequencies with the additional mass of progressive coating cycles (Figure 5). The shift from additional mass decreases logarithmically as energy from the surface acoustic waves decreases as 1/e with distance, resulting in less mechanical coupling. In contrast, signal attenuation is linear with the number of coating cycles (Figure 6) as additional mass progressively dampens transmission of the acoustic energy. Both effects indicate that the film thickness increases with number of coating cycles. We note here that we did not record impedance scans for all SAWs prior to this coating study and thus report final values and not absolute changes in device electrical properties. However, impedance scans on a series of uncoated SAWs from the same fabrication wafer exhibit a variation in the center frequency less than 0.1 MHz. Insertion losses of the group ranged from -12 to -15 dB, which is consistent with the scatter seen in Figure 5.

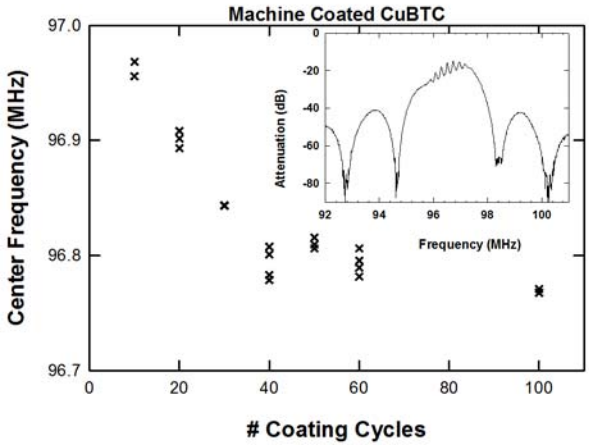

Figure 5. Shift in center frequency as a function of the number of Cu-BTC coating cycles. Inset shows a typical impedance scan.

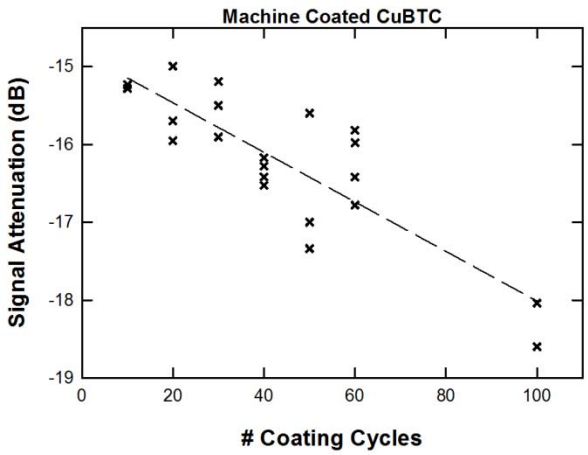

Figure 6. Shift in signal attenuation as a function of the number of Cu-BTC coating cycles.

2.3.3. Humidity Sensing

The time-dependent response of a Cu-BTC coated SAW sensor shows that the device is capable of a rapid and reproducible response to water vapor concentration. The sensors respond in parallel with the chilled mirror reference with a phase delay of approximately one minute, which is consistent with their relative position in the flow stream, tubing lengths, and flow rates. For extreme decreases in humidity (e.g. 42% to 3 ppmv), a bakeout step between successive cycles of the humidity generator is necessary to eliminate hysteresis that presumably occurs as a result of the buildup of H_2O within the film. The sensor response tracks the chilled mirror reference, as seen in Figure 7, where each peak traced a single cycle of the humidity generator. These cycles were comprised of a series of 10°C steps from -70 to +10°C frost point with an 11 hour regeneration sequence between high and low humidity steps. With each successive cycle, the response of the sensor decreased, reaching approximately 50% response after 10 cycles. This decrease is consistent with an accumulation of H_2O molecules in the pores of the film. Our previous experience with Cu-BTC-coated MCL indicated that much of this physisorbed water can be removed by mild heating in flowing dry N_2. In these experiments, we heated the sensor to 55-60°C for 2 hours following each cycle of the humidity generator. This eliminated the hysteresis and fully regenerated the response of the device (Figure 8). Repeated cycling of individual devices under these conditions gave no indication that these exposures damaged the coatings in any way. This is particularly noteworthy because the duration of each temperature step was at least four hours and the total cycle time was four days.

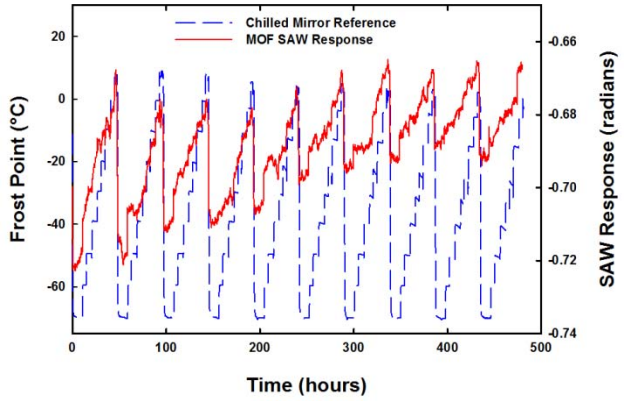

Figure 7. Reponse of a SAW sensor hand-coated with Cu-BTC as a function of time and water vapor concentration (as indicated by frost point). No heater was used between cycles.

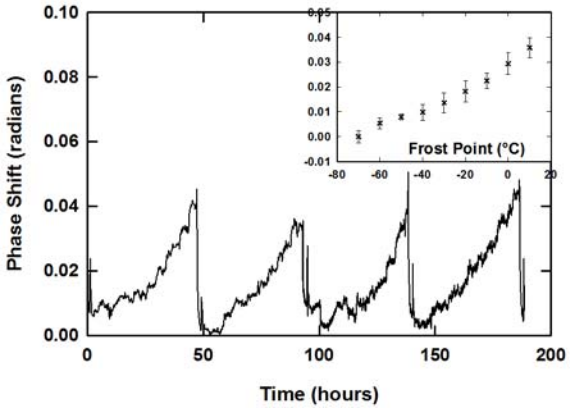

Figure 8. Reponse of same SAW sensor from Figure 7 after addition of heater and inter-cycle regeneration at 60°C. The inset shows the response as a function of frost point with error bars (see Table 2 for corresponding H_2O concentration).

The response to humidity of SAWs with different numbers of LBL coating cycles, and thus MOF thickness, is shown in Figure 9 for coatings of 20 to 100 cycles (from 70 to 350 nm thick). Response with humidity appears linear at low concentrations on this log-linear plot as the MOF's surface area accumulates a monolayer of water. Subsequently, mass condensation of water produces a steeper slope. Other experimental results and our modeling suggests the response will have another inflection above 50% RH (>12°C frost point) and asymptotically approach a final value as water saturates in the pores. As expected, thinner coatings have lower sensitivity, with a very poor response for the 10 cycle-coated SAWs. However, coating thickness cannot be increased to an arbitrarily large value without impacting performance. As seen in Figure 9, the response to water vapor reaches a maximum value at 60 coating cycles, which equates to an approximate thickness of 200 nm. Thicker coatings add mass at a distance from the surface that

does not couple well with the surface acoustic waves, but continue to dampen the energy nonetheless. In addition, 60 and 100 cycle SAWs showed progressively longer equilibration times, with the 100 cycle SAWs failing to level off after 4 to 6 hours of constant exposure.

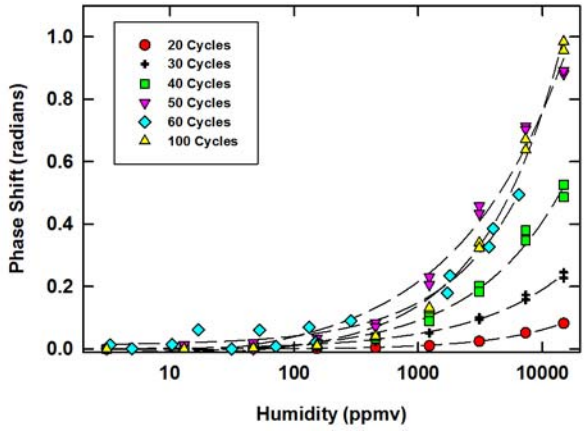

Figure 9. Response of Cu-BTC SAWs with different number of coating cycles to various humidity levels.

The automated LBL process produces uniform and reproducible Cu-BTC coatings, but is relatively slow. This process requires approximately 20 hours to deposit a 100-nm film at room temperature, although we recently determined that film growth at 62°C can reduce this by a factor of two.[61] A limited number of sensors were also coated using a manual procedure in which devices were alternately submerged in solutions of copper acetate and trimesic acid. Growth by this method is faster, yielding 150-nm thick coatings in only 6 hours. Aside from the tedious nature of the process, we find coating uniformity with this method is more difficult to control than with the automated LBL process. However, the sensitivity of these devices is higher than devices coated by the automated method. Data for a sensor coated in this manner is shown in Figure 10, demonstrating sensitivity to -85ºC frost point (0.28 ppmv). A response at even lower concentrations appears to be possible provided longer system equilibration times. The sensor response as a function of frost point setting (inset 7) displays a degree of uncertainty due to various factors such as moisture hysteresis from limited bakeout temperature (55-60°C), mid-term sensor drift, and incomplete equilibration. It has to be mentioned that this temperature is generally not sufficient to fully remove the water molecules coordinated to Cu(II) centers from the bulk material, however, our results show the physisorbed water is largely removed. The non-equilibrium condition created by flowing dry gas over a thin film of Cu-BTC may also be sufficient to desorb some of the coordinated water. It can be seen that equilibrium is still being established after 4 hours for most steps. Humidity settings below -70°C were outside the working range of the chilled-mirror reference and could not be verified. The reason for the enhanced sensitivity of devices coated manually is unclear, though AFM images show a much more irregular surface with occasional large (1-2 micron) islands amongst a thinner, but rough background coating.

We characterized both types of films using GIXRD (Figure 11) and AFM (Figure 12), from which we determined that Cu-BTC is indeed present on the surface and covers the entire area of

the device. As in the case of machine-coated SAWs, the XRD pattern of the hand-dipped SAW revealed characteristic features of crystalline Cu-BTC, with a slight preferred crystallographic orientation along the (*111*) direction. The AFM measurements on the hand-dipped SAW revealed relatively flat areas with some larger micron-sized features on the surface (RMS roughness ~70 nm), in contrast to a machine-coated SAW, which shows no large features and a RMS surface roughness of ~45 nm. However, when RMS analysis on the hand-dipped SAW device was done, excluding the large surface features, a much lower value for the RMS roughness was obtained, ~12 nm (Figure 12), compared with ~42 nm for a similarly flat area on the surface of the machine-coated SAW. In summary, although the overall RMS roughness of the hand-dipped SAW device is larger due to the presence of large micron-sized features, the underlying surface is smoother compared to a similar machine-coated SAW device. Clearly, a systematic study of the effects of surface roughness is needed, but this is outside the scope of the present work.

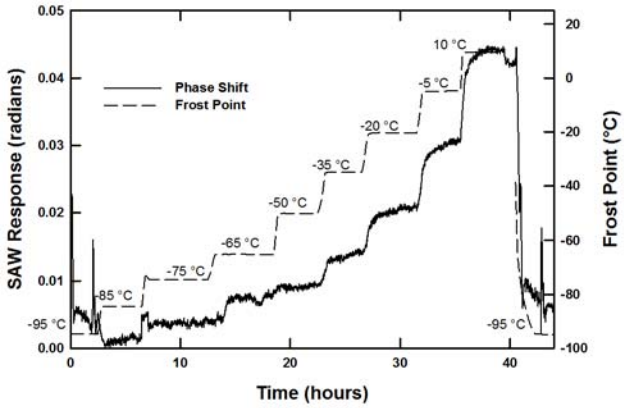

Figure 10. Response of the hand-dipped SAW sensor to humidity challenge. Data spikes at e.g. t=6 hours, commonly coincided with the humidity generator instrument changing the internal ice block temperature.

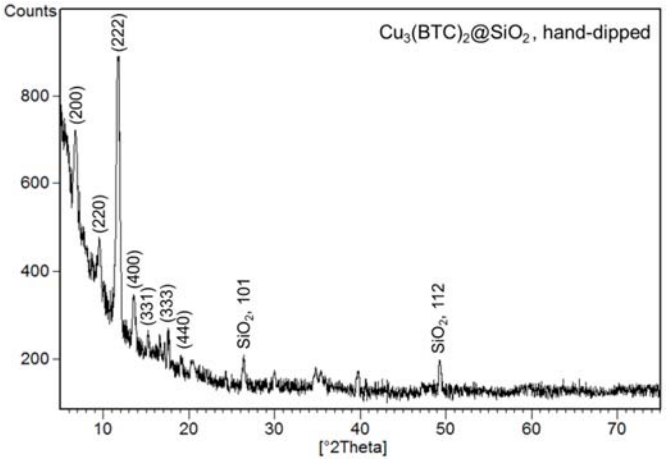

Figure 11. Grazing incidence XRD diffraction pattern at ω = 0.3° for the $Cu_3(BTC)_2$ film deposited on the surface of the SAW device using the hand-dipping method.

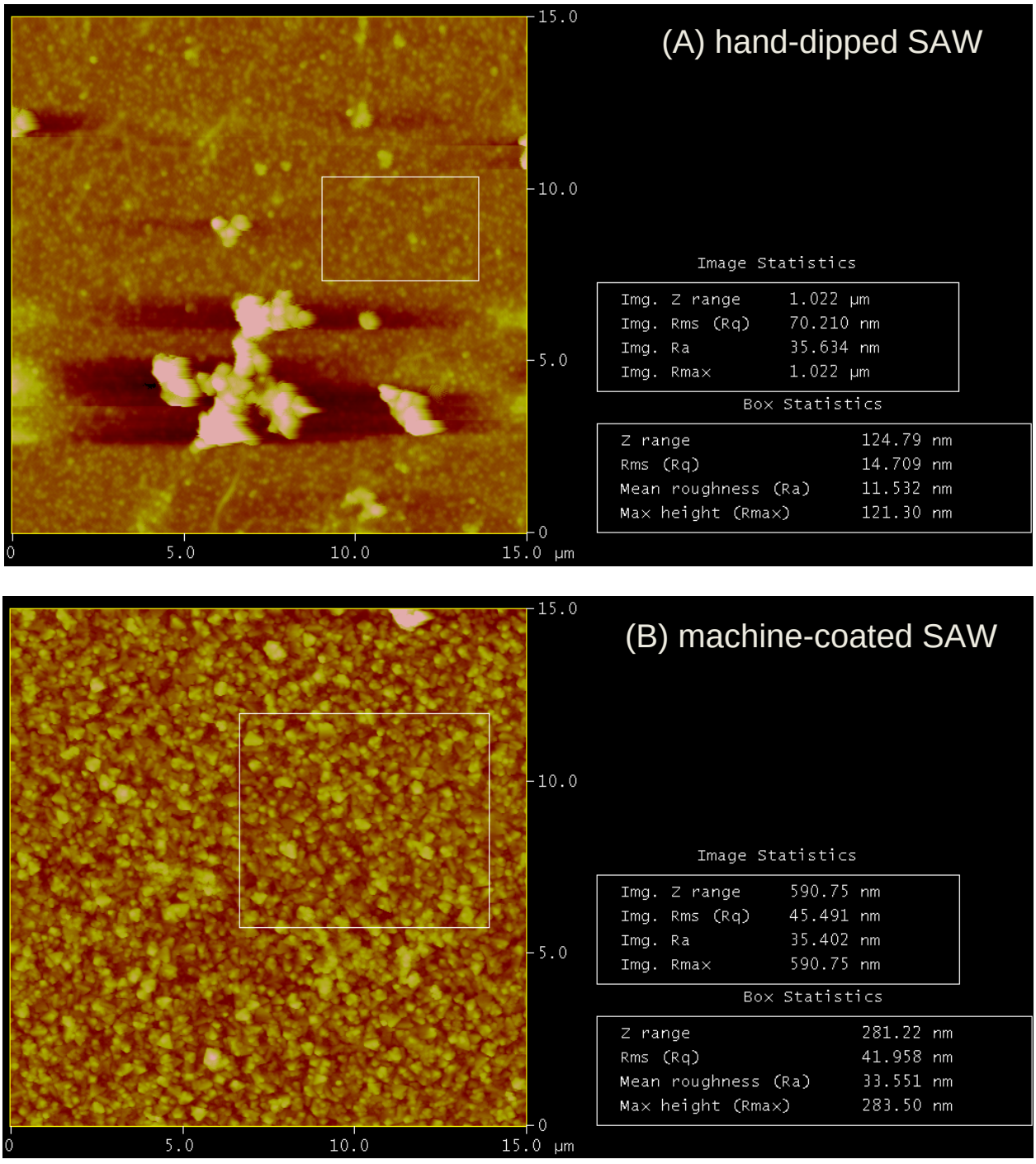

Figure 12. AFM images of $Cu_3(BTC)_2$ films deposited on the surface of SAW devices using (A) the hand-dipping method, and (B) the machine step-by-step- method. The RMS surface roughness of the entire 15x15 µm image (A) is ~70 nm, while the RMS roughness of image (B) is 45 nm. The RMS roughness of the selected areas in (A) and (B) are ~15 and ~42 nm, respectively.

2.3.4. GCMC Simulation

GCMC simulation results show that the initial uptake of H_2O molecules in the activated Cu-BTC structure occurs at the open Cu-sites (Figure 13). This is consistent with the structure of the as-created MOF, in which H_2O molecules are coordinated to the metal sites. Experimental[23,62] and theoretical[8,63] studies have also shown that initial H_2O uptake begins at the metal centers of Cu-BTC. This behavior has been attributed to the relative hydrophobicity of pores due to the linker chemistry.[23]

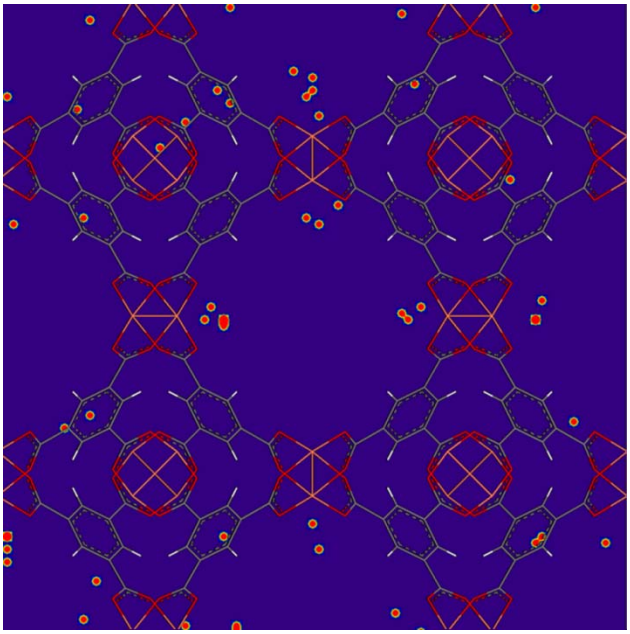

Figure 13. Probability density plot of H_2O adsorption in Cu-BTC at ~9000 ppmv from GCMC simulation. The primary initial uptake sites are located near Cu atoms. The average Cu-OW separation is about 2.5 Å. Cu, O, C, and H atoms are depicted in orange, red, grey, and white, respectively.

Previous density functional theory (DFT) calculations[64] have shown the optimized Cu-OW (Cu-OH_2) distance to be 2.19 Å for a single water molecule near a copper paddlewheel structure (2.22 Å for two water molecules per paddlewheel), in good agreement with XRD structural data for Cu-BTC[52] (2.17 Å). Here, the Cu-OW separation distances calculated from GCMC simulations are distributed over a range from 2.3 to 2.8 Å, which is consistent with previous GCMC simulation (2.35 Å).[63] The discrepancy between DFT and GCMC results could be due to changes in local framework geometry upon H_2O adsorption, which were not allowed in the current GCMC simulations, but were observed in DFT calculations. Other contributions include temperature (GCMC calculations were done at 298 K while DFT calculations were done at 0 K) and forcefield effects (GCMC calculations of CH_4 adsorption in Cu-BTC using UFF parameters are known to have overestimated Cu-CH_4 separation distances[65]).

The simulated water adsorption isotherm for Cu-BTC is shown in Figure 14. The initial uptake of H_2O below 3 mbar (-8°C frost point) is linear with respect to vapor pressure (Figure 15). This region corresponds to adsorption at open Cu-sites and the slope of an isotherm here is suitable

for calculating Henry's constant (3.6 mmol/cm^3-atm). Above the initial linear uptake regime (at about 7°C frost point or 10 mbar), some cages in the MOF structures begin to fill with H_2O molecules and adsorption of H_2O is no longer linear with respect to pressure. A multi-step isotherm for H_2O uptake in Cu-BTC has been shown previously by experiment,[23,24] with the initial stage assigned to adsorption at open Cu-sites, followed by pore-filling. This is also consistent with our data.

The saturation process initially manifests as the complete filling of individual pores rather than an even distribution of H_2O molecules throughout the MOF structure. This indicates that hydrogen bonding between H_2O molecules is energetically more favorable than H_2O-MOF interactions at "intermediate" water vapor pressures (-3 to 16°C frost point, equal to 5700 to 22,000 ppmv – between the linear initial uptake region and complete saturation of the structure). Thus, clustering of water molecules is favored over an even distribution. Similar behavior has been reported for H_2O adsorption in PCN-14 (a MOF with Cu paddle-wheels and multi-pore structure similar to Cu-BTC) at 10 mbar.[8] However, because GCMC simulations are stochastic and do not include diffusion considerations, it is not clear whether this mechanism of pore-filling is realistic or if a wider distribution of water adsorption sites should be expected in this pressure range. The complete filling of all pores is seen above about 16°C frost point (18 mbar). Full saturation (100% relative humidity) is predicted at 10 mbar (7°C frost point) and 298 K for the SPC/E model used here.[66] This is in good agreement with the onset of saturation observed in the isotherm simulations, with uptake continuing until all pores are completely saturated at 16ºC frost point.

Based on the calculated Henry's constant (3.6 mmol/cm^3-atm), a minimum MOF layer thickness can be calculated for H_2O detection at a given humidity level. For a SAW device functioning at 100 MHz, the sensitivity is about 0.23 ng/cm^2.[36] Assuming a Cu-BTC layer of uniform minimum thickness *t* on the SAW device, *t* can be calculated as the sensing limit divided by the water uptake per unit volume, assuming perfect coupling of the coating to the oscillating surface. Water uptake per unit volume of Cu-BTC in the linear region of low uptake is simply the Henry's constant multiplied by the vapor pressure of interest. At a frost point of -40°C (P_{water} = 1.3 x 10^{-4} atm = 153 ppmv), the minimum MOF thickness required for water detection is calculated to be about 270 nm. This is in good agreement with the thickness of Cu-BTC layer (200 nm) found experimentally to yield optimum water detection at low frost points. Experimental uptake is close to the theoretical limit. Overestimation of the minimum MOF layer thickness implies that the calculated Henry's constant is too low, which is consistent with the results shown in Figure 14b, in which the simulation curve lies below the experimental curve at low humidity (i.e., the sensing limit). For a minimum thickness of 200 nm, the Henry's constant should be about 4.9 mmol/cm^3-atm.

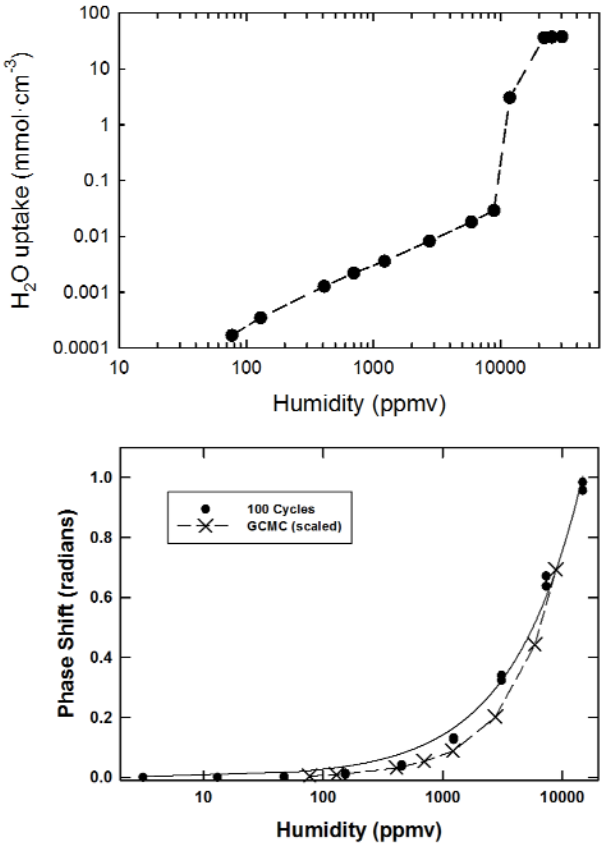

Figure 14. Top: Water adsorption isotherm calculated from GCMC simulation. Bottom: Scaled GCMC isotherm along-side 100-cycle experimental data with exponential best-fit.

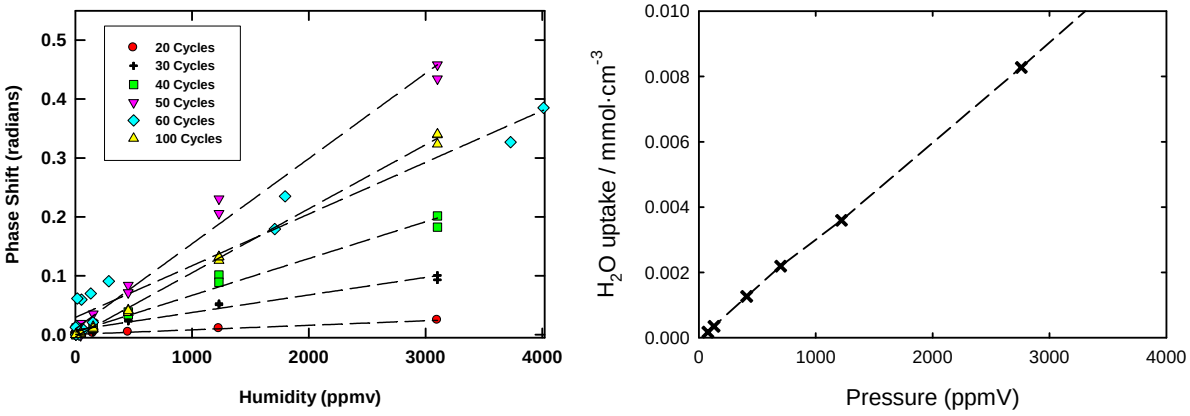

Figure 15. Linear response at low water concentration for experimental (left) and simulated (right) uptake.

2.4. Conclusions

The results presented here represent the first convincing evidence that MOF functionalization of compact sensing technologies such as SAWs and MCLs can compete with state-of-the art humidity sensing methods.[67] Though very simple in implementation, our drift characteristics were limited by long-term drift of the electronics. This likely masked higher precision and accuracy performance of the sensor. Stability of the sensor response over repeated cycles of continuous exposure to water vapor at concentrations as high as 42.5% RH indicates that Cu-BTC films are very durable, which bodes well for their use in real-world situations.

In addition to this demonstration, our results have two implications for practical device design involving MOF films. First, attaching the MOF film to the device through strong covalent bonds to the silicon dioxide surface, rather than via a SAM attached to the gold electrodes, provides a much more thermally stable interface. This allows the device to be heated to temperatures necessary to quickly remove adsorbed water and regenerate the sensor. Second, approximate boundaries for the minimum and maximum practical coating thickness were established. Although these will be to some extent device-specific, the results highlight the fact that one cannot arbitrarily chose the coating thickness (e.g., use extremely thick films) to enhance sensitivity. Cu-BTC is a relatively rigid structure; our previous work with MCL indicates that water uptake by a 100-nm Cu-BTC film induces only a 0.016% change in the lattice parameter,[26] while XRD indicates a lattice expansion of 0.45% upon rehydration of the exchangeable sites on the Cu paddlewheels.[68] The density of Cu-BTC is also high compared with some MOFs (1.22 g cm^{-3}),[52] which should promote coupling of surface acoustic waves. These facts suggest that the coating thickness that maximizes SAW sensor response will be lower for more flexible MOFs having lower densities than Cu-BTC, resulting in less mass-induced frequency shift.

The simulated uptake of H_2O in Cu-BTC shows a multi-step isotherm composed of three uptake regimes. A linear adsorption ("Henry's") regime involves adsorption at open Cu-sites, while a subsequent pore-filling regime provides a transition to a fully-saturated material. The onset of saturation corresponds to the saturation vapor pressure of the water model used here. Based on the initial uptake rate of H_2O in Cu-BTC, the minimum thickness to reach the detection limit shown here was calculated to be in agreement with the MOF layer thicknesses tested. This suggests that the MOF layer is efficient in adsorbing H_2O.

Finally, we show that the details of the MOF film growth process can, somewhat unexpectedly, make a significant difference in the resulting device sensitivity. As noted above, we are unable to draw a firm conclusion at this point concerning the origin of the enhanced sensitivity imparted by using the manual coating technique. We are planning additional experiments to understand the details of this effect. Nevertheless, the automated LBL method appears to work very well in our application, producing consistent films that lead to reproducible device performance. Overall, these results provide considerable encouragement and motivation for continued development of MOFs for sensing purposes, and we anticipate future reports describing their use to detect a wide field of small molecules.

2.5. References

1. Furukawa, H.; Ko, N.; Go, Y. B.; Aratani, N.; Choi, S. B.; Choi, E.; Yazaydin, A. O.; Snurr, R. Q.; O'Keeffe, M.; Kim, J.; Yaghi, O. M. *Science* **2010**, *329*, 424-428.
2. Li, J. R.; Kuppler, R. J.; Zhou, H. C. *Chemical Society Reviews* **2009**, *38*, 1477-1504.
3. Bai, Y.; He, G. J.; Zhao, Y. G.; Duan, C. Y.; Dang, D. B.; Meng, Q. J. *Chemical Communications* **2006**, 1530-1532.
4. Chen, B.; Yang, Y.; Zapata, F.; Lin, G.; Qian, G.; Lobkovsky, E. B. *Adv. Mater.* **2007**, *19*, 1693-1696.
5. Lan, A. J.; Li, K. H.; Wu, H. H.; Olson, D. H.; Emge, T. J.; Ki, W.; Hong, M. C.; Li, J. *Angewandte Chemie-International Edition* **2009**, *48*, 2334-2338.
6. Zou, X.; Zhu, G.; Hewitt, I. J.; Sun, F.; Qiu, S. *Dalton Transactions* **2009**, 3009-3013.
7. Greathouse, J. A.; Ockwig, N. W.; Criscenti, L. J.; Guilinger, T. R.; Pohl, P.; Allendorf, M. D. *Phys. Chem. Chem. Phys.* **2010**, *12*, 12621-12629.
8. Zeitler, T. R.; Allendorf, M. D.; Greathouse, J. A. *The Journal of Physical Chemistry C* **2011**, *116*, 3492-3502.
9. Cavka, J. H.; Jakobsen, S.; Olsbye, U.; Guillou, N.; Lamberti, C.; Bordiga, S.; Lillerud, K. P. *J. Am. Chem. Soc.* **2008**, *130*, 13850-13851.
10. Grate, J. W. *Chem. Rev.* **2000**, *100*, 2627-2647.
11. Allendorf, M. D.; Schwartzberg, A.; Stavila, V.; Talin, A. A. *Chem.-Eur. J.* **2011**, *17*, 11372-11388.
12. Achmann, S.; Hagen, G.; Kita, J.; Malkowsky, I. M.; Kiener, C.; Moos, R. *Sensors* **2009**, *9*, 1574-1589.
13. Beauvais, L. G.; Shores, M. P.; Long, J. R. *J. Am. Chem. Soc.* **2000**, *122*, 2763-2772.
14. Lee, H.; Jung, S. H.; Han, W. S.; Moon, J. H.; Kang, S.; Lee, J. Y.; Jung, J. H.; Shinkai, S. *Chem.-Eur. J.* **2011**, *17*, 2823-2827.
15. Lu, Z.-Z.; Zhang, R.; Li, Y.-Z.; Guo, Z.-J.; Zheng, H.-G. *J. Am. Chem. Soc.* **2011**, *133*, 4172-4174.
16. Lu, G.; Hupp, J. T. *J. Am. Chem. Soc.* **2010**, *132*, 7832-7833.
17. Kreno, L. E.; Hupp, J. T.; Van Duyne, R. P. *Analytical Chemistry* **2010**, *82*, 8042-8046.
18. Allendorf, M. D.; Bauer, C. A.; Bhakta, R. K.; Houk, R. J. T. *Chemical Society Reviews* **2009**, *38*, 1330-1352.
19. Meek, S. T.; Greathouse, J. A.; Allendorf, M. D. *Adv. Mater.* **2011**, *23*, 249-267.
20. Kreno, L. E.; Leong, K.; Farha, O. K.; Allendorf, M.; Van Duyne, R. P.; Hupp, J. T. *Chem. Rev.* **2011**, *112*, 1105-1125.
21. Greathouse, J. A.; Allendorf, M. D. *J Am Chem Soc* **2006**, *128*, 10678-10679.
22. Kaye, S. S.; Dailly, A.; Yaghi, O. M.; Long, J. R. *J. Am. Chem. Soc.* **2007**, *129*, 14176-14177.
23. Kusgens, P.; Rose, M.; Senkovska, I.; Frode, H.; Henschel, A.; Siegle, S.; Kaskel, S. *Microporous and Mesoporous Materials* **2009**, *120*, 325-330.
24. Biemmi, E.; Darga, A.; Stock, N.; Bein, T. *Microporous and Mesoporous Materials* **2008**, *114*, 380-386.
25. Wang, Q. M.; Shen, D. M.; Bulow, M.; Lau, M. L.; Deng, S. G.; Fitch, F. R.; Lemcoff, N. O.; Semanscin, J. *Micropor. Mesopor. Mat.* **2002**, *55*, 217-230.

26. Allendorf, M. D.; Houk, R. J. T.; Andruszkiewicz, L.; Talin, A. A.; Pikarsky, J.; Choudhury, A.; Gall, K. A.; Hesketh, P. J. *J. Am. Chem. Soc.* **2008**, *130*, 14404-14405.
27. Fletcher, A. J.; Thomas, K. M.; Rosseinsky, M. J. *J. Solid State Chem.* **2005**, *178*, 2491-2510.
28. Uemura, K.; Matsuda, R.; Kitagawa, S. *J. Solid State Chem.* **2005**, *178*, 2420-2429.
29. Venkatasubramanian, A.; Lee, J.-H.; Stavila, V.; Robinson, A.; Allendorf, M. D.; Hesketh, P. J. *Sensor. Actuat. B-Chem.*
30. Wohltjen, H.; Dessy, R. *Anal. Chem.* **1979**, *51*, 1458-1464.
31. Wohltjen, H.; Dessy, R. *Anal. Chem.* **1979**, *51*, 1465-1470.
32. Wohltjen, H.; Dessy, R. *Anal. Chem.* **1979**, *51*, 1470-1475.
33. Grate, J. W.; Martin, S. J.; White, R. M. *Anal. Chem.* **1993**, *65*, A940-A948.
34. Grate, J. W.; Martin, S. J.; White, R. M. *Anal. Chem.* **1993**, *65*, A987-A996.
35. Janata, J.; Josowicz, M.; Vanysek, P.; DeVaney, D. M. *Anal. Chem.* **1998**, *70*, 179R-208R.
36. Ballantine, D. S.; White, R. M.; Martin, S. J.; Ricco, A. J.; Zellers, E. T.; Frye, G. C.; Wohltjen, H. *Acoustic Wave Sensors. Theory, Design, and Physico-Chemical Applications*; Academic Press: San Diego, 1997.
37. Janata, J. *Principles of Chemical Sensors*; 2nd ed.; Springer: New York, 2009.
38. Vetelino, K. A.; Story, P. R.; Mileham, R. D.; Galipeau, D. W. *Sensor Actuat B-Chem* **1996**, *35*, 91-98.
39. Hoummady, M.; Bonjour, C.; Collin, J.; Lardetvieudrin, F.; Martin, G. *Sensor Actuat B-Chem* **1995**, *27*, 315-317.
40. Pfeifer, K. B. *Langmuir* **1995**, *11*, 4793-4796.
41. Pfeifer, K. B. F., Gregory C.; Schneider, Thomas W; Sandia Corporation: USA, 1996.
42. Ricco, A. J.; Frye, G. C.; Martin, S. J. *Langmuir* **1989**, *5*, 273-276.
43. Siegal, M. P.; Yelton, W. G.; Overmyer, D. L.; Provencio, P. P. *Langmuir* **2004**, *20*, 1194-1198.
44. Yelton, W. G.; Pfeifer, K. B.; Staton, A. W. *J. Electrochem. Soc.* **2002**, *149*, H1-H5.
45. Pfeifer, K. B.; Frye, G. C.; Schneider, T. W.; USPTO, Ed.; Sandia Corporation, Albuquerque, NM: USA, 1994, p 13.
46. Martin, S. J.; Ricco, A. J.; Ginley, D. S.; Zipperian, T. E. *IEEE Trans. Ultrason. Ferroelectr. Freq. Control* **1987**, *34*, 142-147.
47. Cernosek, R. W.; Frye, G. C.; Martin, S. J.; USPTO, Ed.; Sandia Corporation, Albuquerque, NM: USA, 1998.
48. Bein, T.; Brown, K.; Frye, G. C.; Brinker, C. J. *J Am Chem Soc* **1989**, *111*, 7640-7641.
49. Shekhah, C.; Wang, H.; Kowarik, S.; Schreiber, F.; Paulus, M.; Tolan, M.; Sternemann, C.; Evers, F.; Zacher, D.; Fischer, R. A.; Woll, C. *J Am Chem Soc* **2007**, *129*, 15118-+.
50. Shekhah, O.; Wang, H.; Strunskus, T.; Cyganik, P.; Zacher, D.; Fischer, R.; Woell, C. *Langmuir* **2007**, *23*, 7440-7442.
51. Greathouse, J. A.; Kinnibrugh, T. L.; Allendorf, M. D. *Industrial & Engineering Chemistry Research* **2009**, *48*, 3425-3431.
52. Chui, S. S. Y.; Lo, S. M. F.; Charmant, J. P. H.; Orpen, A. G.; Williams, I. D. *Science* **1999**, *283*, 1148-1150.
53. Martin, M. G. *MCCCS Towhee* http://towhee.sourceforge.net
54. Rappe, A. K.; Casewit, C. J.; Colwell, K. S.; Goddard, W. A.; Skiff, W. M. *Journal of the American Chemical Society* **1992**, *114*, 10024-10035.
55. Berendsen, H. J. C.; Grigera, J. R.; Straatsma, T. P. *J. Phys. Chem.* **1987**, *91*, 6269-6271.

56. Allen, M. P.; Tildesley, D. J. *Computer Simulation of Liquids*; Oxford University Press: Oxford, 1996.
57. Xu, Q.; Zhong, C. L. *Journal of Physical Chemistry C* **2010**, *114*, 5035-5042.
58. Shekhah, O.; Wang, H.; Zacher, D.; Fischer, R. A.; Woell, C. *Angew. Chem. Int. Edit.* **2009**, *48*, 5038-5041.
59. Somasundaran, P., *Encyclopedia of surface and colloid science*; Ed.; CRC Press, **2006**; Vol. 1.
60. Hermes, S.; Schroder, F.; Chelmowski, R.; Woll, C.; Fischer, R. A. *Journal of the American Chemical Society* **2005**, *127*, 13744-13745.
61. Stavila, V.; Volponi, J.; Katzenmeyer, A. M.; Dixon, M. C.; Allendorf, M. D. *Chem. Sci.* **2012**, *3*, 1531-1540.
62. Gul-E-Noor, F.; Jee, B.; Poppl, A.; Hartmann, M.; Himsl, D.; Bertmer, M. *Physical Chemistry Chemical Physics* **2011**, *13*, 7783-7788.
63. Castillo, J. M.; Vlugt, T. J. H.; Calero, S. *Journal of Physical Chemistry C* **2008**, *112*, 15934-15939.
64. Grajciar, L.; Bludsky, O.; Nachtigall, P. *J. Phys. Chem. Lett.* **2010**, *1*, 3354-3359.
65. Chen, L.; Grajciar, L.; Nachtigall, P.; Düren, T. *The Journal of Physical Chemistry C* **2011**, *115*, 23074-23080.
66. Errington, J. R.; Panagiotopoulos, A. Z. *The Journal of Physical Chemistry B* **1998**, *102*, 7470-7475.
67. Chen, Z.; Lu, C. *Sens. Lett.* **2005**, *3*, 274-295.
68. Prestipino, C.; Regli, L.; Vitillo, J. G.; Bonino, F.; Damin, A.; Lamberti, C.; Zecchina, A.; Solari, P. L.; Kongshaug, K. O.; Bordiga, S. *Chemistry of Materials* **2006**, *18*, 1337-1346.

3. MOF-COATED MICROCANTILEVER SENSORS FOR VOC DETECTION

3.1. Introduction

The need for a highly efficient molecular framework for applications in gas separation, sensing and storage has pushed the frontiers in the nanoporous materials research. Porous Metal-Organic Framework (MOF) has emerged as an important class of materials possessing many desirable properties expected in a molecular sieve such as tailorable permanent nanoporosity, complete desorption, high degree of chemical and thermal stability and analyte specific adsorption. A typical MOF consists of metal cations such as Zn (II) linked by anionic organic linkers groups such as carboxylates, yielding a rigid but open framework that can accommodate guest molecules. Adsorption of analyte molecules in these MOFs is governed by a number of mechanisms (1). In rigid MOFs, uptake is controlled primarily by adsorbate-pore surface interaction and steric interactions. In addition, however, some MOFs exhibit a degree of structural flexibility not observed in conventional recognition layers (1-8).

We recently demonstrated that this property can be used for chemical detection by strain-based transduction mechanisms (9). Thus, the suitability of MOFs with strain based chemical sensors like the piezoresistive microcantilever makes it an ideal candidate for chemical sensing. In this paper, we primarily focus on the results of adsorption of volatile organic compounds obtained on cantilever arrays coated with the well characterized HKUST-1 MOF. The HKUST-1 MOF was selected because of its ability to adsorb a number of species (10), high surface area and previously demonstrated suitability to strain based microcantilever sensor (9, 11). Through such a study we aim to expand the notional space of the analytes that can be used with these microcantilevers and hence obtain their adsorption properties using very small amounts of sample.

HKUST-1 has the structure of formula $Cu_3(BTC)_2(H_2O)_x$, comprises a binuclear Cu_2 paddlewheel unit (12). Its structure consists of two types of “cages” and two types of “windows” separating these cages. Large primary cages (13.2 and 11.1 Å in diameter) are interconnected by 9 Å windows of square cross section. The large cages are also connected to tetrahedral shaped secondary pockets of roughly 6 Å through triangular shaped windows of about 4.6 Å (3.5 Å in the hydrated form).

In this paper, we will briefly discuss the fabrication procedure of the microcantilever array, the MOF film deposition, the experimental setup and the characterization methods in the Methods section. We shall then focus on the response for water, methanol, isopropanol and acetone with the HKUST-1 MOF in the Results and Discussion sections.

3.2. Methods

3.2.1. Microcantilever Array Fabrication

N-doped piezoresistive microcantilever array sensors were fabricated using microfabrication techniques with dimensions 230 µm in length and 80 µm in width, as described in reference (11). The layer configuration of the device is shown in Figure 16; it was optimized for maximum response using COMSOL multiphysics modeling, the results of which will not be presented here as it is beyond the scope of the paper.

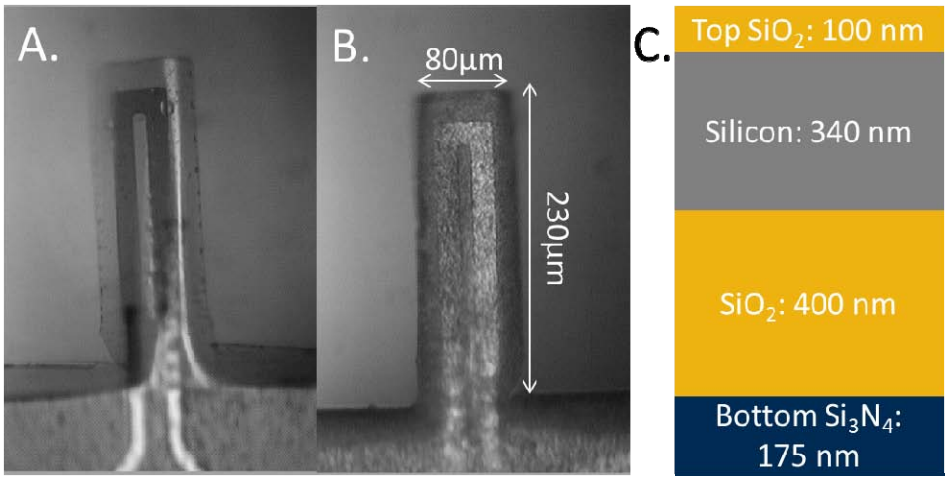

Figure 16. (A)Uncoated microcantilever sensor. (B) MOF coated microcantilever sensor. (C)Layer structureof the cantilever device.

3.2.2. Characterization

Post fabrication, each device was subjected to careful characterization by measuring the resistance of the cantilever array and collecting an optical image of the array as shown in Figure 16A. Subsequently, the devices were sent to Sandia National Laboratory for MOF film deposition. Upon receipt of the coated devices, the resistances were measured again to ensure that the device was not damaged during the deposition process and an optical image of the coated cantilever was obtained, as shown in Figure 16B. Finally, the device was wirebonded to the measurement package and loaded into the experimental setup. Device resistance was measured throughout the experimental cycle.

3.2.3. Cantilever Array Response Measurement Set up

Measurements were made in a custom test cell, where a Wheatstone bridge was used to obtain the cantilever response. Dry nitrogen was used as carrier gas and the analyte concentrations were regulated using a hydrator. A high flow rate mass flow controller (MFC1) was used in conjunction with a low flow rate MFC (MFC4) to introduce a range of diluted concentrations of Volatile Organic Compounds (VOCs) to the device chamber (Figure 17). The response was

obtained by measuring the voltage across the Wheatstone bridge. The bridge consisted of two known resistors and two MOF coated microcantilevers in an arrangement which added response from the two devices.

All experiments were conducted at room temperature (23 °C) and at atmospheric pressure. MOF film was activated by removing adsorbed water by flow of nitrogen for 900s at 40 °C prior to beginning of the experiment. Higher temperatures are necessary to ensure complete removal of water, however, physical limitations such as the integrity of the self assembled monolayers (SAMs) coatings on gold and the physical integrity of the cantilever limit the temperature of activation. Our previous experience showed failure of the SAM coating at temperatures above 50 °C at atmospheric pressure. Temperatures exceeding 190 °C at low vacuum are required to completely dehydrate the MOF (13). Change in voltage was used to ensure a steady state was reached before introducing the first analyte.

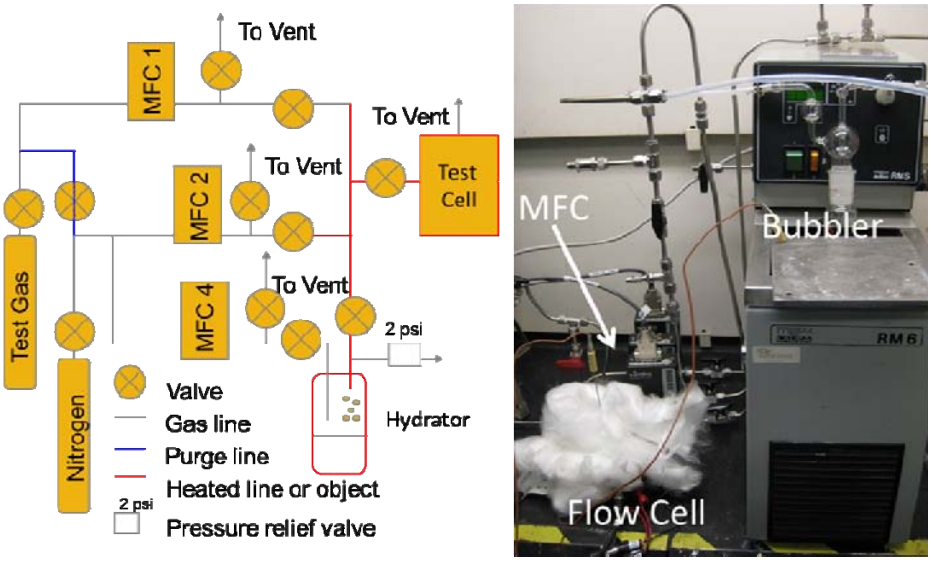

Figure 17. Three MFC's allow for testing gasses, VOC's and mixtures of both. MFC1 is dedicated to carrying purging gas at high flow rate, MFC2 for delivery gases and MFC4 for delivery of VOC's. Gas lines and the hydrator have the capability to be heated.

3.2.4. HKUST-1 Thin Film Deposition

The MOF thin film was deposited by a procedure similar to that described in (11,14). Since the deposition procedure had been adequately validated before (11), only optical images of the MOF coated cantilever (Figure 16B) were obtained to ensure the presence of MOF film on the cantilevers. The MOF is coated onto one side of the beam.

3.3. Results and Discussion

Previously we presented our response for water, chloroform and hexane for the HKUST-1 MOF (15). Following the encouraging signs we have expanded our study to other VOCs including

methanol, isopropanol and acetone and compared it with the adsorption measurements from water. In this section we will discuss our results.

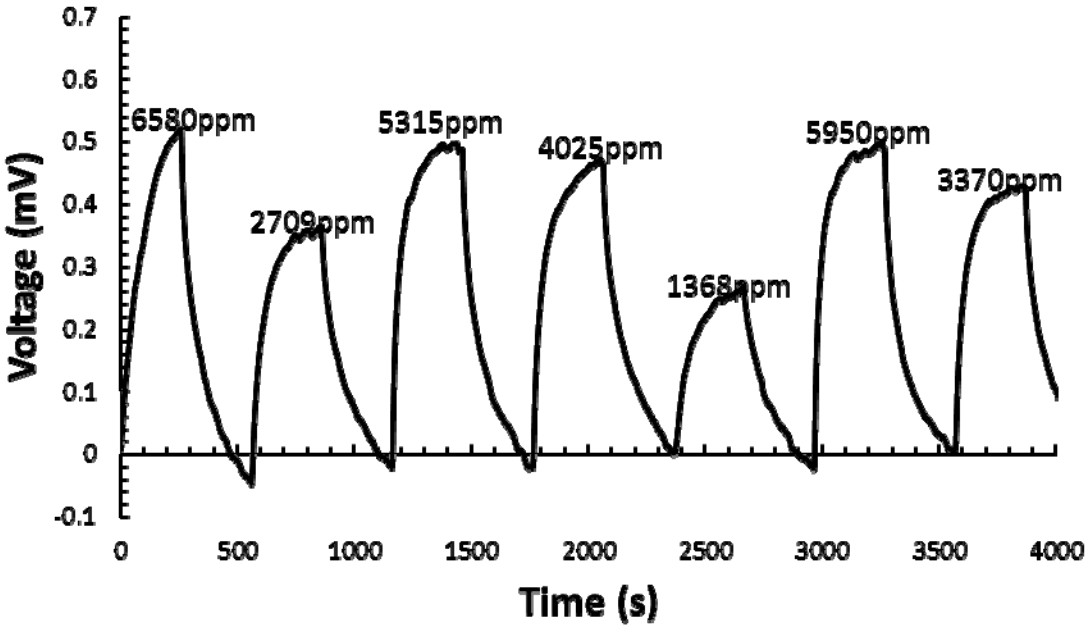

Figure 18. Response to methanol with HKUST-1 at 23°C.

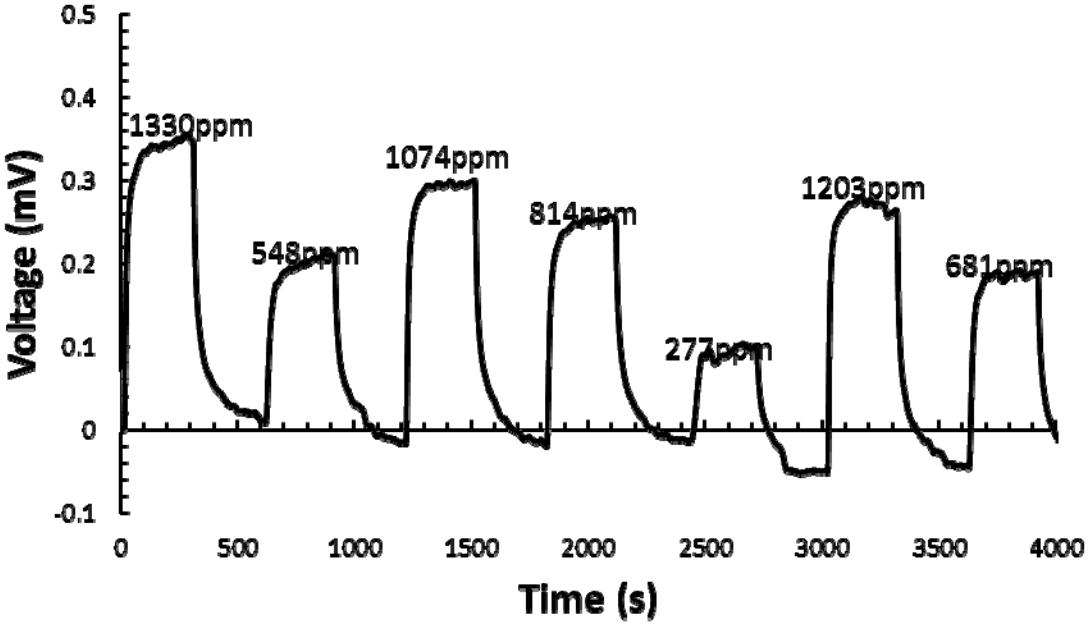

Figure 19. Response to water with HKUST-1 at 23 °C.

Figure 18 shows a sample of 4000 seconds of the transient response with a HKUST-1 coated cantilever for methanol in our experiment. Figure 19 shows similar response to water.

Experiments started with introduction of analyte vapor into the flow cell (at 0 s) at a known concentration. The analyte vapor flow was halted once equilibrium was reached and nitrogen purge was started. Thus the cycle was repeated for different concentrations in a random order. This cyclic procedure remained same for all the analytes. From the data in Figures 18 and 19, it is evident that the sensor returns to a rough base line, suggesting reversibility may be occurring. From such transient response data for analytes including water, methanol, isopropyl alcohol and acetone, we have obtained the time constants for exposure and return to a dry nitrogen purge.

In this paper we have defined the time constant as the time taken to reach 63.2 % of the equilibrium value either during adsorption or desorption for approximately the same concentration. From Table 5 we see that the time constants vary significantly for each analyte for approximately the same concentration. We also observe that the desorption time constant is higher than the adsorption time constant. While the exact mechanism for this behavior is not known, we feel this may be due to the strong Van der Waals forces and hydrogen bonding between the analytes and the open MOF metal centers available for adsorption. However it should also be noted that the MOFs may not be fully dehydrated because of physical limitations imposed by the deposition procedure and the cantilever structure. To further understand the observed behavior of time constants between analytes, we must consider the complex geometry of the HKUST-1 MOF in conjunction with the physicochemical properties of the analytes listed in Table 6.

Based on the geometry of the MOF and the physicochemical property of the analytes, the limiting dimension for transient adsorption/desorption process would be the size of the triangular shaped windows connecting the large primary cages with the tetrahedral shaped secondary pockets. Water being smaller than this triangular shaped windows (~4.6 Å) would pass through this passage with relative ease compared to methanol. The reason for higher time constants for methanol compared to water is currently unknown. Comparing this with the large analytes (isopropanol and acetone) whose kinetic diameters are larger than this window, would imply that these large analytes would mainly be adsorbed in the primary cages, hence resulting in lower adsorption. However as with methanol and water, the reason for the difference in time constants between isopropanol and acetone is not completely clear.

Table 5. Time constants for HKUST-1 coated microcantilever sensors at 23 °C.

Analyte	Time Constant (s) (Adsorption)	Time Constant (s) (Desorption)	Concentration (ppm)
Water	14.1	24.6	2539
Methanol	44.8	86.7	2709
Isopropanol	17.5	19.6	2559
Acetone	56.7	81.3	2930

Table 6. Physicochemical properties of fluids used in this study

Analyte	Kinetic Diameter (Å)	Dipole Moment (D)
Water	2.65 (16)	1.85 (16)
Methanol	3.8 (17)	1.7 (16)
Isopropanol	4.7 (18)	1.7 (19)
Acetone	4.7 (20)	2.9 (19)

Figure 20 shows the equilibrium response in terms of differential voltage versus analyte concentration for different analytes on the HKUST-1 coated cantilever. From the figure we observe that in general the vapor uptake is highest for water, followed by methanol, isopropanol and finally acetone. The reason for this behavior can be traced back to important physicochemical properties like kinetic diameter and dipole moment as listed in Table 6. From Table 6, we observe that as the kinetic diameter of the analyte increases, the equilibrium adsorption generally decreases. This is consistent with the fact that as the size of the analyte increases, fewer molecules can be accommodated into the pore framework.

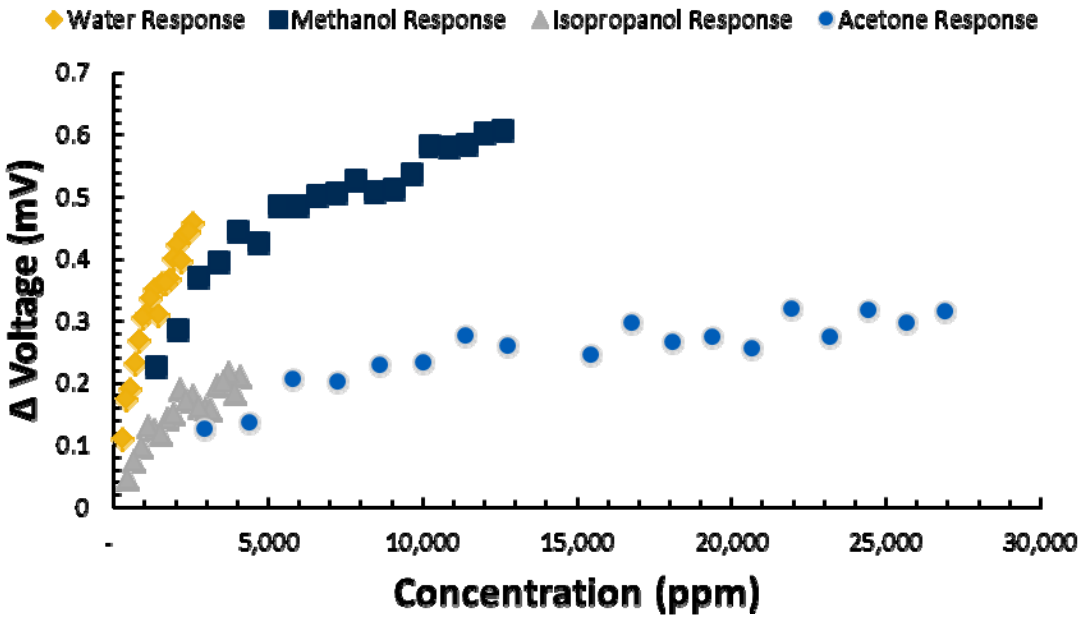

Figure 20. Response to VOCs with HKUST-1 coated cantilevers at 23 °C.

3.4. Conclusions

This work has demonstrated chemically induced strain based detection utilizing HKUST-1 MOF on microfabricated cantilever sensors. The characteristic response to four analytes, specifically, acetone, isopropanol, methanol and water provides some degree of discrimination based upon response time. From our experiments with different VOCs and water, we gained a fundamental

insight into the adsorption process of these analytes and our preliminary experiments prove that it is possible to obtain quantitative parameters relevant to the adsorption process with very small amounts of MOF sample. However, we do agree that further improvements can be applied to our setup to obtain the thermodynamic parameters of adsorption. The compatibility of HKUST-1 MOF with strain based piezoresistive microcantilever sensors is encouraging for us to explore the detection of a mixture of analytes with an array of microcantilevers functionalized with different MOFs to take advantage of their respective chemical selectivity.

3.5. References

1. J. R. Li, R. J. Kuppler, H. C. Zhou, *Chem. Soc. Rev.*, **38**, 1477-1504(2009).
2. D. S. Coombes, F. Cora, C. Mellot-Draznieks, R. G. Bell, *J. Phys. Chem. C*, **113**, 544-552(2009).
3. T. Devic, P. Horcajada, C. Serre, F. Salles, G. Maurin, B. Moulin, D. Heurtaux, G. Clet, A. Vimont, J. M. Greneche, B. Le Ouay, F. Moreau, E. Magnier, Y. Filinchuk, J. Marrot, J. C. Lavalley, M. Daturi, G. Ferey, *J. Am. Chem. Soc.*, **132**, 1127-1136(2010).
4. A. J. Fletcher, K. M. Thomas, M. J. Rosseinsky, *J. Solid State Chem.*, **178**, 2491-2510(2005).
5. P. K. Thallapally, *Abstr. Pap. Am. Chem. Soc.*, **238** (2009).
6. K. Uemura, R. Matsuda, S. Kitagawa, *J. Solid State Chem.*, **178**, 2420-2429(2005).
7. L/ E/ Kreno, K. Leong, O. K. Farha, M. Allendorf, R. P. Van Duyne, J. T. Hupp, *Chem. Rev.*, **112**, 1105-1125(2011).
8. M. D. Allendorf, A Schwartzberg, V. Stavila, A. A. Talin, *Chem.-Eur. J.* **17**, 11372-11388(2011).
9. M. D. Allendorf, R. J. T. Houk, L. Andruszkiewicz, A. A. Talin, J. Pikarsky, A. Choudhury, K. A. Gall, P. J. Hesketh, *J. American Chemical Society*, **130**, 14404-14405(2008).
10. S. Bordiga, L. Regli, F. Bonino, E. Groppo, C. Lamberti, B. Xiao, P.S. Wheatley, R. E. Morris, A. Zecchina, *Physical Chemistry Chemical Physics*, **9**, 2676-2685 (2007)
11. J. H. Lee, R. J. T. Houk, J. A. Greathouse, M. D. Allendorf, P. J. Hesketh, *Hilton Head Workshop 2010: A Solid-State Sensors, Actuators and Microsystems Workshop*, Hilton Head, SC, June (2010).
12. D. Farruseng, C. Daniel, C. Gaudillere, U. Ravon, Y. Schurmann, C. Mirodatos, D. Dubbeldam, H. Frost, R. Q. Snurr, *Langmuir*, **25**(13)**,** 7383(2009)
13. A. Venkatasubramanian, J. H. Lee, R. J. T. Houk, M. D. Allendorf, S. Nair, P. J. Hesketh, *Fall Meeting of the ECS*, Las Vegas, October (2010).
14. V. Stavila, J. Volponi, A.M. Katzenmeyer, M. C. Dixon, M. D. Allendorf, *Chemical Science*, **3**, 1531–1540(2012).
15. I. Ellern, A. Venkatasubramanian, J. H. Lee, P. J. Hesketh, M. D. Allendorf, *Fall Meeting of the ECS*, Boston, MA, October (2011).
16. J. E. ten Elshof, C.R. Abadal, J. Sekulic, S. R. Chowdhury, D. H. A. Blank, *Microporous and Mesoporous Materials*, **65**, 197-208 (2003).
17. Q. Zhu, J. N. Kondo, S. Inagaki, T. Tatsumi, *Topics in Catalysis*, **52**, 1272-1280 (2009)
18. X. Qiao, T. S. Chung, W. F. Guo, T. Matsuura, M. M. Teoh, *Journal of Membrane Science*, **252**, 37-49 (2005)
19. B. E. Poling, J. M. Prasznitz, J. P. O'Connell, *The Properties of Gases and Liquids*, p. A.20-A.34, McGraw-Hill, New York (2001).
20. H. Zhou, Y. Su, X. Chen, Y. Wan, *Separation and Purification Technology*, **79**, 375-384 (2011).

4. MOFS FOR LOW-PRESSURE DETECTION OF METHANE[2]

4.1. Introduction

Enhanced methane detection will facilitate advances in a number of important technical problems, including mine safety, greenhouse gas production, and detection of natural gas leaks. The generally weak interaction between methane and most materials makes detection of low gas concentrations a challenge that has been attacked from many angles using a number of detection methodologies.[1] Currently, the state-of-the-art in detection limit of methane (parts per billion—ppb—levels) can be reached by infrared laser,[2,3] photoacoustic sensors,[4] and gas chromatography,[5] while electrochemical, optical, and solid state technologies allow for parts per million (ppm) detection.[1,6] In some cases, these technologies are relatively bulky. Reducing the size of the sensor package by functionalizing an electro-mechanical or micro-electro-mechanical sensor (MEMS) with an NFM thin film to provide selectivity and enhance sensitivity would allow the detection of low levels of methane in a greater array of environments.

While most of the research effort involving gas uptake by NFMs has focused on high pressure (~35 bar) storage applications,[7] recent work has shown that NFMs could make ideal coating materials to enhance gas uptake and detection at low pressure.[8-12] Chemical sensors based on mass uptake, such as the quartz crystal microbalance (QCM),[13,14] surface acoustic wave (SAW)[14-16] sensors, and MEMS devices such as microcantilevers (MCL)[17] employ transduction mechanisms that rely on an analyte being adsorbed by the device surface. Coating these device surfaces with a highly adsorbent material such as an NFM is therefore essential, since the devices themselves have small surface areas and possess no inherent chemical specificity. Because the porosity, flexibility, and chemical functionality of NFMs can be tailored by appropriate selection of organic linker (or the ions connecting linkers), it is possible to use an NFM to increase sensitivity to a specific analyte. To our knowledge, methane detection limits for sensors that include NFM thin films have not yet been reported.

For high-pressure storage applications using NFMs, it has been shown that high surface areas and free volumes lead to high gas uptake.[18,19] Much effort has gone into creating materials with ever greater surface areas and free volumes to increase storage capacity at a given pressure. However, at low pressures, these factors do not correlate well with gas uptake. In fact, free volume is largely "wasted space" and a detriment to uptake at low pressure.[20,21] The choice of sorbent material clearly depends on the application; NFMs with little capacity for high-pressure methane storage may be excellent candidates for low-level methane detection. The molecular modeling work described herein provides a better understanding of the key factors governing low pressure adsorption in NFMs, which is crucial for efficient screening of materials for gas sensing.

Computational screening of NFMs for adsorption applications is a growing field of study[22] and is a critically important tool for efficiently selecting NFMs with specific properties from the ever-

[2] Todd R. Zeitler, Mark D. Allendorf, Jeffery A. Greathouse "Grand Canonical Monte Carlo Simulation of Low-pressure Methane Adsorption in Nanoporous FrameworkMaterials for Sensing Applications," *J. Phys. Chem. C*, 116 (2012), 3492.

expanding list of published structures. This first step toward NFM selection and/or design allows a rapid selection of a few candidate NFMs before costly gas uptake experiments are performed to select an NFM for a specific application. Classical techniques such as molecular dynamics and Monte Carlo simulation allow computationally inexpensive force field methods to be used to calculate material properties of interest.[23] A downside to screening a large number of diverse materials with different chemical compositions is the lack of validated force fields for each NFM in a given screening set. However, by using a general force field approach such as the Universal[24] or DREIDING[25] force fields, a large set of NFMs may be initially ranked according to some simulated property for more detailed computational or experimental analysis. A number of computational screening studies have been published relating to the storage or separation of industrially relevant small gases[26-36] and also chemical detection of larger organics.[10,31]

Here, we present results of grand canonical Monte Carlo (GCMC) simulations of methane adsorption for select NFMs to assess their capacity for adsorption at low pressure. Additionally, CH_4/N_2 and CH_4/H_2O mixture simulations were performed to test the relative selectivity of promising candidate materials for methane uptake in inert (N_2) or humid (H_2O) environments. The NFMs examined in this work (Table 7) were selected to cover a wide range of NFM properties, including demonstrated potential for high methane uptake (PCNs), "open" metal sites (M_2(dhtp) and Cu-containing MOFs, including PCNs, Cu-BTC, and NOTTs), and extremely high surface area (COFs and UMCMs). Models for each NFM are shown in the Supporting Information. Here we define open metal sites as those metal sites that do not have all of their coordination sites filled. For example, in M_2(dhtp), each metal atom has six potential atomic coordination sites, only five of which are filled. The initial loading of an NFM has been shown to be in smaller, cage-like cavities, rather than large, empty pores.[33,37] For this reason, a set of NFMs with a significant range of pore sizes was selected. Materials with pore sizes on the order of the diameter of the gas of interest tend to show enhanced uptake at low pressure.[27,33,38]

Table 7. Properties of NFMs investigated in this study, arranged by isosteric heat of adsorption (Q_{st}).

NFM	Metal	V_{free}[a] (%)	S.A.[a] (m^2/g)	ρ_{crys} (g/cm^3)	Q_{st} (kJ/mol)	k_H[b] (mmol cm^{-3}-atm)	PLD[c] (Å)	Ref.
M_2(dhtp)-DMF	Zn	16.6	1506	1.77	28.4	2.04	3.8	d
	Ni	14.8	1485	1.75	26.6	2.60	2.1	d
	Co	12.6	1413	1.73	21.1	0.45	2.7	d
M_2(dhtp)-NH_2	Ni	58.9	1873	1.25	14.5	0.90	8.3	d
	Zn	60.3	1829	1.28	14.3	1.08	8.7	d
	Co	60.3	1933	1.23	10.8	0.88	8.6	d
M_2(dhtp)	Mg[e]	62.4	2532	0.91	14.8	0.87	10.8	39
	Zn[e]	62.8	1885	1.22	13.7	0.86	10.9	40
	Co[e]	63.0	1959	1.18	13.6	0.69	11.0	41
	Ni[e]	61.8	1908	1.19	10.5	0.71	10.8	42
PCN-14	Cu	64.2	3337	0.83	21.0	2.14	4.5	43
Cu-BTC[e]	Cu	69.8	2770	0.88	20.0	1.46	6.5	44
PCN-11	Cu	72.5	3101	0.75	19.1	0.78	6.5	45
NOTT-102	Cu	75.4	3655	0.59	16.5	0.90	5.5	46
NOTT-103	Cu	73.6	3524	0.64	16.5	0.97	5.0	46
NOTT-101	Cu	72.8	3359	0.68	16.1	0.90	5.5	46
NOTT-100[e]	Cu	66.6	2909	0.93	15.8	1.39	4.8	47
COF-102	-	76.8	4642	0.42	11.4	0.45	7.9	48
COF-103	-	78.6	4737	0.39	11.3	0.37	8.5	48
UMCM-2	Zn	84.2	3676	0.40	9.5	0.23	8.1	49
COF-108	-	91.1	4625	0.17	7.8	0.13	19.1	48
UMCM-1	Zn	84.2	3789	0.39	5.4	0.22	23.2	50
COF-105	-	90.7	4761	0.18	3.9	0.21	16.0	48

[a]Surface area and free volume of each NFM were calculated via Connolly surfaces[51] in Materials Studio (Accelrys, Inc.), using a 1 Å probe radius.
[b]Henry's constant was calculated as the slope of the adsorption isotherm in the linear region below 5 mbar.
[c]Pore-limiting diameter (PLD) is defined as the minimum pore diameter in the largest pore that spans the NFM structure [27] and was calculated using the HOLE program,[52] which takes into account van der Waals radius when calculating pore size. In this study, diffusion through the pore was not considered.
[d]Structure created in current work.
[e]Zn_2(dhtp) = MOF-74,[40] M_2(dhtp) = M-MOF-74,[53] = CPO-27-M[54] = M/DOBDC,[55] Cu-BTC[56] = HKUST-1[44], NOTT-100[57] = MOF-505[47]

4.2. Simulation Methods

4.2.1. Structural Models

Except where noted below, models for the NFMs in this work (Table 7) were taken from published single-crystal X-ray diffraction structures. Non-orthogonal unit cells were made orthogonal for ease of simulation and analysis (this was the case for all NFMs, except for the COFs and Cu-BTC). Solvent molecules were deleted where appropriate, yielding an "activated" structure. In some cases with site disorder (e.g., UMCM-2), the structure was made to represent the chemical formula in the original paper.

Table 8. Typical characteristics of three sensing devices.

Sensor Type[a]	Sensing Area (cm^2)	Minimum Detectable Mass	Sensing Limit, L_s (ng/cm^2)	Relative Sensitivity[b]
QCM	1.0	1 ng	1.0	1
SAW	0.10	1 pg	0.01	100
MCL	0.00025	1 fg	0.004	250

[a]Resonant frequencies assumed for this comparison are: QCM = 5 MHz,[84] SAW = 100 MHz,[84] MCL = 300 kHz.[85]
[b]Sensitivity relative to sensitivity of QCM.

MOF structures based on the 2,5-dihydroxyterephthalate (dhtp) linker are noted for their high density of open metal sites that display enhanced binding of small molecules.[39] An atomic structure is not available for the Mn version of the M_2(dhtp) series (also known as M-MOF-74, CPO-27-M, and M/DOBDC analogs). While one group[32] has cited Ref. 58 for its Mn_2(dhtp) model, this reference only provides unit cell parameters (noting that it is "isostructural" with other members of this series) and not atom positions. For this reason, Mn_2(dhtp) is not included in this work.

For structures in the M_2(dhtp) series, models including attached solvent molecules were investigated to determine the effect of solvent interactions and pore size on methane uptake. For the Zn_2(dhtp) model, dimethylformamide (DMF) solvent molecules were given atomic positions based on the original structure,[40] with site disorder in the DMF molecule handled as above. For the Ni_2(dhtp) and Co_2(dhtp) models, in which H_2O molecules occupy the open metal sites in the as-synthesized structure,[41,42] we replaced these with DMF molecules having coordinates determined via geometry optimization of atomic positions using universal force field (UFF)[24] parameters with atomic charges assigned from a charge-equilibration algorithm,[59] keeping framework atoms fixed at their crystallographic coordinates. Additionally, for structures in the M_2(dhtp) series, amine functionalization of the linker was investigated by replacing one hydrogen atom on each linker ring with an amine (NH_2) group. The final position of the amine group was determined as described above for DMF. While the geometry-optimized structure shows a likely configuration of the amine group on the linker, it is also possible that the amine group could rotate into another position (there is no lack of room in the pore, for example).

However, the necessity of using a rigid model in the simulations for computational economy prevents us from completely exploring this possibility.

4.2.2. Force Field

Because methane has no dipole moment, it can be represented as a single-site model for room-temperature simulations.[60,61] Electrostatic interactions between methane and framework atoms are therefore not included in our simulations. UFF[24] parameters are applied to NFM framework atoms and solvent molecules (DMF or amine). All potential parameters are given in Table 10. Parameters for methane-NFM and methane-solvent interactions were determined by Lorentz-Berthelot combination rules.[62] This combination of force field parameters has been used successfully to model gas adsorption and diffusion by NFMs.[32,34,63,64] For mixture simulations, the SPC/E model[65] was used for H_2O. A three-site TraPPE model[66] was used for N_2. Because the models used for H_2O and N_2 include charged species, the framework atoms for the NFMs involved in mixture simulations were also prescribed charges. Framework charges were determined using the CBAC method of Zhong et al.[67-69] except that SPC/E model charges were used for structural water molecules.

Table 9. Calculated Henry's constants for pure methane and mixture simulations of three representative NFMs

input stream	H_2O or N_2 content	Henry's Constant (mmol/cm^3-atm)		
		PCN-14	Cu-BTC	Zn_2(dhtp)
pure CH_4	0% R.H. H_2O	2.14	1.46	0.86
mixture	10% R.H. H_2O	2.15	1.47	0.15
mixture	100% R.H. H_2O	2.15	1.45	0.00
pure CH_4	coordinated H_2O[a]	3.30	1.93	-
mixture	1 bar N_2	2.00	1.29	0.84

[a]Bound to the open metal sites.

4.2.3. GCMC Simulation

Adsorption of methane was investigated via GCMC simulation (constant methane chemical potential μ, volume V, temperature T 298 K) using the Towhee program[71] for rigid framework models of NFMs. The following probabilities were employed for GCMC moves involving methane particles: insertion/deletion (50%); translation (25%); intrabox reinsertion (25%). For mixture simulations, the probabilities were modified as follows to allow for rotation and configurational-biased growth of H_2O and N_2 molecules: insertion/deletion (40%); translation (15%); intrabox reinsertion (15%); rotation (15%); growth (15%). For each chemical potential, 10^7 steps were used to equilibrate the system, and a further 10^7 were used for data collection. A cutoff radius of 12.5 Å and multiple unit cells were used so that each cell parameter had a minimum dimension of 25 Å. Rigid frameworks (i.e., no framework NFM or solvent atoms are allowed to move) have been found to be sufficient for this type of calculation,[10,72] and were used here in all cases.

The Towhee code requires analyte chemical potentials rather than pressures as input. As in our previous work,[73] we used "empty box" GCMC simulations (i.e., simulations without an NFM framework) to determine methane pressure at a given chemical potential. To calculate excess adsorption (N_{ex}) from total or absolute adsorption (N_{abs}),[73] we have used the definition $N_{ex} = N_{abs} - V_g\rho_g$, where V_g is the void volume of the NFM structure as determined by the Connolly surface method (Table 7) and ρ_g is the gas density calculated from the empty box simulations.

4.2.4. Q_{st} and Henry's Constant

The Henry's constant quantifies the initial affinity of a host material for a guest and was calculated as the slope of the adsorption isotherm in the linear region below 5 mbar. The isosteric heat of adsorption (Q_{st}) at infinite dilution[74] was calculated from a fixed-loading simulation of a single methane molecule in a given framework. For each NFM, Q_{st} was evaluated as follows: $Q_{st} = \langle E_{gh} \rangle - \langle E_g \rangle - \langle E_h \rangle - RT$, where E_{gh} is the simulation energy of the single guest molecule in the NFM host framework, E_g is the energy of the guest molecule in the ideal reference state (equal to zero in all cases considered here), E_h is the energy of the host framework with no gas present, R is the gas constant and T is temperature in K.

4.3. Results and Discussion

4.3.1. High Pressure Results

Isotherms for total methane adsorption at 298 K are shown in Figure 21. While many studies of materials for gas storage applications examine excess adsorption (which can be experimentally measured),[75] for low-level detection applications, absolute or total uptake is more relevant. Because we are interested in identifying trends in methane adsorption for the selected NFMs for screening purposes, close agreement with experimental isotherms is not crucial. However, our predicted isotherms for the M_2(dhtp) series agree very well with simulated isotherms from Ye, et al.[32] (Figure 22), which were shown to compare well with experimental measurements.[39] The simulated COF results agree qualitatively (i.e., COFs 102 and 103 show similar adsorption behavior) with the experimental measurements of Furukawa, et al.[18] Previous modeling results of these COFs qualitatively agree with the current model.[76,77] There is also reasonable agreement between experimental data and our simulated isotherm for UMCM-1 (Figure 23). One simulation study of methane uptake in the UMCMs exists,[32] which shows very similar behavior between UMCM-1 and UMCM-2.

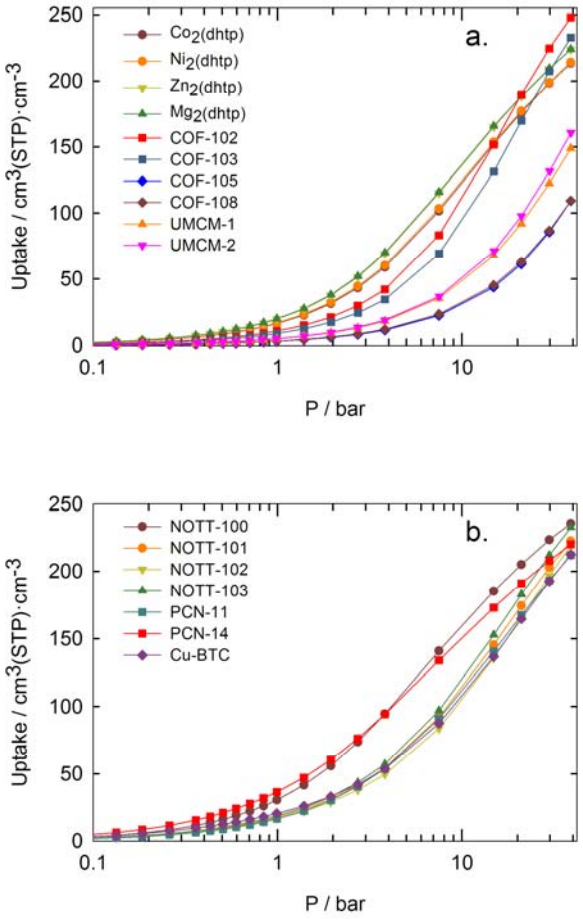

Figure 21. **Methane adsorption isotherms at 298 K for: a) M_2(dhtp) series, UMCM series, COF series, and b) Cu-based NFMs.**

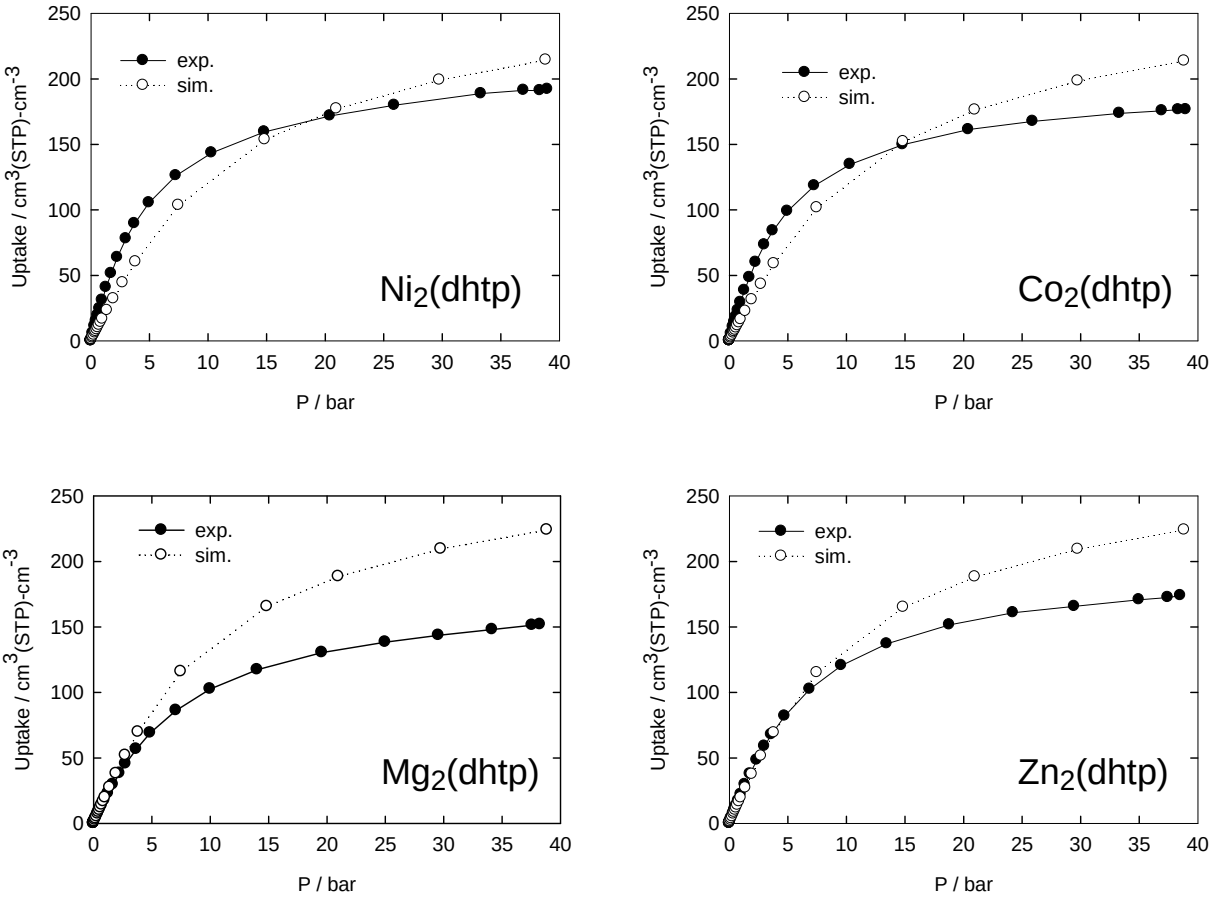

Figure 22. Excess volumetric methane adsorption for M_2(dhtp) at 298 K, compared with experimental values.[1]

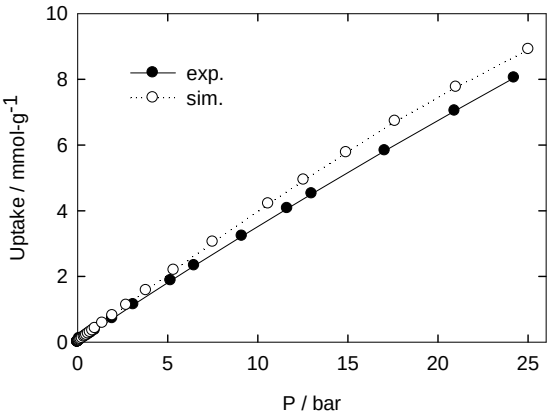

Figure 23. Excess methane adsorption for UMCM-1 at 298 K, compared with experimental values.[2]

The excellent agreement between our model and experimental results[45] for PCN-11 at low and high pressure is shown in Figure 25. Additionally, good agreement is seen for two other copper-based MOFs (Figures 25 and 26). To date, no methane adsorption studies (experimental or theoretical) have been reported for the NOTT compounds. Simulated methane adsorption isotherms for PCN-11 and PCN-14 have not been previously reported, although an investigation of their methane adsorption behavior was recently reported.[33] Notably, there is also good agreement with previous simulation[78,79] and experiment[56] for methane adsorption by Cu-BTC (also known as HKUST-1) at low pressure. Overall, the excellent agreement between published adsorption isotherms and those obtained using the present models gives us confidence in our approach for computational screening.

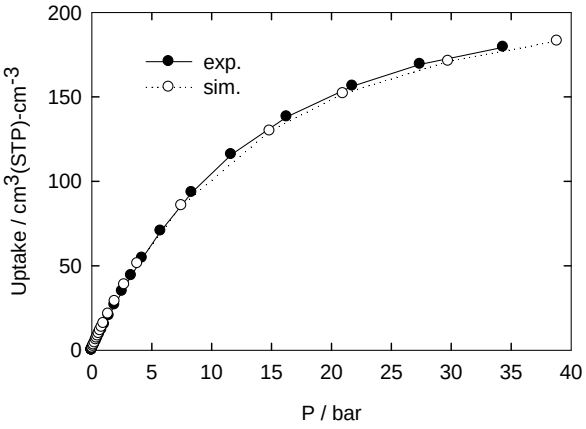

Figure 24. Excess volumetric methane adsorption for PCN-11 at 298 K, compared with experimental values.[45]

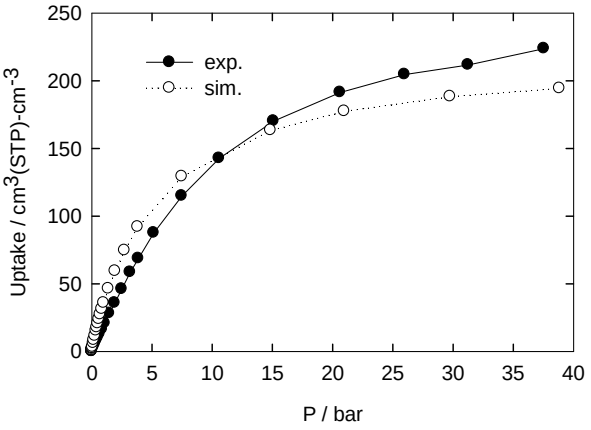

Figure 25. Excess volumetric methane adsorption for PCN-14 at 290 K, compared with experimental values.[3]

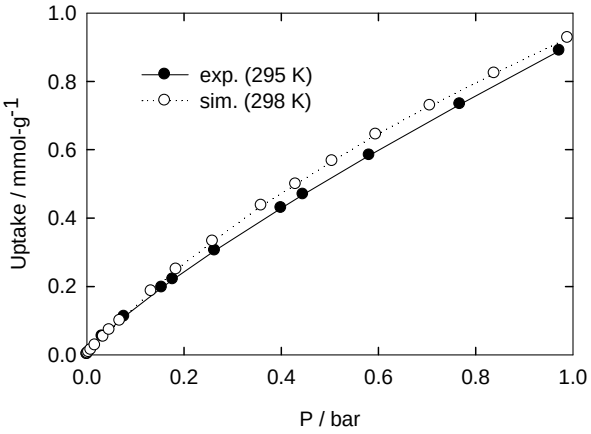

Figure 26. Excess methane adsorption for Cu-BTC, compared with experimental values.[4]

4.3.2. Low Pressure Results

Many of the NFMs studied here were chosen for their remarkable methane adsorption capacity at high pressure. However, a comparison of Figure 21 and Figure 27 shows that while at high pressures (35-40 bar) there is little relative difference in methane uptake, at low pressures, there can be great differences. In fact, some NFMs with little methane capacity at high pressure are the best performers at low pressure. For example, Cu-BTC outperforms Zn_2(dhtp) and NOTT-103 below 1 bar, but has the lowest uptake of the three above 2 bar. Similarly, below about 4 bar, PCN-14 has a greater uptake than NOTT-100, but in the high pressure regime, these roles are reversed. Most dramatically, COF-102 shows the lowest uptake at low pressure (Figure 27), but is the best performer of all NFMs considered here above 20 bar (Figure 21a).

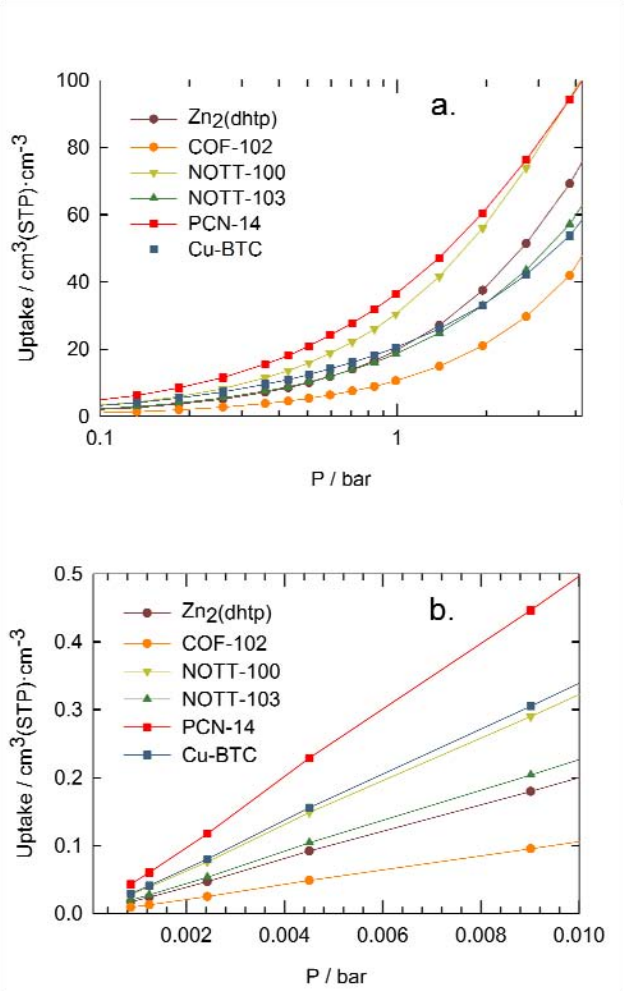

Figure 27. Adsorption isotherms for selected NFMs at moderate (a) and very low (b) pressure. The ranking of a group of NFMs with respect to uptake is pressure dependent.

Because they are a measure of initial adsorption behavior, Henry's constant and the isosteric heat of adsorption are good predictors of low pressure adsorption. Pore size plays a more important role in predicting initial adsorption behavior in NFMs than properties such as surface area or free volume.[7,31,33] Figure 28 shows the inverse relationship between Q_{st} and pore-limiting diameter (PLD) for the NFMs in Table 7. A similar plot for some of the same NFMs can be found in Ref. 32, though interatomic distances rather than van der Waals radii were apparently used to calculate pore diameters (these authors report pore diameters on the order of 13.5 Å for the M_2(dhtp) series, while our calculated values are ~10.8 Å). Figure 28 clearly shows the enhancement of Q_{st} as the PLD approaches the kinetic diameter of a methane molecule (~3.8 Å).[80] Differences in methane Q_{st} values within the M_2(dhtp) series can be attributed to the potential parameters used for each metal (Table 10), in particular the large van der Waals well depths for Mg and Zn compared to Co or Ni.

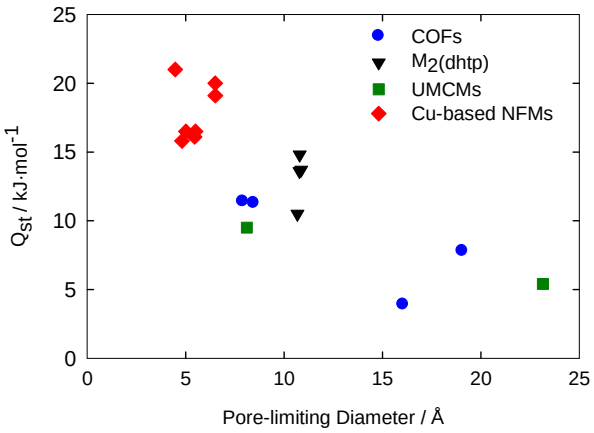

Figure 28. Isosteric heat of adsorption (Q_{st}) versus pore-limiting diameter for selected NFMs.

Table 10. Potential parameters for methane,[60,61], nitrogen,[66] water,[70] NFM framework atoms,[24] and coordinated solvent molecules[24] in this study.[a]

Atom	σ (Å)	ε/k_B (K)
CH_4	3.73	148.0
C	3.43	52.8
H	2.57	22.1
N	3.26	34.7
O	3.12	30.2
B	3.64	90.6
S	3.59	137.9
Si	3.83	202.3
Co	2.56	7.0
Cu	3.11	2.5
Mg	2.69	55.9
Ni	2.52	7.5
Zn	2.46	62.4
$N\text{-}N_2$[b]	3.31	36.0
N-COM	0.00	0.0
OW[c]	3.17	78.2
HW	0.00	0.0

[a]For nonbonded energy $E_{ij} = 4\varepsilon_{ij}[(\sigma_{ij}/r)^{12} - [(\sigma_{ij}/r)^6]$ between single-site methane molecules and framework atoms separated by a distance r.
[b]The N_2 model is made up of a central N-COM atom bonded to two $N\text{-}N_2$ atoms at a distance of 0.55 Å, forming an angle of 180°.
[c]The H_2O model is made up of a central OW atom bonded to two HW atoms at a distance of 1.0 Å, forming an angle of 109.47°.

It should also be noted that PLD is not a complete description of the pore and in some cases pores associated with the PLD may not contain the sites of initial uptake. One example of this is Cu-BTC, where the initial uptake occurs in the small cages, while the PLD is calculated for a different pore (by the definition of Haldoupis et al.[27]). The details of how PLD is defined with respect to pore shape and the location of the initial uptake sites can account for the differences in Q_{st} and k_H for the Cu-based NFMs, all of which have similar PLDs but varying adsorption properties. For example, while the PLD of NOTT-100 is only slightly greater than that of PCN-14, its Q_{st} value is nearly 5 kJ/mol less favorable. This discrepancy can be partly explained by differences in pore shape. As seen in Fig. S6, the geometry and electronic environment of the PCN-14 pore leads to highly localized binding of a methane molecule. In contrast, methane adsorption in NOTT-100 is relatively diffuse, possibly due to the lower degree of conjugation in the biphenyltetracarboxylate linker compared to the 9,10-diphenylanthracenetetracarboxylate linker in PCN-14. These differences are consistent with the greater Q_{st} value in PCN-14 compared with NOTT-100. In general, however, the overall correlation of PLD with Q_{st} and k_H is clearly excellent.

Our results show that NFMs with smaller pore diameters have a greater ability to adsorb methane at low pressures. In particular, the Cu-based NFMs studied here show the greatest Q_{st} values, indicating significant methane uptake at low pressure. A similar plot comparing Henry's constant values with PLD (Figure 29) shows a similar trend—a dramatic increase at low PLD values. These trends in initial methane uptake are confirmed by recent neutron diffraction results, which show deuterated methane initially adsorbed by Cu-BTC in the small cavities and subsequently at open metal sites in the large cavities.[37]

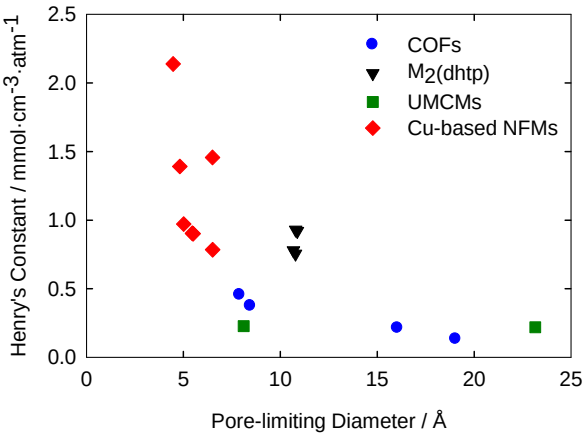

Figure 29. Henry's constant versus pore-limiting diameter for selected NFMs.

4.3.3. Functionalization with Coordinated Solvent

A number of experimental studies[31,81,82] have used linker functionalization to enhance uptake. The amine (NH_2) group represents a small yet synthetically simple way to modify the chemical and physical property of organic linkers. In an effort to enhance van der Waals interactions between a methane molecule and the framework, and thus enhance uptake, amine

functionalization was carried out by exchanging one half of the hydrogen atoms of M_2(dhtp) on each linker with an NH_2 group. In as-synthesized Zn_2(dhtp) (MOF-74),[40] DMF occupies the pores while coordinating open metal sites. The Ni and Co versions[41,42] of this NFM were synthesized with H_2O as their solvent, but the effect of decreasing pore size on CH_4 adsorption was examined by replacing H_2O with DMF, followed by a geometry optimization of the DMF molecule. The only available structure of the Mg_2(dhtp)[39] is the activated compound (i.e., a "relaxed" structure following solvent removal), so a version with DMF was not investigated here.

Figure 30 shows that amine functionalization results in a slight increase in methane uptake at low pressures for the M_2(dhtp) MOFs, while DMF functionalization results in even more significant low-pressure methane uptake. These results can be further quantified by defining enhancement as the proportional increase in uptake by the functionalized NFM compared to the activated NFM. Figure 31 shows that there is a ~25% enhancement of methane uptake at low pressure (< 10 mbar) with inclusion of one amine group on each linker for each member of the M_2(dhtp) series. DMF functionalization results in even more dramatic enhancement. For gas storage applications, solvent would be removed to both increase available pore volume and expose reactive metal sites. Amine functionalization reduces the PLD of M_2(dhtp) MOFs from 10.9 Å to approximately 8.6 Å, while coordinated DMF results in a PLD approximately the same size as a methane molecule (Table 7). The enhanced methane uptake at low pressure by the functionalized M_2(dhtp) MOFs is due to increased van der Waals interactions in the smaller pore.[33,38]

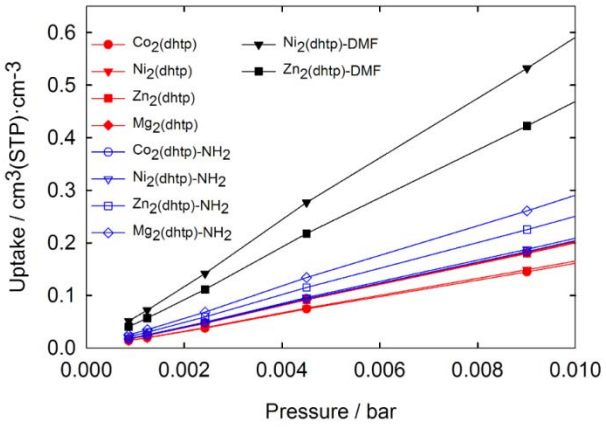

Figure 30. Methane adsorption isotherms at 298 K for the M_2(dhtp) series, including functionalized NFMs.

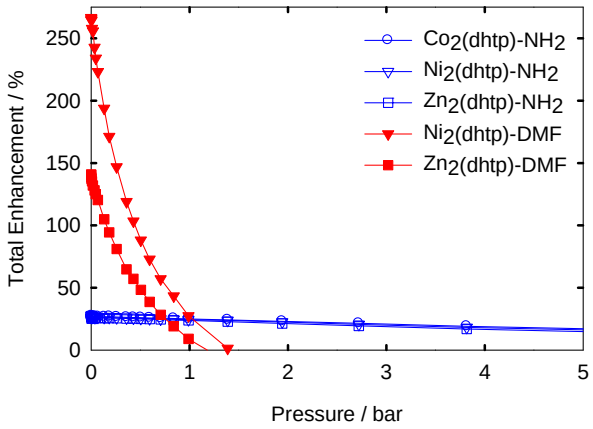

Figure 31. Enhancement of methane uptake as a function of pressure for functionalized M_2(dhtp) series NFMs.

Figure 32 shows two-dimensional probability density plots of methane adsorption in both activated (i.e., with pore solvent removed) and functionalized Zn_2(dhtp). As expected for the activated NFM, the greatest uptake occurs at the open metal sites (which in a 2-D projection form the vertices of a hexagon). Enhanced uptake at these sites is seen with amine-functionalization. This is likely due to increased van der Waals interactions with the amine group, as well as a reduction in pore diameter. Interestingly, even though DMF functionalization limits methane adsorption essentially to the center of the pore, adsorption is greatly enhanced at these sites.

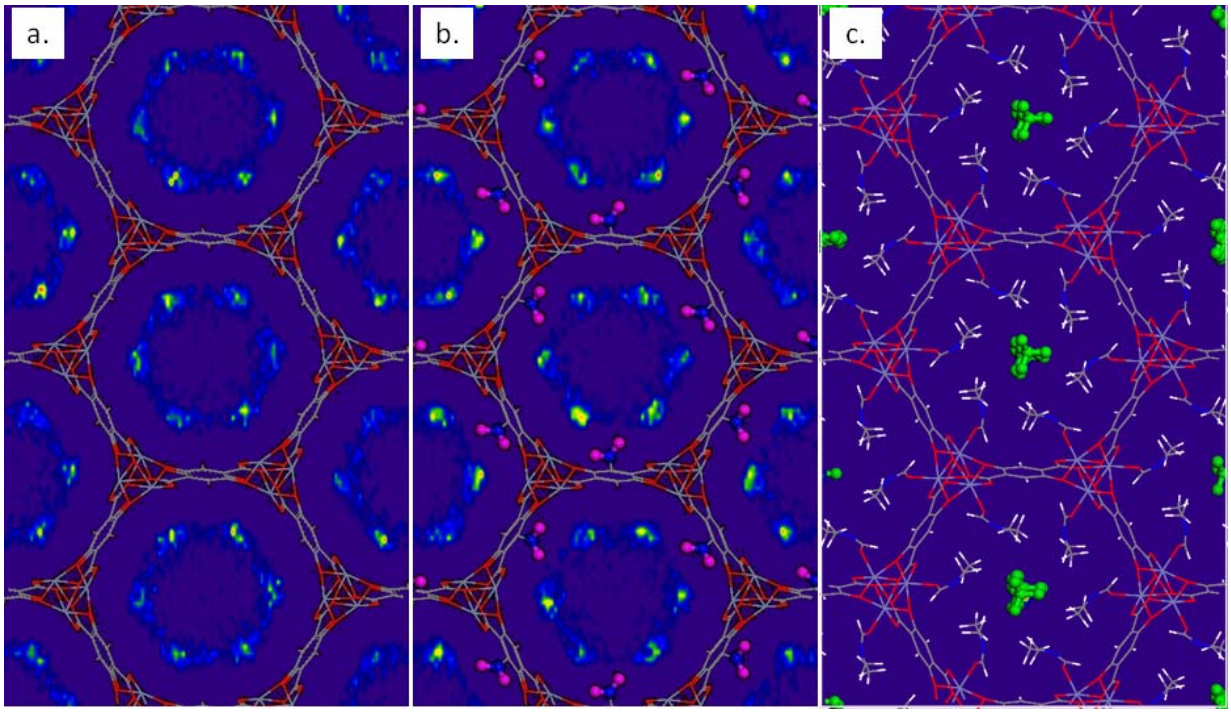

Figure 32. Probability density plots in the *xy* plane of methane adsorption in: a) Zn_2(dhtp), b) Zn_2(dhtp)-NH_2, c) Zn_2(dhtp)-DMF at 298 K and 2 atm. In c), methane positions are shown as a 5-site model, for clarity. Density plots for Ni_2(dhtp) and Co_2(dhtp) are similar and shown as Figures 33 and 34.

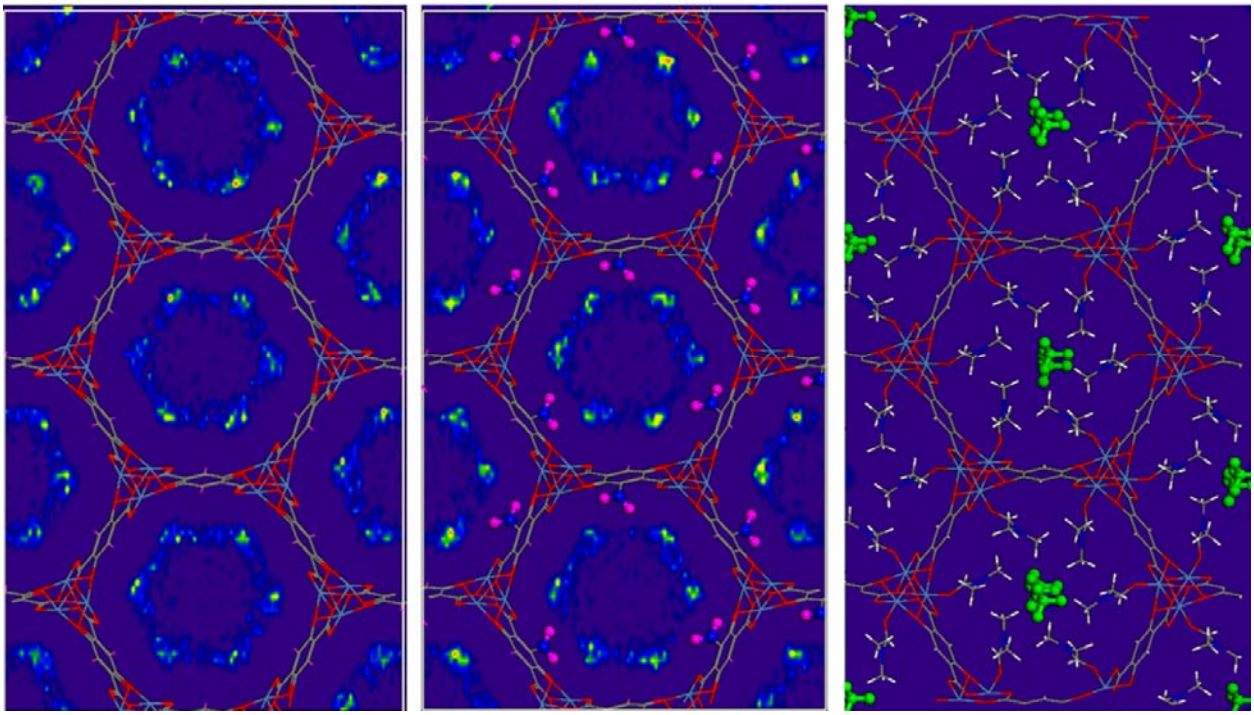

Figure 33. Probability density plots in the *xy* plane of methane adsorption in: a) Ni_2(dhtp), b) Ni_2(dhtp)-NH_2, c) Ni_2(dhtp)-DMF at 298 K and 2 atm. In c), methane positions are shown as a 5-site model, for clarity.

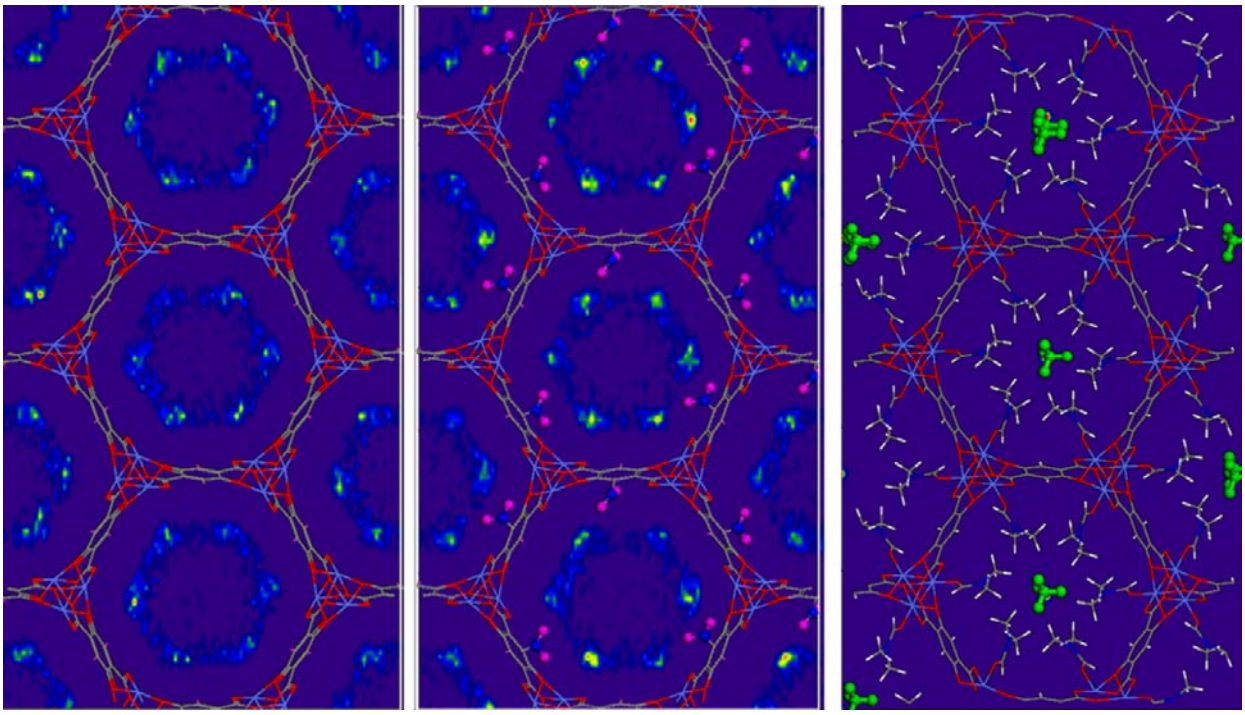

Figure 34. Probability density plots in the *xy* plane of methane adsorption in: a) Co_2(dhtp), b) Co_2(dhtp)-NH_2, c) Co_2(dhtp)-DMF at 298 K and 2 atm. In c), methane positions are shown as a 5-site model, for clarity.

A comparison of Q_{st} values (Figure 35) and Henry's constants (Figure 36) for functionalized M_2(dhtp) shows the expected relationship to pore diameter. The loss of open metal sites is compensated by a corresponding reduction in pore diameter, and a net enhancement of uptake is seen. However, the presence of the bulkier DMF molecules decreases the pore size to that of a methane molecule, such that there are increased interactions throughout the pore.

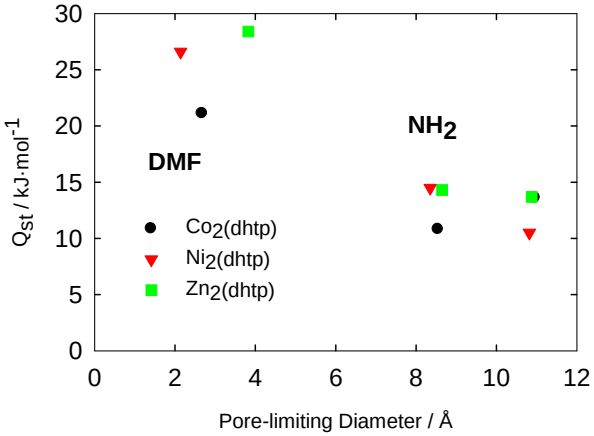

Figure 35. Isosteric heat of adsorption (Q_{st}) versus pore-limiting diameter for functionalized M_2(dhtp) MOFs.

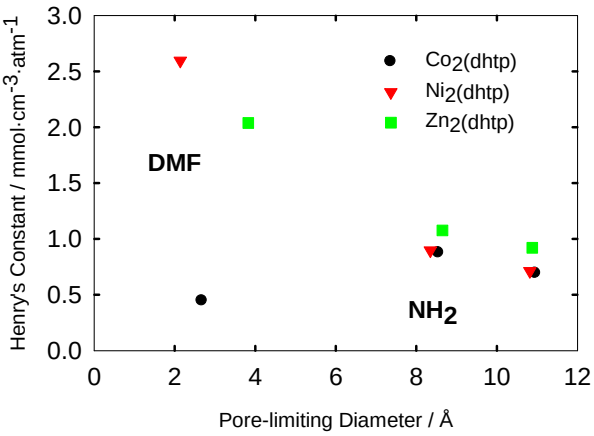

Figure 36. Henry's constant versus pore-limiting diameter for modified M_2(dhtp) series.

We note that the Henry's constant for DMF-functionalized Co_2(dhtp) (Figure 36) is much lower than expected. An examination of the accessible diameter along the pore (essentially, a 1-D van der Waals surface, Figure 37) helps to explain this anomaly. The PLDs of Ni_2(dhtp)-DMF (2.14 Å) and Co_2(dhtp)-DMF (2.68 Å) following optimization of the DMF molecule in the pore are both below the expected threshold of 3.73 Å (the van der Waals diameter of the modeled methane). Yet the one-dimensional methane density profiles (Figure 37) show that both DMF-functionalized MOFs have accessible regions large enough to accommodate a methane molecule. At their widest points, Ni_2(dhtp)-DMF has a slightly larger pore diameter than Co_2(dhtp)-DMF (Figure 37). At the low pressures for which the adsorption isotherm is linear, there is relatively little methane uptake by Co_2(dhtp)-DMF, and thus the Henry's constant is relatively small.

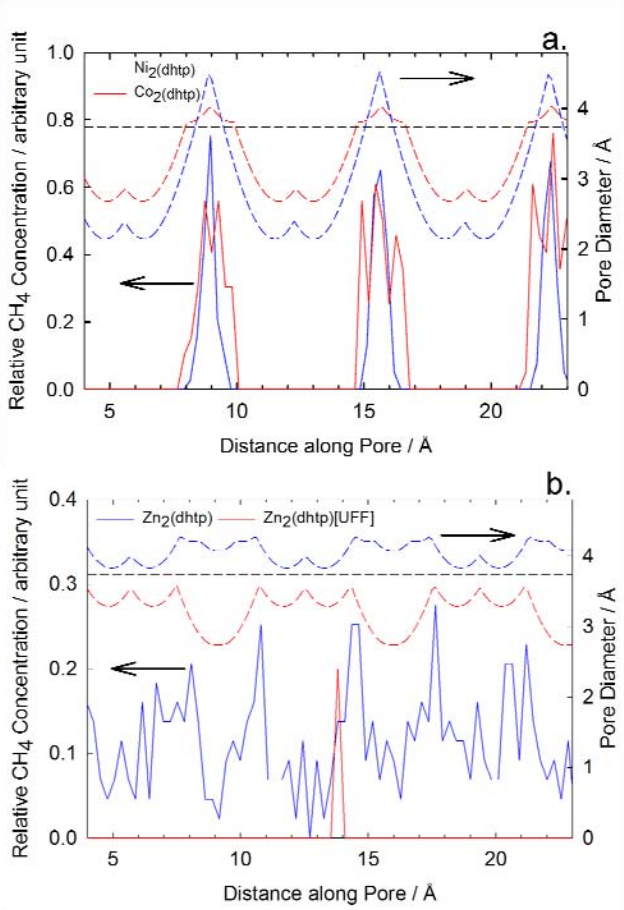

Figure 37. One-dimensional density profiles (solid lines) along the pore channel at 2 bar for: a) Ni_2(dhtp)-DMF and Co_2(dhtp)-DMF and b) Zn_2(dhtp)-DMF and Zn_2(dhtp)-DMF[UFF]. Also shown are the corresponding pore diameters for each NFM as a function of distance through the channel (dashed lines). The dotted horizontal line represents a pore diameter equal to the van der Waals diameter of the modeled methane molecule (3.73 Å).

Interestingly, when the DMF structure is optimized at the open metal sites in Zn_2(dhtp)-DMF, the pore structure changes such that the *maximum* diameter is about 3.6 Å (whereas in the as-synthesized, solvent-free case the minimum diameter is about 3.8 Å), and adsorption at 2 bar drops from 27 to 0.12 cm^3(STP)/cm^3. Figure 37b shows the difference between the original Zn_2(dhtp)-DMF pore structure and the UFF-optimized DMF structure (Zn_2(dhtp)-DMF[UFF]). While the pore diameter of the unoptimized Zn_2(dhtp)-DMF is always above the threshold (and thus methane is adsorbed all along the pore), for Zn_2(dhtp)-DMF[UFF], the pore diameter is below the threshold at all points, and there is only one methane molecule adsorbed over the entire 10^7 steps of the GCMC simulation. The results in Figure 37 indicate that using UFF force field parameters to find the energy-optimized position of coordinated DMF molecules is not a perfect solution, and we might not expect that an experimentally created Ni_2(dhtp)-DMF would have such a small pore diameter. Nevertheless, the enhancement of methane uptake due to pore size reduction, even by eliminating open metal sites, has been clearly shown. An additional factor not considered here is that of gas diffusion within the pores. In designing a material whose PLD is optimized to accommodate gases with a specific size range, the adsorbed gas particles

must also be able to overcome diffusion barriers. Diffusion considerations have been used previously to screen NFMs for potential methane uptake based on both adsorption and diffusion properties.[27]

4.3.4. Detection Limits

The minimum analyte concentration necessary to register a sensor signal can be considered the detection limit. The sensing limit of a device is based on the minimum frequency shift that can be measured and is expressed in terms of mass of analyte per unit area of the sensor. By comparing the adsorption behavior of a material at low analyte loading, we gain insight into that material's sensitivity for a particular analyte. In this way, candidate materials can be computationally screened for their suitability for sensing applications.

Of the three sensing devices considered (QCM, SAW, and MCL), each has a different sensing limit resulting from their respective transduction mechanism and unequal sensing areas. Typical sensing areas and approximate minimum detectable masses for these three devices are given in Table 8. A thin film of a selected NFM could be deposited on each of these devices. The NFM film thickness required to detect a given methane concentration is easily derived from a simple consideration of volumetric uptake, gas density, volume of NFM (sensing area multiplied by thickness), and the definition of Henry's constant. For a given sensing limit (minimum detectable mass divided by device sensing area), and based on the calculated uptake density at a given pressure (from GCMC simulation), the minimum NFM film thickness for methane detection can be calculated by the following:

$$t = \frac{L_s}{100 * \rho_{gas,STP} * N_{total}} = \frac{L_s}{2440 * \rho_{gas,STP} * k_H * P_{gas}} \quad (1)$$

where t is the minimum NFM thickness (nm), L_s is the sensing limit of the device (ng·cm^{-2}), N_{total} is the total gas uptake by the NFM (on a volume(STP)/volume basis), ρ_{gas} is the density of the analyte gas at STP (298 K and 1 atm), k_H is the Henry's constant (mmol/cm^3·atm), and P_{gas} is the partial pressure of the analyte (atm). The density of methane at STP is 6.56 x 10^{-4} g·cm^{-3},[83] which was reproduced here (6.60 x 10^{-4} g·cm^{-3}) via GCMC simulation of bulk methane as a validation of the methane potential parameters used in the current study. This relationship is valid in the linear region of the adsorption isotherm where Henry's Law holds. While Q_{st} is useful for establishing the thermodynamics of gas adsorption at low pressure, in these simulations its effect is limited to a single adsorbate per simulation cell. Here the Henry's constant finds more utility as it allows for extrapolation to much lower concentrations such that we can reach the limit of detection of a practical device without having to simulate an unreasonably large simulation cell.

Table 11. Typical characteristics of three sensing devices.

Sensor Type[a]	Sensing Area (cm^2)	Minimum Detectable Mass	Sensing Limit, L_s (ng/cm^2)	Relative Sensitivity[b]
QCM	1.0	1 ng	1.0	1
SAW	0.10	1 pg	0.01	100
MCL	0.00025	1 fg	0.004	250

[a]Resonant frequencies assumed for this comparison are: QCM = 5 MHz,[84] SAW = 100 MHz,[84] MCL = 300 kHz.[85]
[b]Sensitivity relative to sensitivity of QCM.

Calculated minimum NFM thicknesses for methane detection with PCN-14 (the NFM with greatest low-pressure uptake performance in this study) are shown in Figure 38 for all three devices. The three lines are based on the same loading uptake values (Figure 21b), but scaled relative to one another by the sensing limit of the indicated device. The results show that as a best-case scenario (i.e., defect-free NFM coatings, ignoring competitive adsorption from other gases), a 100-nm thick film of PCN-14 could be used in an MCL-based sensor to detect a methane level of about 10 ppm (a film twice as thick could detect to 5 ppm), while the same film on a SAW device could detect methane levels as low as 25 ppm. On a QCM, a 100-nm thick film could detect about 2500 ppm (2.5 mbar) of methane.

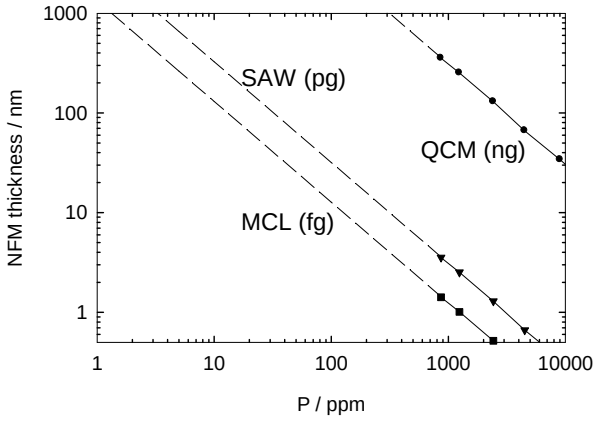

Figure 38. Minimum PCN-14 film thickness to achieve detectable levels of methane in three sensing devices, based on sensor specifications in Table 8. Dashed lines indicate values extrapolated based on the Henry's constant for methane adsorption by PCN-14.

4.3.5 Selectivity for Methane over H_2O and N_2

While the pure methane simulation results presented above provide useful guidance for selecting NFM structures that are promising for methane uptake, the selectivity of the NFM for methane in the presence of other gases is also an important consideration for sensing applications. Two gases often present in the background gases of a sensor are nitrogen and water. We therefore performed GCMC simulations using mixtures of methane with these gases, selecting three MOFs

(PCN-14, Cu-BTC, and Zn_2(dhtp)) representative of the structural types that exhibit good methane uptake based on their Henry's constants (Table 7). For CH_4/N_2 simulations, the loading pressure of N_2 was kept constant at 1 bar. Simulations of CH_4/H_2O mixtures were run for varying water content, including 10 and 100% relative humidity (R.H.). Based on the SPC/E water model used here, a water vapor pressure of 0.01 bar represents full saturation (100% R.H.) at 298 K.[70]

For PCN-14 and Cu-BTC, which have open metal sites, additional pure methane simulations were run for modified structures in which water molecules were bound to each of the open metal (Cu(II)) sites in the structures. In both cases, oxygen positions for these structural water molecules were obtained from the original crystal structure files, and hydrogen positions were obtained by an optimization routine identical to that described above for NH_2 and DMF positions on modified M_2(dhtp) structures. The atomic positions of the coordinated water molecules were kept fixed as part of the framework during the pure methane simulations. Results for mixture simulations are summarized in Table 12. We note that methane k_H values are only slightly lower (2-12%) in the presence of 1 bar N_2.

Table 12. Calculated Henry's constants for pure methane and mixture simulations of three representative NFMs

input stream	H_2O or N_2 content	Henry's Constant (mmol/cm^3-atm)		
		PCN-14	Cu-BTC	Zn_2(dhtp)
pure CH_4	0% R.H. H_2O	2.14	1.46	0.86
mixture	10% R.H. H_2O	2.15	1.47	0.15
mixture	100% R.H. H_2O	2.15	1.45	0.00
pure CH_4	coordinated H_2O[a]	3.30	1.93	-
mixture	1 bar N_2	2.00	1.29	0.84

[a]Bound to the open metal sites.

The results of these mixture simulations demonstrate that chemical intuition is not an infallible guide to selecting the best NFM for methane sensing. Surprisingly, methane uptake by PCN-14 is not affected by the presence of water at up to 100% R.H., indicating that CH_4 and H_2O molecules do not compete for the same sites at very low CH_4 content. In fact, while some snapshots of the simulation show individual large cages completely filled with water molecules (Figure 39), there is no effect on overall uptake in the Henry's regime. Several simulations were extended by an additional 2×10^7 steps with no change in water loading. The selective filling of some pores with water while other pores remain empty indicates the strong preference for water to form hydrogen-bonded clusters. Moreover, when all open Cu sites are coordinated by H_2O molecules (the as-synthesized condition), CH_4 uptake actually *increases*. In this case, it is likely that the modified pore structure (i.e., reduced pore size) provides additional sites for methane uptake. In the presence of a constant background of N_2, the GCMC results indicate only a slight (7%) decrease in CH_4 uptake. These relatively minimal effects of background N_2 and water vapor confirm that PCN-14 is an excellent candidate methane sensing.

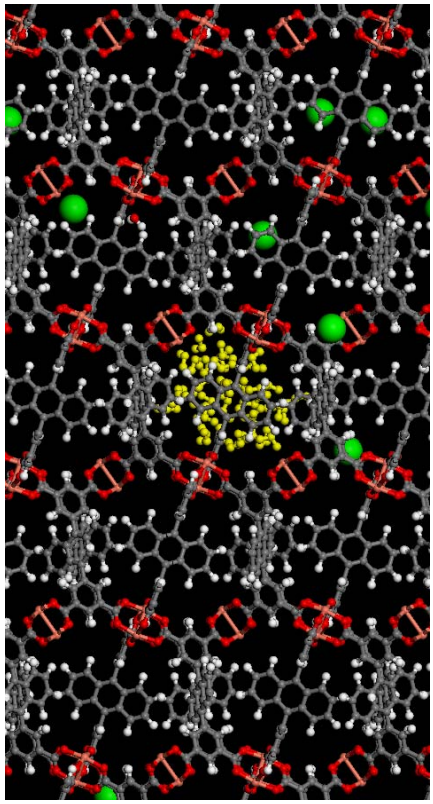

Figure 39. Simulation snapshot for a mixture of 50 mbar CH_4:0.01 bar H_2O in PCN-14. Green spheres represent CH_4 molecules and yellow spheres belong to H_2O molecules.

The behavior of Cu-BTC in the presence of H_2O is similar to PCN-14; there is no effect on methane uptake. Inspection of the density profiles (Figure 40) suggests that there is no competition between CH_4 and H_2O for adsorption sites, and thus no effect on CH_4 uptake due to H_2O. This result is in agreement with another modeling investigation showing that water and methane are adsorbed at separate sites in the Cu-BTC structure—water at the open metal sites and methane in the small cages.[86] However, in that study, CH_4/H_2O mixture simulation results were not presented, so the effects of a true competition for adsorption sites were not determined.

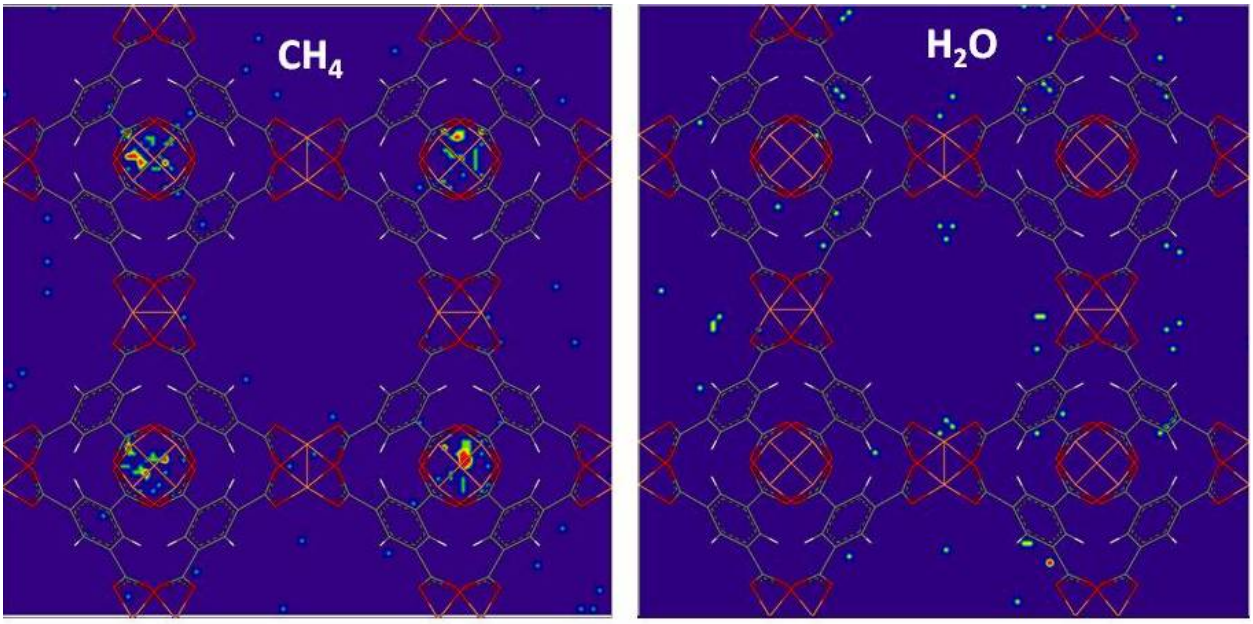

Figure 40. Probability density plots of methane and water adsorption in Cu-BTC for a mixture of 70 mbar CH_4:0.01 bar H_2O.

It should also be noted that the results of recent studies of CH_4 uptake in Cu-BTC indicate that classical GCMC simulations are not able to fully describe the interaction of CH_4 with open Cu sites because the Lennard-Jones description of short-range interatomic interaction using UFF does not allow CH_4-Cu separations as small as those found via neutron powder diffraction[37] or electronic-scale DFT calculations.[87] However, in these studies there is no CH_4 adsorption at open Cu sites for loadings below 25 molecules per unit cell. In the pressure region considered here for the mixture study of Cu-BTC (below 70 mbar), CH_4 uptake is only a fraction of a molecule per unit cell. So, although GCMC simulations with UFF are not able to properly describe CH_4-Cu interactions at higher uptake levels, the CH_4 uptake considered here is well below the onset of adsorption at open Cu sites predicted by DFT calculations.[87] New methods for deriving appropriate potential parameters to better describe the interaction between small analyte molecules and open metal sites are the subjects of recent work.[87-88]

However, as with PCN-14, in the as-synthesized condition in which the Cu open metal sites are occupied by chemisorbed water, in a dry atmosphere the uptake of methane is actually enhanced relative to the fully activated material in which there is no chemisorbed water. This is reminiscent of previous work showing enhanced CO_2 uptake in the presence of coordinated water on the Cu open metal sites in Cu-BTC.[86,87] In that same work, no effect on CH_4 uptake was seen due to coordinated H_2O, although only one half of the Cu open metal sites were fully coordinated. Unfortunately, because of the extremely low analyte concentrations considered here, analysis of density profiles and individual snapshots from the simulation do not fully resolve the mechanism by which coordinated water affects methane adsorption. However, a plausible explanation for the behavior of Cu-BTC with respect to coordinated water is that enhanced methane uptake results from reduced pore size in the large cage, as well as van der Waals interactions between CH_4 molecules and the rigid water molecules. We cannot rule out, however, the possibility that new adsorption sites are created when water molecules coordinate

to the open metal sites in Cu-BTC. In any case, the lack of effect on methane uptake at 100% R.H., coupled with enhanced uptake predicted when Cu-sites are occupied by water molecules, suggests that the presence of water is not a barrier to methane sensing by Cu-BTC.

The presence of 1 bar N_2 leads to a 12% decrease in methane uptake in Cu-BTC, as there is some competition for adsorption sites. In contrast to the CH_4/H_2O mixture case discussed above, the probability density profile clearly shows the presence of the competing N_2 molecules in the small cages where initial methane uptake occurs (Figure 41). However, as in the case of water vapor, this relatively small decrease in methane uptake due to the presence of N_2 does not eliminate Cu-BTC as a promising candidate for methane sensing in an inert environment.

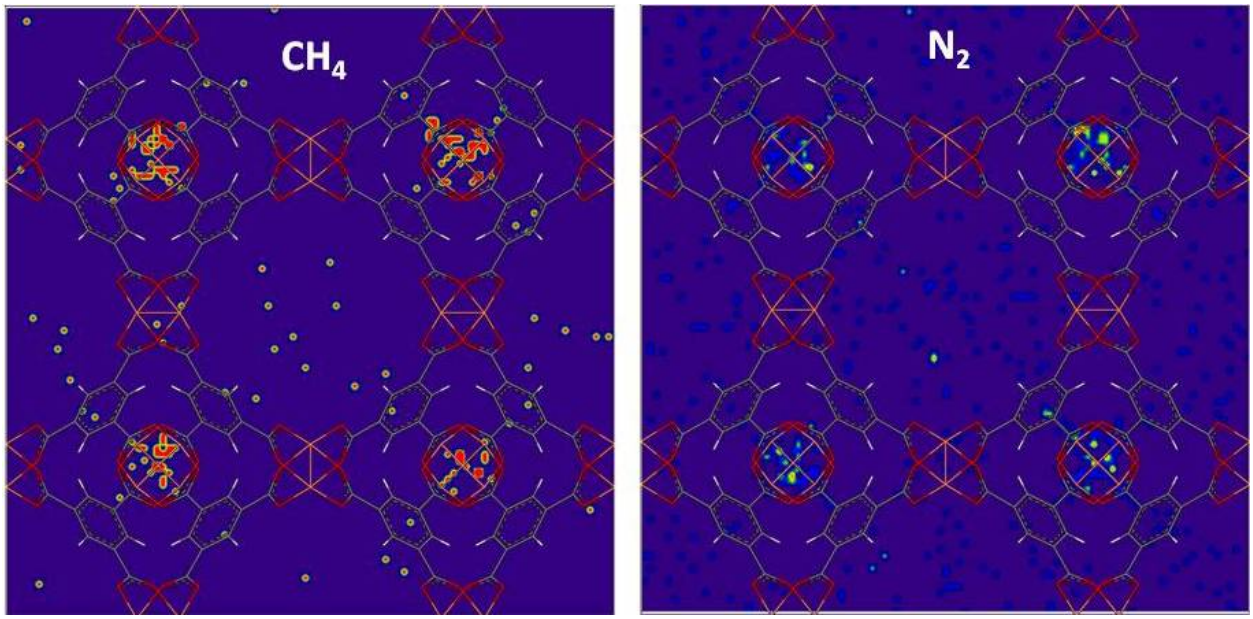

Figure 41. Probability density plots of methane and nitrogen adsorption in Cu-BTC for a mixture of 70 mbar CH_4:1 bar N_2.

The results of mixture simulations for Zn_2(dhtp) differ significantly from those of the two Cu-based NFMs discussed above. For this NFM, the presence of water drastically decreases the uptake of methane. At 10% R.H., methane uptake is reduced by 83% and at full water saturation there is no methane uptake at all. In both cases, the large pores of the Zn_2(dhtp) structure are completely filled with water molecules. In contrast, a background of N_2 causes only a slight (2%) decrease in methane uptake in the Henry's law regime. These results indicate that NFMs from the M_2(dhtp) series may be useful for methane sensing in N_2 environments, but only in the absence of water.

We conclude that methane sensing using NFM coatings is feasible, even in humid environments or in a dilute inert atmosphere. Our principal assumption regarding detection limits (i.e., that methane adsorption can be estimated by uptake in the Henry's regime of single-component isotherms) largely holds true. In the case of PCN-14 discussed in Section 3.4, estimated detection limits are only slightly modified when mixtures with N_2 and/or H_2O are considered. Finally, these results reveal that relationship between analyte uptake and background environment is

sometimes non-intuitive, underlining the importance of considering the specific detection environment when designing an NFM coating for a sensing application.

4.4. Conclusions

Grand canonical Monte Carlo simulation was used to screen a set of NFMs by quantifying a detection limit for methane at low pressures of interest to chemical sensing applications. Atomistic detail of the initial methane adsorption process was also achieved. While some of the NFMs were chosen based on their large pore volumes and demonstrated ability to store large quantities of methane at high pressure, these materials are poor performers for methane uptake at low pressure. Instead, we discovered a direct relationship between methane detection limit and pore-limiting diameter. Specifically, Cu-based NFMs considered here with PLDs similar to the diameter of a methane molecule have the largest isosteric heats of adsorption and Henry's constants. From these results we identified PCN-14 as the most promising NFM for methane detection of those considered. Additional insight was gained by functionalizing M_2(dhtp) pores at the open metal sites, which allows us to correlate specific sites for methane uptake with the corresponding pore diameter. This level of atomistic detail concerning the adsorption process highlights the important of molecular simulation in materials screening. Finally, the detection limit of methane for a hypothetical NFM thin film was calculated based on total methane uptake and the sensing limits of three common gas sensing devices. These results are encouraging and show that sensors that require analyte adsorption for detection should be able to detect very low (ppm) levels of weakly interacting gases when functionalized with NFM thin films. Finally, based on the screening results reported here, competitive methane uptake was tested for three promising candidate materials in the presence of a secondary gas (N_2 or H_2O). Two Cu-based NFMs (PCN-14 and Cu-BTC) show minimal (0-10%) influence of a background gas on methane uptake. While Zn_2(dhtp) shows a drastic reduction in methane uptake in the presence of water, it remains a strong candidate for use in a methane detector in an inert (N_2) environment.

4.5. References

1. Lawrence, N. S. *Talanta* **2006**, *69*, 385-392.
2. Werle, P.; Maurer, K.; Kormann, R.; Mucke, R.; D'Amato, F.; Lancia, T.; Popov, A. *Spectroc. Acta Pt. A-Molec. Biomolec. Spectr.* **2002**, *58*, 2361-2372.
3. Nadezhdinskii, A.; Berezin, A.; Chernin, S.; Ershov, O.; Kutnyak, V. *Spectroc. Acta Pt. A-Molec. Biomolec. Spectr.* **1999**, *55*, 2083-2089.
4. Grossel, A.; Zeninari, V.; Joly, L.; Parvitte, B.; Courtois, D.; Durry, G. *Spectroc. Acta Pt. A-Molec. Biomolec. Spectr.* **2006**, *63*, 1021-1028.
5. Worthy, D. E. J.; Levin, I.; Trivett, N. B. A.; Kuhlmann, A. J.; Hopper, J. F.; Ernst, M. K. *J. Geophys. Res.* **1998**, *103*, 15995-16007.
6. Massie, C.; Stewart, G.; McGregor, G.; Gilchrist, J. R. *Sensor. Actuat. B-Chem.* **2006**, *113*, 830-836.
7. Zhou, W. *Chem. Rec.* **2010**, *10*, 200-204.
8. Allendorf, M. D.; Houk, R. J. T.; Andruszkiewicz, L.; Talin, A. A.; Pikarsky, J.; Choudhury, A.; Gall, K. A.; Hesketh, P. J. *J. Am. Chem. Soc.* **2008**, *130*, 14404-14405.
9. Allendorf, M. D.; Bauer, C. A.; Bhakta, R. K.; Houk, R. J. T. *Chem. Soc. Rev.* **2009**, *38*, 1330-1352.
10. Greathouse, J. A.; Ockwig, N. W.; Criscenti, L. J.; Guilinger, T. R.; Pohl, P.; Allendorf, M. D. *Phys. Chem. Chem. Phys.* **2010**, *12*, 12621-12629.
11. Lee, J.-H.; Houk, R. T. J.; Robinson, A.; Greathouse, J. A.; Thornberg, S. M.; Allendorf, M. D.; Hesketh, P. J.; Thomas, G., Islam, M. S., Achyut, K. D., Eds.; SPIE: 2010; Vol. 7679, p 767927.
12. Lan, A. J.; Li, K. H.; Wu, H. H.; Olson, D. H.; Emge, T. J.; Ki, W.; Hong, M. C.; Li, J. *Angew. Chem. Int. Edit.* **2009**, *48*, 2334-2338.
13. Dultsev, F. N.; Kolosovsky, E. A. *Langmuir* **2009**, *25*, 12195-12200.
14. Arshak, K.; Moore, E.; Lyons, G. M.; Harris, J.; Clifford, S. *Sens. Rev.* **2004**, *24*, 181-198.
15. Sang-Mok, C.; Muramatsu, H.; Nakamura, C.; Miyake, J. *Mater. Sci. Eng. C, Biomin. Supramol. Syst.* **2000**, *C12*, 111-123.
16. Pohl, A. *IEEE Trans. Ultrason. Ferroelectr. Freq. Control* **2000**, *47*, 317-332.
17. Boisen, A.; Dohn, S.; Keller, S. S.; Schmid, S.; Tenje, M. *Rep. Prog. Phys.* **2011**, *74*.
18. Furukawa, H.; Yaghi, O. M. *J. Am. Chem. Soc.* **2009**, *131*, 8875-8883.
19. Mendoza-Cortes, J. L.; Han, S. S.; Furukawa, H.; Yaghi, O. M.; Goddard, W. A. *J. Phys. Chem. A* **2010**, *114*, 10824-10833.
20. Duren, T.; Sarkisov, L.; Yaghi, O. M.; Snurr, R. Q. *Langmuir* **2004**, *20*, 2683-2689.
21. Frost, H.; Duren, T.; Snurr, R. Q. *J. Phys. Chem. B* **2006**, *110*, 9565-9570.
22. Meek, S. T.; Greathouse, J. A.; Allendorf, M. D. *Adv. Mater.* **2011**, *23*, 249-267.
23. Duren, T.; Bae, Y. S.; Snurr, R. Q. *Chem. Soc. Rev.* **2009**, *38*, 1237-1247.
24. Rappe, A. K.; Casewit, C. J.; Colwell, K. S.; Goddard, W. A.; Skiff, W. M. *J. Am. Chem. Soc.* **1992**, *114*, 10024-10035.
25. Mayo, S. L.; Olafson, B. D.; Goddard, W. A. *J. Phys. Chem.* **1990**, *94*, 8897-8909.
26. Ma, Q. T.; Yang, Q. Y.; Zhong, C. L.; Mi, J. G.; Liu, D. H. *Langmuir* **2010**, *26*, 5160-5166.
27. Haldoupis, E.; Nair, S.; Sholl, D. S. *J. Am. Chem. Soc.* **2010**, *132*, 7528-7539.
28. Krishna, R.; van Baten, J. A. *Langmuir* **2010**, *26*, 3981-3992.
29. Babarao, R.; Jiang, J. W.; Sandler, S. I. *Langmuir* **2009**, *25*, 5239-5247.
30. Mu, W.; Liu, D. H.; Yang, Q. Y.; Zhong, C. L. *Micropor. Meospor. Mat.* **2010**, *130*, 76-82.

31. Farrusseng, D.; Daniel, C.; Gaudillere, C.; Ravon, U.; Schuurman, Y.; Mirodatos, C.; Dubbeldam, D.; Frost, H.; Snurr, R. Q. *Langmuir* **2009**, *25*, 7383-7388.
32. Ye, Q. G.; Yan, S. Y.; Liu, D. H.; Yang, Q. Y.; Zhong, C. L. *Mol. Simulat.* **2010**, *36*, 682-692.
33. Wu, H.; Simmons, Jason M.; Liu, Y.; Brown, Craig M.; Wang, X.-S.; Ma, S.; Peterson, Vanessa K.; Southon, Peter D.; Kepert, Cameron J.; Zhou, H.-C.; Yildirim, T.; Zhou, W. *Chem.-Eur. J.* **2010**, *16*, 5205-5214.
34. Xue, C. Y.; Yang, Q. Y.; Zhong, C. L. *Mol. Simulat.* **2009**, *35*, 1249-1255.
35. Yazaydın, A. O.; Snurr, R. Q.; Park, T.-H.; Koh, K.; Liu, J.; LeVan, M. D.; Benin, A. I.; Jakubczak, P.; Lanuza, M.; Galloway, D. B.; Low, J. J.; Willis, R. R. *J. Am. Chem. Soc.* **2009**, *131*, 18198-18199.
36. Liu, Y. H.; Liu, D. H.; Yang, Q. Y.; Zhong, C. L.; Mi, J. G. *Ind. Eng. Chem. Res.* **2010**, *49*, 2902-2906.
37. Getzschmann, J.; Senkovska, I.; Wallacher, D.; Tovar, M.; Fairen-Jimenez, D.; Düren, T.; van Baten, J. M.; Krishna, R.; Kaskel, S. *Micropor. Meospor. Mat.* **2010**, *136*, 50-58.
38. Chen, B. L.; Xiang, S. C.; Qian, G. D. *Accounts Chem. Res.* **2010**, *43*, 1115-1124.
39. Wu, H.; Zhou, W.; Yildirim, T. *J. Am. Chem. Soc.* **2009**, *131*, 4995-5000.
40. Rosi, N. L.; Kim, J.; Eddaoudi, M.; Chen, B. L.; O'Keeffe, M.; Yaghi, O. M. *J. Am. Chem. Soc.* **2005**, *127*, 1504-1518.
41. Dietzel, P. D. C.; Morita, Y.; Blom, R.; Fjellvag, H. *Angew. Chem. Int. Edit.* **2005**, *44*, 6354-6358.
42. Dietzel, P. D. C.; Panella, B.; Hirscher, M.; Blom, R.; Fjellvag, H. *Chem. Commun.* **2006**, 959-961.
43. Ma, S.; Sun, D.; Simmons, J. M.; Collier, C. D.; Yuan, D.; Zhou, H. C. *J. Am. Chem. Soc.* **2008**, *130*, 1012-1016.
44. Chui, S. S. Y.; Lo, S. M. F.; Charmant, J. P. H.; Orpen, A. G.; Williams, I. D. *Science* **1999**, *283*, 1148-1150.
45. Wang, X.-S.; Ma, S.; Rauch, K.; Simmons, J. M.; Yuan, D.; Wang, X.; Yildirim, T.; Cole, W. C.; López, J. J.; Meijere, A. d.; Zhou, H.-C. *Chem. Mater.* **2008**, *20*, 3145-3152.
46. Lin, X.; Jia, J.; Zhao, X.; Thomas, K. M.; Blake, A. J.; Walker, G. S.; Champness, N. R.; Hubberstey, P.; Schröder, M. *Angew. Chem. Int. Edit.* **2006**, *45*, 7358-7364.
47. Chen, B.; Ockwig, N. W.; Millward, A. R.; Contreras, D. S.; Yaghi, O. M. *Angew. Chem. Int. Edit.* **2005**, *44*, 4745-4749.
48. El-Kaderi, H. M.; Hunt, J. R.; Mendoza-Cortes, J. L.; Cote, A. P.; Taylor, R. E.; O'Keeffe, M.; Yaghi, O. M. *Science* **2007**, *316*, 268-272.
49. Koh, K.; Wong-Foy, A. G.; Matzger, A. J. *J. Am. Chem. Soc.* **2009**, *131*, 4184-4185.
50. Kyoungmoo Koh, Antek G. W.-F. Adam J. M. *Angew. Chem. Int. Edit.* **2008**, *47*, 677-680.
51. Connolly, M. L. *Science* **1983**, *221*, 709-713.
52. Smart, O. S.; Neduvelil, J. G.; Wang, X.; Wallace, B. A.; Sansom, M. S. P. *J. Mol. Graph. Model.* **1996**, *14*, 354-&.
53. Britt, D.; Furukawa, H.; Wang, B.; Glover, T.; Yaghi, O. *P. Natl. Acad. Sci. USA* **2009**, *106*, 20637-20640.
54. Dietzel, Pascal D. C.; Johnsen, Rune E.; Blom, R.; Fjellvåg, H. *Chem.-Eur. J.* **2008**, *14*, 2389-2397.
55. Caskey, S. R.; Wong-Foy, A. G.; Matzger, A. J. *J. Am. Chem. Soc.* **2008**, *130*, 10870-10871.

56. Wang, Q. M.; Shen, D. M.; Bulow, M.; Lau, M. L.; Deng, S. G.; Fitch, F. R.; Lemcoff, N. O.; Semanscin, J. *Micropor. Meospor. Mat.* **2002**, *55*, 217-230.
57. Lin, X.; Telepeni, I.; Blake, A. J.; Dailly, A.; Brown, C. M.; Simmons, J. M.; Zoppi, M.; Walker, G. S.; Thomas, K. M.; Mays, T. J.; Hubberstey, P.; Champness, N. R.; Schroder, M. *J. Am. Chem. Soc.* **2009**, *131*, 2159-2171.
58. Zhou, W.; Wu, H.; Yildirim, T. *J. Am. Chem. Soc.* **2008**, *130*, 15268-+.
59. Rappe, A. K.; Goddard, W. A. *J. Phys. Chem.* **1991**, *95*, 3358-3363.
60. Martin, M. G.; Siepmann, J. I. *J. Phys. Chem. B* **1998**, *102*, 2569-2577.
61. Goodbody, S. J.; Watanabe, K.; Macgowan, D.; Walton, J.; Quirke, N. *J. Chem. Soc.-Faraday Trans.* **1991**, *87*, 1951-1958.
62. Allen, M. P.; Tildesley, D. J. *Computer Simulation of Liquids*; Oxford University Press: Oxford, 1996.
63. Assfour, B.; Seifert, G. *International Journal of Hydrogen Energy* **2009**, *34*, 8135-8143.
64. Nalaparaju, A.; Babarao, R.; Zhao, X. S.; Jiang, J. W. *ACS Nano* **2009**, *3*, 2563-2572.
65. Berendsen, H. J. C.; Grigera, J. R.; Straatsma, T. P. *Journal of Physical Chemistry* **1987**, *91*, 6269-6271.
66. Potoff, J. J.; Siepmann, J. I. *AIChE J.* **2001**, *47*, 1676-1682.
67. Xu, Q.; Zhong, C. L. *J. Phys. Chem. C* **2010**, *114*, 5035-5042.
68. Meng, C. C.; Zhong, C. L. *J. Phys. Chem. C* **2010**, *114*, 9945-9951.
69. Zhong, C. L., Personal communication.
70. Errington, J. R.; Panagiotopoulos, A. Z. *J. Phys. Chem. B* **1998**, *102*, 7470-7475.
71. Martin, M. G. *MCCCS Towhee* http://towhee.sourceforge.net
72. Yang, Q. Y.; Zhong, C. L.; Chen, J. F. *J. Phys. Chem. C* **2008**, *112*, 1562-1569.
73. Greathouse, J. A.; Kinnibrugh, T. L.; Allendorf, M. D. *Ind. Eng. Chem. Res.* **2009**, *48*, 3425-3431.
74. Snurr, R. Q.; Bell, A. T.; Theodorou, D. N. *J. Phys. Chem.* **1993**, *97*, 13742-13752.
75. Gumma, S.; Talu, O. *Langmuir* **2010**, *26*, 17013-17023.
76. Garberoglio, G. *Langmuir* **2007**, *23*, 12154-12158.
77. Lan, J. H.; Cao, D. P.; Wang, W. C. *Langmuir* **2010**, *26*, 220-226.
78. Yang, Q. Y.; Zhong, C. L. *ChemPhysChem* **2006**, *7*, 1417-1421.
79. Karra, J. R.; Walton, K. S. *Langmuir* **2008**, *24*, 8620-8626.
80. Li, J. R.; Kuppler, R. J.; Zhou, H. C. *Chem. Soc. Rev.* **2009**, *38*, 1477-1504.
81. Eddaoudi, M.; Kim, J.; Rosi, N.; Vodak, D.; Wachter, J.; O'Keefe, M.; Yaghi, O. M. *Science* **2002**, *295*, 469-472.
82. Couck, S.; Denayer, J. F. M.; Baron, G. V.; Remy, T.; Gascon, J.; Kapteijn, F. *J. Am. Chem. Soc.* **2009**, *131*, 6326-6327.
83. *CRC Handbook of Chemistry and Physics*; 84th ed.; Lide, D. R., Ed.; CRC Press: Boca Raton, FL, 2004.
84. Ballantine, D. S.; White, R. M.; Martin, S. J.; Ricco, A. J.; Zellers, E. T.; Frye, G. C.; Wohltjen, H. *Acoustic Wave Sensors. Theory, Design, and Physico-Chemical Applications*; Academic Press: San Diego, 1997.
85. Jin, D. Z.; Liu, H.; Li, X. X.; Liu, M.; Zuo, G. M.; Wang, Y. L.; Yu, H. T.; Ge, X. H. In *2006 1st IEEE International Conference on Nano/Micro Engineered and Molecular Systems, Vols 1-3*; IEEE: New York, 2006, p 832-836.
86. Castillo, J. M.; Vlugt, T. J. H.; Calero, S. *J. Phys. Chem. C* **2008**, *112*, 15934-15939.
87. Chen, L.; Grajciar, L.; Nachtigall, P.; Düren, T. *J. Phys. Chem. C* **2011**, *115*, 23074-23080.

88. Fischer, M.; Kuchta, B.; Firlej, L.; Hoffmann, F.; Fröba, M. *J. Phys. Chem. C* **2010**, *114*, 19116-19126.
89. Yazaydin, A. O.; Benin, A. I.; Faheem, S. A.; Jakubczak, P.; Low, J. J.; Willis, R. R.; Snurr, R. Q. *Chem. Mater.* **2009**, *21*, 1425-1430.
90. Willis, R. R.; Low, J. J.; Faheem, S. A.; Benin, A. I.; Snurr, R. Q.; Yazaydin, A. O. 2009.

[Blank page following section.]

5. COMPUTATIONAL SCREENING TO IDENTIFY MOF COATINGS FOR O2 DETECTION

5.1. Introduction

The detection of oxygen in air is a particularly challenging issue, especially given that the size of an O_2 molecule is nearly the same as that of a N_2 molecule, which complicates molecular sieving techniques. This could be important for detection of oxygen in inert atmospheres (e.g., N_2) where the oxidation of a metal component—or simply the presence of oxygen—would be disastrous. Currently, synthetic zeolites[1-3] and carbon molecular sieves,[3] and membranes[4] are used for O_2/N_2 separation from air, usually by selectively adsorbing N_2. Increasing O_2 adsorption capacity is important for increasing O_2/N_2 selectivity from air because O_2 is less abundant than N_2 in air, thus less energy is required for enriching an air stream.[5] By selecting a better candidate material for O_2 adsorption, the efficiency of room temperature O_2/N_2 separation via pressure-swing adsorption (PSA) or pressure-vacuum-swing adsorption (PVSA) can be enhanced.

Nanoporous framework materials (NFMs) are a new class of materials (including metal-organic frameworks—MOFs) with tunable pore sizes and functionality that can be used for gas storage,[6] selective gas adsorption,[7] and low-level gas detection[8] applications. The incorporation of an NFM as a coating on a small detector (e.g., crystal microbalance (QCM),[9-10] surface acoustic wave (SAW)[10-12] sensor, or MEMS device such as a microcantilever (MCL)[13]) has previously been shown.[14-17] Detecting low concentrations of small gases using NFMs is an important problem that has been studied experimentally[7-8] and via computational simulation[15, 18-19] for a number of gases.

Previous NFM modeling efforts have focused on screening a large number of structures for their uptake of small gases,[19-22] although they have focused on the uptake of the relatively simple noble gases and methane. Many experimental studies to date have focused on selective adsorption of oxygen over nitrogen in NFMs, especially at low temperatures (~77-87 K).[23-24] However, the detection of oxygen at room temperature has yet to be studied systematically for a large number of structures. Here, we have undertaken a computational study of low-level oxygen uptake for a broad range of NFM structures using a combination of classical GCMC and quantum DFT simulations. Structures were selected based on experimental O_2 uptake and/or selectivity, as well as a large-scale screening of structures for Ar (which is similar in size to O_2) uptake. Additionally, other MOF (including some with open metal sites—here we define open metal sites as those metal sites that do not have all of their coordination sites filled), covalent-organic framework (COF), zinc imidazolate framework (ZIF), ionic-MOF, zeolitic MOF (ZMOF), MIL (developed by the Institut Lavoisier), and porphyrin structures were included for comparison.

5.2. Simulation Details

5.2.1. NFM Selection

The 100 structures investigated here have been divided into six principal categories: COFs, porphyrin structures, "screened" structures (described below), structures interesting because of published experimental O_2 uptake ("literature review"), structures with open metal sites, and "other" (including ZIF, ZMOF, ionic-MOF, MIL, and Zn-based MOF structures) (Table 13). In some cases, a single structure falls into multiple categories—the "screened" and "literature review" categories take precedence over other categories, with secondary associations noted parenthetically in Table 14.

Table 13. Number of NFM Structures in Each Category Investigated in This Study

Structure Type	No. of Structures
COF	4
Literature Review	35
Open Metal-Site	15
Porphyrin	4
Screened	24
Other	18

The COF structures represent a set of high surface area and free volume structures initially developed by Yaghi et al.[25] Porphyrin structures are three dimensional frameworks with metalloporphyrins incorporated as linkers.[26-27] Ionic-MOF structures have charged frameworks and charge-balancing interstitial ions. The interstitial ions were kept in their crystallographic positions and not allowed to move during the simulations.

The "screened" set of structures was taken from a separate set of GCMC simulations that investigated Ar uptake in more than 2,000 NFM structures.[28] As noted below, some of these 3-D framework structures are not considered to be MOFs (clathrate or zeolitic structures were included in the set of NFM structures investigated). Spherical adsorbates such as noble gases are easier for large-scale adsorption studies because atomic charges for framework atoms are not needed.[20, 22] However, because Ar and O_2 are similar in size (kinetic diameters of 3.542 and 3.467 Å for Ar and O_2, respectively[7]), and the relationship between pore size and analyte size has been shown to be indicative of analyte uptake at low concentrations,[18-19, 29-30] the uptake of Ar can be considered a reasonable indicator of O_2 uptake, such that Ar screening results were used to develop a set of NFM structures to investigate O_2 uptake. Those structures showing the greatest Ar Henry's constant (k_H) or isosteric heat of adsorption (Q_{st}) were chosen for the current study.

Finally, a literature search for investigations of O_2 uptake in NFMs resulted in the "literature review" set of structures.[4, 6, 24, 31-35] Although in most cases, these studies were done at low temperature, those NFMs that showed exceptionally high O_2 uptake and/or selectivity over N_2 were chosen for the current room temperature (298 K) study. In addition to the specific structures

selected for this category, analogues to these structures (e.g., those that have identical linkers, but different metal center identities) that have not been studied experimentally were also included.

5.2.2. Structural Models

Models for the NFMs in this work (Table 14) were taken from published single-crystal X-ray diffraction structures. In some cases, non-orthogonal unit cells were made orthogonal for ease of analysis. Solvent molecules were deleted where appropriate, yielding an “activated” structure. In some cases with site disorder (e.g., UMCM-2), the structure was made to represent the chemical formula in the original paper. Crystal structures can be found using the Cambridge Crystallographic Database along with the reference codes given in Table 14.

Table 14. Properties of NFMs Investigated in This Study, Arranged by Category Type

NFM ID	NFM Name	CCDC REFCODE[a]	Category	Metal	V_{free}[b] (%)	S.A.[b] (m^2/g)	ρ_{cryst} (g/cm^3)	LCD[c] (Å)	PLD[c] (Å)	Q_{st} [O_2] (kJ/mol)	k_H [O_2][d] (mmol/ cm^3·atm)	k_H [N_2][d] (mmol/ cm^3·atm)	Selectivity[e] [O_2/N_2]
1	COF-102	REZVIC	COF	-	76.8	4642	0.42	9.0	8.6	9.3	0.19	0.16	1.21
2	COF-103	REZVOI	COF	-	78.6	4737	0.39	9.7	9.1	9.4	0.19	-	-
3	COF-105	REZVUO	COF	-	90.7	4761	0.18	18.8	16.0	-2.1	0.09	-	-
4	COF-108	REZWAV	COF	-	91.1	4625	0.17	27.4	19.0	6.2	0.08	0.07	1.24
5	MIL141(Cs)	(863577)	lit. review (MIL)	Ni, Fe	40.8	2507	1.24	5.0	4.2	18.5	1.04	1.11	0.94
6	MIL141(K)	(863577)	lit. review (MIL)	Ni, Fe	41.2	2793	1.12	5.2	4.5	17.7	0.92	0.99	0.94
7	MIL141(Li)	(863577)	lit. review (MIL)	Ni, Fe	42.8	2941	1.10	4.7	4.3	18.8	1.08	1.12	0.96
8	MIL141(Na)	(863577)	lit. review (MIL)	Ni, Fe	43.2	2849	1.11	5.2	4.3	18.2	1.01	1.09	0.93
9	MIL141(Rb)	(863577)	lit. review (MIL)	Ni, Fe	42.1	2701	1.17	5.1	4.3	18.3	0.93	0.99	0.94
10	MIL-53(Al)-lt	SABWAU	lit. review (MIL)	Al	22.4	1950	1.46	2.4	1.8	12.7	0.00	0.00	477.79
11	MIL-53(Al)-ht	SABVUN	lit. review (MIL)	Al	53.8	3235	0.98	6.9	6.6	15.7	1.00	0.79	1.27
12	Zn(TCNQ-TCNQ)bpy	MUVGUG	lit. review	Zn	46.1	3838	0.98	5.2	3.7	20.2	1.89	1.18	1.60
13	CUK-1	NEVVIU	lit. review	Co	44.3	1938	1.46	6.3	5.5	14.5	0.50	-	-
14	PCN-13	TIRQOB	lit. review	Zn	46.6	2556	1.19	5.3	4.4	18.1	1.29	-	-
15	$Mg_3(ndc)_3$	QAQRUW	lit. review	Mg	56.9	3647	0.85	2.4	1.4	14.3	0.55	-	-
16	$Ni_2(cyclam)_2(mtb)$	QOCBEQ	lit. review	Ni	45.2	3016	0.97	7.4	4.2	16.7	1.38	-	-
17	Cu(bdt)	VEMMOQ	lit. review	Cu	66.9	3492	0.86	1.8	1.3	11.9	0.31	-	-
18	Cd(bpndc)(4,4'-bpy)	EFANOP	lit. review	Cd	91.3	1958	1.52	4.1	1.4	23.8	1.23	-	-
19	$Cu(dhbc)_2$(4,4'-bpy)	WUSXIR	lit. review	Cu	35.5	2367	1.23	4.5	2.3	20.4	1.88	-	-
20	SNU-15	COZMUA	lit. review	Co	71.9	3608	0.64	9.2	5.2	11.2	0.27	-	-
21	SNU-25	MUDLON	lit. review	Mg	65.2	4069	0.63	10.6	8.2	14.5	0.44	-	-
22	SNU-50'	ALANAD	lit. review	Zn	53.9	3030	0.93	8.1	5.2	9.3	0.10	-	-
23	MAMS-1	PICLET	lit. review	Ni	34.7	2679	1.31	4.4	1.8	16.3	0.35	-	-
24	Mn-formate	IJOMOJ02	lit. review	Mn	39.2	2002	1.62	4.9	3.8	14.7	0.23	-	-
25	FMOF-1	PITYUN	lit. review	Ag	46.1	2090	1.76	6.2	5.4	10.0	0.11	-	-
26	Co_2(DMF)	WUTKIG	lit. review	Co	51.7	3015	1.03	4.8	2.0	18.4	1.47	-	-
27	$Co_2(bpbp)_2bdc(PF_6)_4$	(815290)	lit. review	Co	22.0	2082	1.47	3.7	1.3	19.4	0.04	0.01	3.65
28	PCN-17(Yb)	POBMOJ	lit. review	Yb	59.4	2561	1.13	16.1	2.0	16.5	0.61	-	-

29	PCN-17(Dy)	FUTTUK	lit. review	Dy	60.3	2626	1.10	16.3	1.8	15.8	0.51	-	-
30	PCN-17(Er)	FUTVAS	lit. review	Er	59.9	2567	1.12	16.2	2.0	15.8	0.53	-	-
31	PCN-17(Y)	FUTVEW	lit. review	Y	59.9	3030	0.94	16.2	1.9	16.1	0.56	-	-
32	Mn(TCNQ-TCNQ)bpy	BUSQEM	lit. review	Mn	46.8	4092	0.95	5.2	3.6	19.9	1.77	-	-
33	Ag(TCNQ)	DEHRIR	lit. review	Ag	1.4	273	2.04	1.9	0.9	-429.5	0.00	-	-
34	Cd(TCNQ)	(784861)	lit. review	Cd	59.3	3702	0.82	7.5	4.0	14.1	0.56	-	-
35	Co(TCNQ)	(784862)	lit. review	Co	57.0	3964	0.77	7.0	3.8	14.6	0.61	-	-
36	Fe(TCNQ)	(784863)	lit. review	Fe	58.6	4611	0.65	6.8	4.2	14.2	0.60	-	-
37	Zn(dtp)	BIYTEJ	lit. review (ZMOF)	Zn	46.6	2344	1.39	6.5	6.3	14.1	0.31	-	-
38	Cr-BTC	(supp. info[34])	lit. review (open metal)	Cr	70.9	2983	0.80	12.5	6.8	14.2	0.36	0.26	1.38
39	Fe_2(dhtp)	(supp. info[33])	lit. review (open metal)	Fe	62.7	2040	1.15	11.1	10.7	11.0	0.24	0.18	1.28
40	Zn_2(dhtp)	FIJDOS	open metal	Zn	62.8	1885	1.22	11.7	10.9	10.9	0.32	0.40	0.78
41	Ni_2(dhtp)	LEJRIC	open metal	Ni	61.8	1908	1.19	11.6	10.8	7.8	0.28	-	-
42	Co_2(dhtp)	NAVJAW	open metal	Co	63.0	1959	1.18	11.1	10.9	10.9	0.27	-	-
43	Mg_2(dhtp)	(supp. info[36])	open metal	Mg	62.4	2532	0.91	11.6	10.8	11.7	0.32	-	-
44	Ru-BTC	IVESOS	open metal	Ru	70.4	2355	1.02	11.7	6.9	14.3	0.39	0.29	1.37
45	PCN-11	MOCKAR	open metal	Cu	72.5	3101	0.75	10.8	3.6	7.4	0.32	-	-
46	NOTT-100 (MOF-505)	LASYOU	open metal	Cu	66.6	2909	0.93	10.0	3.5	12.6	0.42	0.35	1.19
47	NOTT-101	CESFOW	open metal	Cu	72.8	3359	0.68	11.1	5.3	12.3	0.30	0.24	1.27
48	NOTT-103	CESFIQ	open metal	Cu	73.6	3524	0.64	11.0	5.9	12.4	0.33	-	-
49	NOTT-102	PUBROU	open metal	Cu	75.4	3655	0.59	11.0	5.0	12.5	0.31	-	-
50	PCN-14	XITYOP	open metal	Cu	64.2	3337	0.83	6.8	4.9	15.4	0.50	0.43	1.15
51	Cu-BTC (HKUST-1)	FIQCEN	open metal	Cu	69.8	2770	0.88	13.2	6.5	14.7	0.38	0.28	1.36
52	MOF-143	(780451)	open metal	Cu	85.3	3937	0.34	20.2	8.5	7.6	0.13	-	-
53	MOF-388	(780453)	open metal	Cu	84.0	3942	0.33	27.1	13.8	9.1	0.14	-	-
54	MOF-399	(780452)	open metal	Cu	94.0	4282	0.13	42.8	24.2	5.5	0.07	-	-
55	PPF-4	QOQBII	porphyrin	Zn	75.2	3814	0.53	11.6	10.2	10.0	0.20	0.16	1.26
56	PPF-5	MOYZUW	porphyrin	Ni, Zn	29.0	3815	0.48	11.2	10.1	9.5	0.18	0.14	1.26

57	PIZA-4	IMUKUW	porphyrin	Zn	71.9	4196	0.56	12.0	7.4	10.8	0.22	0.17	1.28
58	PIZA-1	KAJPUH*	porphyrin	Co	72.5	3714	0.62	8.9	5.1	11.5	0.30	0.24	1.23
59	FOQSUA	FOQSUA	screening [kH]	Cu	24.6	2099	1.67	3.4	2.9	20.2	0.20	-	-
60	EVOMOR01	EVOMOR01	screening [kH]	Mn	31.1	2180	1.26	4.5	2.3	21.4	2.05	1.38	1.48
61	EXUMEP	EXUMEP	screening [kH]	Mn	28.6	1973	1.50	5.2	1.2	22.5	2.67	2.12	1.26
62	HIMSAY	HIMSAY	screening [kH]	Zn	46.1	3938	0.99	5.1	3.5	20.2	1.87	1.15	1.63
63	LEMMAS	LEMMAS	screening [kH]	Zn	36.2	2466	1.36	4.7	3.1	21.8	2.23	1.57	1.42
64	LEZGED	LEZGED	screening [kH]	Mn, Na	25.4	2000	1.49	4.5	0.7	24.5	2.79	1.82	1.53
65	QIWSUK	QIWSUK	screening [kH]	Zn	23.5	2346	1.32	4.0	1.3	25.4	2.35	1.07	2.19
66	UFEVEH	UFEVEH	screening [kH]	Cd	26.9	2472	1.30	4.6	2.1	23.2	1.99	-	-
67	UFUNIS	UFUNIS	screening [kH]	Cu	32.5	2086	1.43	4.4	3.7	22.1	2.42	1.63	1.48
68	VEJZEQ	VEJZEQ	screening [kH]	Co	35.1	3119	1.22	5.6	2.4	21.3	2.91	2.08	1.40
69	VELVIS	VELVIS	screening [kH]	Zn	4.4	384	1.24	5.6	2.4	21.4	3.03	2.17	1.39
70	VOLQUJ	VOLQUJ	screening [kH]	Zn	14.7	1494	1.63	4.7	1.0	28.1	2.17	1.85	1.17
71	YIVSOM	YIVSOM	screening [kH]	Cd	16.0	1425	1.59	4.5	1.1	25.7	2.94	-	-
72	ECAVEK	ECAVEK	screening [kH]	Ge	35.1	1162	3.08	4.7	3.7	23.0	4.78	-	-
73	GIWNUV	GIWNUV	screening [Qst]	Cu	7.9	685	2.21	4.2	1.7	28.0	0.48	0.18	2.62
74	JITHIE	JITHIE	screening [Qst]	Co	23.1	2286	1.44	3.0	2.1	1.9	0.26	-	-
75	KOKCUJ	KOKCUJ	screening [Qst]	Cu	20.0	1984	1.54	4.2	1.5	21.5	0.43	0.27	1.60
76	LIQTEL	LIQTEL	screening [Qst]	Zn	17.7	1543	1.67	3.7	1.3	23.8	0.30	-	-
77	MOFGOE	MOFGOE	screening [Qst]	Cu	16.3	1270	1.98	3.7	2.3	26.2	0.22	0.03	6.72
78	VEGWOU	VEGWOU	screening [Qst]	Zn	17.4	1434	1.59	3.5	0.9	26.7	0.94	0.24	3.89
79	WINCEC	WINCEC	screening [Qst]	Co	24.0	1830	1.54	3.5	2.1	24.6	0.77	-	-
80	XEPCIF	XEPCIF	screening [Qst]	Ni	15.0	1845	1.40	3.7	1.1	27.1	0.66	-	-
81	YAPYUK	YAPYUK	screening [Qst]	Co	12.9	1198	1.74	2.7	1.2	26.5	0.55	0.25	2.22
82	YORKAS	YORKAS	screening [Qst]	Cu	26.4	1988	1.48	3.9	1.8	23.3	0.82	-	-
83	Cryptophane-A	OJITOR	other (clathrate)	-	12.8	1708	1.28	1.9	1.2	31.4	19.48	-	-
84	ZIF-8	OFERUN	other (ZIF)	Zn	52.4	2809	0.92	11.5	3.2	11.9	0.24	0.20	1.22
85	ZIF-68	GITTUZ	other (ZIF)	Zn	52.9	3006	1.03	10.7	7.9	14.1	0.33	-	-
86	ZIF-69	GITVAH01	other (ZIF)	Zn	49.0	2773	1.15	8.0	5.0	15.5	0.38	-	-

87	rho-ZMOF	TEFWIL	other (ZMOF)	In	58.7	2294	1.12	18.2	5.7	14.3	0.32	-	-
88	sod-ZMOF	TEFWOR	other (ZMOF)	In	46.8	2154	1.44	1.9	1.1	17.7	0.96	-	-
89	rht-MOF	LIZWEX	other (ionic MOF)	Cu	76.7	3054	0.70	18.4	3.7	11.0	0.19	-	-
90	soc-MOF	RIDCEN	other (ionic MOF)	In	62.3	2478	1.12	6.4	5.7	13.4	0.51	-	-
91	UMCM-1	KISXIU	other (Zn-based)	Zn	84.2	3789	0.39	23.9	23.1	7.7	0.12	-	-
92	UMCM-2	XUGSUO	other (Zn-based)	Zn	84.2	3676	0.40	22.6	8.8	7.6	0.12	-	-
93	MOF-508a (open)	EDADIX	other (Zn-based)	Zn	41.8	2687	1.24	5.5	3.7	18.9	1.05	0.74	1.41
94	MOF-508b (closed)	EDADIX	other (Zn-based)	Zn	26.5	2398	1.49	3.3	1.5	21.4	0.10	-	-
95	MOF-205 (DUT-6)	SUKXUS01	other (Zn-based)	Zn	84.6	3783	0.38	22.8	8.4	7.6	0.13	-	-
96	MOF-177	ERIRIG	other (Zn-based)	Zn	82.6	3794	0.43	11.2	9.9	8.1	0.14	-	-
97	MIL-53(Cr)-lt	GUSNEN	other (MIL)	Cr	22.6	2217	1.53	2.4	1.5	10.7	0.00	0.00	51.02
98	MIL-53(Cr)-ht	MINVUA01	other (MIL)	Cr	54.6	3089	1.04	7.0	6.5	13.8	0.45	0.33	1.37
99	MIL-47(V)-lt	IDIWIB	other (MIL)	V	56.6	3271	1.05	6.5	6.2	13.4	0.35	0.38	0.93
100	MIL-47(V)-ht	IDIWOH	other (MIL)	V	59.3	3213	1.00	7.6	7.1	12.8	0.34	0.36	0.93

[a]The CCDC reference code for a given structure; numbered entries signify structures available only through online database at time of manuscript submission; some structures only available in supporting information of paper; one structure only available from author (PIZA-1).

[b]Surface area and free volume of each NFM were calculated via Connolly surfaces[37] in Materials Studio (Accelrys, Inc.), using a 1 Å probe radius.

[c]Henry's constant was calculated as the slope of the adsorption isotherm in the linear region below 2.5 mbar.

[d]Pore-limiting diameter (PLD) is defined as the minimum pore diameter in the largest pore that spans the NFM structure[20] and was calculated according to Ref. [20], which takes into account van der Waals radius when calculating pore size. Largest cavity diameter (LCD) is the maximum pore diameter in the largest pore that spans the NFM structure. In this study, diffusion through the pore was not considered.

[e]Selectivity is calculated as the ratio $k_H[O_2]/k_H[N_2]$.

5.2.3. Force Field and Charge Assignment

One distinct limitation of studying a wide variety of structures computationally is having appropriate interatomic potentials to describe the interactions among atoms in the framework and analytes of interest. The use of the universal force field (UFF[38]) has been established for short-range interactions to model gas adsorption and diffusion by NFMs in large-scale screening work.[19, 22, 39-42] A three-site model was used for O_2,[43] the SPC/E model[44] was used for H_2O, and a three-site TraPPE model[45] was used for N_2. Parameters for analyte-NFM interactions were determined by Lorentz-Berthelot combination rules.[46]

Long-range electrostatic interactions are handled via Coulombic interactions, which require the assignment of charges to framework atoms. These charges are not included in UFF, but have been derived for a small number of structures, usually using expensive quantum-mechanical (e.g., density functional theory (DFT)) calculations. Charges derived for a given structure in this manner are not generally transferable to other structures, although Zhong's CBAC method[47-49] of charge assignment has been shown to be successful. A database of charges has been developed specifically for use with NFM structures and the CBAC method, where an atom with a given bonding environment (e.g., a C atom bonded to one C and two O atoms) has been assigned a charge based on an average calculated for that atom in an identical bonding environment from DFT calculations in multiple structures. To maintain charge neutrality in the unit cell, these charges are adjusted slightly for each structure.

While the CBAC method is powerful for the efficient screening of a large number of structures, it has a distinct limit of usefulness—it relies on an appropriate database of atom type/bonding environment combinations. Due to the great variety of published structures, not all of these combinations are represented in the current database. Developing distinct charges for each structure of interest in the current work using expensive DFT calculations would make this work intractable and may be unnecessary in order to screen good candidates for O_2 detection.

We tested the effect of framework charges on a set of 22 structures. Using the CBAC method, charges were assigned and adjusted to maintain charge neutrality in the simulation cell. Results for O_2 uptake in structures with assigned atomic charges are compared to those for the same frameworks in which all atoms had a charge assignment of zero (Figure 42). The charges assigned to atoms in the O_2 molecule were identical in all cases. Overall, there is little effect of framework charge on O_2 uptake. This result allows us to investigate a wider range of materials, including those materials for which no framework charges are currently available. The results shown in Table 14 are for simulations performed with all framework atoms given a charge of zero.

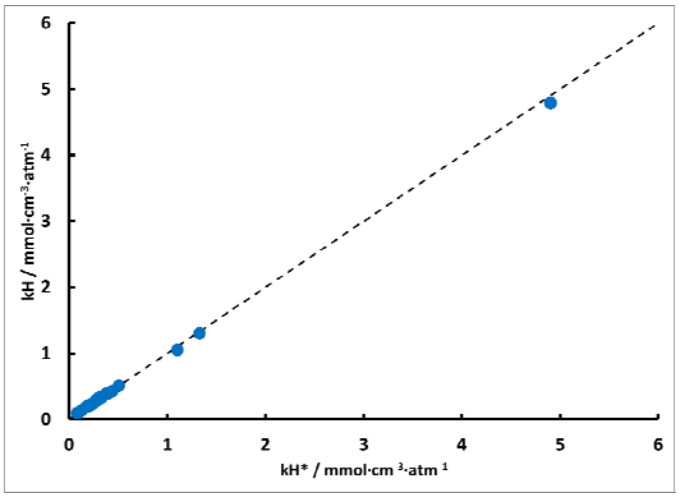

Figure 42. Henry's constants for simulations with (k_H*) and without (k_H) atomic charges for framework atoms.

5.2.4. GCMC Simulation

Configurational-biased grand canonical Monte Carlo (GCMC) simulations were performed for O_2 uptake in each structure represented in Table 14. In some cases, adsorption of N_2 was also investigated. GCMC simulation (constant chemical potential μ, volume V, temperature T 298 K) was performed using the Towhee program[50] for rigid framework models of NFMs. The following probabilities were employed for GCMC moves: insertion/deletion (40%); translation (15%); intrabox reinsertion (15%); rotation (15%); growth (15%). Adsorption isotherms were created by calculating uptake for a series of μ-values corresponding to fixed adsorbate pressures. For each chemical potential, 10^7 MC steps were used to equilibrate the system, and a further 10^7 were used for data collection. A cutoff radius of 12.5 Å and multiple unit cells were used so that each simulation cell parameter had a minimum dimension of 25 Å. Rigid frameworks (i.e., no framework NFM or interstitial atoms are allowed to move) have been found to be sufficient for this type of calculation,[51-52] and were used here in all cases. Flexible framework models exist for only a few well-studied NFMs.[53]

Henry's constant of adsorption (k_H) was calculated as the slope of the adsorption isotherm in the linear low-pressure regime below 2.5 mbar. In contrast to many NFM adsorption studies for which maximum (saturation) adsorption is of interest (e.g., those studies for which gas storage capacity is of interest), here we consider the low-pressure region of the adsorption isotherm to be a good indicator of a material's performance due to our interest in the low-level detection of O_2.

The Towhee code requires analyte chemical potentials rather than pressures as input. As in our previous work,[54] we used "empty box" GCMC simulations (i.e., simulations without an NFM framework) to determine adsorbate pressure at a given chemical potential. In contrast to gas storage studies where excess adsorption is important, for sensing applications, absolute or total adsorption is of use because *all* adsorption is of interest. Here, total adsorption isotherms were used to calculate k_H.

Isosteric heat of adsorption (Q_{st}), the energy of adsorption for a single molecule) was calculated from a constant-volume GCMC simulation of a single adsorbate molecule in an NFM framework. Total system energy was averaged over the final 10^7 MC steps of a $2x10^7$ step simulation. The Q_{st} was calculated by

$$Q_{st} = E(NFM) + E(O_2) – E(NFM+O_2),$$

where $E(NFM)$, $E(O_2)$, and $E(NFM+O_2)$ are the average system energies for the NFM only, a single O_2 molecule, and the NFM with a single O_2 molecule.

5.2.5. DFT Simulation

Further analysis of O_2 binding energies was performed for selected structures using electronic-scale, periodic planewave calculations. The VASP package (v. 5.2)[55-58] was used to perform all DFT calculations with parameters outlined in Watanabe and Sholl's work[59] (PW91-GGA[60-61] exchange-correlation functional, 500 eV energy cutoff, Γ-point calculation only, 10^{-4} energy convergence criterion, 3×10^{-2} eV/Å ionic force convergence criterion). A single crystallographic unit cell was used, except with the Cu-BTC, Cr-BTC, and GIWNUV structures where a rhombohedral primitive cell was used (as in Ref. 59) to reduce the expense of the calculation. Some previous studies have looked at small gas adsorption in NFMs using plane-wave calculations.[59, 62-63]

Lattice parameters were first optimized, followed by an optimization of atomic coordinates without change to lattice parameters with a 650 eV cutoff and a final optimization of atomic coordinates with a 500 eV cutoff (E(NFM)). Then, an O_2 molecule was introduced to the structure at the site of interest, after which all atomic coordinates were optimized ($E(NFM+O_2)$). Finally, the energy of a single O_2 molecule was calculated for a simulation box of identical size ($E(O_2)$).

The binding energy of O_2 was calculated by:

$$E_b = E(NFM) + E(O_2) – E(NFM+O_2),$$

where $E(NFM)$, $E(O_2)$, and E(NFM+O2) are the total system energies for the NFM only, the O_2 molecule only, and the NFM with an adsorbed O_2 molecule, respectively.

5.3. Results and Discussion

5.3.1. Henry's Constant and Isosteric Heat of Adsorption Calculations

GCMC results for Henry's constant and isosteric heat of adsorption are tabulated in Table 14 and plotted in Figures 43 and 44. Table 16 and Table 15 show the best performers as ranked by k_H and Q_{st}.

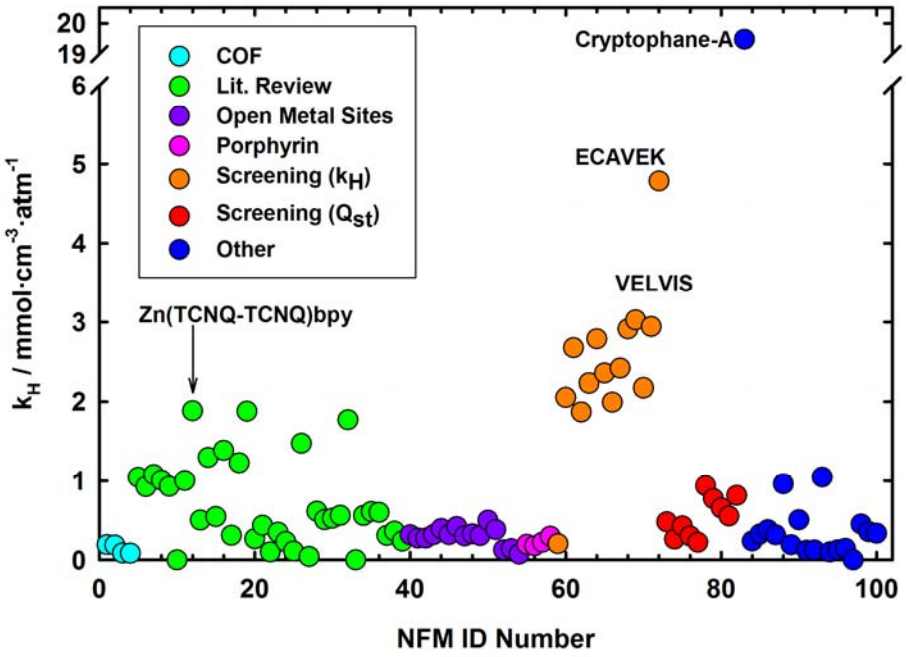

Figure 43. Henry's constants (k_H) for O_2 uptake plotted according to NFM ID assigned in Table 14.

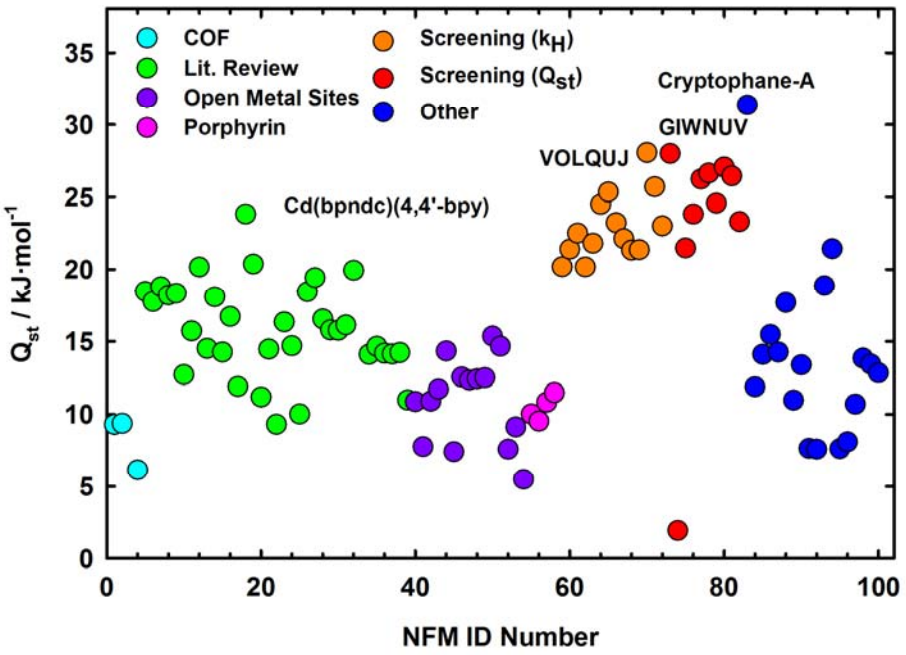

Figure 44. Isosteric heats of adsorption (Q_{st}) O_2 uptake plotted according to NFM ID assigned in Table 14.

Table 15. Properties of NFMs Investigated in This Study, Ranked by k_H

CCDC REFCODE[a]	Category	Metal	V_{free}[b] (%)	S.A.[b] (m^2/g)	ρ_{cryst} (g/cm^3)	LCD[c] (Å)	PLD[c] (Å)	Q_{st} [O_2] (kJ/mol)	k_H [O_2][d] (mmol/ cm^3·atm)	k_H [N_2][d] (mmol/ cm^3·atm)	Selectivity[e] [O_2/N_2]
OJITOR	other (clathrate)	-	12.8	1708	1.28	1.9	1.2	31.4	19.48	-	-
ECAVEK	screening [kH]	Ge	35.1	1162	3.08	4.7	3.7	23.0	4.78	-	-
VELVIS	screening [kH]	Zn	4.4	384	1.24	5.6	2.4	21.4	3.03	2.17	1.39
YIVSOM	screening [kH]	Cd	16.0	1425	1.59	4.5	1.1	25.7	2.94	-	-
VEJZEQ	screening [kH]	Co	35.1	3119	1.22	5.6	2.4	21.3	2.91	2.08	1.40
LEZGED	screening [kH]	Mn, Na	25.4	2000	1.49	4.5	0.7	24.5	2.79	1.82	1.53
EXUMEP	screening [kH]	Mn	28.6	1973	1.50	5.2	1.2	22.5	2.67	2.12	1.26
UFUNIS	screening [kH]	Cu	32.5	2086	1.43	4.4	3.7	22.1	2.42	1.63	1.48
QIWSUK	screening [kH]	Zn	23.5	2346	1.32	4.0	1.3	25.4	2.35	1.07	2.19
LEMMAS	screening [kH]	Zn	36.2	2466	1.36	4.7	3.1	21.8	2.23	1.57	1.42
VOLQUJ	screening [kH]	Zn	14.7	1494	1.63	4.7	1.0	28.1	2.17	1.85	1.17
EVOMOR01	screening [kH]	Mn	31.1	2180	1.26	4.5	2.3	21.4	2.05	1.38	1.48
UFEVEH	screening [kH]	Cd	26.9	2472	1.30	4.6	2.1	23.2	1.99	-	-
MUVGUG	lit. review	Zn	46.1	3838	0.98	5.2	3.7	20.2	1.89	1.18	1.60
WUSXIR	lit. review	Cu	35.5	2367	1.23	4.5	2.3	20.4	1.88	-	-
HIMSAY	screening [kH]	Zn	46.1	3938	0.99	5.1	3.5	20.2	1.87	1.15	1.63
BUSQEM	lit. review	Mn	46.8	4092	0.95	5.2	3.6	19.9	1.77	-	-
WUTKIG	lit. review	Co	51.7	3015	1.03	4.8	2.0	18.4	1.47	-	-
QOCBEQ	lit. review	Ni	45.2	3016	0.97	7.4	4.2	16.7	1.38	-	-
TIRQOB	lit. review	Zn	46.6	2556	1.19	5.3	4.4	18.1	1.29	-	-

iven structure; numbered entries signify structures available only through online database at time of manuscript submission; upporting information of paper; one structure only available from author (PIZA-1).

ach NFM were calculated via Connolly surfaces[37] in Materials Studio (Accelrys, Inc.), using a 1 Å probe radius.

s the slope of the adsorption isotherm in the linear region below 2.5 mbar.

efined as the minimum pore diameter in the largest pore that spans the NFM structure[20] and was calculated according to van der Waals radius when calculating pore size. Largest cavity diameter (LCD) is the maximum pore diameter in the largest . In this study, diffusion through the pore was not considered.

Table 16. Properties of NFMs Investigated in This Study, Ranked by Q_{st}

Rank	NFM ID	NFM Name	CCDC REFCODE[a]	Category	Metal	V_{free}[b] (%)	S.A.[b] (m^2/g)	ρ_{cryst} (g/cm^3)	LCD[c] (Å)	PLD[c] (Å)	Qst [O_2] (kJ/mol)	k_H [O_2][d] (mmol/ cm^3·atm)	k_H [N_2][d] (mmol/ cm^3·atm)	Selectivity[e] [O_2/N_2]
1	83	Cryptophane-A	OJITOR	other (clathrate)	-	12.8	1708	1.28	1.9	1.2	31.4	19.48	-	-
2	70	VOLQUJ	VOLQUJ	screening [kH]	Zn	14.7	1494	1.63	4.7	1.0	28.1	2.17	1.85	1.17
3	73	GIWNUV	GIWNUV	screening [Qst]	Cu	7.9	685	2.21	4.2	1.7	28.0	0.48	0.18	2.62
4	80	XEPCIF	XEPCIF	screening [Qst]	Ni	15.0	1845	1.40	3.7	1.1	27.1	0.66	-	-
5	78	VEGWOU	VEGWOU	screening [Qst]	Zn	17.4	1434	1.59	3.5	0.9	26.7	0.94	0.24	3.89
6	81	YAPYUK	YAPYUK	screening [Qst]	Co	12.9	1198	1.74	2.7	1.2	26.5	0.55	0.25	2.22
7	77	MOFGOE	MOFGOE	screening [Qst]	Cu	16.3	1270	1.98	3.7	2.3	26.2	0.22	0.03	6.72
8	71	YIVSOM	YIVSOM	screening [kH]	Cd	16.0	1425	1.59	4.5	1.1	25.7	2.94	-	-
9	65	QIWSUK	QIWSUK	screening [kH]	Zn	23.5	2346	1.32	4.0	1.3	25.4	2.35	1.07	2.19
10	79	WINCEC	WINCEC	screening [Qst]	Co	24.0	1830	1.54	3.5	2.1	24.6	0.77	-	-
11	64	LEZGED	LEZGED	screening [kH]	Mn, Na	25.4	2000	1.49	4.5	0.7	24.5	2.79	1.82	1.53
12	18	Cd(bpndc)(4,4'-bpy)	EFANOP	lit. review	Cd	91.3	1958	1.52	4.1	1.4	23.8	1.23	-	-
13	76	LIQTEL	LIQTEL	screening [Qst]	Zn	17.7	1543	1.67	3.7	1.3	23.8	0.30	-	-
14	82	YORKAS	YORKAS	screening [Qst]	Cu	26.4	1988	1.48	3.9	1.8	23.3	0.82	-	-
15	66	UFEVEH	UFEVEH	screening [kH]	Cd	26.9	2472	1.30	4.6	2.1	23.2	1.99	-	-
16	72	ECAVEK	ECAVEK	screening [kH]	Ge	35.1	1162	3.08	4.7	3.7	23.0	4.78	-	-
17	61	EXUMEP	EXUMEP	screening [kH]	Mn	28.6	1973	1.50	5.2	1.2	22.5	2.67	2.12	1.26
18	67	UFUNIS	UFUNIS	screening [kH]	Cu	32.5	2086	1.43	4.4	3.7	22.1	2.42	1.63	1.48
19	63	LEMMAS	LEMMAS	screening [kH]	Zn	36.2	2466	1.36	4.7	3.1	21.8	2.23	1.57	1.42
20	75	KOKCUJ	KOKCUJ	screening [Qst]	Cu	20.0	1984	1.54	4.2	1.5	21.5	0.43	0.27	1.60

[a]The CCDC reference code for a given structure; numbered entries signify structures available only through online database at time of manuscript submission; some structures only available in supporting information of paper; one structure only available from author (PIZA-1).
[b]Surface area and free volume of each NFM were calculated via Connolly surfaces[37] in Materials Studio (Accelrys, Inc.), using a 1 Å probe radius.
[c]Henry's constant was calculated as the slope of the adsorption isotherm in the linear region below 2.5 mbar.
[d]Pore-limiting diameter (PLD) is defined as the minimum pore diameter in the largest pore that spans the NFM structure[20] and was calculated according to Ref. [20], which takes into account van der Waals radius when calculating pore size. Largest cavity diameter (LCD) is the maximum pore diameter in the largest pore that spans the NFM structure. In this study, diffusion through the pore was not considered.
[e]Selectivity is calculated as the ratio $k_H[O_2]/k_H[N_2]$.

The COFs do not perform well with respect to k_H—their large surface areas and free volumes may be good for high gas loading applications, but do not lead to high uptakes in the low-loading regime. Their lack of metal centers may explain the low Q_{st} values for COFs, as metal-O_2 interaction energies could substantially increase Q_{st}.

Open metal-site and porphyrin structures perform equally well for k_H and Q_{st}, at about average levels for the structures investigated here. This is surprising based on the expected ability of O_2 to complete the coordination shell of undercoordinated metals (e.g., Zn in MOF-74), as well as the known affinity of porphyrins for O_2.[64-68] The higher than average free volume for open metal-site structures could partially be responsible for the low k_H values, as those structures require relatively large pores for solvent removal in order to create the open metal sites. It is also possible that the classical model (UFF) used to describe framework atoms here is not adequate to properly represent the true interactions between metals and O_2 (this would likely have a larger effect on Q_{st} than k_H). To investigate this possibility further, DFT calculations for O_2 binding energy (analogous to Q_{st}) were performed (see DFT Calculations Section).

Those structures from the "literature review" category yield a relatively wide range of k_H (0-1.9 mmol/cm^3·atm) and Q_{st} (11-24 kJ/mol) values. Because these structures were selected for this category based solely on the fact that they showed promising experimental O_2 uptake, we might expect a low correlation among the results (hence, a wide range of results). While some were selected based on high volumetric O_2 uptake, others were selected for their high O_2/N_2 selectivity, independent of volumetric O_2 uptake. Additionally, in many cases, experiments were performed at cryogenic temperatures, so an NFM's uptake at room temperature could be significantly lower than that at lower temperatures. That many of these structures outperform all COF, open metal-site, and "other" structures is at least a partial verification of our method to screen a large number of structures and find NFMs with high O_2 uptake.

The three best performers from this group (regarding k_H) are Zn(TCNQ-TCNQ)bpy[23], Cu(dhbc)2(4,4'-bpy),[69] and Mn(TCNQ-TCNQ)bpy.[70] Initially, due to the high uptake shown by Zn(TCNQ-TCNQ)bpy and Mn(TCNQ-TCNQ)bpy, additional NFMs with TCNQ linkers were investigated with mediocre (Cd, Co, Fe) to negligible (Ag) O_2 uptake correlated to pore size (AgTCNQ pores are too small to accept O_2). Also, the Cd(bpndc)(4,4'-bpy) structure shows a relatively high Q_{st} of about 24 kJ/mol (this structure is known to be flexible with guest-dependent gate-opening pressures).[71]

NFM structures from the "other" category also show a wide range of k_H and Q_{st} results, as expected because the structures are not correlated to one another. A number of structures are shown to have higher k_H and Q_{st} than open metal-site and porphyrin NFMs. The highest uptake is found for the Cryptophane-A structure,[72] which is not a MOF structure (it has no metal), but rather more closely resembles a clathrate structure. That it was found to have the highest k_H and Q_{st} values of all structures considered here is most likely due to the enclosed cage structure of the clathrate (~4.8 Å in diameter), similar in size to an O_2 molecule. A close agreement between cage and adsorbate sizes has been shown to lead to increased interaction energy due to the simultaneous interactions of the adsorbate with multiple walls of the pore.[3-4, 26-27] The GCMC simulation technique allows for the insertion of molecules into parts of the structure whereas O_2 molecules may not necessarily be able to diffuse experimentally because the cages are not

connected, so it is possible that the Cryptophane-A structure will not be a viable candidate for gas uptake applications.

Other notable NFM structures from this group are sod-ZMOF and MOF-508 (open and closed structures). Interestingly, MOF-508b (closed, guest-free phase) has a k_H value 10 times lower than the open version, but a Qst that is higher by 2.5 kJ/mol. This may be attributed to the smaller free volume of MOF-508b (thus, lower k_H), while the smaller pore diameter of MOF-508b yields a higher Q_{st} due to a better fit of the O_2 molecule in the pore (i.e., greater interactions with the pore). MOF-508 is known to exhibit reversible framework transformations (which cannot be captured using the present modeling framework).[73]

The "screened" structures (those from the previous study of Ar uptake[28]) are divided into two subsets, those selected for their high Ar uptake (Subset I) and those selected for large Ar Qst values (Subset II). As shown in Figure 43, those from Subset I clearly have the highest kH values—nearly all values are higher than those of all the categories, including the structures that have shown the best known experimental results. Thus, with respect to the initial adsorption regime important to detection applications, nearly all structures from the screened results (Subset I) are predicted to exhibit higher O_2 uptake than the best structures from experiment. This result emphasizes the power of large-scale screening for selecting materials for detection applications, as well as confirms the close relationship expected between Ar and O_2 results via GCMC simulations.

Structures from Subset II do not show exceptional O_2 uptake compared to the other structures investigated here (on par with structures from the open metal sites and "other" categories, but lower than the best performers from the "literature review" category), which may be expected because they were selected for their large Q_{st} values and not k_H values. However, Figure 44 shows that Subset II structures have among the highest calculated Q_{st} values for all of the structures investigated here. This result is further evidence of the utility of the screening process. Interestingly, the structures from Subset I show equally high Q_{st} values as those from Subset II. Overall, the screened structures show the highest k_H and Q_{st} values of all structures studied here (apart from the Cryptophane-A structure discussed above). Further, we have shown two distinct classes of "good performers," those with both high k_H and Q_{st} values, and those with low k_H and high Q_{st}.

The overall best performer from the screened results is the ECAVEK structure (k_H), a zeolitic germanate structure. While it is a 3D periodic structure, it is not considered a MOF. The high uptake could be due to the large L-J ε parameter for Ge (191 K, compared to 62.4 K for Zn). The VELVIS, YIVSOM, and VEJZEQ structures are MOF structures that also show very high O_2 uptake. Based on Qst values, the VOLQUJ, GIWNUV, and XEPCIF structures are the most energetically favorable for O_2 uptake with calculated heats of adsorption greater than 27 kJ/mol.

Both k_H and Q_{st}, as calculated here, are a measure of the initial uptake of O_2; k_H indicates the overall uptake at low pressures, while Q_{st} gives an indication of the energetics of initial adsorption. They are related by the density of available sites. So, while a structure with a relatively high Q_{st} value is thermodynamically favored to uptake an adsorbate, if there are

relatively few available sites in that structure, the overall uptake may be lower than that for a structure with a lower Q_{st} but more sites.

Based on the results of the screening here, the structures with the highest Q_{st} values include those from both Subsets of screened results (Figure 45). There does not seem to be any loss in adsorption energy by selecting a structure with a high k_H value from Subset I. This result represents an ideal case for the detection of small adsorbates: a strong thermodynamic driver for adsorption accompanied by a high capacity for the adsorbate. Only considering MOF-like structures, the VELVIS, YIVSOM, and VEJZEQ structures are good candidates for high O_2 uptake at low pressure.

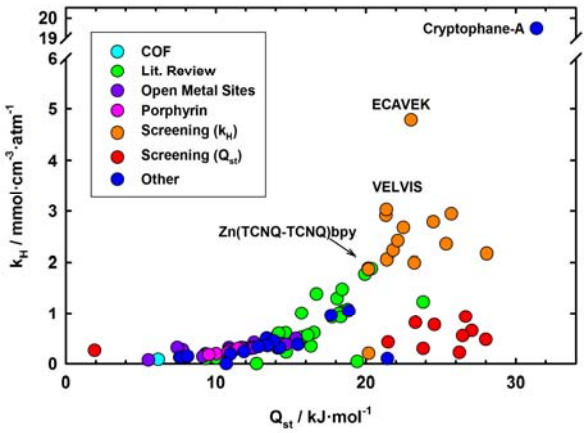

Figure 45. Henry's constants (k_H) for O_2 plotted versus isosteric heat of adsorption (Q_{st}).

Overall, pore size is a reasonable (although incomplete) indicator of O_2 uptake (Figure 46). Pore-limiting diameter (PLD) is defined as the size of the largest sphere that can fit at any point along a pore that spans the entire structure.[20] Below a threshold of about 5 Å PLD, k_H values dramatically increase. A relatively small pore allows for greater adsorbate-adsorbent interaction via interaction with multiple framework atoms, which results in greater Q_{st} and (with a relatively high density of adsorption sites) k_H values. The highest Q_{st} values exist for the smallest PLD (as expected), although there is a relatively large range of values at low PLD.

This large range of values Q_{st} can be partially attributed to the definition of PLD employed here. The PLD refers only to size of the largest sphere that can fit at any point along a pore that spans the entire structure, but some small cages (which can be ideal as adsorption sites[19, 74-75]) are excluded. One example of an NFM for which this is the case is Cu-BTC, which has a PLD of 6.5 Å, but the entrances into its small cages are about 3.5 Å in diameter. Clearly, although there is a striking correlation between calculated uptakes and PLD, a single value for pore diameter is not sufficient to describe all possible adsorbate environments in a given structure. Additionally, it is probable that the UFF parameters used here do not fully describe the metal-adsorbate interactions. These interactions are more examined in closer detail in the DFT Calculations section. Interestingly, the screened results and experimental ("lit. review") structures all have

relatively small PLD, indicating that a promising candidate material for high O_2 uptake is likely to have relatively small pore diameters.

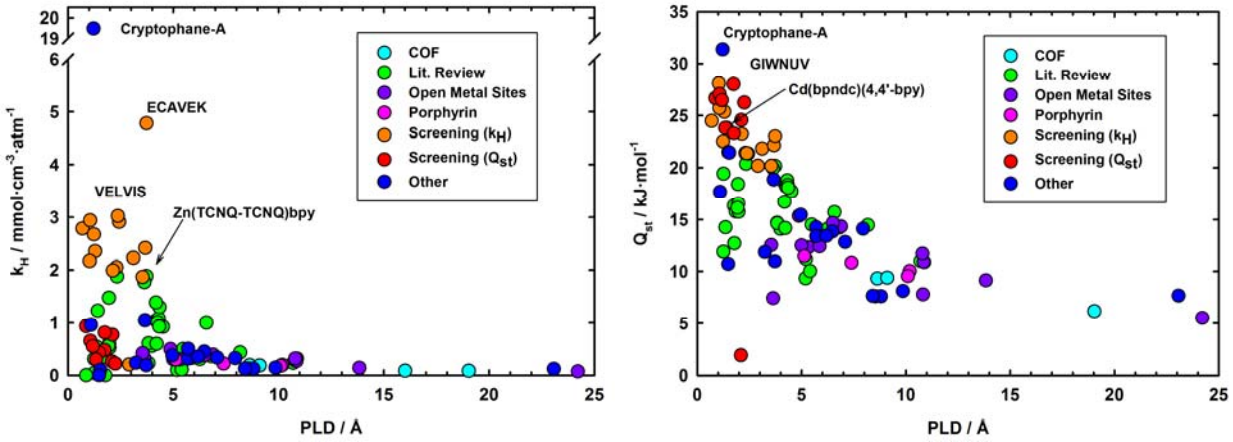

Figure 46. A) Henry's constants (k_H) and B) isosteric heats of adsorption (Q_{st}) for O_2 plotted versus pore-limiting diameter.

5.3.2. Selectivity and Mixture Simulations

In addition to pure uptake numbers and Q_{st} values for O_2, the selectivity of one adsorbate specie over another is crucial to detection applications. It could be the case that a given NFM is a relatively good adsorber of O_2, but if it is equally likely to pick up N_2, and the application requires the detection of O_2 in a predominantly N_2 environment, the usefulness of that NFM for the detection application could be reduced. So while our simulation technique tells us the relative ability of an NFM to uptake O_2 among all the structures studied, selectivity is an additional piece of information that describes the usefulness of the NFM for a given application.

Previous simulation studies for NFMs have shown the usefulness of calculating adsorbate selectivities (defined as the ratio of k_H values from independent isotherms) to rank the ability of an NFM to uptake a given adsorbate competitively.[54, 76-77] Although this definition of selectivity assumes that adsorbates of different species do not interact with each other, for an overall idea of the selectivity, this gives a good idea for screening purposes. A more sophisticated approach to calculating selectivity as a function of pressure is using the ideal adsorbed solution theory (IAST);[28, 78] however, a simple definition of selectivity is used here. One limitation of our models is that flexibility is not taken into account, although it has been shown to be important in selective uptake of small gases.[70, 79]

Henry's constants for N_2 adsorption were calculated for 42 selected structures in order to calculate selectivities. Figure 47 shows selectivity values calculated for selected structures of interest. In some cases, artificially high selectivities were calculated due to taking the ratio of two very small numbers (i.e., the error in those calculations is great in magnitude compared to the selectivity value). For example, the MIL-53(Al)-lt structure shows very low O_2 and N_2 k_H values (6×10^{-4} vs. 1×10^{-6}), but the ratio yields a selectivity of 478. A threshold O_2 k_H value of

at least 0.1 mmol/cm^3·atm was chosen as a minimum requirement for the NFM to appear in Figure 47 and Table 17.

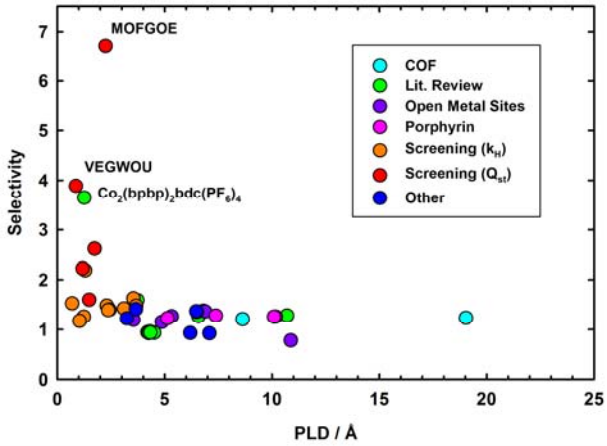

Figure 47. Selectivity of O_2 over N_2 plotted versus pore-limiting diameter for selected structures.

Table 17. Properties of NFMs Investigated in This Study, Ranked by Selectivity

Rank	NFM ID	NFM Name	CCDC REFCODE[a]	Category	Metal	V_{free}[b] (%)	S.A.[b] (m^2/g)	ρ_{cryst} (g/cm^3)	LCD[c] (Å)	PLD[c] (Å)	Qst [O_2] (kJ/mol)	k_H [O_2][d] (mmol/ cm^3·atm)	k_H [N_2][d] (mmol/ cm^3·atm)	Selectivity[e] [O_2/N_2]
1	77	MOFGOE	MOFGOE	screening [Qst]	Cu	16.3	1270	1.98	3.7	2.3	26.2	0.22	0.03	6.72
2	78	VEGWOU	VEGWOU	screening [Qst]	Zn	17.4	1434	1.59	3.5	0.9	26.7	0.94	0.24	3.89
3	27	$Co_2(bpbp)_2bdc(PF_6)_4$	(815290)	lit. review	Co	22.0	2082	1.47	3.7	1.3	19.4	0.04	0.01	3.65
4	73	GIWNUV	GIWNUV	screening [Qst]	Cu	7.9	685	2.21	4.2	1.7	28.0	0.48	0.18	2.62
5	81	YAPYUK	YAPYUK	screening [Qst]	Co	12.9	1198	1.74	2.7	1.2	26.5	0.55	0.25	2.22
6	65	QIWSUK	QIWSUK	screening [kH]	Zn	23.5	2346	1.32	4.0	1.3	25.4	2.35	1.07	2.19
7	62	HIMSAY	HIMSAY	screening [kH]	Zn	46.1	3938	0.99	5.1	3.5	20.2	1.87	1.15	1.63
8	75	KOKCUJ	KOKCUJ	screening [Qst]	Cu	20.0	1984	1.54	4.2	1.5	21.5	0.43	0.27	1.60
9	12	Zn(TCNQ-TCNQ)bpy	MUVGUG	lit. review	Zn	46.1	3838	0.98	5.2	3.7	20.2	1.89	1.18	1.60
10	64	LEZGED	LEZGED	screening [kH]	Mn, Na	25.4	2000	1.49	4.5	0.7	24.5	2.79	1.82	1.53
11	60	EVOMOR01	EVOMOR01	screening [kH]	Mn	31.1	2180	1.26	4.5	2.3	21.4	2.05	1.38	1.48
12	67	UFUNIS	UFUNIS	screening [kH]	Cu	32.5	2086	1.43	4.4	3.7	22.1	2.42	1.63	1.48
13	63	LEMMAS	LEMMAS	screening [kH]	Zn	36.2	2466	1.36	4.7	3.1	21.8	2.23	1.57	1.42
14	93	MOF-508a (open)	EDADIX	other (Zn-based)	Zn	41.8	2687	1.24	5.5	3.7	18.9	1.05	0.74	1.41
15	68	VEJZEQ	VEJZEQ	screening [kH]	Co	35.1	3119	1.22	5.6	2.4	21.3	2.91	2.08	1.40
16	69	VELVIS	VELVIS	screening [kH]	Zn	4.4	384	1.24	5.6	2.4	21.4	3.03	2.17	1.39
17	38	Cr-BTC	(supp. Info.)	lit. review (open metal)	Cr	70.9	2983	0.80	12.5	6.8	14.2	0.36	0.26	1.38
18	98	MIL-53(Cr)-ht	MINVUA01	other (MIL)	Cr	54.6	3089	1.04	7.0	6.5	13.8	0.45	0.33	1.37
19	44	Ru-BTC	IVESOS	open metal	Ru	70.4	2355	1.02	11.7	6.9	14.3	0.39	0.29	1.37
20	51	Cu-BTC (HKUST-1)	FIQCEN	open metal	Cu	69.8	2770	0.88	13.2	6.5	14.7	0.38	0.28	1.36

[a]The CCDC reference code for a given structure; numbered entries signify structures available only through online database at time of manuscript submission; some structures only available in supporting information of paper; one structure only available from author (PIZA-1).
[b]Surface area and free volume of each NFM were calculated via Connolly surfaces[37] in Materials Studio (Accelrys, Inc.), using a 1 Å probe radius.
[c]Henry's constant was calculated as the slope of the adsorption isotherm in the linear region below 2.5 mbar.
[d]Pore-limiting diameter (PLD) is defined as the minimum pore diameter in the largest pore that spans the NFM structure[20] and was calculated according to Ref. [20], which takes into account van der Waals radius when calculating pore size. Largest cavity diameter (LCD) is the maximum pore diameter in the largest pore that spans the NFM structure. In this study, diffusion through the pore was not considered.
[e]Selectivity is calculated as the ratio $k_H[O_2]/k_H[N_2]$.

The top-ranking structures for selectivity are from the "screened" category, although some structures from the "literature review" category also show selective adsorption of O_2 over N_2. The best performers are the MOFGOE, VEGWOU, and $Co_2(bpbp)_2bdc(PF_6)_4$ structures, each with an O_2/N_2 selectivity greater than 3. For comparison, an experimental study of an $AgBr/SiO_2$ oxygen-selective adsorbent designed for PSA systems showed an O_2/N_2 selectivity of 2.87 at 1 atm and 295 K[80] and an Na-A zeolite has an O_2 selectivity of 3.8 from air at 243 K.[81]

The top four selectivity performers from the "literature review" category are the $Co_2(bpbp)_2bdc(PF_6)_4$,[32] Zn(TCNQ-TCNQ),[23] Cr-BTC,[34] and $Fe_2(dhtp)$[33] structures; in each case, experimental O_2 and N_2 isotherms up to 1 bar have been published. For Zn(TCNQ-TCNQ)bpy, the published values are for a cryogenic temperature (77 K) and are not comparable to the room temperature simulation results. A comparison of the GCMC-generated isotherms with experimental data for the other three structures is shown in Figure 48.

For all three structures represented in Figure 48, there is an immediate jump in experimental O_2 uptake below 0.1 bar, nearly saturating the available adsorption sites (there are only slight increases in adsorption up to 1 bar). The nearly infinite slope of the adsorption O_2 adsorption isotherm compared to the small slope of the N_2 isotherm suggests that there are specific adsorption sites for O_2 adsorption that are not available for N_2. Interestingly, the slopes of the O_2 and N_2 isotherms are very similar in all three cases following the immediate uptake of O_2.

In contrast, the simulation isotherms do not show an immediate, dramatic O_2 uptake at low pressure, but rather a linear uptake region up to 1 bar for both O_2 and N_2. In all cases, the O_2 adsorption is underpredicted and the N_2 adsorption is overpredicted. The overprediction of N_2 adsorption could be attributed to the model being a perfect representation of the crystalline material for which all possible adsorption sites are available, whereas experimentally, surface defects may exist which restrict access to some adsorption sites. Additionally, the GCMC technique allows for the adsorption of N_2 into any part of the structure without any diffusion constraints. Thus it is possible that the lower N_2 uptake seen experimentally is partially due to barriers to N_2 diffusion through the structure.

However, the difference in O_2 isotherm shapes represents a fundamental breakdown of the GCMC model to describe O_2 uptake in these three materials. Clearly, the initial uptake of O_2 seen experimentally is not replicated in the simulations. Apparently, the combination of UFF parameters with the O_2 model does not sufficiently represent O_2-NFM interactions. Additional work could be done to specifically develop O_2-NFM cross-terms for the force field that would help replicate the experimental results, but in practice, this requires extensive work and is rarely done. Also, it is possible that the flexibility of the NFM structure plays a role in selective adsorption[70, 82]—this could not be captured in the current simulation scheme using rigid frameworks, and would require the development of a flexible forcefield model, few of which currently exist.[83-84] Additionally, the classical GCMC technique does not always capture adsorption at open metal sites because the Lennard-Jones description of short-range interatomic interaction using UFF does not allow gas-metal separations as small as those found via neutron powder diffraction[74] or electronic-scale DFT calculations;[85] all three of these structures have open metal sites.

Overall, the selectivity calculations based on GCMC results do not agree well with experimental results. Although the current scheme distinguishes between O_2 and N_2 for $Co_2(bpbp)_2bdc(PF_6)_4$, (O_2/N_2 selectivity of 3.65), the selectivities calculated for Cr-BTC and Fe_2(dhtp) (1.38 and 1.28, respectively) are modest when compared to experiment. While the modeling effort here has shown selective uptake of O_2 over N_2 in some cases, the GCMC technique is not sufficient to properly replicate experimental results. Higher level electronic-scale calculations can not give higher-quality adsorption isotherms, but they can provide adsorption energies to compare with GCMC-derived Q_{st} values. DFT calculations are the subject of a later section of this paper.

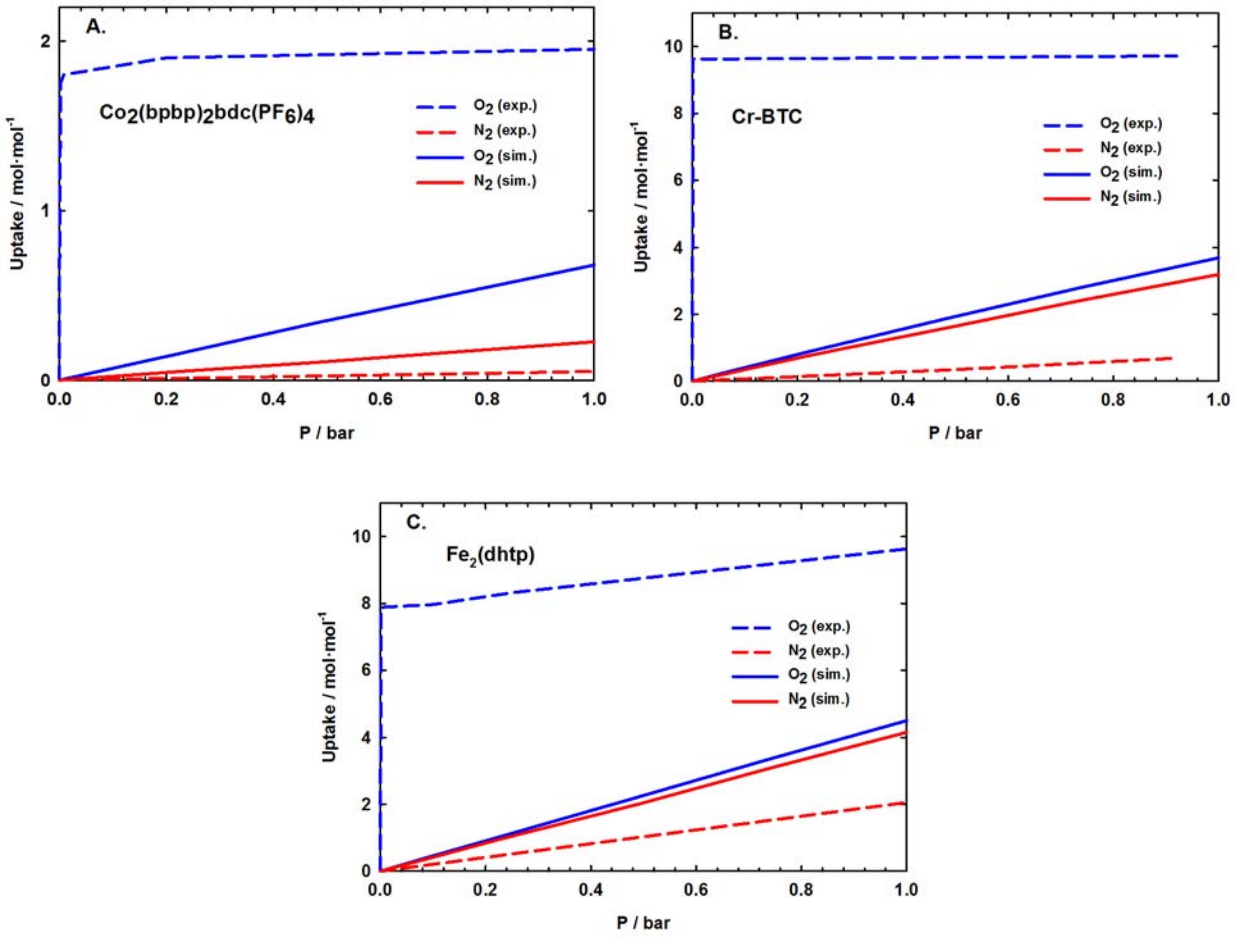

Figure 48. Comparison of GCMC simulation and experimental isotherms for O_2 and N_2 uptake in the A) $Co_2(bpbp)_2bdc(PF_6)_4$, B) Cr-BTC, and C) Fe_2(dhtp) structures at 298 K.

5.3.3. Mixture Simulations

In addition to comparing independent isotherms to calculate selectivity (as above), competitive adsorption can be analyzed via mixture simulations in which multiple adsorbates are taken up by the NFM.[19, 86-87] Table 18 shows the results of O_2/H_2O and O_2/N_2 mixture simulations for ten selected NFM structures (three open metal-site and seven "screened" structures). The mixture

simulations were devised to be extreme cases for O_2 detection—trace amounts of O_2 in the presence of 100% relative humidity (R.H.) water or 1 bar N_2.

The three open metal-site structures (PCN-14, Cu-BTC, and MOF-74) show little to no effect of the presence of a second adsorbate (H_2O or N_2) on the uptake of O_2. The Henry's constants from the "screened" structures show no reduction due to the presence of H_2O; however, O_2 uptake is significantly lowered in the presence of N_2 (40-70%). This effect of N_2 on the adsorption of O_2 may restrict their use as detectors in N_2 environments or as O_2/N_2 separators.

Table 18. O_2 Henry's Constant Comparison for O_2/H_2O and O_2/N_2 Mixture Simulations

input stream	H_2O/N_2 content	Henry's Constant (mmol/cm^3·atm)									
		PCN-14	Cu-BTC	MOF-74	ECAVEK	VELVIS	VEJZEQ	YIVSOM	LEZGED	VOLQUJ	EXUMEP
pure O_2	-	0.52	0.41	0.32	5.1	3.2	3.1	2.9	2.9	2.8	2.8
mixture	100% R.H.	0.53	0.41	0.31	5.0	3.2	3.1	2.9	2.9	2.8	2.8
mixture	1 bar N_2	0.50	0.37	0.31	2.3	1.8	1.8	1.1	1.8	0.8	1.4

5.3.4. DFT Binding Energy Calculations

Binding energies for O_2 and N_2 adsorption calculated via DFT calculations are summarized in Table 19 for 10 structures. Overall, there is not good agreement between GCMC-calculated Q_{st} values and DFT-calculated binding energies (E_b) for O_2. In fact, in many cases, adsorption of O2 or N2 is not predicted to be thermodynamically favorable (negative values in Table 19). The E_b values should be a better estimation of the true interaction energies than Q_{st} values because they are done at a higher level of theory. The DFT calculations allow the structure to relax when a molecule is adsorbed—this structural optimization is not permitted in the GCMC simulations for lack of a flexible force field model. Another difference between the two techniques is that GCMC simulations are performed at 298 K, whereas the DFT calculations are done for 0 K structures. Gas uptake is known to be temperature-dependent in some structures; however, temperature likely has little effect on the binding of a single adsorbate molecule.

Table 19. Binding Energies for O_2 and N_2 from DFT Calculations and Q_{st} from GCMC Simulations

NFM Name (Adsorption Site)	O_2 Binding Energy[a]			N_2 Binding Energy[a]	
	E_b (eV)	E_b (kJ/mol)	Q_{st}[b] (kJ/mol)	E_b (eV)	E_b (kJ/mol)
Cu-BTC (Cu site)	0.04	4	14.7	0.88	85
Cu-BTC (small cage site)	0.23	23		0.03	3
Cr-BTC (Cr site)	-0.74	-71	14.2	-0.22	-21
Cr-BTC (small cage site)	-0.42	-41		0.04	4
Fe_2(dhtp) (Fe site)	1.62	156	11.0	0.39	38
Zn_2(dhtp) (Zn site)	-0.57	-55	10.9	-0.05	-5
PPF-5 (Ni site)	-1.16	-112	9.5	-0.42	-41
Cd(bpndc)(4,4'-bpy) (pore)	-1.47	-142	23.8	-2.32	-224
Zn(TCNQ-TCNQ)bpy (small pore)	-1.28	-123	20.2	-0.64	-62
Zn(TCNQ-TCNQ)bpy (large pore)	-0.45	-43		-0.09	-9
$Co_2(bpbp)_2bdc(PF_6)_4$ (Co sites)	3.30	318	19.4	0.66	64
MOFGOE (Cu site)	-1.39	-134	26.2	-1.06	-102
GIWNUV (Cu site)	-1.28	-123	28.0	-1.50	-144
GIWNUV (pore)	-0.85	-82		-0.22	-21

[a]Positive values of binding energy indicate thermodynamically favorable adsorption.
[b]Q_{st} values are from GCMC simulation in this work.

No experimental Q_{st} or E_b values are known for O_2 in the structures examined here. One DFT study of O_2 uptake at an open metal site in Cu-BTC used a cluster model in a periodic simulation cell—the VASP-calculated binding energy was estimated to be between 13.5 (GGA) and 35.6 (LDA) kJ/mol.[62] Here, the fully periodic structure is used and the binding energy of O_2 is predicted to be only 4 kJ/mol at the Cu site, but 23 kJ/mol at the small cage site (interestingly, the GCMC results show a preference of O_2 uptake in the small cage site, as well). The Cr-BTC structure is nearly identical to the Cu-BTC structure, and the Q_{st} values are nearly identical, but the DFT-calculated binding energy for O_2 is much lower (less thermodynamically favorable) for Cr-BTC. It is not clear why this is the case, or why N_2 uptake is predicted to be more favorable than O_2 uptake when experimentally, there is a significant O_2 uptake at very low pressure.[34]

On the other hand, in the Fe_2(dhtp) structure, the binding of O_2 is highly favored over N_2, in agreement with experiment.[33] The adsorption of O_2 at the open Fe site has such a high predicted binding energy that it would not be predicted to be reversible. Experimentally, O_2 adsorption is fully reversible at 211 K, but is irreversible at 298 K, so it may not be a good candidate for room temperature sensing of O_2 (where a quick regeneration of the detection device is important).[33] In contrast, the isostructural Zn_2(dhtp) is predicted to have preferential adsorption of N_2 over O_2.

This is in agreement with the GCMC uptake results, where an O_2/N_2 selectivity of 0.78 is predicted, although the calculated Q_{st} values are nearly identical for the two structures.

The Zn(TCNQ-TCNQ)bpy structure was studied for its high experimental O_2/N_2 selectivity.[23] However, this selectivity is only high above a threshold pressure (~30% of the saturation pressure at 77 K); otherwise the selectivity is very low. This could explain the relatively close predicted values of binding energy for O_2 and N_2 for this structure, as we are at the infinite dilution limit.

Finally, the most dramatic difference in O_2 and N_2 binding energies is for the $Co_2(bpbp)_2bdc(PF_6)_4$ structure, which is predicted to have an extremely high O_2 binding energy. This could explain the high O_2/N_2 selectivity observed experimentally. The relative attraction of O_2 over N_2 in the dicobalt complex is clearly established based on the DFT results (Figure 49).

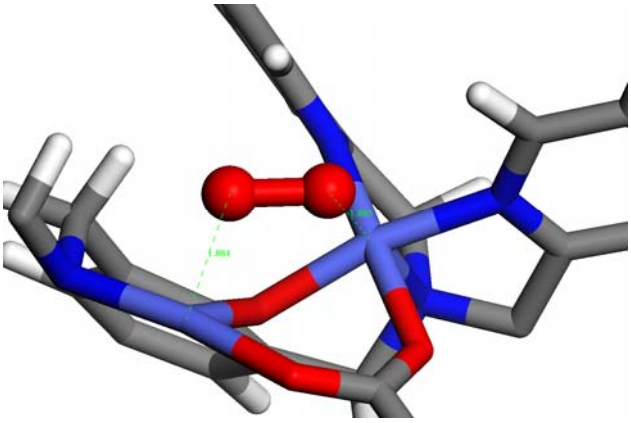

Figure 49. DFT-optimized structure of an O_2 molecule at the dicobalt complex in $Co_2(bpbp)_2bdc(PF_6)_4$ (C, H, O, N, and Co atoms are colored grey, white, red, dark blue, and light blue, respectively).

5.4. Conclusion

A screening of 100 NFM structures for O_2 uptake via comparison of Henry's constant of adsorption and isosteric heat of adsorption was done via classical GCMC simulation with UFF. The limitations of using a general, rigid force field (e.g., general metal-O_2 parameters, no flexible framework) for interatomic interactions to study gas uptake and energetics are clear for O_2, perhaps more so than for noble gases. However, a preliminary screening of Ar uptake in a set of more than 2,000 structures yielded a subset of structures that outperform most structures found to have good O_2 uptake experimentally.

Additionally, the GCMC results do show preferential O_2 uptake for those structures with small pores—this result could be used as a first screening step in selecting a candidate material for O_2 uptake. Mixture simulations indicate that the presence of background H_2O or N_2 could hinder O_2 uptake for some NFMs, but not for others. This distinction could be important in selecting a material for detection of O_2 in an inert (i.e., N_2) environment.

The most obvious failing of the screening via GCMC simulation approach is apparent when comparing O_2 uptake isotherms with experiment—the GCMC results greatly underestimate the O_2 uptake at low pressure, probably due to electronic-scale considerations (e.g., metal-O_2 interactions). DFT calculations cannot give adsorption isotherms for comparison, but O_2 binding energy calculations show preferential binding of O_2 over N_2 for Fe_2(dhtp) and $Co_2(bpbp)_2bdc(PF_6)_4$. For Cr-BTC, the opposite is true, in contrast to experiment. Overall, the ranking of a large number of candidate materials for O_2 uptake via computational screening remains a complicated issue—GCMC can provide some insight into promising materials, but more expensive DFT calculations are also helpful for calculating binding energy at specific adsorption sites.

5.5. References

1. McKee, D. W. Separation of an Oxygen-Nitrogen Mixture. 3,140,933, 1964.
2. Fitch, F. R.; Bulow, M.; Ojo, A. V. Adsorptive Separation of Nitrogen from Other Gases. 1995.
3. Sircar, S.; Rao, M. B.; Golden, T. C., *Adsorption and Its Applications in Industry and Environmental Protection, Vol I: Applications in Industry* **1999,** *120*, 395-423.
4. Jeazet, H. B. T.; Staudt, C.; Janiak, C., *Chem. Commun.* **2012,** *48* (15), 2140-2142.
5. Yang, R. T., *Adsorbents: Fundamentals and Applications*. John Wiley & Sons, Inc.: Hoboken, New Jersey, USA, 2003.
6. Kuppler, R. J.; Timmons, D. J.; Fang, Q. R.; Li, J. R.; Makal, T. A.; Young, M. D.; Yuan, D. Q.; Zhao, D.; Zhuang, W. J.; Zhou, H. C., *Coordination Chemistry Reviews* **2009,** *253* (23-24), 3042-3066.
7. Li, J. R.; Kuppler, R. J.; Zhou, H. C., *Chem. Soc. Rev.* **2009,** *38* (5), 1477-1504.
8. Kreno, L. E.; Leong, K.; Farha, O. K.; Allendorf, M.; Van Duyne, R. P.; Hupp, J. T., *Chem. Rev.* **2011,** *112* (2), 1105-1125.
9. Dultsev, F. N.; Kolosovsky, E. A., *Langmuir* **2009,** *25* (20), 12195-12200.
10. Arshak, K.; Moore, E.; Lyons, G. M.; Harris, J.; Clifford, S., *Sens. Rev.* **2004,** *24* (2), 181-198.
11. Sang-Mok, C.; Muramatsu, H.; Nakamura, C.; Miyake, J., *Mater. Sci. Eng. C, Biomin. Supramol. Syst.* **2000,** *C12* (1-2), 111-123.
12. Pohl, A., *IEEE Trans. Ultrason. Ferroelectr. Freq. Control* **2000,** *47* (2), 317-332.
13. Boisen, A.; Dohn, S.; Keller, S. S.; Schmid, S.; Tenje, M., *Rep. Prog. Phys.* **2011,** *74* (3), 036101.
14. Allendorf, M. D.; Houk, R. J. T.; Andruszkiewicz, L.; Talin, A. A.; Pikarsky, J.; Choudhury, A.; Gall, K. A.; Hesketh, P. J., *J. Am. Chem. Soc.* **2008,** *130* (44), 14404-14405.
15. Lee, J.-H.; Houk, R. T. J.; Robinson, A.; Greathouse, J. A.; Thornberg, S. M.; Allendorf, M. D.; Hesketh, P. J. In *Investigation of Microcantilever Array with Ordered Nanoporous Coatings for Selective Chemical Detection*, Thomas, G.; Islam, M. S.; Achyut, K. D., Eds. SPIE: 2010; p 767927.
16. Venkatasubramanian, A.; Lee, J.-H.; Stavila, V.; Robinson, A.; Allendorf, M. D.; Hesketh, P. J., *Sensor. Actuat. B-Chem.* (0).
17. Robinson, A. L.; Stavila, V.; Zeitler, T. R.; White, M. I.; Thornberg, S. M.; Greathouse, J. A.; Allendorf, M. D., *Anal. Chem.* **2012**.
18. Farrusseng, D.; Daniel, C.; Gaudillere, C.; Ravon, U.; Schuurman, Y.; Mirodatos, C.; Dubbeldam, D.; Frost, H.; Snurr, R. Q., Heats of Adsorption for Seven Gases in Three Metal-Organic Frameworks: Systematic Comparison of Experiment and Simulation. *Langmuir* **2009,** *25* (13), 7383-7388.
19. Zeitler, T. R.; Allendorf, M. D.; Greathouse, J. A., Grand Canonical Monte Carlo Simulation of Low-Pressure Methane Adsorption in Nanoporous Framework Materials for Sensing Applications. *J. Phys. Chem. C* **2011,** *116* (5), 3492-3502.
20. Haldoupis, E.; Nair, S.; Sholl, D. S., Efficient Calculation of Diffusion Limitations in Metal Organic Framework Materials: A Tool for Identifying Materials for Kinetic Separations. *J. Am. Chem. Soc.* **2010,** *132* (21), 7528-7539.

21. Keskin, S.; Sholl, D. S., *Langmuir* **2009,** *25* (19), 11786-11795.
22. Wilmer, C. E.; Leaf, M.; Lee, C. Y.; Farha, O. K.; Hauser, B. G.; Hupp, J. T.; Snurr, R. Q., *Nat Chem* **2012,** *4* (2), 83-89.
23. Shimomura, S.; Higuchi, M.; Matsuda, R.; Yoneda, K.; Hijikata, Y.; Kubota, Y.; Mita, Y.; Kim, J.; Takata, M.; Kitagawa, S., *Nature Chemistry* **2010,** *2* (8), 633-637.
24. Zhang, S. M.; Chang, Z.; Hu, T. L.; Bu, X. H., *Inorg. Chem.* **2010,** *49* (24), 11581-11586.
25. Cote, A. P.; Benin, A. I.; Ockwig, N. W.; O'Keeffe, M.; Matzger, A. J.; Yaghi, O. M., Porous, Crystalline, *Science* **2005,** *310* (5751), 1166-1170.
26. Smithenry, D. W.; Wilson, S. R.; Suslick, K. S., *Inorg. Chem.* **2003,** *42* (24), 7719-7721.
27. Kosal, M. E.; Chou, J.-H.; Wilson, S. R.; Suslick, K. S., *Nature Materals* **2002,** *1*, 118-121.
28. Van Heest, T.; Teich-McGoldrick, S. L.; Greathouse, J. A.; Allendorf, M. D.; Sholl, D. S., *J. Phys. Chem. C* **2012,** *116* (24), 13183-13195.
29. Zhou, W., *Chem. Rec.* **2010,** *10* (3), 200-204.
30. Wu, H.; Simmons, Jason M.; Liu, Y.; Brown, Craig M.; Wang, X.-S.; Ma, S.; Peterson, Vanessa K.; Southon, Peter D.; Kepert, Cameron J.; Zhou, H.-C.; Yildirim, T.; Zhou, W., *Chem.-Eur. J.* **2010,** *16* (17), 5205-5214.
31. Fateeva, A.; Devautour-Vinot, S.; Heymans, N.; Devic, T.; Greneche, J. M.; Wuttke, S.; Miller, S.; Lago, A.; Serre, C.; De Weireld, G.; Maurin, G.; Vimont, A.; Ferey, G., *Chem. Mater.* **2011,** *23* (20), 4641-4651.
32. Southon, P. D.; Price, D. J.; Nielsen, P. K.; McKenzie, C. J.; Kepert, C. J., *J. Am. Chem. Soc.* **2011,** *133* (28), 10885-10891.
33. Bloch, E. D.; Murray, L. J.; Queen, W. L.; Chavan, S.; Maximoff, S. N.; Bigi, J. P.; Krishna, R.; Peterson, V. K.; Grandjean, F.; Long, G. J.; Smit, B.; Bordiga, S.; Brown, C. M.; Long, J. R., *J. Am. Chem. Soc.* **2011,** *133* (37), 14814-14822.
34. Murray, L. J.; Dinca, M.; Yano, J.; Chavan, S.; Bordiga, S.; Brown, C. M.; Long, J. R., *J. Am. Chem. Soc.* **2010,** *132* (23), 7856-+.
35. Li, J.-R.; Sculley, J.; Zhou, H.-C., *Chem. Rev.* **2011,** *112* (2), 869-932.
36. Wu, H.; Zhou, W.; Yildirim, T., *J. Am. Chem. Soc.* **2009,** *131* (13), 4995-5000.
37. Connolly, M. L., *Science* **1983,** *221* (4612), 709-713.
38. Rappe, A. K.; Casewit, C. J.; Colwell, K. S.; Goddard, W. A.; Skiff, W. M., Uff, *J. Am. Chem. Soc.* **1992,** *114* (25), 10024-10035.
39. Ye, Q. G.; Yan, S. Y.; Liu, D. H.; Yang, Q. Y.; Zhong, C. L., *Mol. Simulat.* **2010,** *36* (9), 682-692.
40. Assfour, B.; Seifert, G., *International Journal of Hydrogen Energy* **2009,** *34* (19), 8135-8143.
41. Nalaparaju, A.; Babarao, R.; Zhao, X. S.; Jiang, J. W., *ACS Nano* **2009,** *3* (9), 2563-2572.
42. Xue, C. Y.; Yang, Q. Y.; Zhong, C. L., *Mol. Simulat.* **2009,** *35* (15), 1249-1255.
43. Hansen, N.; Agbor, F. A. B.; Keil, F. J., *Fluid Phase Equilibria* **2007,** *259* (2), 180-188.
44. Errington, J. R.; Panagiotopoulos, A. Z., *J. Phys. Chem. B* **1998,** *102* (38), 7470-7475.
45. Potoff, J. J.; Siepmann, J. I., *AIChE J.* **2001,** *47* (7), 1676-1682.
46. Allen, M. P.; Tildesley, D. J., *Computer Simulation of Liquids*. Oxford University Press: Oxford, 1996.
47. Xu, Q.; Zhong, C. L., *J. Phys. Chem. C* **2010,** *114* (11), 5035-5042.
48. Meng, C. C.; Zhong, C. L., *J. Phys. Chem. C* **2010,** *114* (21), 9945-9951.
49. Zhong, C. L., updated atomic charges for new atom types ed.; 2010.
50. Martin, M. G. *MCCCS Towhee*, 5.2; 2009.

51. Yang, Q. Y.; Zhong, C. L.; Chen, J. F., *J. Phys. Chem. C* **2008,** *112* (5), 1562-1569.
52. Greathouse, J. A.; Ockwig, N. W.; Criscenti, L. J.; Guilinger, T. R.; Pohl, P.; Allendorf, M. D., *Phys. Chem. Chem. Phys.* **2010,** *12* (39), 12621-12629.
53. Greathouse, J. A.; Allendorf, M. D., *J. Phys. Chem. C* **2008,** *112* (15), 5795-5802.
54. Greathouse, J. A.; Kinnibrugh, T. L.; Allendorf, M. D., *Ind. Eng. Chem. Res.* **2009,** *48* (7), 3425-3431.
55. Kresse, G.; Furthmuller, J., *Computational Materials Science* **1996,** *6* (1), 15-50.
56. Kresse, G.; Furthmuller, J., *Phys. Rev. B* **1996,** *54* (16), 11169-11186.
57. Kresse, G.; Hafner, J., *Phys. Rev. B* **1994,** *49* (20), 14251-14269.
58. Kresse, G.; Hafner, J., *Phys. Rev. B* **1993,** *47* (1), 558-561.
59. Watanabe, T.; Sholl, D. S., *J. Chem. Phys.* **2010,** *133* (9).
60. Perdew, J. P.; Chevary, J. A.; Vosko, S. H.; Jackson, K. A.; Pederson, M. R.; Singh, D. J.; Fiolhais, C., *Phys. Rev. B* **1993,** *48* (7), 4978-4978.
61. Perdew, J. P.; Chevary, J. A.; Vosko, S. H.; Jackson, K. A.; Pederson, M. R.; Singh, D. J.; Fiolhais, C., *Phys. Rev. B* **1992,** *46* (11), 6671-6687.
62. Chenggang, Z.; Lujie, C.; Shihao, W.; Qiuju, Z.; Liang, C., *Computational and Theoretical Chemistry* **2011,** *976* (1-3).
63. Wu, H.; Simmons, J. M.; Srinivas, G.; Zhou, W.; Yildirim, T., *J. Phys. Chem. Lett.* **2010,** *1* (13), 1946-1951.
64. Amao, Y.; Okura, I., *J. Porphyr. Phthalocyanines* **2009,** *13* (11), 1111-1122.
65. Furuto, T.; Lee, S. K.; Amao, Y.; Asai, K.; Okura, I., *J. Photochem. Photobiol. A-Chem.* **2000,** *132* (1-2), 81-86.
66. Collman, J. P.; Brauman, J. I.; Fitzgerald, J. P.; Sparapany, J. W.; Ibers, J. A., *J. Am. Chem. Soc.* **1988,** *110* (11), 3486-3495.
67. Collman, J. P.; Brauman, J. I.; Doxsee, K. M.; Halbert, T. R.; Hayes, S. E.; Suslick, K. S., *J. Am. Chem. Soc.* **1978,** *100* (9), 2761-2766.
68. Collman, J. P.; Brauman, J. I.; Suslick, K. S., *J. Am. Chem. Soc.* **1975,** *97* (24), 7185-7186.
69. Yamazaki, T.; Takahashi, Y.; Yoshida, D., *J. Colloid Interface Sci.* **2011,** *362* (2), 463-469.
70. Shimomura, S.; Matsuda, R.; Kitagawa, S., *Chem. Mater.* **2010,** *22* (14), 4129-4131.
71. Tanaka, D.; Nakagawa, K.; Higuchi, M.; Horike, S.; Kubota, Y.; Kobayashi, L. C.; Takata, M.; Kitagawa, S., *Angew. Chem. Int. Edit.* **2008,** *47* (21), 3914-3918.
72. Taratula, O.; Hill, P. A.; Khan, N. S.; Carroll, P. J.; Dmochowski, I. J., *Nat Commun* **2010,** *1*, 148.
73. Chen, B. L.; Liang, C. D.; Yang, J.; Contreras, D. S.; Clancy, Y. L.; Lobkovsky, E. B.; Yaghi, O. M.; Dai, S., *Angew. Chem. Int. Edit.* **2006,** *45* (9), 1390-1393.
74. Getzschmann, J.; Senkovska, I.; Wallacher, D.; Tovar, M.; Fairen-Jimenez, D.; Düren, T.; van Baten, J. M.; Krishna, R.; Kaskel, S., *Micropor. Mesopor. Mat.* **2010,** *136* (1-3), 50-58.
75. Castillo, J. M.; Vlugt, T. J. H.; Calero, S., *J. Phys. Chem. C* **2008,** *112* (41), 15934-15939.
76. Ryan, P.; Farha, O. K.; Broadbelt, L. J.; Snurr, R. Q., *AIChE J.* **2011**, n/a-n/a.
77. Sarkisov, L., *J. Phys. Chem. C* **2012,** *116* (4), 3025-3033.
78. Valenzuela, D. P.; Myers, A. L.; Talu, O.; Zwiebel, I., *AIChE J.* **1988,** *34* (3), 397-402.
79. Hamon, L.; Llewellyn, P. L.; Devic, T.; Ghoufi, A.; Clet, G.; Guillerm, V.; Pirngruber, G. D.; Maurin, G.; Serre, C.; Driver, G.; van Beek, W.; Jolimaitre, E.; Vimont, A.; Daturi, M.; Ferey, G., *J. Am. Chem. Soc.* **2009,** *131* (47), 17490-17499.
80. Jayaraman, A.; Yang, R. T., *Chem. Eng. Sci.* **2005,** *60* (3), 625-634.
81. Izumi, J.; Suzuji, M., *Adsorpt.-J. Int. Adsorpt. Soc.* **2000,** *6* (3), 205-212.

82. Thallapally, P. K.; Tian, J.; Kishan, M. R.; Fernandez, C. A.; Dalgarno, S. J.; McGrail, P. B.; Warren, J. E.; Atwood, J. L., *J. Am. Chem. Soc.* **2008,** *130* (50), 16842-+.
83. Zheng, B.; Sant, M.; Demontis, P.; Suffritti, G. B., *J. Phys. Chem. C* **2011,** *116* (1), 933-938.
84. Greathouse, J. A.; Allendorf, M. D., *J. Am. Chem. Soc.* **2006,** *128* (33), 10678-10679.
85. Chen, L.; Grajciar, L.; Nachtigall, P.; Düren, T., *J. Phys. Chem. C* **2011,** *115* (46), 23074-23080.
86. Gallo, M.; Glossman-Mitnik, D., *J. Phys. Chem. C* **2009,** *113* (16), 6634-6642.
87. Liu, B.; Yang, Q.; Xue, C.; Zhong, C.; Chen, B.; Smit, B., *J. Phys. Chem. C* **2008,** *112* (26), 9854-9860.

6. LARGE ANALYTE SCREENING USING GRAD CANONICAL MONTE CARLO[3]

6.1. Introduction

The exceptionally high surface areas and tunable pore chemistries of metal-organic frameworks (MOFs) and related nanoporous crystalline structures make them attractive for applications involving gas storage and chemical separations. The majority of work to date concerns light gases, such as hydrogen,[1] methane,[2-6] noble gases,[7-13] and CO_2,[14-17] as well as key separations required to purify them.[18] These applications generally involve high pressures and relatively high impurity concentrations.

In contrast, very little attention has been paid to adsorption of gases by MOFs at the very low pressures and/or concentrations relevant to detection of trace materials, such as explosives, chemical weapons, and volatile organic compounds (VOCs). Use of MOFs as the chemical recognition element of a sensor has been demonstrated, however. Winter et al. described the use of a quartz microbalance coated with a MOF to screen for uptake of various hydrocarbons.[19] Coating a microcantilever with HKUST-1 enables detection of water vapor, alcohols, and CO_2 as a result of the stress induced at the interface between the MOF layer and the microcantilever.[20] Sensing concepts using luminescent MOFs to detect explosives[21] and other molecules[22] were recently demonstrated. Ni et al. also showed that IRMOF-1 can trap and preconcentrate organic phosphonates, which are surrogates for nerve agents.[23] These results and the enormous variety of MOF structures suggest there is great potential for enhancing both the uptake and selectivity for a particular analyte, but at the same time highlight the need for approaches to rapidly screen structural variations to avoid unproductive synthetic efforts. At the low concentrations relevant to chemical detection, the interaction energy between framework and adsorbate is needed to predict a material's potential for use in sensing applications. Previous work on zeolite adsorbents has led to some surprising results. For example, calorimetric studies of small alkane adsorption by zeolites show that the isosteric heat of adsorption decreases as the pore volume increases.[24]

Molecular simulation, and in particular classical force field methods, is becoming a key tool in the search for new MOFs with properties tailored for specific applications.[25] Initially, benchmark studies of pure MOFs and single-component adsorption were performed to establish the utility and accuracy of various force fields. More recently, however, molecular simulation is achieving traction as a screening tool for adsorption of gases by MOFs.[14, 26-30] For example, Keskin and Sholl[31-32] and Barbarao et al.[30] used Grand Canonical Monte Carlo (GCMC) methods to evaluate MOF structures for CH_4/CO_2 separation. The value of simulations is particularly high for detection of compounds such as explosives and chemical weapons, since it is both experimentally difficult (especially at the very low partial pressures relevant to sensing) and hazardous to measure adsorption isotherms for these analytes. However, the only example we are aware of to date is the work of Xiong et al., who computed isotherms for adsorption of the

[3] A. Greathouse, N. W. Ockwig, L. J. Criscenti, T. R. Guilinger, P. Pohl, M. D. Allendorf „Computational Screening of Metal-Organic Frameworks for Large-Molecule Chemical Sensing," *Phys. Chem. Chem. Phys.*, **12 (**2010), 12621.

explosive RDX by IRMOF-1.[33] They find that under conditions typical of sensing applications (i.e., total pressures ≤ 1 bar, *P* (RDX) < 10^{-4} bar in air), the uptake of RDX is linear with pressure. Clearly, there is a need to apply these now well-developed computational methods to understand adsorption of other large and potentially strongly adsorbing molecules within MOFs and related framework materials.

In this work, we describe GCMC calculations for seven MOFs composed of carboxylate linkers of various types. Several representative isoreticular MOFs (IRMOF)[34] are examined, along with MIL-53 (a Cr-based MOF)[35] and the well-known Cu-paddlewheel structure HKUST-1.[36] The MOFs are listed in Table 20, and the organic linkers are shown in Figure 50. Adsorption isotherms are computed for a total of ten analytes, described in Table 21, representing VOCs, polyaromatic hydrocarbons (PAHs), chemical warfare agents (CWAs), and explosives. A wide range of analyte pressures is examined, extending from 10^{-6} kPa (10 ppb concentration in air) to 10^{-6} kPa (100 ppm), thus spanning the entire range of conditions relevant to chemical sensing for both homeland security applications and industrial process monitoring. The results indicate that these compounds interact much more strongly with the MOF pores than any of the small molecules reported previously. Furthermore, differences in loading behavior and heats of adsorption are observed that demonstrate it is possible to achieve adsorbate selectivity. In general, this investigation illustrates the value of molecular simulation for MOF design. It also supports the hypothesis that the synthetic flexibility inherent in MOFs can be exploited to achieve materials with highly tailored adsorption properties.

Table 20. Calculated Surface Areas and Free Volumes Using the Connolly Surface Method[37] With a Probe Radius of 1 Å .

MOF	formula	lattice parameter (Å)[a]	surface area ($m^2 \cdot g^{-1}$) [b]	% free volume (Connolly) [b]	% free volume (MC)[c]
IRMOF-1	$Zn_4O(O_2C\text{-}C_6H_4\text{-}CO_2)$	25.8	3352	79.1	78.0
IRMOF-2	$Zn_4O(O_2C\text{-}C_6H_3Br\text{-}CO_2)$	25.8	2677	77.1	
IRMOF-3	$Zn_4O(O_2C\text{-}C_6H_3NH_2\text{-}CO_2)$	25.7	3317	76.9	76.4
IRMOF-7	$Zn_4O(O_2C\text{-}C_{10}H_6\text{-}CO_2)$	25.8	3414	73.0	71.8
IRMOF-8	$Zn_4O(O_2C\text{-}C_{10}H_6\text{-}CO_2)$	30.1	3541	82.8	82.2
HKUST-1 (H_2O)	$Cu_3[C_6H_3(CO_2)_3(H_2O)_3]$	26.3	3142	64.2	
HKUST-1 (dry)	$Cu_3[C_6H_3(CO_2)_3]$	26.3	2748	70.5	70.4
CrMIL-53lp[d]	$Cr(OH)(O_2C\text{-}C_6H_4\text{-}CO_2)$	6.8 x 16.7 x 13.0	3049	55.4	

[a] Experimental lattice parameters taken from the literature.[34-36]
[b] Calculated using the Connolly surface method.[37]
[c] Literature values of select free volumes using a Monte Carlo integration technique.[38-39]
[d] The large pore (lp) form of CrMIL-53 was used.

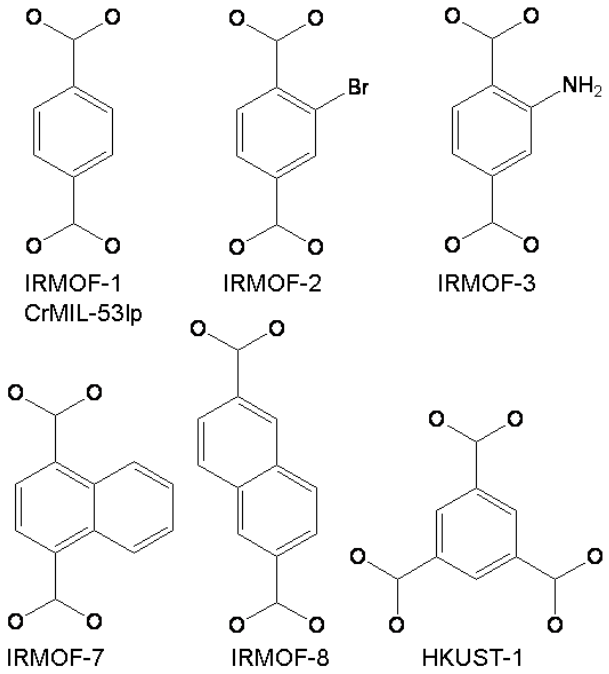

Figure 50. Organic linkers for the MOFs considered in this study.

Table 21. Formula, Abbreviation, Structure, and Kinetic Diameter of Analytes.

analyte		structure	kinetic diameter (Å)[a]
o-xylene	OX	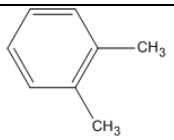	6.81
m-xylene	MX	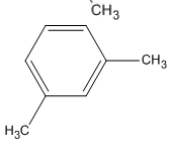	6.55
p-xylene	PX	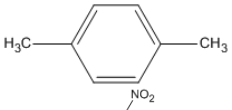	5.98
1,3,5-trinitrotoluene	TNT	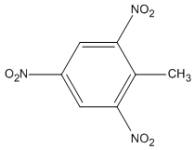	8.54
1,3,5-trinitro-1,3,5-triazacyclohexane	RDX	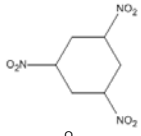	8.49
ethyl dimethylamino-cyanophosphonate	GA	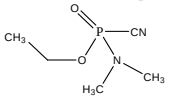	7.41
O-ethyl-S-[2-(diethylamino)ethyl] methylphosphonothioate	VM	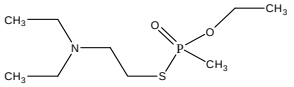	8.14
naphthalene	NA	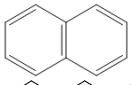	6.57
anthracene	ANTH	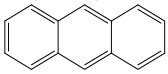	6.59
phenanthrene	PHEN	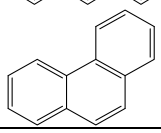	7.51

[a] Kinetic diameters were obtained assuming a Lennard-Jones 6-12 relationship with the molecular diameter.[40] The minimum cross-sectional diameter was obtained by measuring the relevant interatomic distance after geometry optimization, and adding the van der Waals radii of the terminal atoms.

6.2. Methods

Estimates of MOF surface areas and free volumes are given in Table 20. The surface areas and pore volumes are efficiently calculated using Connolly surfaces.[37] Although more robust methods have been used to estimate free volumes, the simple approach used here is effective when examining trends in adsorption for a variety of MOFs. In fact, free volumes obtained from a Monte Carlo integration technique for IRMOFs 1, 3, 7, 8, and HKUST-1 (dry)[38-39] are very

close to the values reported in Table 20 from the simpler Connolly surface analysis. Molecular models of all MOFs are given as Electronic Supplementary Information.

Monte Carlo simulations were performed at 298 K using the Sorption module of Materials Studio (Accelrys, Inc.). Single component adsorption isotherms were obtained from GCMC simulation over the pressure range 10^{-6} kPa – 10^{-2} kPa. Isosteric heats of adsorption (Q_{st})[41] were obtained at infinite dilution from constant volume simulations with a loading of one molecule per simulation cell.[27] Framework atoms were held at their crystallographic coordinates throughout the simulations. In the absence of transferrable potential parameters for MOFs that include framework flexibility, using the crystallographic coordinates is the most consistent approach. This approximation is also adequate when using molecular simulation as a screening tool as we do here.

For CrMIL-53lp and HKUST-1, structural OH and waters were included, respectively, to better represent analyte detection in (humid) atmospheric conditions. These oxygen positions were also taken from the crystal structures. H atoms were added manually, and their final positions were determined from geometry optimization. The Zn-IRMOFs do not contain any uncoordinated metal sites, so structural water is not a consideration. Although the Zn-IRMOFs are unstable at high humidity,[42-43] they are stable at low humidity.[44]

Analyte molecules were also treated as rigid bodies, but each inserted molecule was randomly selected from 20 conformations from a previous molecular dynamics simulation (Materials Studio, Forcite module). The configurational bias Monte Carlo method[45] was used for trial moves involving molecule insertion, deletion, conformer exchange, and regrowth. Trial moves involving molecule rotation and translation were also included. For the Zn-IRMOFs and HKUST-1, the simulation cell consisted of one unit cell, while a 4 x 2 x 2 supercell was used for CrMIL-53lp. Long-range electrostatics were computed using Ewald summation with an accuracy of 1.0×10^{-4} kcal·mol^{-1}. A cutoff distance of 12 Å was used for short-range interactions. Each simulation consisted of 2×10^6 trial moves, and the last 1×10^6 moves were used for averaging. The relatively small number of trial moves is justified given the low analyte fugacities that were considered. We confirmed this by recalculating the adsorption isotherm for GA adsorption by CrMIL-53lp with a total of 6×10^6 steps. Only slight differences in GA loading are seen at any pressure (Figure 51). As additional validation of our method, we calculated Q_{st} for two other molecules (methane and *n*-butane) in IRMOF-1 for comparison with published values.[2, 27] Using a single-site methane model at 35 bar, our value of Q_{st} is 2.34 kcal·mol^{-1}, in good agreement with the value of 2.53 kcal·mol^{-1} reported previously.[2] For *n*-butane at infinite dilution, our value of Q_{st} is 6.66 kcal·mol^{-1}, in good agreement with the corresponding simulation (5.83 kcal·mol^{-1}) and experimental (6.02 kcal·mol^{-1}) values.[27] This level of accuracy is more than sufficient to ensure that trends are properly represented.

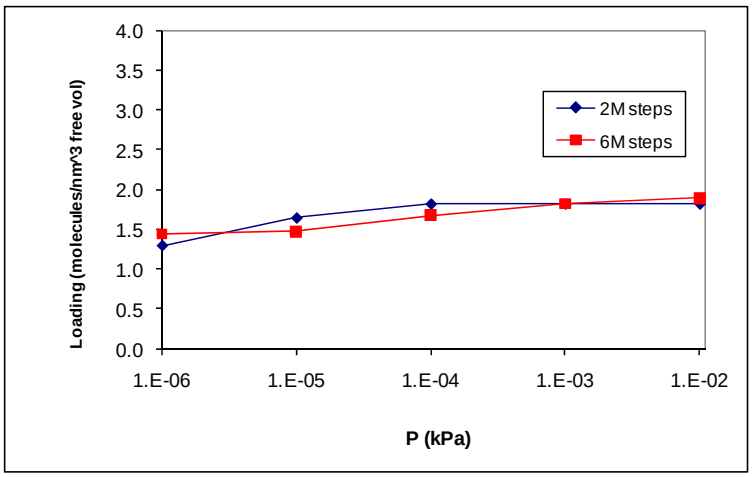

Figure 51. Adsorption isotherms for GA adsorption in CrMIL-53lp at 2 x 10^6 steps and 6 x 10^6 steps. Data were averaged over the final 1 x 10^6 steps and 3 x 10^6 steps, respectively.

While it is reasonable to approximate aromatic molecules such as xylene or naphthalene as rigid, the validity of this approximation is less obvious for more flexible molecules like GA or VM. Consequently, we compared the Q_{st} values computed by GCMC with molecular dynamics simulations in which full analyte flexibility was included using the Consistent Valence Force Field (CVFF)[46] parameters for intramolecular energy terms. Results were compared for 2 analytes (naphthalene and VM) at high and low values of Q_{st}. The GCMC and MD results differ by only 0.5 kcal·mol^{-1} – 4.8 kcal·mol^{-1} (Table 22), and both methods show the same trend in Q_{st} values. MD simulations can also be used to calculate guest diffusivity in MOF pores, which is another important factor in gas adsorption and separation. However, our aim in this paper is to compare guest loadings and adsorption energies, which is best accomplished with GCMC simulation.

Table 22. Comparison of Isosteric Heats of Adsorption (kcal·mol^{-1}) at 298 K for Rigid Analyte (GCMC) and Flexible Analyte (Molecular Dynamics) at Infinite Dilution.

MOF	analyte	Q_{st}	
		GCMC (rigid)	MD (flexible)[a]
IRMOF-1	NAPH	15.3	11.8
IRMOF-7	NAPH	20.3	17.2
IRMOF-1	VM	15.3	15.8
IRMOF-3	VM	24.4	29.2

[a] Results for molecular dynamics (MD) simulation were obtained using the Forcite module of Materials Studio. Simulations were 2.0 ns long with a timestep of 1.0 fs, and data from the final 1.0 ns were used according to $Q_{st} = \langle E_{gh} \rangle - \langle E_g \rangle - RT$, where E_{gh} is the average potential energy of the adsorbed guest, E_g is the average potential energy of the analyte in an ideal gas reference state (1 molecule in a box with no framework), and RT is the thermal energy.

Force field parameters were taken from the literature and will only be summarized here. Because frameworks and analytes were treated as rigid bodies, only nonbonded interactions (electrostatics and van der Waals) were included in the simulations. Parameters for analyte atoms were taken from CVFF without modification. CVFF is a general force field for organic molecules that is applicable to a broad range of organic analytes and is compatible with the MOF atomic parameters discussed below. For the Zn-IRMOFs, both van der Waals interactions and atomic charges were based on the parameters developed previously for IRMOFs 1, 10, and 16.[47] The van der Waals parameters were based on the CVFF and adjusted through an iterative process to fit experimental lattice parameters and adsorption isotherms. Atomic parameters for IRMOF-1, 7, and 8 were used as published.[47] Although IRMOFs 7 and 8 were not included in the original parameterization, their linkers contain atom types similar to IRMOFs 1, 10, and 16. van der Waals parameters for the Br and NH_2 functional groups in IRMOFs 2 and 3 were taken from CVFF without modification. Atomic charges for IRMOFs 2 and 3 were obtained from ab initio calculations using, for consistency, the same model chemistry reported previously applied to IRMOFs 1, 10, and 16.[47] Details of the ab initio calculations and atomic charges for all MOFs are given in the Electronic Supplementary Information. Parameters for HKUST-1 and CrMIL-53lp, including atomic charges, were taken directly from the literature.[48-49] Unfortunately, no unique set of van der Waals parameters has been found that can reproduce reported adsorption isotherms for HKUST-1. Here we use published parameters based on the OPLS-AA force field,[50] with a slight modification of the epsilon parameter for the carboxylate oxygen to improve the agreement with experiment for hydrogen adsorption.[48] Previous models for HKUST-1 have not included structural water, so parameters from the Simple Point Charge (SPC)[51] model were used. Some recent work has shown that guest loadings in GCMC simulations are sensitive to atomic charge assignments,[52] but our goal is to compare trends in guest loading using a consistently derived set of atomic charges. The recent attempt by Xu and Zhong[53] to assign atomic charges using a connectivity-based approach appears promising for computational screening.

6.3. Results

Our computed adsorption isotherms allow us to compare trends in adsorption over a wide range of pressures. For brevity, only a few isotherms are shown in Figure 52, but all isotherms are available as Electronic Supplementary Information. The predicted isotherms for IRMOF-3 and CrMIL-53lp are particularly interesting because they illustrate the effect of pore volume on analyte loading and the effect of pore geometry on analyte selectivity at low pressure. For IRMOF-3, smaller molecules with a low Q_{st} (xylenes, naphthalene) show little or no loading at the lowest pressures, while the PAH molecules with a high Q_{st} are already filling pores at 10^{-6} kPa. At higher pressures, molecular packing issues dominate, so small molecules exhibit higher loading than large molecules despite the trends in Q_{st}. The crossover in uptake between small molecules and large molecules that occurs between 10^{-5} kPa and 10^{-3} kPa (Figure 52a) is quite similar to trends in the adsorption of light gases and hydrocarbons by MOFs.[28] All molecules are near their maximum loading capacity in CrMIL-53lp at 10^{-6} kPa, but the volumetric capacity is much lower than the IRMOFs.

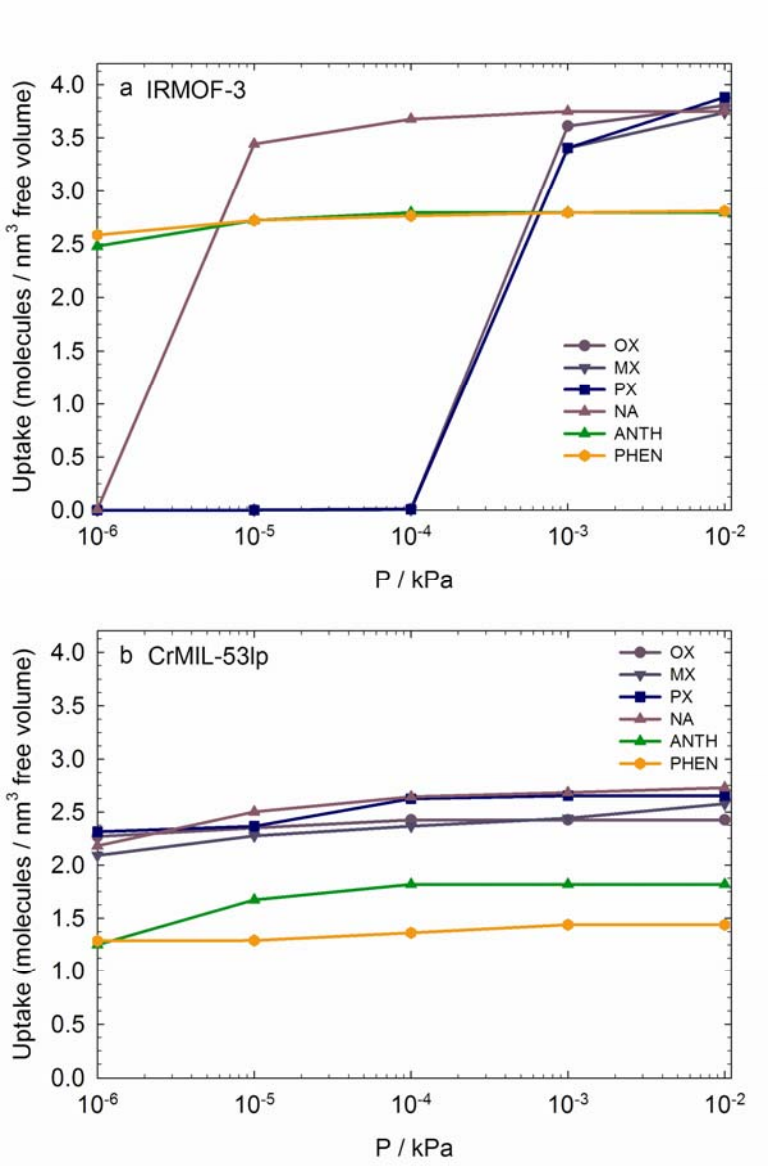

Figure 52. Adsorption isotherms for two classes of analyte (xylenes and PAHs) in (a) IRMOF-3 and (b) CrMIL-53lp.

A comparison of analyte uptake at high loading pressures allows us to rank MOFs by their propensity for analyte capture, which is relevant to both sensing applications and potential use as analyte preconcentrators. Analyte loading at 10^{-2} kPa is shown in Figure 53 as a function of gravimetric ($mg \cdot g^{-1}$) and volumetric ($molecules \cdot nm^{-3}$ free volume) uptake. Most analytes have reached their loading limit at this low pressure. IRMOF-8 shows a much higher gravimetric uptake than the other MOFs, based on its much larger free volume. Not surprisingly, CrMIL-53lp shows one of the lowest gravimetric and volumetric uptakes based on its small pore volume. Free volume effects are normalized in Figure 53b, showing similar volumetric loadings for the Zn-IRMOFs. The general trend of decreased loading with increasing analyte size (or mass) is also seen in Figure 53b. Smaller molecules are able to pack more densely in the open pore spaces, resulting in higher volumetric loading. Within the Zn-IRMOF series, analyte loading is

proportional to free volume. With their smaller pores, HKUST-1 and CrMIL-53lp do not show the same uptake as the Zn-IRMOFs over the range of analytes considered. Based on these results, materials with larger pores (such as the Zn-IRMOFs) would be ideal candidates for pre-concentration of analytes.

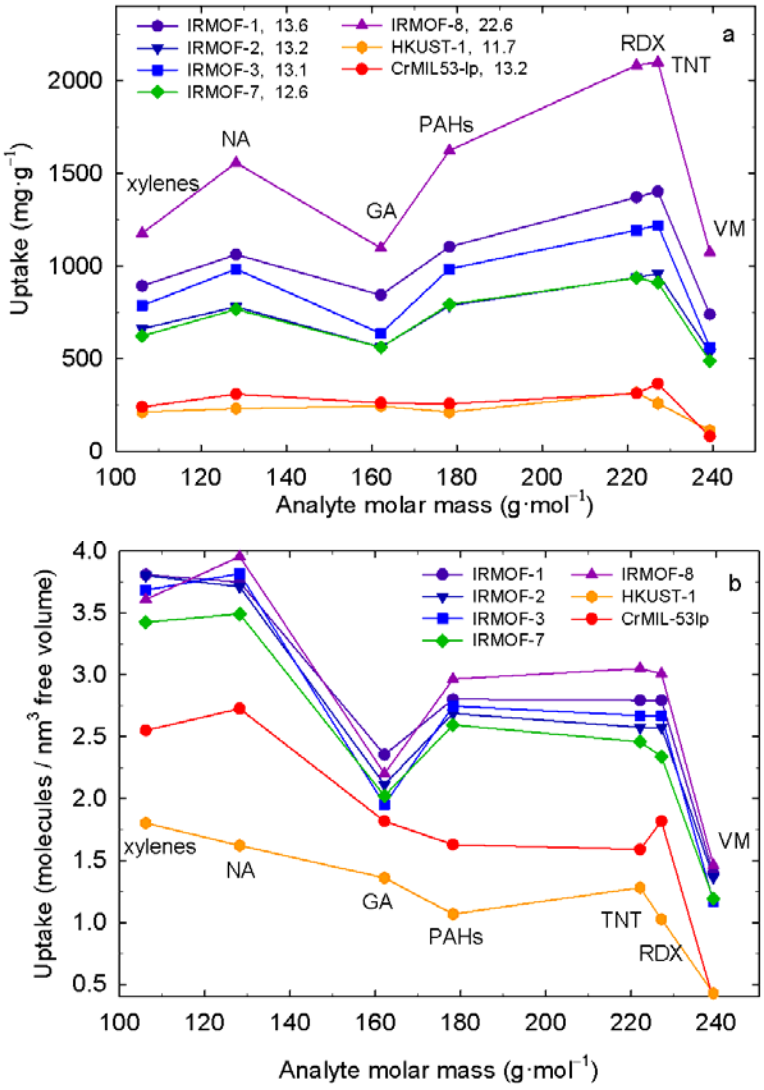

Figure 53. Uptake as a function of analyte molar mass for all MOFs at a loading pressure of 10^{-2} kPa. Uptake is given in both gravimetric (a) and volumetric (b) units. Each MOF is identified in the legend with its corresponding free volume (nm^3) based on the simulation cell. Labels indicate each analyte type.

To evaluate these MOFs for their potential use in chemical detection schemes, a comparison of analyte uptake at trace concentrations is needed. The volumetric uptake of each MOF at 10^{-6} kPa is shown in Figure 54. At this low concentration (10 ppb in air), short-range interactions between analyte and MOF should dominate over pore size or pore volume considerations. Two features characteristic of individual MOFs are noteworthy. First, CrMIL-53lp is the only MOF considered here that shows a significant uptake of xylenes even at this low pressure. The smaller pores in

CrMIL-53lp are lined with phenyl groups, creating an ideal environment for the adsorption of small aromatic molecules. Second, the Zn-IRMOFs show relatively high analyte uptake across the entire range.

We can loosely rank this series of MOFs according to their ability to adsorb specific analytes under simulated sensing conditions (10 ppb). For aromatic compounds, both analyte size and pore chemistry play a role. The selectivity of CrMIL-53lp for xylenes, as described above, is likely due to the number and orientation of the aromatic rings within its pores. Pore size and surface area evidently are not factors here, since the Zn-IRMOFs adsorb very little xylene. In contrast, there is a wide range of naphthalene (NA) uptake: IRMOF-2 ≈ IRMOF-3 > IRMOF-7 > CrMIL-53lp > HKUST-1 3 > IRIMOF-1 ≈ IRMOF-8. IRMOFs 2 and 3 contain functional groups (Br and NH_2, respectively) that protrude into the pore space and enhance naphthalene adsorption. IRMOFs 1 and 8 contain no pore-occupying functional groups and show the lowest uptake of naphthalene. This demonstrates again that, as in the case of the xylenes, linker functionalization is quite important and can override a high pore volume. This effect is reversed for the two PAHs, where the order (highest to lowest) is IRMOF-8 > IRMOF-1 ≈ IRMOF-3 > IRMOF-2 > IRMOF-7 > CrMIL-53-lp > HKUST-1. Here, as expected, the uptake of large PAH molecules is proportional to free volume.

Although the analyte loadings shown in Figures 53-54 depict situations in which the analyte kinetic diameter (Table 21) appears too large to fit the through the pore aperture (Table 20), it has been verified both by simulation[54] and experiment[55] that organic linkers exhibit hindered rotation. Framework flexibility effects have been used to explain the adsorption of molecules that are too large to fit through a pore aperture.[56] The GCMC algorithm works by randomly inserting and deleting molecules in the available pore volume, regardless of whether the molecule could actually fit through the aperture. Molecular dynamics simulations that take into account molecular and framework flexibility are needed to further screen candidate MOFs for adsorption and separation applications.

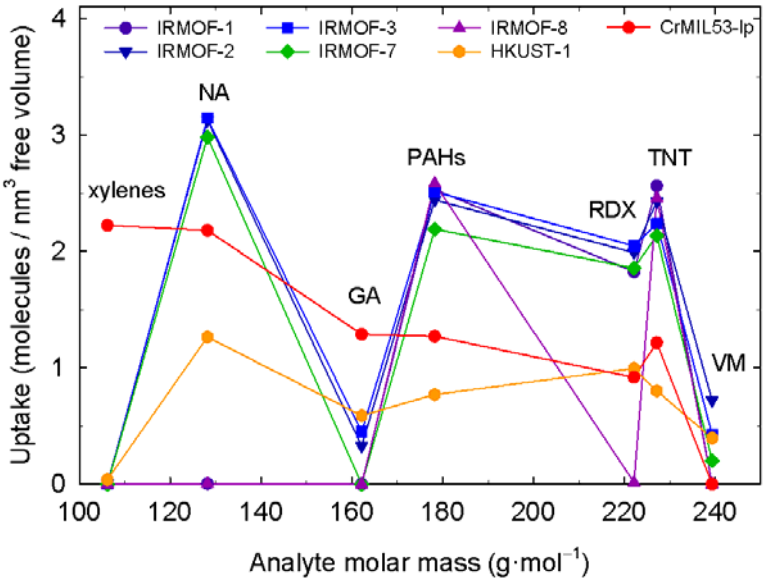

Figure 54. Uptake as a function of molar mass at a loading pressure of 10^{-6} kPa.

A comparison of isosteric heats of adsorption at infinite dilution (Figure 55) allows us to predict trends in analyte detection at low concentration. The magnitude of the adsorption energies in Figure 55 are consistent with experimental values reported in zeolites, for example 21.6 kcal·mol^{-1} for *p*-xylene in NaX and 25.5 kcal·mol^{-1} for naphthalene in NaX.[57] Even the lowest energies shown here (~ 12 kcal·mol^{-1}) are large compared with those reported for small molecules and straight-chain hydrocarbons, producing the high uptakes at 10^{-6} kPa shown in Figure 54. For example, some experimental values for enthalpies of adsorption at infinite dilution are 1.5 kcal·mol^{-1} (N_2), 2.2 kcal·mol^{-1} (CH_4), 3.6 kcal·mol^{-1} (CO_2), and 6.0 kcal·mol^{-1} (*n*-C_4H_{10}).[27] The corresponding energies for H_2O in MOFs are higher (11–12 kcal·mol^{-1}).[58-59] These values suggest that competitive binding by the components of air will not interfere with detection of the analytes considered here. In contrast, the measured zero-coverage Q_{st} of 19.1 kcal·mol^{-1} for *o*-xylene adsorbed by the MOF Zn(BDC)(DABCO)$_{0.5}$ indicates that aromatic molecules interact much more strongly with the framework.[60] This value is comparable to our simulation results for Q_{st} values for *o*-xylene adsorption by Zn-IRMOFs at infinite dilution, which range from 12.6 kcal·mol^{-1} to 17.7 kcal·mol^{-1}.

Of the MOFs considered here, CrMIL-53lp shows the highest values of Q_{st}, and IRMOF-1 shows the lowest. From the results in Figure 55 and considering its smaller, phenyl-lined pores, it appears that CrMIL-53lp has the most promise for low-concentration analyte detection. However, there is not a direct correspondence between Q_{st} and low-pressure loading, since several other MOFs have higher analyte loadings at 10^{-6} kPa (Figure 54). These higher loadings are clearly the result of functionalization of the MOF organic linker groups, which leads to increased values of Q_{st}. In particular, within the Zn-IRMOF series, Q_{st} increases when functional groups are present in the pore (IRMOF-2, -3, and -7). The effect is small for naphthalene and PAH. However, the polar molecules GA and VM are bound more tightly by IRMOFs 2 and 3, which contain electronegative NH_2 and Br groups. We also determined Q_{st} values for dehydrated HKUST-1 (data not shown). The removal of structural water in HKUST-1 decreases Q_{st} by < 12 % for all analytes except the explosives. For TNT and RDX in HKUST-1, removing the structural water molecules results in greatly decreased Q_{st} values (21 % and 24 %, respectively). A low-energy snapshot from the fixed loading simulation of TNT in HKUST-1 (Figure 56) shows that the nitrate groups in TNT are able to coordinate to several structural water molecules while maintaining an orientation with respect to the linker aromatic ring that maybe favorable to π-π interactions.

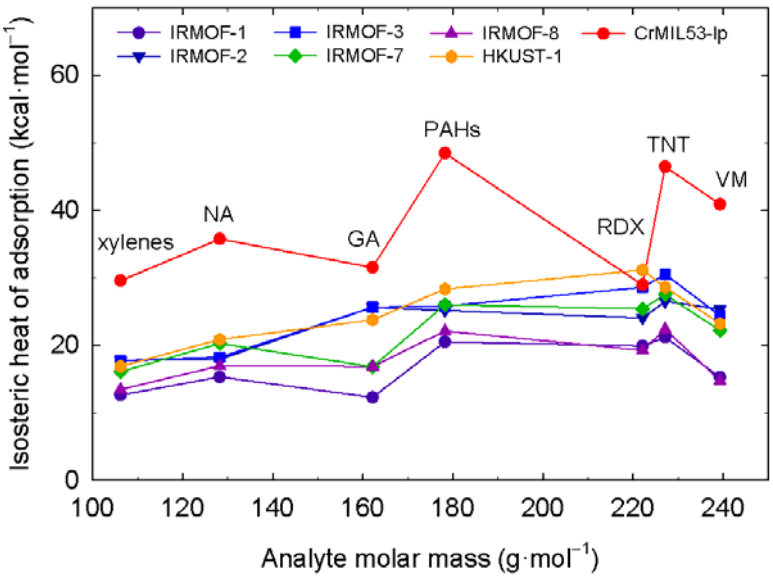

Figure 55. Isosteric heats of adsorption at infinite dilution (1 molecule per simulation cell) as a function of analyte molar mass for each MOF.

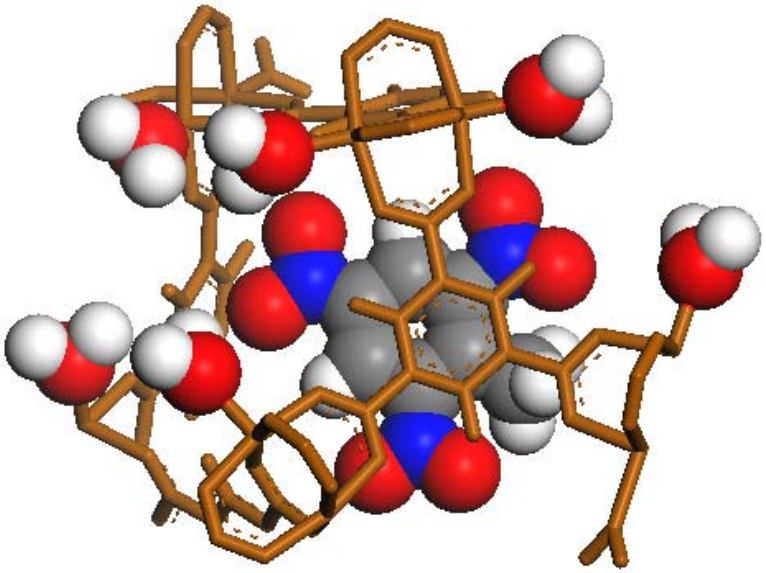

Figure 56. Snapshot from a fixed loading simulation showing a low-energy configuration of TNT in HKUST-1. Only a portion of the framework is shown for clarity. The TNT molecule and nearby water molecules (H-O distance < 4.5 Å) are shown as large spheres.

The orientation and interplanar distances predicted for aromatic adsorbates suggest that π-π stacking plays a significant role in producing the high loadings and large Q_{st} values for aromatic guests. Figure 56 shows that aromatic molecules such as TNT adsorb with an alignment of phenyl rings that appears to maximize π-π interactions between guest and host, based on recent

calculations.[61] The rings are in an offset coplanar geometry and the range of distances between ring centroids is 3.2 – 3.8 Å, somewhat shorter than that predicted for the non-aromatic RDX molecule (3.4 – 4.3 Å). The xylenes were the only type of aromatic analyte that did not adsorb to the MOFs in this way. For all MOFs except HKUST-1, the uptake of TNT exceeds that of RDX at 10^{-6} kPa pressure. IRMOF-8 shows no RDX loading compared to 2.5 molecules·nm^{-3} free volume for TNT. Although the two molecules are roughly the same size and both contain NO_2 groups, the lack of an aromatic ring in RDX and its nonplanar structure conspire to reduce its uptake relative to TNT. Additional confirmation of this conclusion comes from the fact that, with the exception of GA adsorption by IRMOF-2, analytes in the CWA class (GA, VM) interact only weakly with any of the MOFs we studied. The GA molecule is typically located near a Zn_4O vertex to maximize the electrostatic interactions with framework Zn atoms, as seen in Figure 57.

These results suggest that π-π interactions contribute strongly to the low-pressure adsorption of the aromatic molecules. Such interactions are known to strengthen benzene adsorption by IRMOF-1,[62] and help to explain the very large adsorption energies (49 kcal·mol^{-1}) seen in our simulations. Additionally, recent density functional theory calculations on functionalized arenes have shown that the combination of hydrogen bonding and π-π stacking leads to significant intermolecular interactions.[63] The ab initio interaction energies for dimers of small aromatic molecules range from 2 kcal·mol^{-1} to 4 kcal·mol^{-1}.[64-65] However, the corresponding value for much larger coronene dimers (seven fused phenyl rings) can be as high as 21.7 kcal·mol^{-1}.[66] We should note, however, although the van der Waals well depth used by CVFF to describe an aromatic carbon is significantly deeper than for an aliphatic carbon (0.148 kcal mol^{-1} vs. 0.04 kcal mol^{-1}, respectively), we do not expect that this force field can fully capture the interactions between aromatic rings, which are evidently quite complex.[61]

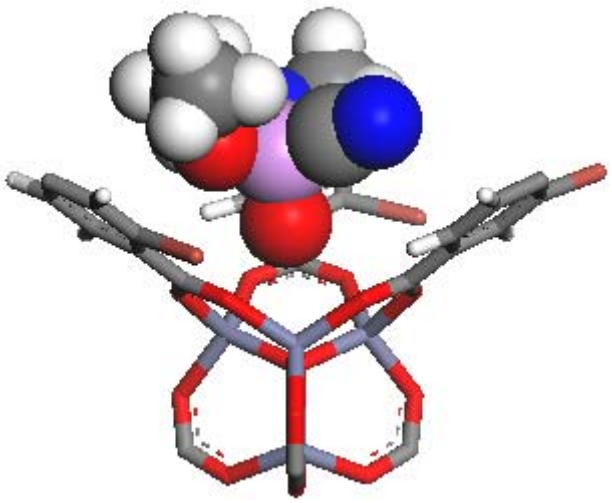

Figure 57. Snapshot from a fixed loading simulation showing a low-energy configuration of GA in IRMOF-1. Only a portion of the framework is shown for clarity.

From a chemical detection standpoint, a key quantity is the minimum partial pressure at which detectable amounts of analyte are first adsorbed. Based on the adsorption isotherms presented here, we use a loading of 0.5 molecules·nm^{-3} free volume to define the minimum pressure at the

onset of adsorption. These values are given in Table 23 for all analytes and MOFs. For reference, a loading of 0.5 molecules·nm^{-3} in IRMOF-1 corresponds to 6.8 molecules per unit cell or approximately 1 molecule per pore. Values of minimum pressures such as those presented in Table 23 can be generated quickly using GCMC simulation as a first step in the computational screening of materials for chemical detection. For CrMIL-53lp, the results are consistent with the volumetric uptake data and adsorption energies shown previously. At the lowest pressure considered in this study (10^{-6} kPa), appreciable amounts of each analyte are already adsorbed. Only slightly less sensitive is HKUST-1, particularly for the non-aromatic molecules in the CWA class. The strong response exhibited by HKUST-1 in microcantilever experiments[20] suggests that this MOF may be useful for trace level-chemical detection technologies. Also noteworthy are the low detection limits predicted for the functionalized Zn-IRMOFs (IRMOFs 2, 3, and 7), presumably due to the stronger short-range interactions between guest molecules and the functional groups (Br, NH_2, and phenyl ring, respectively).

Table 23. Minimum Pressure (kPa) for Analyte Adsorption of 0.5 molecules·nm–3.

	xylenes	TNT	RDX	GA	VM[a]	NA	ANTH	PHEN	linker[b]
IRMOF-1	**10^{-3}**	10^{-6}	10^{-6}	**10^{-3}**	**10^{-4}**	**10^{-5}**	10^{-6}	10^{-6}	BDC
IRMOF-2	**10^{-4}**	10^{-6}	10^{-6}	**10^{-5}**	10^{-6}	10^{-6}	10^{-6}	10^{-6}	Br-BDC
IRMOF-3	**10^{-4}**	10^{-6}	10^{-6}	**10^{-5}**	**10^{-5}**	10^{-6}	10^{-6}	10^{-6}	NH_2-BDC
IRMOF-7	**10^{-4}**	10^{-6}	10^{-6}	**10^{-3}**	**10^{-5}**	10^{-6}	10^{-6}	10^{-6}	C_4H_4-BDC
IRMOF-8	**10^{-2}**	10^{-6}	**10^{-5}**	**10^{-2}**	**10^{-3}**	**10^{-5}**	10^{-6}	10^{-6}	NDC
HKUST-1	**10^{-5}**	10^{-6}	10^{-6}	10^{-6}		10^{-6}	10^{-6}	10^{-6}	BTC
CrMIL-53lp	10^{-6}	10^{-6}	10^{-6}	10^{-6}		10^{-6}	10^{-6}	10^{-6}	BDC

[a] Loadings for VM in HKUST-1 and CrMIL-53lp never reached 0.5 molecules·nm^{-3}.
[b] BDC = benzene dicarboxylate, NDC = naphthalene dicarboxylate, BTC = benzene tricarboxylate

6.4. Conclusions

A series of grand canonical Monte Carlo calculations simulating the uptake of organic analytes by a series of MOFs reveal several interesting trends in low-pressure adsorption and preconcentration of these molecules. The MOFs included in this study comprise a range of metals, pore sizes, and organic linker functionalization. A broad spectrum of organic analytes is considered, including small aromatics, polycyclic aromatic hydrocarbons, explosives, and non-aromatic chemical warfare agents. Both the computed isotherms and the predicted isosteric heats of adsorption demonstrate that these analytes interact much more strongly with MOFs than small molecules and aliphatic hydrocarbons. In particular, compounds containing aromatic rings have Q_{st} in excess of 12 kcal mol^{-1}, compared with small-molecule values that are typically less than 10 kcal mol^{-1}. An important corollary is that MOFs exhibiting high adsorption energies and significant loading at low pressure are not necessarily well suited for storing the same analyte at higher pressure, where, in addition to framework-analyte interactions, pore volume and surface area must also be considered to maximize storage capacity. These considerations indicate that the chemical intuition developed thus far for optimizing MOFs for applications involving high loading pressures and weakly interacting gases is not necessarily relevant to chemical sensing.

Based on these results, we conclude that the interaction energy between MOFs and larger organic molecules is sufficiently strong to consider the use of MOFs as components of low-concentration molecular sensors. Furthermore, a high degree of molecular selectivity should be possible, since even without any fine tuning the MOF structures considered here exhibit a wide variation in their uptake of analytes. For example, all of the Zn-IRMOFs considered here are able to distinguish between TNT and a closely related molecule (*o*-xylene) at the ppb level (Figure 54). Consequently, synthetic tuning of the organic linker with the assistance of atomistic modeling should result in MOFs with very high selectivities. Another encouraging conclusion we draw from this work is that Q_{st} for these analytes is so much higher than for the most abundant atmospheric components that they should not interfere significantly with analyte uptake.

Finally, our GCMC approach, in which we used a relatively small number of MC moves, reproduces relevant literature data with sufficient accuracy to give confidence that the predicted trends are credible. Of course, as with any molecular simulation, the validity of the results depends on the quality of the force field parameters that were used. In this investigation every effort was made to apply rigorous methods in force field development to this diverse set of MOFs and analytes. We hope that these simulation results will stimulate experimental efforts to provide adsorption isotherms and energies for these classes of analytes, which will enable force field validation. In general, however, this investigation demonstrates that GCMC can be a computationally efficient tool for screening the adsorption behavior of even large molecules, which will be of great value for future synthetic work aimed at tuning MOF adsorption properties for specific applications.

6.5. References

1. L. J. Murray, M. Dinca and J. R. Long, *Chem. Soc. Rev.*, 2009, **38**, 1294-1314.
2. T. Duren, L. Sarkisov, O. M. Yaghi and R. Q. Snurr, *Langmuir*, 2004, **20**, 2683-2689.
3. Y. H. Jhon, M. Cho, H. R. Jeon, I. Park, R. Chang, J. L. C. Rowsell and J. Kim, *J. Phys. Chem. C*, 2007, **111**, 16618-16625.
4. S. Ma, D. Sun, J. M. Simmons, C. D. Collier, D. Yuan and H. C. Zhou, *J. Am. Chem. Soc.*, 2008, **130**, 1012-1016.
5. S. Y. Wang, *Energ. Fuel*, 2007, **21**, 953-956.
6. O. M. Yaghi and Q. W. Li, *MRS Bull.*, 2009, **34**, 682-690.
7. J. A. Greathouse, T. L. Kinnibrugh and M. D. Allendorf, *Ind. Eng. Chem. Res.*, 2009, **48**, 3425-3431.
8. U. Mueller, M. Schubert, F. Teich, H. Puetter, K. Schierle-Arndt and J. Pastre, *J. Mater. Chem.*, 2006, **16**, 626-636.
9. K. J. Ooms and R. E. Wasylishen, *Micropor. Mesopor. Mater.*, 2007, **103**, 341-351.
10. S. Pawsey, I. Moudrakovski, J. Ripmeester, L. Q. Wang, G. J. Exarhos, J. L. C. Rowsell and O. M. Yaghi, *J. Phys. Chem. C*, 2007, **111**, 6060-6067.
11. H. Li, M. Eddaoudi, M. O'Keeffe and O. M. Yaghi, *Nature*, 1999, **402**, 276-279.
12. D. Dubbeldam, H. Frost, K. S. Walton and R. Q. Snurr, *Fluid Phase Equilibr.*, 2007, **261**, 152-161.
13. A. I. Skoulidas, *J. Am. Chem. Soc.*, 2004, **126**, 1356-1357.
14. A. O. Yazaydin, A. I. Benin, S. A. Faheem, P. Jakubczak, J. J. Low, R. R. Willis and R. Q. Snurr, *Chem. Mater.*, 2009, **21**, 1425-1430.
15. Q. Y. Yang, C. Y. Xue, C. L. Zhong and J. F. Chen, *AIChE J.*, 2007, **53**, 2832-2840.
16. A. R. Millward and O. M. Yaghi, *J. Am. Chem. Soc.*, 2005, **127**, 17998-17999.
17. Y. S. Bae, O. K. Farha, A. M. Spokoyny, C. A. Mirkin, J. T. Hupp and R. Q. Snurr, *Chem. Commun.*, 2008, 4135-4137.
18. J. R. Li, R. J. Kuppler and H. C. Zhou, *Chem. Soc. Rev.*, 2009, **38**, 1477-1504.
19. S. Winter, E. Weber, L. Eriksson and I. Csoregh, *New J. Chem.*, 2006, **30**, 1808-1819.
20. M. D. Allendorf, R. J. T. Houk, L. Andruszkiewicz, A. A. Talin, J. Pikarsky, A. Choudhury, K. A. Gall and P. J. Hesketh, *J. Am. Chem. Soc.*, 2008, **130**, 14404-14405.
21. A. J. Lan, K. H. Li, H. H. Wu, D. H. Olson, T. J. Emge, W. Ki, M. C. Hong and J. Li, *Angew. Chem. Int. Ed.*, 2009, **48**, 2334-2338.
22. M. D. Allendorf, C. A. Bauer, R. K. Bhakta and R. J. T. Houk, *Chem. Soc. Rev.*, 2009, **38**, 1330-1352.
23. Z. Ni, J. P. Jerrell, K. R. Cadwallader and R. I. Masel, *Anal. Chem.*, 2007, **79**, 1290-1293.
24. S. Savitz, F. Siperstein, R. J. Gorte and A. L. Myers, *J. Phys. Chem. B*, 1998, **102**, 6865-6872.
25. T. Duren, Y. S. Bae and R. Q. Snurr, *Chem. Soc. Rev.*, 2009, **38**, 1237-1247.
26. D. Dubbeldam, C. J. Galvin, K. S. Walton, D. E. Ellis and R. Q. Snurr, *J. Am. Chem. Soc.*, 2008, **130**, 10884-+.
27. D. Farrusseng, C. Daniel, C. Gaudillere, U. Ravon, Y. Schuurman, C. Mirodatos, D. Dubbeldam, H. Frost and R. Q. Snurr, *Langmuir*, 2009, **25**, 7383-7388.
28. R. Babarao, Y. H. Tong and J. W. Jiang, *J. Phys. Chem. B*, 2009, **113**, 9129-9136.
29. J. W. Jiang and S. I. Sandler, *Langmuir*, 2006, **22**, 5702-5707.

30. R. Babarao, J. W. Jiang and S. I. Sandler, *Langmuir*, 2009, **25**, 5239-5247.
31. S. Keskin and D. S. Sholl, *Langmuir*, 2009, **25**, 11786-11795.
32. S. Keskin and D. S. Sholl, *J. Phys. Chem. C*, 2007, **111**, 14055-14059.
33. R. Xiong, J. T. Fern, D. J. Keffer, M. Fuentes-Cabrera and D. M. Nicholson, *Mol. Sim.*, 2009, **35**, 910-919.
34. M. Eddaoudi, J. Kim, N. Rosi, D. Vodak, J. Wachter, M. O'Keefe and O. M. Yaghi, *Science*, 2002, **295**, 469-472.
35. F. Millange, C. Serre and G. Ferey, *Chem. Commun.*, 2002, 822-823.
36. S. S. Y. Chui, S. M. F. Lo, J. P. H. Charmant, A. G. Orpen and I. D. Williams, *Science*, 1999, **283**, 1148-1150.
37. M. L. Connolly, *Science*, 1983, **221**, 709-713.
38. H. Frost, T. Duren and R. Q. Snurr, *J. Phys. Chem. B*, 2006, **110**, 9565-9570.
39. A. O. Yazaydın, R. Q. Snurr, T.-H. Park, K. Koh, J. Liu, M. D. LeVan, A. I. Benin, P. Jakubczak, M. Lanuza, D. B. Galloway, J. J. Low and R. R. Willis, *J. Am. Chem. Soc.*, 2009, **131**, 18198-18199.
40. M. B. Rao and R. G. Jenkins, *Carbon*, 1987, **25**, 445-446.
41. R. Q. Snurr, A. T. Bell and D. N. Theodorou, *J. Phys. Chem.*, 1993, **97**, 13742-13752.
42. J. A. Greathouse and M. D. Allendorf, *J. Am. Chem. Soc.*, 2006, **128**, 10678-10679.
43. S. S. Kaye, A. Dailly, O. M. Yaghi and J. R. Long, *J. Am. Chem. Soc.*, 2007, **129**, 14176-14177.
44. K. Schrock, F. Schroder, M. Heyden, R. A. Fischer and M. Havenith, *Phys. Chem. Chem. Phys.*, 2008, **10**, 4732-4739.
45. J. I. Siepmann and D. Frenkel, *Mol. Phys.*, 1992, **75**, 59-70.
46. P. Dauber-Osguthorpe, V. A. Roberts, D. J. Osguthorpe, J. Wolff, M. Genest and A. T. Hagler, *Proteins: Struct., Funct., Genet.*, 1988, **4**, 31-47.
47. D. Dubbeldam, K. S. Walton, D. E. Ellis and R. Q. Snurr, *Angew. Chem. Int. Ed.*, 2007, **46**, 4496-4499.
48. Q. Y. Yang and C. L. Zhong, *J. Phys. Chem. B*, 2006, **110**, 17776-17783.
49. F. Salles, A. Ghoufi, G. Maurin, R. G. Bell, C. Mellot-Draznieks and G. Ferey, *Angew. Chem. Int. Ed.*, 2008, **47**, 8487-8491.
50. W. L. Jorgensen, D. S. Maxwell and J. TiradoRives, *J. Am. Chem. Soc.*, 1996, **118**, 11225-11236.
51. H. J. C. Berendsen, J. P. M. Postma, W. F. von Gunsteren and J. Hermans, in *Intermolecular Forces*, ed. B. Pullman, Reidel, Dordrecht, Holland, 1981.
52. R. C. Xiong, D. J. Keffer, M. Fuentes-Cabrera, D. M. Nicholson, A. Michalkova, T. Petrova, J. Leszczynski, K. Odbadrakh, B. L. Doss and J. P. Lewis, *Langmuir*, 2010, **26**, 5942-5950.
53. Q. Xu and C. L. Zhong, *J. Phys. Chem. C*, 2010, **114**, 5035-5042.
54. J. A. Greathouse and M. D. Allendorf, *J. Phys. Chem. C*, 2008, **112**, 5795-5802.
55. J. Gonzalez, R. N. Devi, D. P. Tunstall, P. A. Cox and P. A. Wright, *Micropor. Mesopor. Mater.*, 2005, **84**, 97-104.
56. E. J. Cussen, J. B. Claridge, M. J. Rosseinsky and C. J. Kepert, *J. Am. Chem. Soc.*, 2002, **124**, 9574-9581.
57. D. M. Ruthven and B. K. Kaul, *Ind. Eng. Chem. Res.*, 1993, **32**, 2047-2052.
58. J. M. Castillo, T. J. H. Vlugt and S. Calero, *J. Phys. Chem. C*, 2008, **112**, 15934-15939.

59. P. Kusgens, M. Rose, I. Senkovska, H. Frode, A. Henschel, S. Siegle and S. Kaskel, *Micropor. Mesopor. Mater.*, 2009, **120**, 325-330.
60. M. P. M. Nicolau, P. S. Barcia, J. M. Gallegos, J. A. C. Silva, A. E. Rodrigues and B. L. Chen, *J. Phys. Chem. C*, 2009, **113**, 13173-13179.
61. S. Grimme, *Angew. Chem. Int. Ed.*, 2008, **47**, 3430-3434.
62. S. Amirjalayer and R. Schmid, *Micropor. Mesopor. Mater.*, 2009, **125**, 90-96.
63. E. Bayard, S. Hamel and A. Rochefort, *Org. Electron.*, 2006, **7**, 144-154.
64. R. S. Paton and J. M. Goodman, *J. Chem. Inf. Model.*, 2009, **49**, 944-955.
65. M. P. Waller, A. Robertazzi, J. A. Platts, D. E. Hibbs and P. A. Williams, *J. Comput. Chem.*, 2006, **27**, 491-504.
66. Y. Zhao and D. G. Truhlar, *J. Phys. Chem. C*, 2008, **112**, 4061-4067.

7. MECHANISM OF HKUST-1 FILM GROWTH[4]

7.1. Introduction

Metal-Organic Frameworks (MOFs) have attracted considerable interest as a result of their tunable pore structures and chemical functionalities.[1-5] Their high pore volume and surface area create opportunities for use in gas storage[6], catalysis,[7] and small-molecule separation[8]. The ability of MOFs to reversibly absorb small molecules also makes them attractive for sensing applications, a topic that was recently reviewed.[9] Their highly ordered structure also suggests possibilities for fabricating electronic devices with nanoscale features.[10] In these latter two applications, MOFs have advantages relative to organic polymers and other nanoporous materials due to their relatively high thermal stability, uniform pore structure, and potential to be tailored to enhance uptake of specific analytes or materials such as catalytic or luminescent nanoparticles[11]. One of the most critical enabling technologies for implementing MOFs in sensors and other devices is the assembly of dense films or coatings on various substrates.[10] While synthesis of MOFs as bulk powders is well developed, there is a lack of reliable protocols for growing MOFs on surfaces (also called SURMOFs, surface-mounted MOFs[12,13]) of a desired thickness and morphology, while maintaining their functionality. Understanding how MOF thin films form is therefore a crucial aspect of expanding the repertoire of MOFs that can be deposited and for developing reproducible and practical deposition methods.

Recently, we demonstrated the concept of stress-induced chemical sensing of small molecules using thin films of the MOF $[Cu_3(btc)_2(H_2O)_3]\cdot xH_2O$ (referred to henceforth as $Cu_3(btc)_2$, but also known as HKUST-1;[14] btc = 1,3,5–benzenetricarboxylate) deposited on microcantilevers.[15] Previous work showed that $Cu_3(btc)_2$ can efficiently absorb a wide variety of molecules, including H_2O,[16] NH_3,[17] CO_2,[18] CH_4,[19] C_2H_2,[20] to name just a few. $Cu_3(btc)_2$ also displays capacity equal to or greater than activated carbons in removing such harmful gases as sulfur dioxide, tetrahydrothiophene, benzene, dichloromethane, ethylene oxide, and carbon monoxide.[21] These properties suggest that this MOF could be useful in certain sensing applications, and indeed, we recently demonstrated that coatings of $Cu_3(btc)_2$ on surface acoustic wave (SAW) sensors can be used to detect water vapor at ppm levels.[22] Our sensing devices were coated using the layer-by-layer (LBL) method developed by Wöll and coworkers[23,24], a versatile technique that has been used to create films of several MOFs.[3] Although a number of reports describe the growth of $Cu_3(btc)_2$ on surfaces, most of these are focused on new deposition methods and not on the growth kinetics. For example, thin-film growth of $Cu_3(btc)_2$ on various substrates, including Al_2O_3,[25] SiO_2[26] and various self-assembled monolayers (SAMs)[13,23,24,27-33], has been demonstrated. A growth mechanism was proposed by Shekhah *et al.*,[13] and it is believed to involve step-wise ligand exchange reactions between pre-formed secondary building units (SBUs) and anchored surface groups.[2,23,24,30,34-36] However, none of these studies report actual growth rates and do not address the influence of processing conditions on the growth rate and film properties.

[4] V. Stavila, J. Volponi, A. M. Katzenmeyer, M. C. Dixon, M. D. Allendorf "Kinetics and mechanism of metal-organic framework thin film growth: Systematic investigation of HKUST-1 deposition on QCM electrodes," *Chem. Sci.* **3** (2012), 1531–1540.

Quantification of growth rates and the establishment of a kinetic mechanism require an accurate time-resolved method to monitor the growth process. Shekhah *et al.* used Surface Plasmon Resonance (SPR) to monitor the deposition of $Cu_3(btc)_2$ on Au surfaces functionalized with carboxylate-terminated SAMs. They found that sequential addition of $Cu_2(OAc)_4$ and H_3btc (H_3btc = 1,3,5-benzenetricarboxylic acid) leads to a step-wise mass increase, yielding highly homogenous and crystalline $Cu_3(btc)_2$ coatings.[13,24] However, SPR, being an optical technique, is best suited for the measurement of relatively thin coatings; in addition, to provide quantitative data about the thickness and mass of the adsorbed layer the refractive index of the MOF film must be known. In the investigation described here, we employed a Quartz Crystal Microbalance (QCM), which is an acoustic technique, to monitor the deposition process. This method does not require knowledge of the refractive index and allows measurement of thicker films (up to several microns), which may be necessary for membrane or sensing applications. The QCM technique is based on the piezoelectric property of quartz, in which a mechanical shear oscillation can be induced by an alternating electric field. As molecules absorb onto the electrodes (Au or other metals), the oscillation frequency of the quartz crystal decreases, allowing *in situ* monitoring of the deposition kinetics. The resolution of QCM measurements is on the order of ~1.0 ng/cm^2, which is the reason the technique is also termed "quartz crystal nanobalance". The upper limit of film thickness that the method can be used to measure is several microns, depending on the viscoelastic properties of the applied material.[37] For rigid films, the Sauerbrey equation (**1**) is often used to correlate the observed frequency shifts to deposited mass:[38]

$$\Delta m = \frac{A\sqrt{\rho_q G_q}}{-2 f_0^2}\Delta f \qquad (\mathbf{1})$$

where Δm is the change in mass, A is the surface area of the resonator, ρ_q and G_q are the density and shear modulus of quartz, f_0 is the resonance frequency of the unloaded resonator and Δf is the change in resonance frequency. Although several authors describe the use of the QCM technique to characterize the absorption/desorption characteristics of various molecules on MOFs,[32,39,40,41] no systematic investigations using this technique to monitor the deposition of MOF thin films[42] have appeared.

Herein we describe a systematic investigation of the role of deposition conditions (temperature, concentration, and substrate) on $Cu_3(btc)_2$ growth kinetics and film properties, with the objective of gaining new insight into the elementary reactions leading to film growth that is relevant to the development of MOF-based coating processes. Reaction dynamics were obtained from QCM high-resolution frequency measurements, which are a direct indicator of the rate of MOF film growth, as described above. The structure and morphology of the resulting MOF films were probed *via* grazing incidence X-ray diffraction (GIXRD), reflection-absorption infrared spectroscopy (RAIR), and surface and cross-sectional imaging (SEM, white light interferometry, and AFM). A central feature of this study is the correlation of information from these different techniques to generate a coherent model for MOF film composition, texture, and dynamics at various interfaces. Findings pertinent to the growth of $Cu_3(btc)_2$ on carboxyl- or hydroxy-terminated Au/alkanethiol SAMs, SiO_2 and Al_2O_3 coated electrodes are presented. We compare the growth of $Cu_3(btc)_2$ in different environments (solution, substrate, temperature) and show that there are substantial differences between the mechanism of growth on surfaces versus the

processes controlling bulk powder synthesis. Moreover, we are able to distinguish between an initial nucleation step and subsequent "steady-state" reactions. The resulting data fill an important gap in the understanding of this process, which ultimately will be useful in developing larger-scale processing methods for integrating $Cu_3(btc)_2$ with other materials.

7.2 Results

7.2.1. Growth Rates

The LBL growth method described by Wöll, Fischer, and coworkers is a step-by-step growth method[23,24] that in the case of $Cu_3(btc)_2$ consists of sequentially flowing ethanolic solutions of the metal precursor ($Cu_2(OAc)_4$) and organic linker (H_3btc) over a substrate with solvent washing steps between cycles. During the MOF deposition process ligand exchange reactions take place at the interface between the solid and liquid phases, allowing the metal ions to bind to linker groups at the surface and *vice versa.* [13,23,24,30] Although the QCM is sensitive to extremely small mass changes, realizing the maximum sensitivity of the technique can be difficult, especially with liquids. Typical environmental effects associated with QCM measurements in solutions include: (*i*) temperature changes during the experiment; (*ii*) quality of the surface (deposition on the QCM electrode can be affected by the roughness, porosity, hydrophilicity, etc.); (*iii*) complications can be introduced when viscoelastic films are deposited; (*iv*) adhesion of the film to the surface may affect the measurement accuracy, especially when accumulated stress is present causing films to peel off or partially lift off. In our experiments, these sources of error were minimized by strict temperature control, paying careful attention to the QCM crystal surface functionalization, growing relatively thin coatings of a rigid MOF films (*vide infra*), and optimizing the flow rates used during deposition to minimize instrument noise (A schematic representation of the experimental set-up is presented in Figure 58).

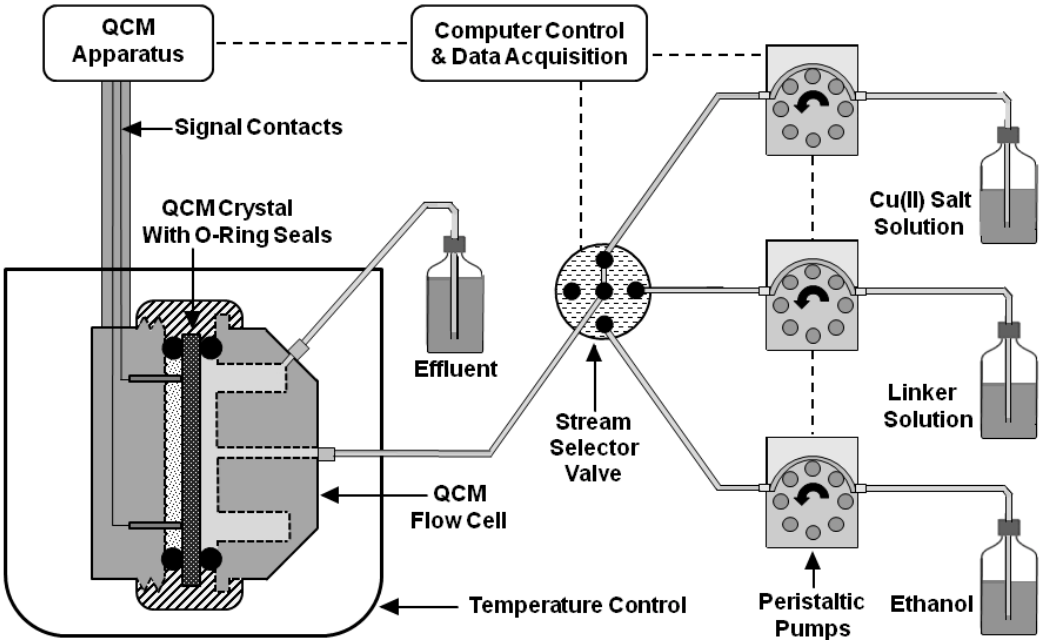

Figure 58. A schematic representation of the QCM experimental setup.

Of the three surfaces examined in our investigation, silica-coated electrodes are the ones most relevant for a detailed kinetic investigation because there is no intervening SAM to complicate the interface chemistry (growth on SAMs was also previously studied in detail[13,23,24,30,36,43,44]). Moreover, for sensing purposes, growing $Cu_3(btc)_2$ on this material is attractive because the strong covalent binding to surface hydroxyl groups is much more stable thermally than thiol-based SAMs. Finally, compared with alumina, which requires an additional processing tool (either atomic-layer deposition or reactive sputtering), growth of silicon oxide is a standard tool available in microelectronics fabrication facilities, making it the most practical interface material for sensing purposes. We therefore confine our mechanistic analysis to growth on silica; however, as will be seen below, the overall reaction kinetics following the initial interface step are very similar among the three surfaces, indicating that once growth is initiated, most likely by the formation of the first SBU, it proceeds in the same way regardless of the underlying substrate. All three deposition surfaces are amorphous, which is again typical of the morphology of these materials available from standard microelectronic processing methods.

The frequency change detected during the step-by-step deposition of $Cu_3(btc)_2$ on a silica-coated QCM crystals is shown in Figure 59, which illustrates the high quality of data possible using the QCM-D instrument. Although the flow rate is constant during the experiment, changing from one reactant to another yields a measurable and distinct frequency change. The overall decrease in resonant frequency correlates with the added mass of adsorbing species; no detectable change in frequency is observed when pure ethanol is introduced into the system. The step-wise changes in frequency correspond to alternate solutions being circulated over the QCM-D crystal and indicate a mass increase over time. A relatively simple relationship between the frequency change and mass uptake is given by the Sauerbrey equation (Equation **1**). However, since there are cases when the Sauerbrey equation does not hold (*e.g.* when the added mass is not rigidly and evenly deposited on the electrode surface), we assessed the impact of the MOF viscoelestic properties by measuring the energy dissipation of the QCM crystals during film growth (Figure 59). A Q-Sense™ QCM-D system operated in pulsed mode with *in situ* dissipation monitoring and Peltier temperature control was used. Measuring the oscillatory decay when the electric field applied to the QCM crystal is turned off provides information concerning the amount of energy dissipated by the MOF layer. The dissipation (D) is inversely proportional to the decay time, τ (Equation **2**):

$$D = \frac{1}{\pi f \tau} \qquad (\mathbf{2})$$

where f is the crystal oscillating frequency. For a soft film, the decay time is small due to increased coupling with the surrounding medium, leading to higher dissipation, whereas for a rigid film, the decay time is large leading to smaller dissipation. After five cycles of alternatively flowing ethanolic solutions of $Cu(OAc)_2$ and H_3btc over a silica-coated QCM-D crystal the total frequency change is 87.5 Hz, while the dissipation remains close to zero (Figure 59). The relatively low dissipation suggests that the MOF film is rigidly attached to the electrode and there is almost no viscoelastic contribution to the frequency change; thus the Sauerbrey equation is valid for this material.

At the beginning of a deposition experiment pure EtOH is circulated over the QCM-D crystal, resulting in a relatively flat baseline. Growth is initiated by the introduction of ethanolic $Cu(OAc)_2$, which causes a sharp drop in frequency that reaches a plateau in ~ 2 minutes (Figure 59). As suggested previously, this behavior indicates that a finite number of adsorption sites is available [45]. The difference in frequency between the EtOH baseline and the plateau is about 4 Hz, which translates into an added mass of ~72 ng/cm^2 using equation (**1**). After the frequency change levels off, pure EtOH is passed over the QCM electrode, resulting in a slight increase in frequency, presumably due to some dissociation of loosely adsorbed copper(II) species. Based on the rapid frequency change, it appears that the adsorption of solution-phase paddle-wheel $Cu_2(OAc)_4$ units at the solid-liquid interface is fast. Copper(II) is known to have high affinity to various surfaces and the overall dynamics of copper(II) salts depositing onto surfaces may be diffusion- or adsorption-rate controlled.[46] Although the QCM measurements do not directly identify the species deposited, we can determine this from the mass gain/cycle and the density of reactive sites per unit area (obtained from the crystal structure). Shekhah *et al.* previously suggested that growth of $Cu_3(btc)_2$ on OH-terminated SAMs occurs preferentially along the (*111*) crystallographic direction and involves paddle-wheel SBUs. Using the same logic and assuming that the observed mass increase during the copper(II) step is due to the adsorption of intact $Cu_2(OAc)_4$ units, this results in 0.181 nmol $Cu_2(OAc)_4$ per cm^2 or $1.1 \cdot 10^{14}$ molecules/cm^2. Even if $Cu_2(OAc)_4$ units require more than one surface active site (e.g. OH groups) to bind, the number of available hydroxyl groups for similarly treated SiO_2 surfaces was reported to be as high as 5 OH groups/nm^2 or $5 \cdot 10^{14}$ surface sites/cm^2.[47] For a complete monolayer surface coverage assuming that the subsequent MOF growth occurs along the (111) crystallographic direction, the expected mass gain was calculated to be 76 ng/cm^2, which is close to the measured value of 72 ng/cm^2 for the first copper step. This is an indication that the initial growth involves paddle-wheel $Cu_2(OAc)_4$ species.

Following the initial exposure to $Cu_2(OAc)_4$, the step-wise process continues by passing an ethanolic solution of trimesic acid over the electrodes. This is again accompanied by a significant decrease in frequency. However, the rate of this frequency change is slower than that of the copper(II) step. Conceptually, incorporation of the btc linker into the film probably involves a metathesis reaction between the coordinated acetate groups on the surface and solvated trimesic acid, which we expect will involve a specific transition state and thus be thermally activated. For the second, third, fourth, and fifth Cu(II) steps the measured mass changes (86, 96, 99 and 107 ng/cm^2, respectively) are slightly larger compared to the first step. The calculated mass changes during the first five H_3btc steps are 255, 230, 224, 214 and 207 ng/cm^2, respectively. This decrease in H_3btc:Cu molar ratio as the cycle progress may be due to differing ratios on the surface between the two precursors during the nucleation and film growth stages (*vide infra*). For each of the H_3btc steps the frequency change and the corresponding Sauerbrey mass change is larger than the amount strictly required by the stoichiometry of the reaction of $Cu_2(OAc)_4$ with H_3btc. This suggests that during the H_3btc step more linker molecules are adsorbed on the surface than required by the 3:2 Cu:btc stoichiometry of HKUST-1, or alternatively, solvent (EtOH), linker, and other molecules (H_2O, AcOH) are trapped inside the newly formed MOF pores, contributing to the observed QCM frequency change. The increase in mass change upon each subsequent cycle may also be explained by an increase in surface coverage or film surface area. Although no structural information for the 5 cycles-coated QCM crystal is available, the

presence of copper on the surface was confirmed by Energy Dispersive Spectroscopy (EDS) (Figure 60).

The relationship between the deposited film thickness (Δh) and Sauerbrey mass is given by the following relationship (**3**):

$$\Delta h = \Delta m \frac{1}{d} \qquad (3)$$

in which Δm is the mass per cm^2 obtained from equation (**1**) and d is the density of film. As mentioned above, after five combined $Cu(OAc)_2/H_3btc$ cycles the total frequency change is 87.5 Hz, which corresponds to ~1.34 $\mu g/cm^2$ added mass. Assuming the film has the density of bulk hydrated $Cu_3(btc)_2$ (0.96 g/cm^3),[14] the deposited film thickness calculated from equation (**3**) is about 13.9 nm, or an average of 2.8 nm per step.

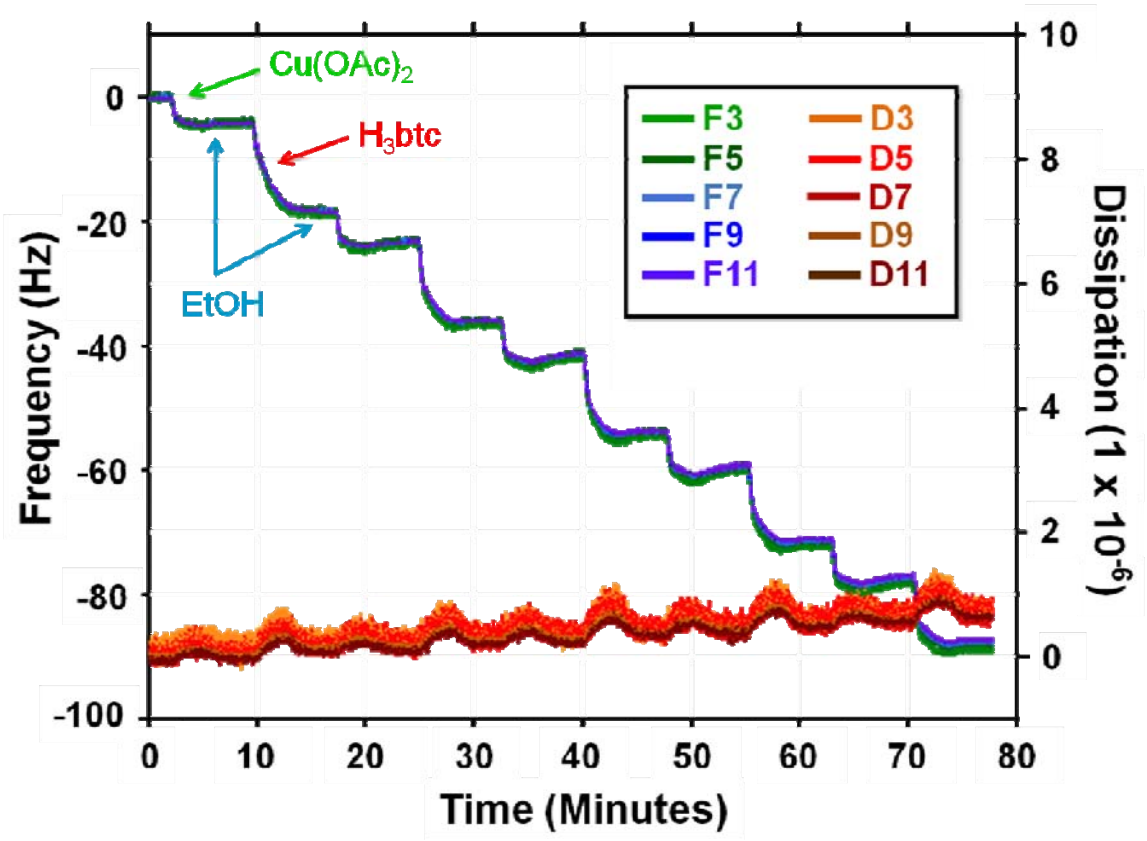

Figure 59. QCM-D results showing changes for various harmonics of the frequency and dissipation after 5 $Cu(OAc)_2$-H_3btc deposition cycles on SiO_2-coated electrodes at 15 °C. The flow rate was maintained constant at 100 µL/min throughout the experiment.

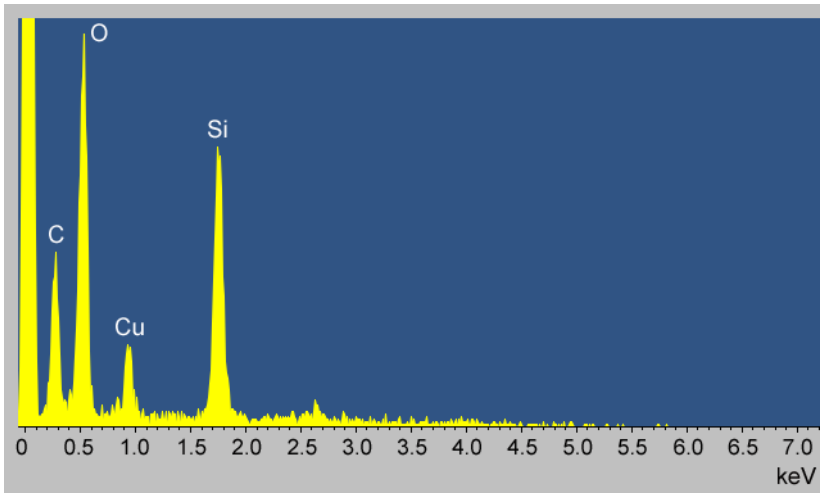

Figure 60. EDS of the $Cu_3(btc)_2$@SiO_2 film obtained after five cycles of $Cu_2(OAc)_4$ + H_3btc step-by-step deposition showing the presence of copper on the surface.

Measurements of the effect of temperature on the Sauerbrey mass after the first three $Cu(OAc)_2$–H_3btc cycles allow us to distinguish between a rapid nucleation process and a slower two-step growth reaction that occurs during subsequent cycles. As seen in Figure 61, in all reaction steps except the first exposure to $Cu(OAc)_2$ solution, the overall growth rate increases as the temperature is increased from 15 to 45 °C. However, the mass uptake during the initial copper(II) exposure is almost independent of temperature. Combining this observation with the shape of the mass uptake curve (a sharp rise followed by a plateau) suggests that copper initially deposits on silica surfaces *via* a fast (zero activation energy) sticking reaction that is limited by the availability of reactive surface sites. If so, the dependence on the Cu(II) species should be zeroth order, a fact that was confirmed experimentally.

Following the fast copper initiation step, the btc linker undergoes a slower, thermally activated reaction in the second half of the cycle (Figure 61). Interestingly, at each of the three temperatures studied, $Cu(OAc)_2$ steps subsequent to the first one produce slightly larger frequency changes. Higher temperatures also give larger frequency changes, thus higher mass uptake. After three $Cu(OAc)_2$/H_3btc cycles the total mass added is 0.97, 1.18 and 1.49 μg/cm^2 at 15, 30 and 45 °C, respectively. Since the concentration of the reagents during the flow cycle is essentially unchanged (only a small fraction of the total Cu(II) or linker available in the solution is consumed by the surface reactions), one can assume a pseudo-first order reaction for the MOF growth process, which is only dependent on the concentration of reactive sites on the surface. This is consistent with the QCM-D measurements showing that, after an initial fast mass uptake, the mass uptake saturates.

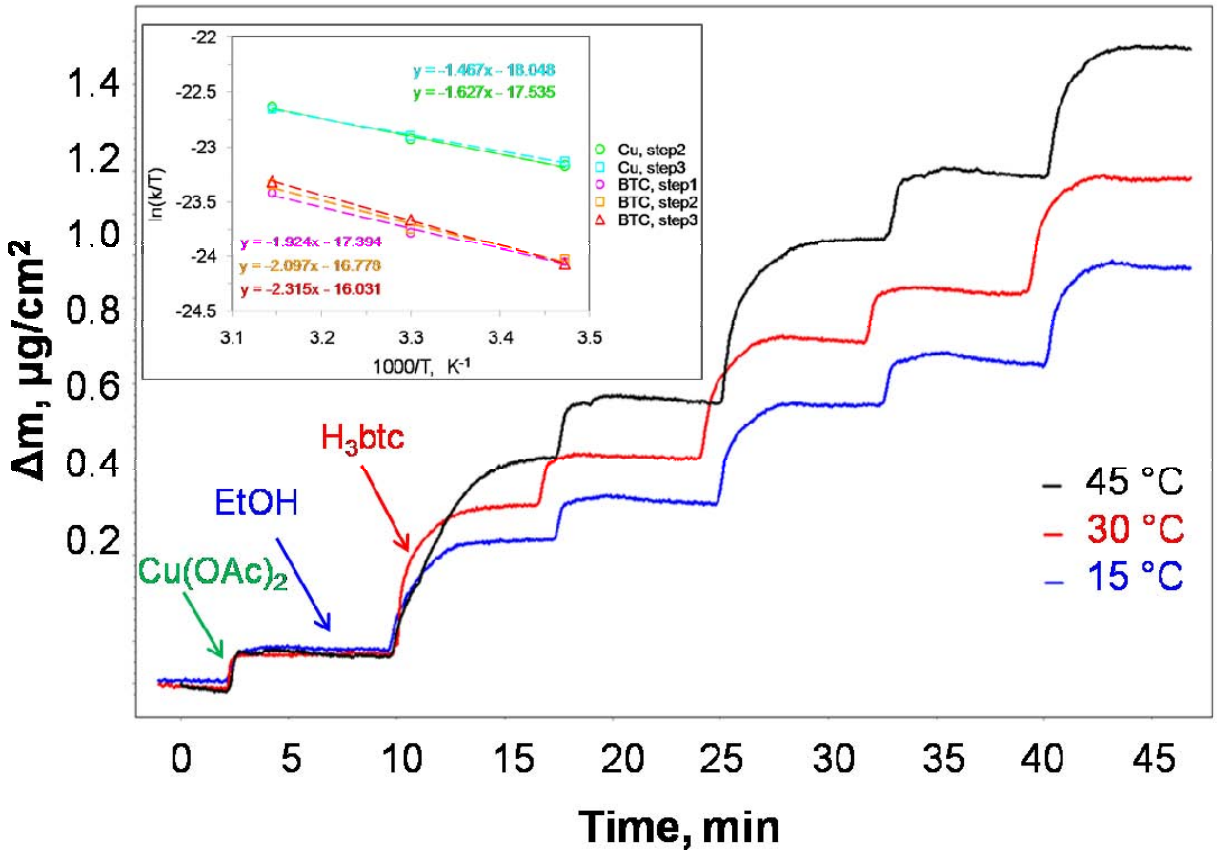

Figure 61. Sauerbrey mass change after three $Cu(OAc)_2$-H_3btc deposition cycles on SiO_2-coated electrodes at 15, 30 and 45 °C. The inset shows the corresponding Eyring-Polanyi plots for each of the individual deposition steps.

7.2.2. Kinetic Analysis

The growth rate corresponding to the individual cycles in Figure 61 was determined from the QCM-D frequency changes (Table 24) and plotted according to the Eyring-Polanyi equation, which is similar to the empiric Arrhenius equation, but it has a theoretical basis as it follows directly from the transition state theory, which can be extended to condensed phase reactions:[48]

$$k = \frac{k_B T}{h} \cdot e^{-\frac{\Delta G^{\ddagger}}{RT}} \qquad (4)$$

where k is the reaction rate constant at temperature T, $\Delta G^{\ddagger}$ is the Gibbs energy of activation, k_B is Boltzmann's constant and h is Plank's constant. In contrast to the Arrhenius equation, which is based on the empirical observation that the rate of a chemical reaction increases with temperature, the Eyring equation is a theoretical construct based on the transition state theory.[45] Since $\Delta G^{\ddagger} = \Delta H^{\ddagger} - T\Delta S^{\ddagger}$, equation (4) can be represented as

$$k = \frac{k_B T}{h} \cdot e^{-\frac{\Delta H^{\ddagger}}{RT}} \cdot e^{\frac{\Delta S^{\ddagger}}{R}} \qquad (5)$$

where $\Delta H^{\ddagger}$ and $\Delta S^{\ddagger}$ are the enthalpy and entropy of the transition state. The linear form of equation (**5**) is:

$$\ln\frac{k}{T} = -\frac{\Delta H^{\ddagger}}{R} \cdot \frac{1}{T} + \ln\frac{k_B}{h} + \frac{\Delta S^{\ddagger}}{R} \qquad (6)$$

We applied the Eyring-Polanyi formalism described above to determine the enthalpy, entropy, pre-exponential factor and activation energy for the first three $Cu(OAc)_2$–H_3btc cycles (Table 24). The initial Cu(II) deposition step (Step 1) has a rate that is independent of the $Cu(OAc)_2$ concentration and temperature, which is typical of adsorption reactions in which no rearrangement or bond breaking in the adsorbate is involved. In contrast, the next steps in the coating process have a distinct temperature dependence. Assuming a pseudo first-order reaction, we calculated the deposition rates for each of the Cu(II) and H_3btc individual coating steps. The resulting activation energies for the second and third Cu(II) deposition steps were calculated to be 16.0 and 14.7 kJ/mol, respectively. Slightly larger activation energies are observed for the three H_3btc deposition steps: 18.5, 19.9 and 21.7 kJ/mol. These low E_a values are consistent with concerted (and likely solvent-assisted) reactions in which bond breaking and formation occur simultaneously.

The entropy of activation $\Delta S^{\ddagger}$ is determined from the intercept of the *ln(k/T) vs. 1/T* plot at y = 0. The calculated values are between -343.3 to -347.6 J/mol·K for the Cu(II) steps and between -330.8 and -342.2 J/mol·K for the H_3btc steps (Table 24). These large negative values lead to small pre-exponential factors *A*. Generally, an entropy decrease is expected as a result of the loss of translational and rotational degrees of freedom when the reactant leaves the liquid phase and binds to the surface. However, they also suggest a “tight” transition state, in which the reactants must adopt a specific geometric orientation for reaction to occur. This is consistent with the metathesis-type reaction that would occur during acetate/btc and btc/acetate exchange (*vide infra*).

Table 24. Reaction rates, calculated activation enthalpy (ΔH‡), entropy (ΔS‡), pre-exponential factors (A) and activation energy (E_a) for the $Cu_3(btc)_2$ step-by-step growth.

Reaction coordinate	*Reaction rate, s^{-1}*			*$\Delta H^{\ddagger}$, kJ/mol*	*$\Delta S^{\ddagger}$, J/K·mol*	*E_a, kJ/mol*	*A, s^{-1}*
	15 °C	*30 °C*	*45 °C*				
$Cu(OAc)_2$, step 1	$2.01 \cdot 10^{-8}$	$2.02 \cdot 10^{-8}$	$2.08 \cdot 10^{-8}$	–	–	–	–
$Cu(OAc)_2$, step 2	$2.49 \cdot 10^{-8}$	$3.34 \cdot 10^{-8}$	$4.69 \cdot 10^{-8}$	13.5	-343.3	16.0±0.5	$1.99 \cdot 10^{-5}$
$Cu(OAc)_2$, step 3	$2.58 \cdot 10^{-8}$	$3.42 \cdot 10^{-8}$	$4.61 \cdot 10^{-8}$	12.2	-347.6	14.7±0.5	$1.19 \cdot 10^{-5}$
H_3btc, step 1	$1.03 \cdot 10^{-8}$	$1.42 \cdot 10^{-8}$	$2.14 \cdot 10^{-8}$	16.0	-342.2	18.5±0.6	$2.30 \cdot 10^{-5}$
H_3btc, step 2	$1.05 \cdot 10^{-8}$	$1.47 \cdot 10^{-8}$	$2.31 \cdot 10^{-8}$	17.4	-337.0	19.9±0.6	$4.25 \cdot 10^{-5}$
H_3btc, step 3	$1.01 \cdot 10^{-8}$	$1.60 \cdot 10^{-8}$	$2.38 \cdot 10^{-8}$	19.2	-330.8	21.7±0.6	$8.98 \cdot 10^{-5}$

7.2.3. Substrate Effects and Film Morphology

The effects of the substrate on the "global" activation energy corresponding to multiple cycles of step-by-step $Cu_3(btc)_2$ growth were investigated using a SRS-200 QCM system, which monitors only changes in fundamental frequency. Since the QCM-D measurements reveal that the added MOF is tightly bound to the surface of the crystals under the experimental conditions tested, the dissipation component is insignificant and can be omitted. MOF growth on four types of substrates was explored: Al_2O_3, SiO_2, and Au functionalized with COOH- and OH-terminated SAMs. In order to compare the deposition rates of $Cu_3(btc)_2$ on various substrates the growth was performed at 32 °C, with constant solution flow rates of 0.1 µL/min. Figure 62 shows the mass change after 20 cycles of QCM crystals exposure to ethanolic solutions of $Cu_2(OAc)_4$ and H_3btc. For all the substrates investigated the $Cu_3(btc)_2$ growth is essentially linear, although the noise level is somewhat higher in this instrument. The fastest growth rate is observed for alumina-coated crystals, while the $Cu_3(btc)_2$@COOH-terminated SAMs display the slowest growth rate of the four substrates.

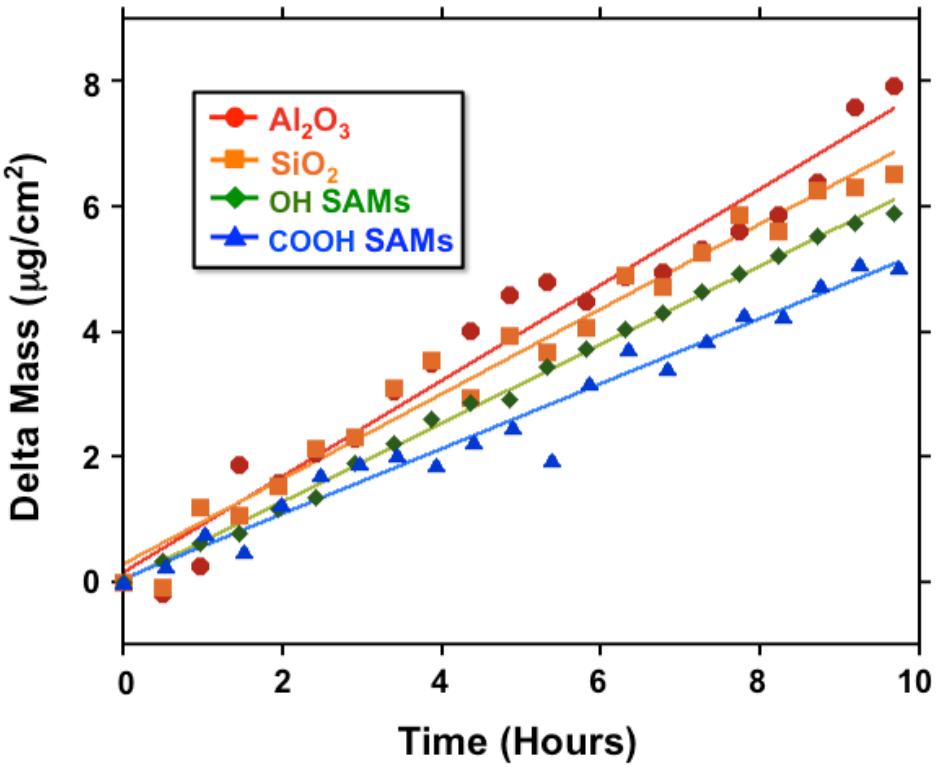

Figure 62. $Cu_3(btc)_2$ deposition on Al_2O_3, SiO_2, and Au functionalized with COOH and OH SAMs at 32 °C.

The identity of the $Cu_3(btc)_2$ films deposited on the four substrates was confirmed by *ex situ* XRD and RAIR spectroscopy measurements (Figure 63). Figure 64 compares the XRD patterns for $Cu_3(btc)_2$ coatings obtained on COOH, OH, SiO_2 and Al_2O_3 surfaces with the indexed diffraction pattern of bulk HKUST-1. The collected GIXRD patterns show characteristic features of crystalline $Cu_3(btc)_2$, with some broadening of the peaks compared to bulk material. The growth on COOH-terminated SAMs results in a film with a preferred orientation along the (*100*) direction. In contrast, a significant preferred orientation along the (*111*) crystallographic direction is observed for $Cu_3(btc)_2$ films grown on OH-terminated SAMs. This agrees with Wöll and co-workers, who first reported that the terminal functional groups can govern the $Cu_3(btc)_2$ film growth.[13,31] Thus, thin films of $Cu_3(btc)_2$ grown using the step-by-step procedure on COOH and OH-terminated SAMs are highly oriented along the (*100*) and (*111*) direction, respectively. The reason for the different film texture lies in the enhanced interactions of the COOH surface groups with the paddle-wheel Cu_2 dimeric units in the (*100*) plane, while the OH groups exhibit preferential binding to the apical position of the Cu^{2+} ions situated in the (*111*) lattice plane.[24,31] In contrast with these previous results,[13,31] $Cu_3(btc)_2$ growth on QCM crystals using continuous-flow conditions results in less oriented films with some preferred orientation along the (*100*) direction for COOH-terminated SAMs and (*111*) texture for OH-terminated SAMs. Shekhah *et al.* observed a similar behavior by correlating the differing film orientations obtained for $Cu_3(btc)_2$ grown on carboxylate- vs. hydroxyl-terminated SAMs with the composition of the growth surface expected from the crystal structure.[13] As far as $Cu_3(btc)_2@SiO_2$ and $Cu_3(btc)_2@Al_2O_3$ coatings are concerned, in both cases the films are polycrystalline, with a slight

preferred orientation along the (*111*) direction. Oxygen plasma treatment of SiO_2 and Al_2O_3-coated QCM crystals is known to produce highly hydroxylated {Si-OH} and {Al-OH} surfaces[46]. These groups have remarkably high polarity and most likely interact with the water molecules of the $[Cu_2(CH_3CO_2)_4(H_2O)_2]$ paddle-wheel secondary building units (SBUs), facilitating the growth along the (*111*) crystallographic direction.

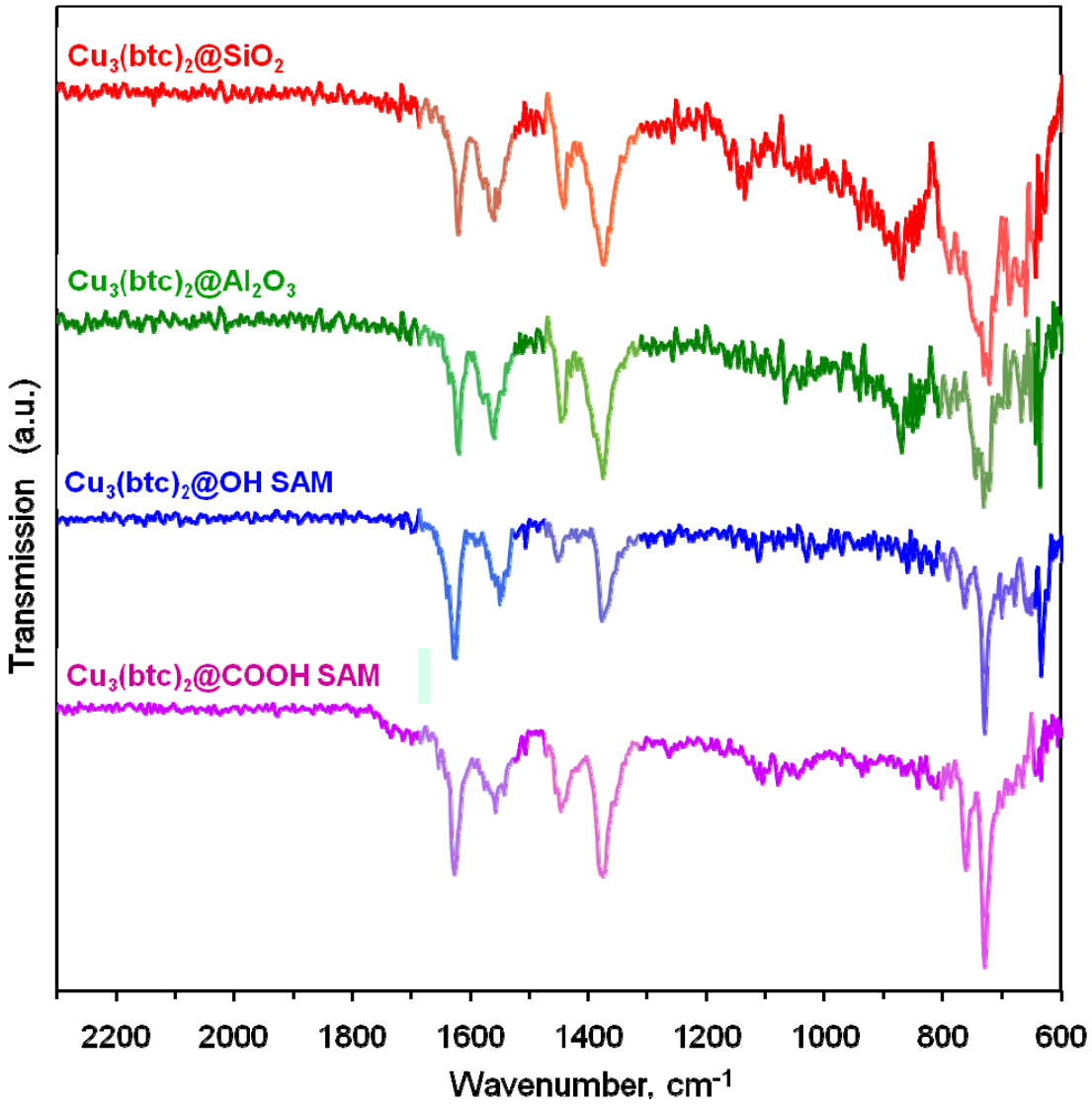

Figure 63. Reflection-Absorption Infrared (RAIR) spectra of $Cu_3(btc)_2$ coatings on various QCM electrodes deposited for 20 cycles at 32 °C.

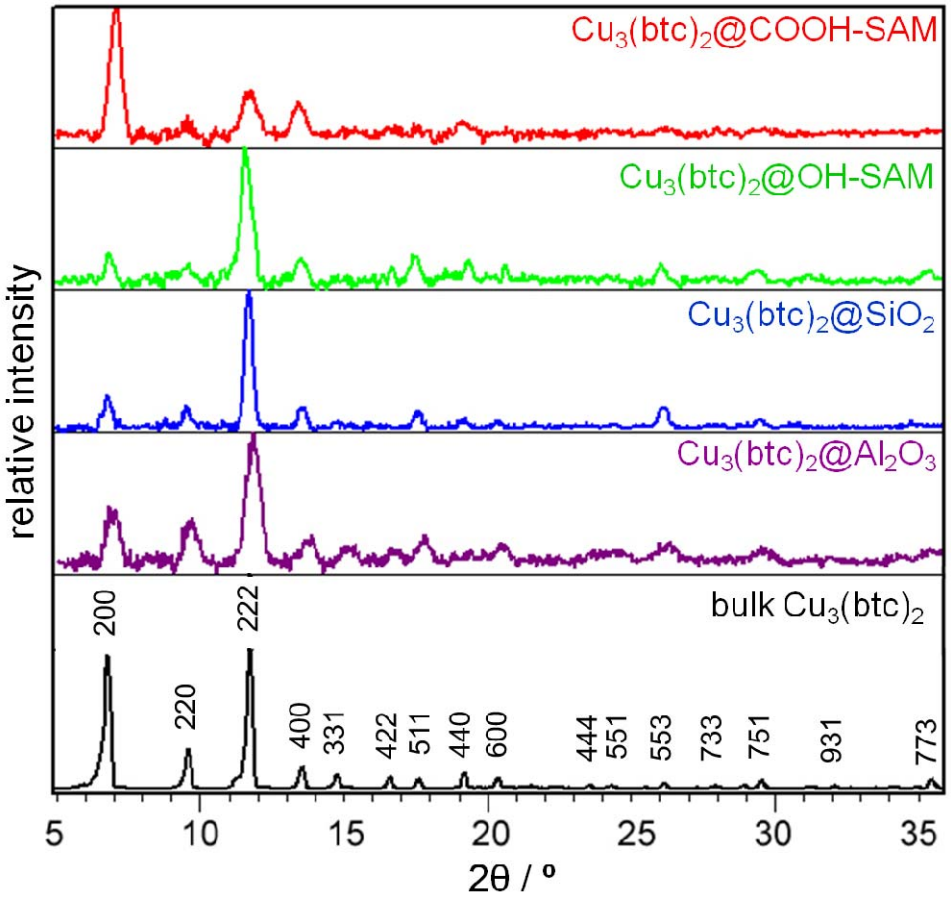

Figure 64. Grazing incidence XRD diffraction patterns at ω = 0.2° for $Cu_3(btc)_2$ films deposited on COOH-terminated SAM, OH-terminated SAM, SiO_2 and Al_2O_3 surfaces, in comparison with bulk HKUST-1. For clarity, only selected *hkl* reflections of bulk $Cu_3(btc)_2$ are labeled.

The difference in global deposition rates on silica and alumina extends to the temperature dependence, which was determined from Eyring-Polanyi plots obtained over a large number of growth cycles and five temperatures (20 °C – 62 °C; Figure 65a-b). As in the case of the QCM-D measurements, the higher temperature accelerated the MOF growth for both SiO_2 and Al_2O_3 substrates. The overall activation energy for $Cu_3(btc)_2$ film growth was derived from the Eyring-Polanyi plots in Figure 65 and is 14.6±1.2 kJ/mol for silica and 11.9±1.1 kJ/mol for alumina. This difference is consistent with the larger mass uptake during $Cu_3(btc)_2$ growth on alumina compared to silica.

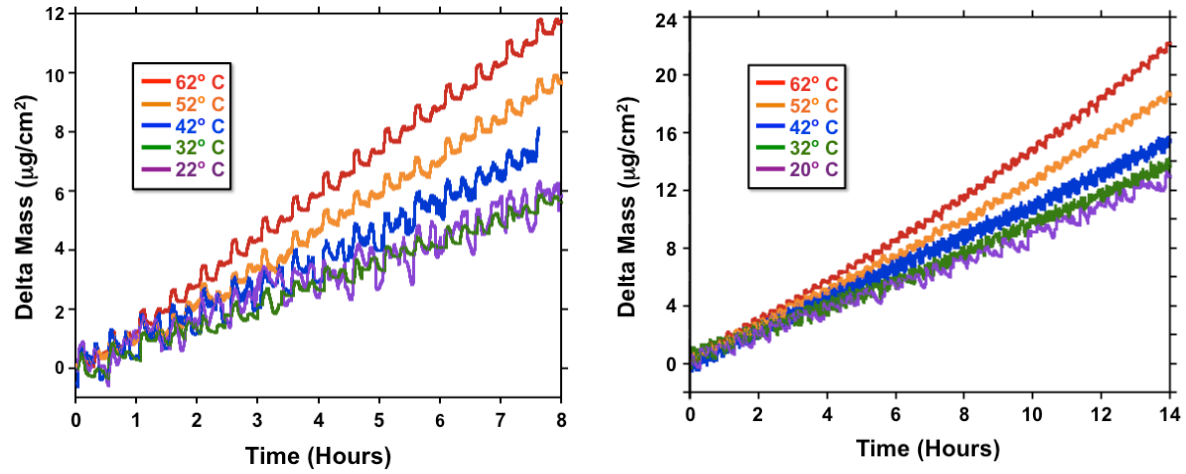

Figure 65. Temperature-dependent studies of $Cu_3(btc)_2$ deposition of on silica-coated (a) and alumina-coated (b) QCM crystals. The activation energies extracted from the Eyring-Polanyi plots are 14.6 and 11.9 kJ/mol for SiO_2 and Al_2O_3-coated electrodes.

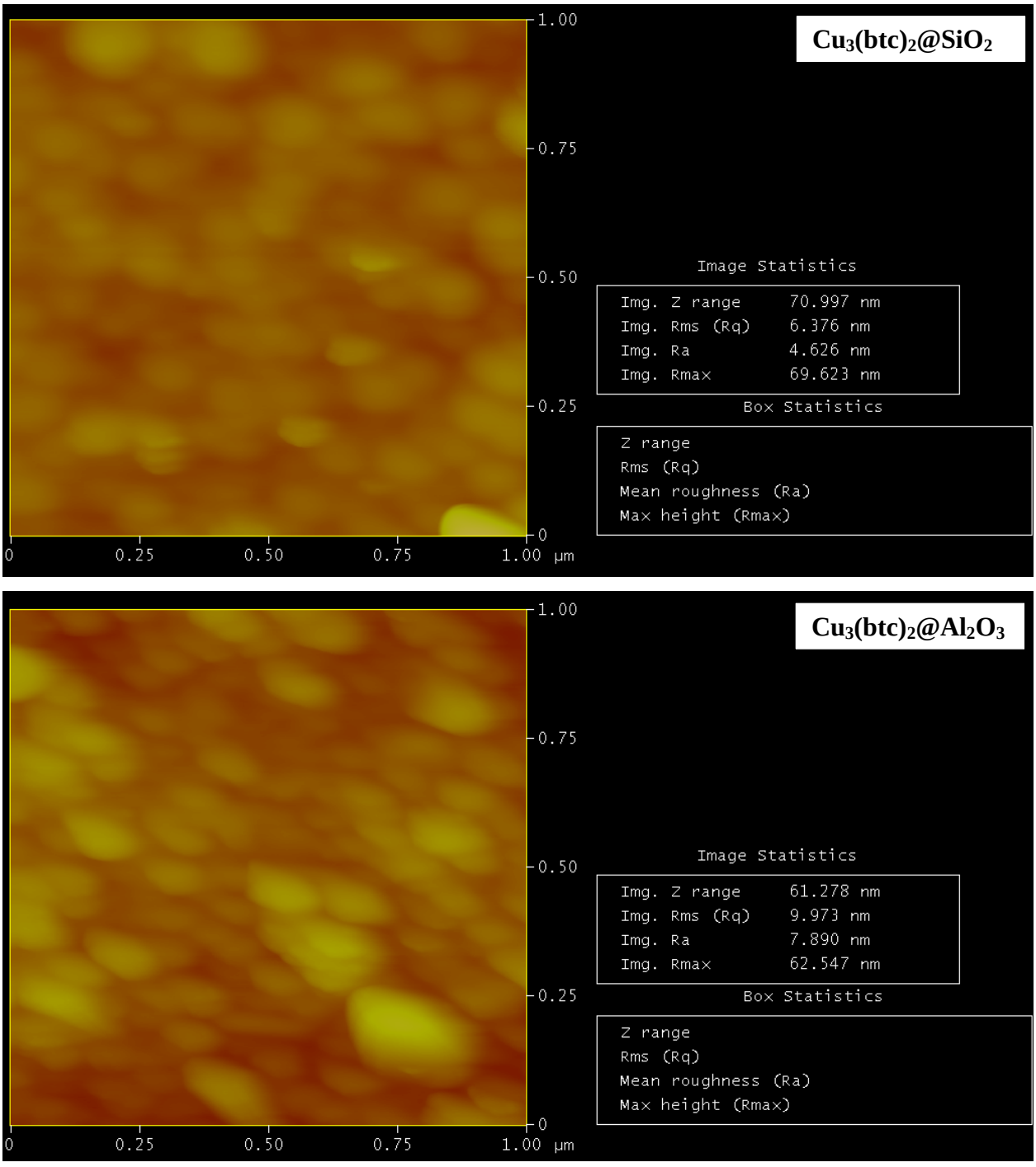

Figure 66. Comparison of root-mean-square (RMS) roughness between $Cu_3(btc)_2@SiO_2$ and $Cu_3(btc)_2@Al_2O_3$ films grown on QCM electrodes for 20 cycles at 32 °C.

The reason for this unexpected, but statistically significant, difference in activation energy between the two oxides under similar flow rates and reactant concentrations is unclear. This difference might originate in differing surface morphologies for the two substrates, which

potentially could have various concentrations of active sites on the surface, resulting in a coverage dependence for the adsorption of reactive precursors from the solution. If this is the case, some difference in the surface properties of the coatings might be observable. Additional characterization was performed to test this hypothesis. First, a comparative analysis of the GIXRD results reveals that the MOF film on silica has a slightly larger degree of texture along the (*100*) crystallographic direction, which may indicate a more homogeneous growth. Second, the surface roughness of the $Cu_3(btc)_2@Al_2O_3$ film is greater than that of the film grown on silica. The measured RMS surface roughness of $Cu_3(btc)_2@SiO_2$ film is 6.4 nm, while the corresponding value for $Cu_3(btc)_2@Al_2O_3$ film is 10.0 nm (Figure 66). This is consistent with an overall higher rate of growth on alumina. Additional evidence supporting this explanation is that the growth rate on alumina increases with time, particularly at 52 °C and 62 °C, resulting in noticeable curvature in the mass *vs*. time plot (Figure 65b). The deviation from the linearity at higher temperatures does not necessarily mean that a different growth mechanism is operative; instead, it may arise from the deposition of $Cu_3(btc)_2$ on non-planar surfaces. Rougher films presumably have higher surface areas; as growth proceeds, the surface area may actually increase, leading to an increase in the rate with time, similar to the observed growth of self-propagating molecular assemblies.[49] Unfortunately, since we cannot control the surface area or reactive site density of our substrates, this explanation is at best speculative at this point.

As mentioned above, the smoothest HKUST-1 films were grown on silica surfaces. We also observe that the full-width at half-maximum (FWHM) of the $Cu_3(btc)_2@SiO_2$ film diffraction peaks is more narrow than that of films grown on other substrates, which may indicate to higher film crystallinity. It is therefore tempting to correlate surface roughness with the crystallinity (or even the extent of disorder) of the films. Unfortunately, this is difficult to do reliably, since the film roughness determined by AFM is due to small nanometer-sized surface features, while the total film thickness contributing to the observed diffraction pattern is much larger, of the order of 100 nm. Furthermore, we note that the observed FWHM of a sample's GIXRD can be influenced by a number of factors, such as grain size and micro strain of the film. Thus, a much more detailed experimental effort will be required to determine what relationship, if any, exists between bulk film crystallinity and surface order, which is outside the scope of this initial investigation of HKUST-1 growth kinetics.

A previous study by Khan *et al.* reported an activation energy value of 133 kJ/mol for bulk $Cu_3(btc)_2$ growth from $Cu(NO_3)_2$ under solvothermal conditions.[50] This value is consistent with the observations of Shekhah *et al.*,[13] who found that HKUST-1 growth from the nitrate salt is much slower than from the acetate, presumably because pre-formed SBUs do not exist in solution. The global activation energies of 14.6±1.2 kJ/mol and 11.9±1.1 kJ/mol that we observe for $Cu_3(btc)_2$ thin film growth on silica and alumina support this hypothesis, being about an order of magnitude lower than the bulk value. This suggests that growth of HKUST-1 on surfaces from nitrate might occur at reasonable rates under solvothermal conditions. Unfortunately, at these temperatures SAMs on Au would decompose. More importantly, at such high temperatures, it is very difficult to confine growth to the surface and control the film thickness.

Typical SEM images of the $Cu_3(btc)_2$ coatings on various substrates after 40 cycles of step-by-step deposition are shown in Figure 67a-d. Fairly uniform films are observed, free of cracks and fissures, indicating that the MOF film is likely dense. Figure 67e shows the transversal cross-

section micrograph of the 40 cycle $Cu_3(btc)_2$ coating on the alumina, indicating an average MOF film thickness of about 100 nm. The film thickness values extracted from QCM measurements using equations (**1**) and (**3**) are about 75% of the SEM values, indicating that the actual film density is lower than the single-crystal $Cu_3(btc)_2$ density assumed in the analysis of the QCM data. Indeed, filling the $Cu_3(btc)_2$ pores with EtOH will likely results in a lower density film, compared to a film filled with water molecules. In addition, the as-synthesized MOF film may have some additional porosity and empty space, which will further reduce the actual density of the film.

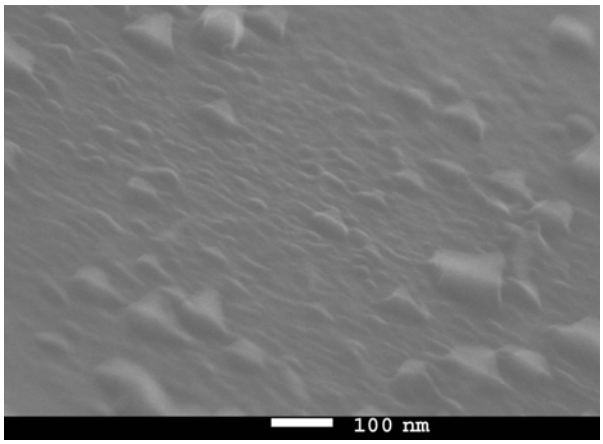

(a) $Cu_3(btc)_2@SiO_2$ (40 cycles)

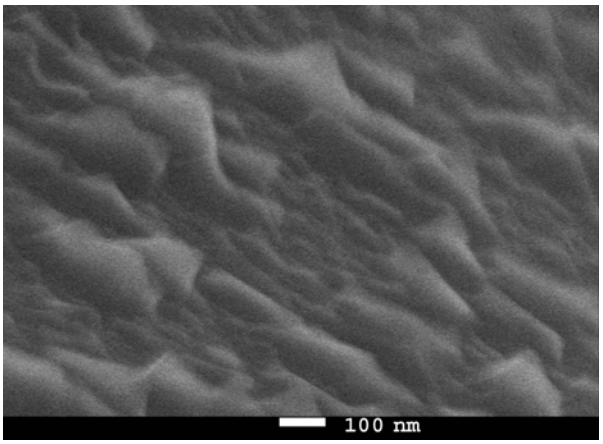

(b) $Cu_3(btc)_2@Al_2O_3$ (40 cycles)

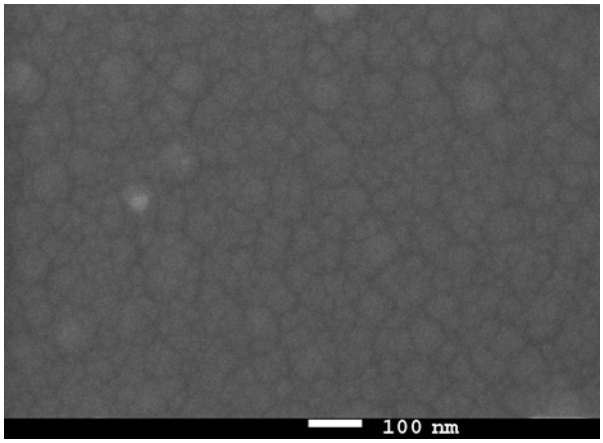

(c) $Cu_3(btc)_2$@COOH SAM (40 cycles)

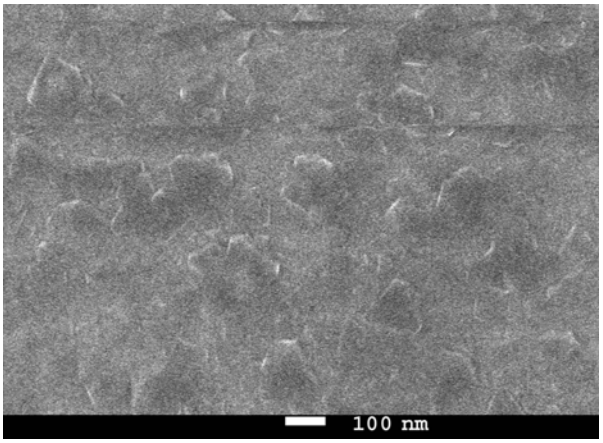

(d) $Cu_3(btc)_2$@OH SAM (40 cycles)

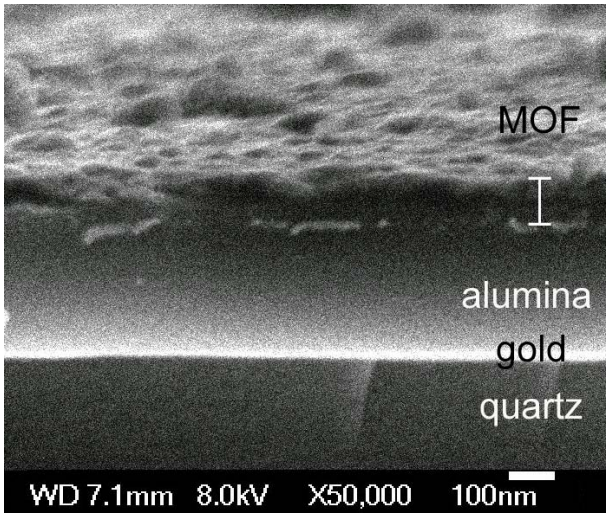

(e) Cross-sectional SEM image, $Cu_3(btc)_2@Al_2O_3$ (40 cycles)

Figure 67. SEM images of $Cu_3(btc)_2$ coatings (40 cycles) on SiO_2, Al_2O_3, COOH-terminated Au SAM (c) OH-terminated SAM (d) and the transversal cross-sectional SEM image of the $Cu_3(btc)_2@Al_2O_3$ coating (e).

A detailed examination of the MOF surface by AFM and profilometry reveals slight differences in surface morphology of the films prepared on different substrates. The AFM images of the $Cu_3(btc)_2$ films deposited on silica have regular smooth surface and dense structure (Figure 68). The smoothest films were obtained on silica, with an average surface roughness of about 6.4 nm, which corresponds to a step height of approx. two to three unit cells [14]. Surface interferometry scans over a larger area of the QCM crystals (tens of microns) for $Cu_3(btc)_2@SiO_2$ also indicate relatively smooth surfaces (Figure 69). Higher surface roughness is observed in the case of $Cu_3(btc)_2@Al_2O_3$ and $Cu_3(btc)_2$ deposited on both COOH and OH-terminated SAMs (between 16 and 27 nm). The initial surface of the silica-coated electrodes was also the smoothest, however, with RMS roughness of less than 1 nm. The Au and alumina surfaces had slightly higher roughness, between 2 and 3 nm. Step height AFM measurements (Figure 68e) on $Cu_3(btc)_2@SiO_2$ surfaces indicate a step height between 2 and 3 nm, which correlates well with the average film thickness extracted from QCM-D measurements. However, this value is larger than what is expected for the deposition of a single pre-formed SBU (1.1 to 1.5 nm, depending on the direction of growth).[51-54] This discrepancy may be due to the fact that more than one SBU per cycle is deposited; moreover, the deposited films are highly hydrated and possibly contain solvent molecules at the surface interphase.

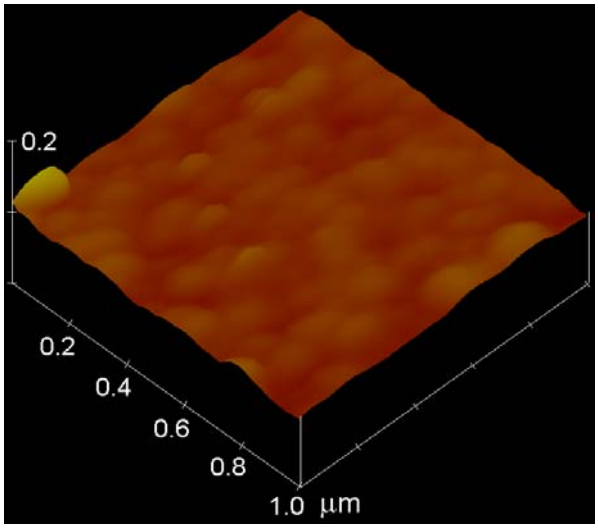

(a) $Cu_3(btc)_2@SiO_2$ (40 cycles)

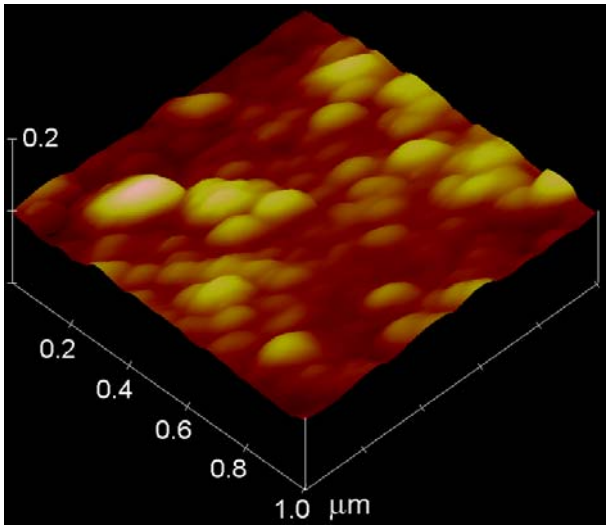

(b) $Cu_3(btc)_2@Al2O_3$ (40 cycles)

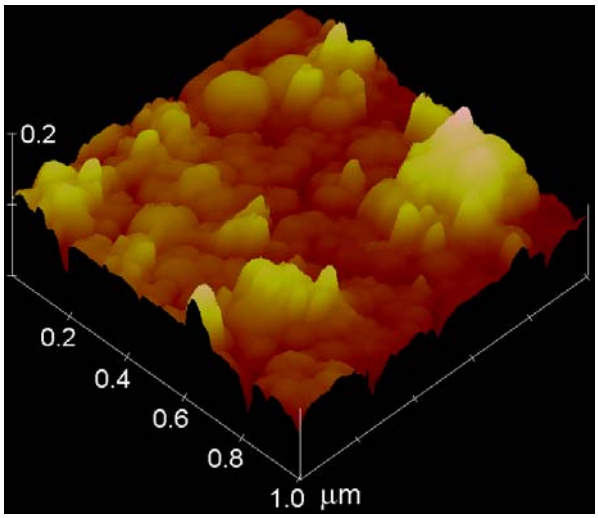

(c) $Cu_3(btc)_2$@COOH SAM (40 cycles)

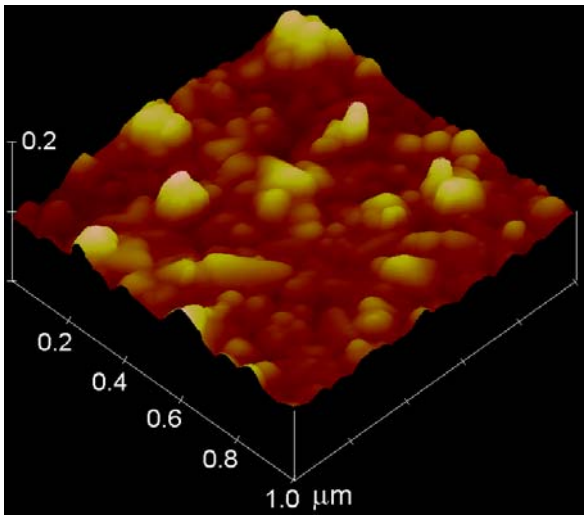

(d) $Cu_3(btc)_2$@OH SAM (40 cycles)

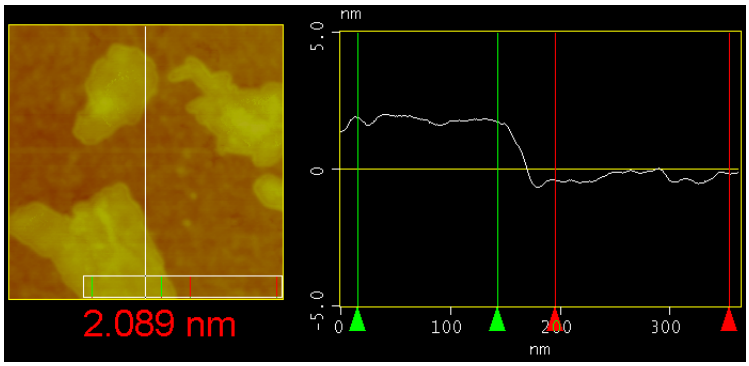

(e) $Cu_3(btc)_2$@SiO_2 (1 cycle)

Figure 68. AFM images of $Cu_3(btc)_2$ films deposited on SiO_2 (a); Al_2O_3 (b); COOH-functionalized SAM (c); OH-functionalized SAM (d) and the step height of the $Cu_3(btc)_2$@SiO_2 coating after 1 cycle (e).

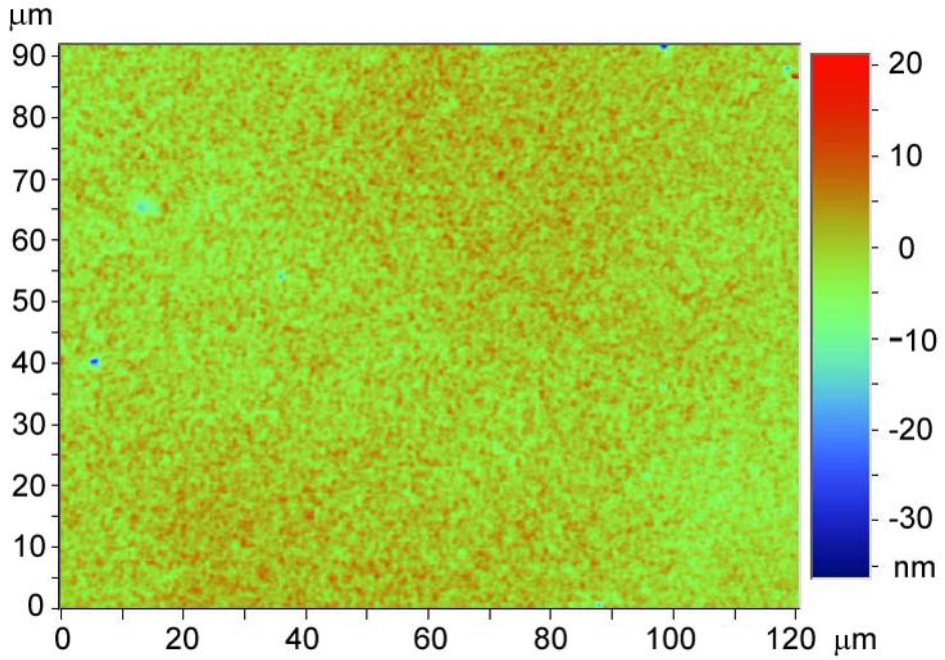

Figure 69. A representative interferometry scan on a large area (121 × 92 µm) of the $Cu_3(btc)_2$@SiO_2 coating obtained after 20 cycles of $Cu_2(OAc)_4$ + H_3btc step-by-step deposition.

7.3. Deposition Mechanism

The results of this investigation, combined with previous studies of HKUST-1 growth in the literature,[13,23,24,42,55] indicate that the step-by-step deposition of $Cu_3(btc)_2$ on surfaces involves the following steps: (*i*) nucleation, in which Cu(II) species (most likely as paddle-wheel $Cu_2(OAc)_4$ units) rapidly adsorb on the surface (k_0); (*ii*) ligand exchange between coordinated acetate and trimesic acid (k_1); (*iii*) $Cu_2(OAc)_4$ addition (k_2), resulting in $Cu_3(btc)_2$ structure formation; and (*iv*) continuous film growth via k_1 and k_2, with $Cu_3(btc)_2$ crystallite coalescence to form a dense film. Figure 70 is a schematic representation of the proposed mechanism of $Cu_3(btc)_2$ film nucleation and growth, using the example of a hydroxylated oxide surface (*e.g.* silica). During the nucleation step (rate k_0), surface OH groups react with $Cu_2(OAc)_4$ species in solution, creating the initial surface precursor to MOF growth. Our results suggest that this process begins immediately after exposure to the Cu(II) solution and surface saturation is reached within minutes. Since this process has no activation energy, but apparently involves hydrolysis of coordinated OAc^- ligands by surface OH, this reaction is likely quite exothermic and perhaps solvent assisted as well. The very early stages of adsorption probably involve conformationally disordered $Cu_2(OAc)_4$ units randomly oriented on the surface. As the surface becomes saturated with Cu(II) species, it is possible they adopt a more uniform packing and become more oriented. Subsequent exposure to a solution of the organic linker results in ligand exchange at rate k_1 and possible further reorientation of the surface $Cu_2(OAc)_4$ to accommodate the bridging btc^{3-} ligands. The QCM measurements indicate that at the initial stage of this reaction, the btc:Cu molar ratio is higher than in subsequent cycles. This could be rationalized assuming that all four bridging acetate ligands in the surface-bound $Cu_2(OAc)_4$ units are replaced by btc^{3-} groups

during the initial H_3btc steps, resulting in a 2:1 btc:Cu molar ratio. Consequently, it is during the next exposure to $Cu_2(OAc)_4$ (occurring at rate k_2) that the bridging btc^{3-} ligands are replaced to create SBUs with the 2:3 btc:Cu molar ratio of the MOF structure. Finally, as the growth proceeds, sequential exposure to solutions of copper(II) acetate and trimesic acid results in $Cu_3(btc)_2$ nuclei that coalesce to generate a continuous film. Although growth on individual crystal surfaces is epitaxial during growth on the substrates used here, the resulting films are polycrystalline and have differing degrees of texture along the (*111*) or (*100*) crystallographic directions. This is in contrast with previous reports of $Cu_3(btc)_2$ growth on SAM-functionalized surfaces, which were highly oriented.[13,31] However, in those cases, the initial substrate was single-crystal silicon, which is highly oriented and much smoother than the surfaces used here.

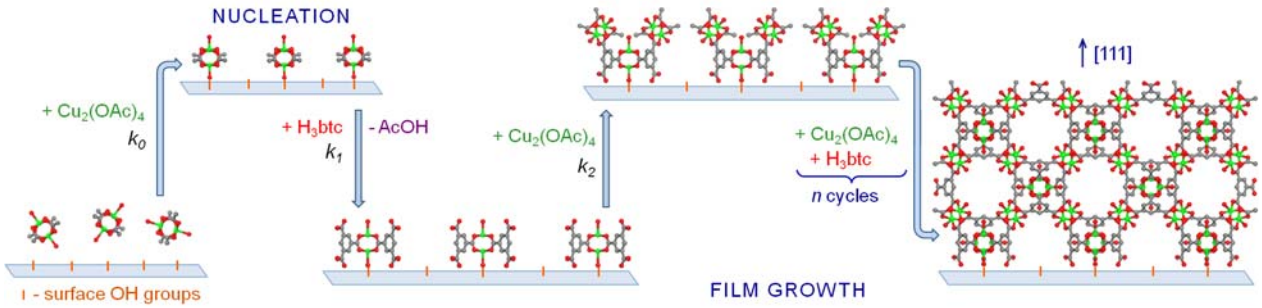

Figure 70. Schematic representation of the proposed model for $Cu_3(btc)_2$ nucleation and growth on oxide surfaces. The atoms are shown as follows: Cu – green, O – red, C – gray.

Although it is not feasible to determine the detailed geometry of the reaction pathway and transition states with any precision from our measurements, it is evident that in both the Cu(II) and btc addition steps an exchange of acetate and btc anions must occur. Furthermore, the mass uptake determined from the QCM frequency changes during the copper(II) steps does not suggest dissociation of the paddle-wheel $Cu_2(OAc)_4$ units into monomers. Rather, the similar transition state thermodynamics (Table 24) suggest a high degree of similarity between the Cu(II) and btc addition reactions. Shekhah *et al.* reached a similar conclusion by correlating the differing film orientations obtained for $Cu_3(btc)_2$ grown on carboxylate- vs. hydroxyl-terminated SAMs with the composition of the growth surface expected from the crystal structure.[13] Reasoning from the results in Table 24, at H_3btc/step 1, the linker likely encounters Cu(II) ions that are coordinated to acetate groups following the initial exposure to the $Cu(OAc)_2$ solution. At this point, an exchange of acetate for btc must occur to initiate formation of the MOF structure. Upon exposure to Cu(II) at the second step ($Cu(OAc)_2$/step 2), the metal cation in solution must exchange the acetate anions coordinated to it (at least partially) with btc bound to the surface. The net effect is again an exchange of organic anions. One would expect similar activation energies for these reactions, since the same bond types are being broken in each case, and indeed, the transition state thermodynamics corresponding to k_1 and k_2 are nearly the same. Furthermore, the relatively low $\Delta H^{\ddagger}$ for these reactions suggests that the activated complex involves both Cu(II) and linker species (represented as {Cu(II)… btc}) and that in {Cu(II)…btc} the bonds are partially broken.[45,48] The solvent likely plays a significant role in stabilizing the transition state.

We note that it is unclear whether these two processes occur *via* a single reaction or a series of individual elementary steps. Overall, however, the reaction thermodynamics in Table 24 are consistent with the fact that $Cu_3(btc)_2$ grows quite easily on surfaces without formation of any significant byproducts. The model depicted in Figure 70 is also consistent with previously published QCM, SPR, and GIXRD results.[13,24,42] Recent experimental reports suggest that, although the step-by-step growth mechanism is valid for some other MOFs,[23,26,34,35,56] it is far from being general. In particular, it is likely not applicable to cases in which the SBU or an analogue thereof does not exist in solution, as is the case here. For example, IRMOF structures require formation of a tetrahedral μ_4-oxo Zn_4O SBU that involves significant rearrangement of bonds from those existing in the typical precursors, such as Zn(II) nitrate or acetate. In such cases, the rate-limiting step may well be a reaction in solution, which would change the observed film growth kinetics and the associated mechanism. In our experience, this is consistent with the greater difficulty associated with growing dense films of IRMOF-1 (MOF-5) on any surface.

7.4. Conclusions

New insights into the step-by-step deposition of $Cu_3(btc)_2$ on silica, alumina, and SAM-functionalized Au surfaces were obtained using the QCM and QCM-D techniques. *In situ* monitoring of MOF growth, coupled with frequency and dissipation measurements, provides data necessary to establish the kinetics of film growth and allows calculation of the reaction rates and transition-state thermodynamics. Using this approach, we propose a comprehensive mechanism for the MOF growth on surfaces. The accurate measurement of frequency changes also allows correlation of the adsorbed mass with the growth conditions. This case study reveals significant differences in the texture and morphology of the resulting MOF coatings based on the substrate used. The temperature-dependent kinetics data show that the activation energy of $Cu_3(btc)_2$ thin-film growth is about an order of magnitude lower than that observed during synthesis of bulk $Cu_3(btc)_2$ crystals. The magnitudes of the activation enthalpy and entropy suggest associative reaction mechanisms for the transition states corresponding to Cu(II) and btc addition.

This work provides some important practical guidelines for the deposition of $Cu_3(btc)_2$ on various surfaces. First, HKUST-1 film growth process is thermally activated, with higher temperatures resulting in accelerated reaction kinetics. Since the step-by-step reactions are slow at room temperature, requiring several days to grow MOF films with thickness of the order of 100 nm, higher temperatures will enable growth rates that are more practical and at temperatures compatible with most devices. Second, the HKUST-1 growth rate is dependent on the composition of the surface; the order of the growth rates is Al_2O_3 > SiO_2 > OH-SAM > CO_2H-SAM. Finally, the morphology of the initial substrate has a substantial impact on the quality of the deposited MOF film, with rougher substrates yielding even rougher films.

The controlled growth of MOFs on surfaces constitutes an important step towards developing successful protocols for coating various substrates, with the ultimate goal of integrating MOFs with various functional devices. While many other MOF systems remain to be explored, this investigation illustrates the basic kinetic principles for $Cu_3(btc)_2$ film growth on several surfaces relevant to functional device applications and is a stimulus for similar detailed studies of other MOFs.

7.5. Acknowledgments

The authors would like to thank Jeff Chames for his skillful technical assistance. We also would like to thank John J. Perry IV for help with the graphical representation of the proposed growth model and useful discussions.

7.6. References

1. S. M. Cohen, *Chem. Sci.*, 2010, **1**, 32-36.
2. D. Zacher, R. Schmid, C. Wöll and R. A. Fischer, *Angew. Chem. Int. Ed.*, 2011, **50**, 176-199.
3. O. Shekhah, J. Liu, R. A. Fischer and C. Wöll, *Chem. Soc. Rev.*, 2011, **40**, 1081-1106.
4. D. Zacher, O. Shekhah, C. Wöll and R. A. Fischer, *Chem. Soc. Rev.*, 2009, **38**, 1418-1429.
5. D. J. Tranchemontagne, J. L. Mendoza-Cortes, M. O'Keeffe and O. M. Yaghi, *Chem. Soc. Rev.*, 2009, **38**, 1257-1283.
6. A. U. Czaja, N. Trukhan and U. Muller, *Chem. Soc. Rev.*, 2009, **38**, 1284-1293.
7. J. Lee, O. K. Farha, J. Roberts, K. A. Scheidt, S. T. Nguyen and J. T. Hupp, *Chem. Soc. Rev.*, 2009, **38**, 1450-1459.
8. J. R. Li, R. J. Kuppler and H. C. Zhou, *Chem. Soc. Rev.*, 2009, **38**, 1477-1504.
9. L. E. Kreno, K. Leong, O. K. Farha, M. Allendorf, R. P. Van Duyne and J. T. Hupp, *Chem. Rev.*, 2012, DOI: 10.1021/cr200324t.
10. M. D. Allendorf, A. Schwartzberg, V. Stavila and A. A. Talin, *Chem.-Eur. J.*, 2011, **17**, 11372-11388.
11. M. Meilikhov, K. Yusenko, D. Esken, S. Turner, G. Van Tendeloo and R. A. Fischer, *Eur. J. Inorg. Chem.*, 2010, **2010**, 3701-3714.
12. A. l. Bétard and R. A. Fischer, *Chem. Rev.*, 2012, DOI: 10.1021/cr200167v.
13. O. Shekhah, H. Wang, D. Zacher, R. A. Fischer and C. Wöll, *Angew. Chem. Int. Ed.*, 2009, **48**, 5038-5041.
14. S. S.-Y. Chui, S. M.-F. Lo, J. P. H. Charmant, A. G. Orpen and I. D. Williams, *Science*, 1999, **283**, 1148-1150.
15. M. D. Allendorf, R. J. T. Houk, L. Andruszkiewicz, A. A. Talin, J. Pikarsky, A. Choudhury, K. A. Gall and P. J. Hesketh, *J. Am. Chem. Soc.*, 2008, **130**, 14404-14406.
16. P. Kusgens, M. Rose, I. Senkovska, H. Frode, A. Henschel, S. Siegle and S. Kaskel, *Micropor. Mesopor. Mater.*, 2009, **120**, 325-330.
17. G. W. Peterson, G. W. Wagner, A. Balboa, J. Mahle, T. Sewell and C. J. Karwacki, *J. Phys. Chem. C*, 2009, **113**, 13906-13917.
18. L. S. Grajciar, A. D. Wiersum, P. L. Llewellyn, J.-S. Chang and P. Nachtigall, *J. Phys. Chem. C*, 2011, **115**, 17925-17933.
19. H. Wu, J. M. Simmons, Y. Liu, C. M. Brown, X. S. Wang, S. Ma, V. K. Peterson, P. D. Southon, C. J. Kepert, H. C. Zhou, T. Yildirim and W. Zhou, *Chem.-Eur. J.*, 2010, **16**, 5205-5214.
20. S. C. Xiang, W. Zhou, J. M. Gallegos, Y. Liu and B. L. Chen, *J. Am. Chem. Soc.*, 2009, **131**, 12415-12419.
21. D. Britt, D. Tranchemontagne and O. M. Yaghi, *Proc. Nat. Acad. Sci.*, 2008, **105**, 11623-11627.
22. A. L. Robinson, M. Allendorf, V. Stavila and S. M. Thornberg, *MRS Proc.*, 2011, **1366**, uu08-02.
23. O. Shekhah, H. Wang, T. Strunskus, P. Cyganik, D. Zacher, R. Fischer and C. Wöll, *Langmuir*, 2007, **23**, 7440-7442.

24. O. Shekhah, H. Wang, S. Kowarik, F. Schreiber, M. Paulus, M. Tolan, C. Sternemann, F. Evers, D. Zacher, R. A. Fischer and C. Wöll, *J. Am. Chem. Soc.*, 2007, **129**, 15118-15119.
25. J. Gascon, S. Aguado and F. Kapteijn, *Micropor. Mesopor. Mater.*, 2008, **113**, 132-138.
26. D. Zacher, A. Baunemann, S. Hermes and R. A. Fischer, *J. Mater. Chem.*, 2007, **17**, 2785-2792.
27. J. L. Zhuang, D. Ceglarek, S. Pethuraj and A. Terfort, *Adv. Fun. Mater.*, 2011, **21**, 1442-1447.
28. A. Schoedel, C. Scherb and T. Bein, *Angew. Chem. Int. Ed.*, 2010, **49**, 7225–7228.
29. M. Darbandi, H. K. Arslan, O. Shekhah, A. Bashir, A. Birkner and C. Wöll, *Phys. Stat. Solidi-Rapid Res. Lett.*, 2010, **4**, 197-199.
30. O. Shekhah, H. Wang, M. Paradinas, C. Ocal, B. Schupbach, A. Terfort, D. Zacher, R. A. Fischer and C. Wöll, *Nat. Mater.*, 2009, **8**, 481-484.
31. C. Munuera, O. Shekhah, H. Wang, C. Wöll and C. Ocal, *Phys. Chem. Chem. Phys.*, 2008, **10**, 7257-7261.
32. E. Biemmi, A. Darga, N. Stock and T. Bein, *Micropor. Mesopor. Mater.*, 2008, **114**, 380-386.
33. E. Biemmi, C. Scherb and T. Bein, *J. Am. Chem. Soc.*, 2007, **129**, 8054-+.
34. O. Shekhah, K. Hirai, H. Wang, H. Uehara, M. Kondo, S. Diring, D. Zacher, R. A. Fischer, O. Sakata, S. Kitagawa, S. Furukawa and C. Wöll, *Dalton Trans.*, 2011, **40**, 4954-4958.
35. K. Yusenko, M. Meilikhov, D. Zacher, F. Wieland, C. Sternemann, X. Stammer, T. Ladnorg, C. Wöll and R. A. Fischer, *CrystEngComm*, 2010, **12**, 2086-2090.
36. R. A. Fischer and C. Wöll, *Angew. Chem. Int. Ed.*, 2009, **48**, 6205-6208.
37. M. R. Deakin and D. A. Buttry, *Anal. Chem.*, 1989, **61**, 1147A-1154A.
38. G. Sauerbrey, *Z. Phys.*, 1959, **155**, 206-222.
39. C.-Y. Huang, M. Song, Z.-Y. Gu, H.-F. Wang and X.-P. Yan, *Env. Sci. Tech.*, 2011, **45**, 4490-4496.
40. L.-F. Song, C.-H. Jiang, C.-L. Jiao, J. Zhang, L.-X. Sun, F. Xu, W.-S. You, Z.-G. Wang and J.-J. Zhao, *Cryst. Growth Des.*, 2010, **10**, 5020-5023.
41. O. Zybaylo, O. Shekhah, H. Wang, M. Tafipolsky, R. Schmid, D. Johannsmann and C. Wöll, *Phys. Chem. Chem. Phys.*, 2010, **12**, 8092-8097.
42. O. Shekhah, *Materials*, 2010, **3**, 1302-1315.
43. K. Szelagowska-Kunstman, P. Cyganik, M. Goryl, D. Zacher, Z. Puterova, R. A. Fischer and M. Szymonski, *J. Am. Chem. Soc.*, 2008, **130**, 14446-14448.
44. R. A. Fischer and C. Wöll, *Angew. Chem. Int. Ed.*, 2008, **47**, 8164-8168.
45. *Chemically Reacting Flow: Theory and Practice*; R. J. Kee, M. E. Coltrin and G. W. Peterson, Ed.; Wiley-InterScience, Inc.: New Jersey, 2003.
46. *Encyclopedia of surface and colloid science*; P. Somasundaran, Ed.; CRC Press, Vol. 1, 2006.
47. R. W. Tillmann, M. Radmacher and H. E. Gaub, *Appl. Phys. Lett.*, 1992, **60**, 3111-3113.
48. *Chemical Kinetics and Dynamics*; J. I. Steinfeld, J. S. Francisco and W. L. Hase, Ed.; Prentice Hall, Inc, New Jersey, 1989.
49. L. Motiei, M. Feller, G. Evmenenko, P. Dutta and M. E. van der Boom, *Chem. Sci.*, 2012, **3**, 66-71.

50. N. A. Khan, E. Haque and S. H. Jhung, *Phys. Chem. Chem. Phys.*, 2010, **12**, 2625-2631.
51. N. S. John, C. Scherb, M. Shoaee, M. W. Anderson, M. P. Attfield and T. Bein, *Chem. Commun.*, 2009, 6294-6296.
52. R. E. Morris, *ChemPhysChem*, 2009, **10**, 327-329.
53. M. Shoaee, M. W. Anderson and M. P. Attfield, *Angew. Chem. Int. Ed.*, 2008, **47**, 8525-8528.
54. M. Shoaee, J. R. Agger, M. W. Anderson and M. P. Attfield, *CrystEngComm*, 2008, **10**, 646-648.
55. J. Nan, X. Dong, W. Wang, W. Jin and N. Xu, *Langmuir*, 2011, **27**, 4309-4312.
56. D. Zacher, K. Yusenko, A. Betard, S. Henke, M. Molon, T. Ladnorg, O. Shekhah, B. Schupbach, T. de los Arcos, M. Krasnopolski, M. Meilikhov, J. Winter, A. Terfort, C. Wöll and R. A. Fischer, *Chem.-Eur. J.*, 2011, **17**, 1448-1455.

[Blank page following section.]

8. MOF @ MEMS: DESIGN OPTIMIZATION FOR HIGH SENSITIVITY CHEMICAL DETECTION USING MICROCANTILEVERS[5]

8.1. Introduction

The need for real-time, compact, and inexpensive chemical detectors is important for applications such as hazardous gas detection, personal exposure monitors, and humidity measurement. However, these applications pose many technical challenges because they require very high sensitivity and specificity in small, economical packages with low power consumption. New sensing concepts based on micro-electrical-mechanical systems (MEMS) offer a potential solution that can be mass-produced at low cost. However, as with many sensor technologies, recognition chemistries are needed to provide specificity to identify a broad range of analytes. Widely applied sensing layers for gas-phase detection include polymer films [1] and metal oxides [2].

Recently, a new class of nanoporous materials known as Metal Organic Frameworks (MOFs)[3] have gained impetus recently due to their salient ,features which include ultra-high surface areas ($> 6000\ m^2\ g^{-1}$ has been reported), pore structure and chemistry that can be modified using rational synthetic design, and a high degree of chemical and thermal stability. MOFs have monolithic pore dimensions comparable in size to zeolites, achieved by coupling inorganic clusters with organic "linkers" groups. A typical MOF consists of metal cations such as Zn (II) linked by anionic organic linkers groups such as carboxylates, yielding a relatively rigid, but open framework that can accommodate guest molecules. As a result, MOFs can function as a chemical recognition layer in chemical sensors that rely on analyte adsorption. Adsorption of small molecules by MOFs is governed by a number of mechanisms [4]. In rigid MOFs, uptake is controlled primarily by adsorbate-pore surface interaction and steric interactions. In addition, however, some MOFs exhibit a degree of structural flexibility not observed in conventional recognition layers [4-9]. We recently demonstrated that this property can be used for chemical detection by strain-based transduction mechanisms [10].

Widely used detection techniques involving adsorption-induced sensing include the Quartz Crystal Microbalance, (QCM), Surface Acoustic Wave sensor (SAWS), and piezoresistive microcantilevers [11-13]. Of these, microcantilever sensors possess exquisite sensitivity, ultra-low power consumption, and simple instrumentation [14].However, proper selection of device materials and their associated mechanical properties is essential to maximize microcantilever sensitivity. The effects of MOF mechanical properties on device performance could be studied experimentally by applying MOFs with different mechanical properties to micro-fabricated cantilevers. However, the integration of MOFs with electronic devices is in its infancy [15] and depositing MOF coatings on MEMS devices is still a major challenge. However, there is a growing body of knowledge concerning MOF mechanical properties, which facilitates the use of computational modeling to probe their influence on the piezoresistive response. Here, we describe a systematic analysis of the properties of MOF recognition layers affecting the

[5] Venkatasubramanian, J.-H. Lee, V. Stavila, A. L. Robinson, M. D. Allendorf, P. J. Hesketh "MOF@MEMS: Design optimization for high sensitivity chemical detection," *Sensors Actuators B*, **169** (2012), 256.

cantilever response of the cantilever, including the Young's modulus, Poisson's ratio, and density. We also examined the effect of the binding layer by which the MOF is attached to the cantilever. The resulting insights provide a path by which mechanical properties can be taken into account in the rational design of MOF-based chemical recognition layers.

8.2. Methods

8.2.1. Cantilever Modeling

In this paper we shall focus our efforts to analyze the effects of the MOF layer and the composition of the cantilever layers on the sensor response. Multiphysics modeling of the sample geometry were carried out in COMSOL Multiphysics modeling software. The different geometrical parameters that may affect the response of the cantilever are its dimensions (length (L) and width (2W)), dimensions of the piezoresistive element (length of the piezoresistive element (L_p), width of the piezoresistor (W_p), thickness of the piezoresistor (t_p) and position of the piezoresistive element from the clamped edge (L_r)), the composition of the cantilever layers, the thickness (t) and mechanical properties of the MOF layer deposited on the cantilever.

The general geometry of the cantilever is shown in Figure 71. It is 100 µm in width (2W) and 230 µm in length (L) fabricated on a <100> Si layer. For enhancing the cantilever response we orient the longitudinal direction of the cantilever by 45° to the wafer flat (<110> direction). In this configuration n-type cantilever is more responsive than p-type cantilever [16, 17]. Since the cantilever is symmetric about the longitudinal axis, simulations were carried out for half width cantilever. The n-type piezoresistive layer were chosen to be 150 µm long (L_p), 20 µm wide (W_p) and 340 nm thick (t_p), positioned at 50 µm (L_r) from the clamped edge and is interfaced to the gold electrode. The gold electrodes are 50 µm long (L_r), 20 µm wide (W_p) and have the same thickness as the piezoresistive layer.

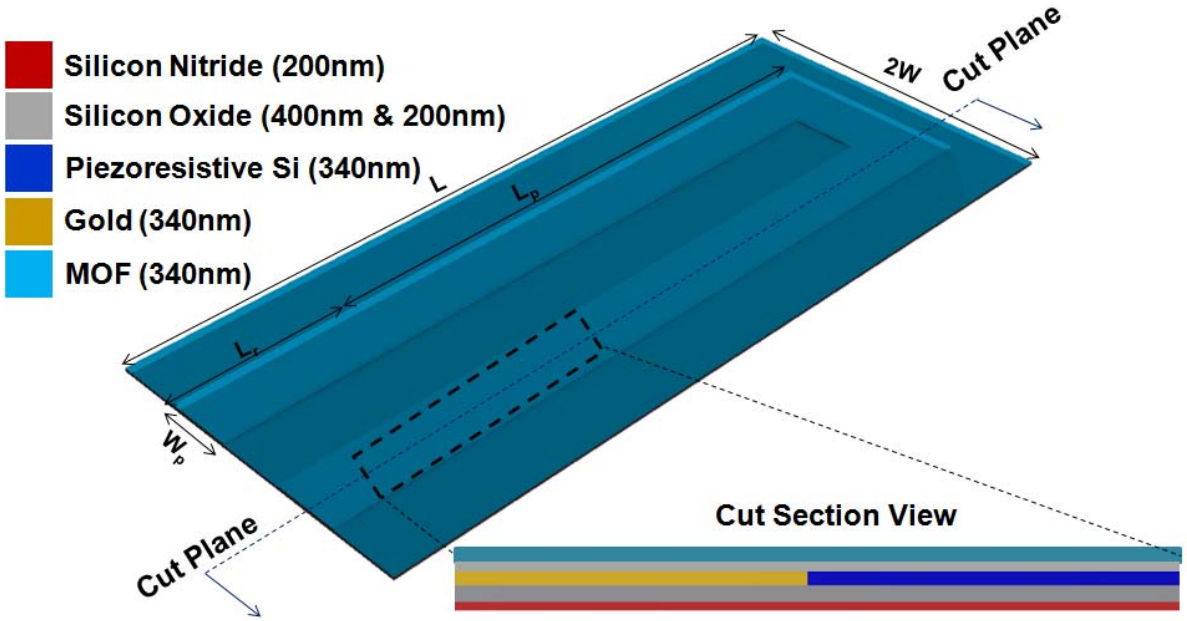

Figure 71. Geometry of the COMSOL model. Inset shows the Cut Section view of the cantilever near the interface between the gold electrode and piezoresistor.

In the COMSOL 3.5a Multiphysics modeling package, initially two physical phenomena were chosen, namely the solid mechanics module and the conductive DC media module, to study the effects on cantilever response from the deposition of Metal Organic Frameworks. The Heat transfer module was also included in the simulation and the results will be presented in subsequent sections concerning the effect of parasitic heating on the cantilever response. The change in resistance of the piezoresistive silicon layer was calculated for a constant amount of volumetric strain due to physical adsorption into the MOF sensing layer. First the resistance was calculated with zero strain, i.e. no adsorption in the MOF, and then a 0.16% volume strain due to chemical adsorption was applied in the MOF sensing layer alone. The difference between the initial resistance and the value with adsorption was divided by the initial resistance and the normalized resistance is plotted as $\Delta R/R$ in the figures. No account was made of thermal changes during adsorption, as the amount of heat generated is minimal and separate calculations show the temperature increase produced is less than a 1/1000 of a degree for the weakly interacting species and at the concentrations studied in this work. The temperature coefficient of resistance of the silicon was not included. The theory of surface stress in piezoresistive microcantilevers is described in detail below. In our calculations, a DC voltage of 0.25 V was applied to one half of the sensing layer, resulting in a total applied voltage of 0.5V per sensor element. The resistance was calculated based from the current flow using Ohm's law. Analyte adsorption was simulated by assuming a value for the thermal expansion coefficient of the sensing layer equivalent to the chemically induced strain. It should be noted that we are simulating adsorption-induced surface in the MOF by approximating it to be equivalent to the stress caused by thermal strain [18]. Hence, we are using an arbitrary value of the thermal expansion coefficient, which may not be the true value for the sensing layer. Using this coefficient, a volumetric strain of 0.16% was applied.

Given the compatibility of MOF layer with strain based sensor and the availability of a variety of MOFs with varying mechanical properties, we have chosen the sensing layer to be an arbitrary MOF for adsorption simulations. While the mechanical and thermal expansion properties of standard materials such as Al_2O_3, SiO_2, Si_3N_4, gold, and single-crystal Si were obtained from the COMSOL materials library, some of the important mechanical properties such as Young's modulus of these MOFs such as HKUST-1, MOF 508, NDC 508were measured using a MTS nanoindenter XP by indenting samples of MOFs deposited on gold coated Si substrate with a diamond tip to depths of 100 to 1000 nanometers. Detailed description of our procedure and raw data are attached in the supplementary section S1. The Young's Modulus (E) of these MOFs along with those of the standard materials is presented in Table 25. In addition to the mechanical property data measured on these MOFs, we have conducted a literature survey and have included the available property data of some of the MOFs. An important point to be noted here is that the values of Young's Modulus presented are the average Young's Modulus. Since MOFs are crystalline materials, Density Functional Theory (DFT) calculations and single crystal nanoindentation studies have shown that the Young's Modulus measurements exhibit elastic anisotropy behavior [19, 20]. Of the reviewed materials, it is shown that MOF 5 displays an anisotropy factor defined as $E_{(100)}/E_{(111)} \approx 3$ [20], whereas ZIFs have an anisotropy factor close to 1 [19]. Due to the variation in anisotropic behavior and the lack of proper information on the

crystal facets of Young's Modulus of different MOFs, we have treated the MOF sensing layer in our modeling to be of constant mechanical property, isotropic in order to obtain a general idea of the sensor behavior. Hence we have chosen an arbitrary MOF having Young's Modulus of 4Gpa, Poisson's ratio of 0.3, thermal expansion coefficient of -1.6E-05K^{-1}, density of 1000 $kgm^{-3}$and a thickness ranging from 140 - 1500 nm. We use this MOF throughout the paper unless a change in any of the stated properties is mentioned.

Table 25: List of Relevant Material Properties used in COMSOL Multi-physics Modeling.

Material	Young's Modulus E (gpa)	Poisson ratio ν	Density ρ (kg/m^3)	Thermal expansion Coefficient α (K^{-1})	Thermal Conductivity k (W/m.K)
Cantilever Layers					
Gold	70	0.44	19300	14.2e-06	317
Piezoresistive sensing layer	E_{11} = 166 E_{12} = 64 E_{44} = 80	0.27	2330	2.6e-06	100-150
Dielectric Layer					
Silicon Dioxide	70	0.17	2200	0.5e-06	1.4
Silicon Nitride	250	0.23	3100	2.3e-06	20
Aluminium Oxide	400	0.22	3965	6.5e-06	35
MOF					
HKUST-1 MOF	11.93±4.05	NA	1220[26]	-4.1e-06[28]	NA
MOF 508	0.45±0.34	NA	NA	NA	NA
MOF 5	2.7±0.1 [20]	0.13-0.3[19, 20]	550 - 1000 [20, 27]	-16e-06 [29]	0.3-0.4[31]
ZIFs	3.25-8.75 [19, 20]	NA	950-1550[20]	NA	
NDC 508	1.49±0.46	NA	NA	NA	

8.2.2. *Theory of Surface Stress in Piezoresistive Microcantilever*

Based on the earlier works by Choudhury et al.[16] and Yang et al.[21], a simple model for the cantilever bending and the strain field accounting for the effect of intrinsic stress and surface stresses is presented using the classical plate model.

Consider a laminated plate structure with five layers as shown in Figure 72. In this model, we put forth the plate model with only the piezoresistor as the midplane. Also an often used simplification, wherein a 3D plate is modeled as a 2D beam with isotropic material properties of each layer and neglecting large deformation effects is applied here to make the model more amenable.

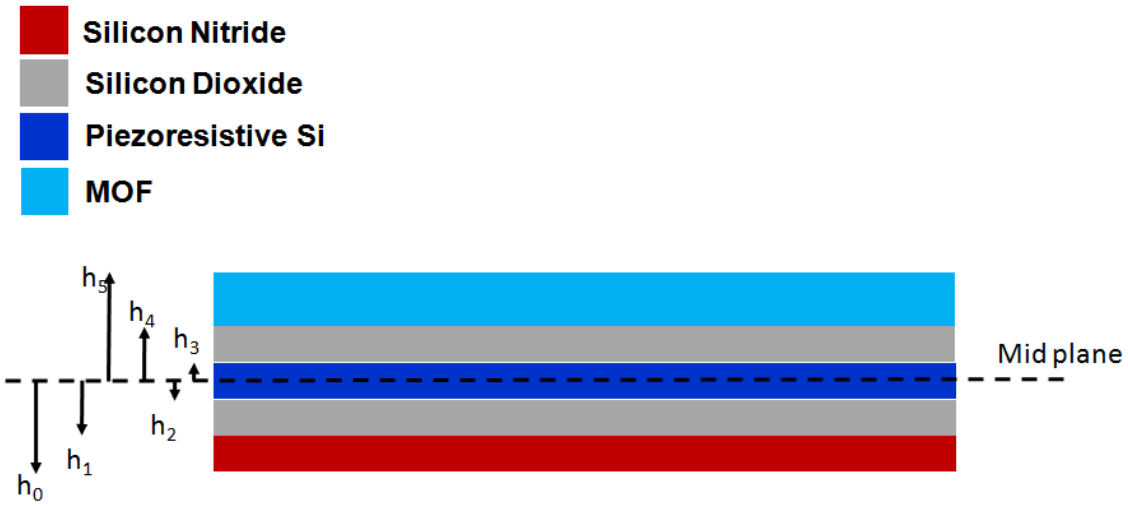

Figure 72. Simplified plate model of the cantilever.

The strain at any point in the laminated cantilever can be described as

$$\varepsilon = \varepsilon^0 + z\beta \qquad (1)$$

Where $\varepsilon^0 = [\varepsilon_x^0 \ \varepsilon_y^0 \ \varepsilon_{xy}^0]$ and $\beta = [\beta_x \ \beta_y \ \beta_{xy}]$ represent the pure tensile or compressive strain in the midplane and pure bending strain respectively. The longitudinal and transverse directions are represented by subscript x and y respectively throughout the literature. The stress in the k^{th} layer of the laminated cantilever is described as

$$\sigma_k = \begin{bmatrix} \sigma_x \\ \sigma_y \\ \sigma_{xy} \end{bmatrix}_k = \tilde{Q}_k(\varepsilon^0 + z\beta) + \sigma_{i,k} + \sigma_s \qquad (2)$$

Where

$$\tilde{Q}_k = \frac{E_k}{1-\nu_k^2}\begin{bmatrix} 1 & \nu_k & 0 \\ \nu_k & 1 & 0 \\ 0 & 0 & \frac{1-\nu_k}{2} \end{bmatrix} \qquad (3)$$

And the intrinsic stresses ($\sigma_{i,k}$) and the surface stress (σ_s) in each layer is defined as

$$\sigma_{i,k} = \begin{bmatrix} \sigma_i \\ \sigma_i \\ 0 \end{bmatrix}_k \qquad \sigma_s = \begin{bmatrix} \sigma_s(z) \\ \sigma_s(z) \\ 0 \end{bmatrix} \tag{4}$$

By integrating the stresses across the thickness, the resultant force N and moment M per unit length are

$$N = \int_{-h_0}^{h_5} \sigma dz \qquad \mathrm{M} = \int_{\mathrm{h}_0}^{h_5} \sigma z dz \tag{5}$$

The force and moment equations may be written as

$$N = A\varepsilon^0 + B\beta + N_i + N_s \tag{6}$$

$$M = B\varepsilon^0 + D\beta + M_i + M_s \tag{7}$$

Where A, B and D represent the extensional, coupling and bending stiffness, A = $\int_{-h_0}^{h_5} \tilde{Q}_k \, dz$, B = $\int_{-h_0}^{h_5} \tilde{Q}_k \, z dz$ and D = $\int_{-h_0}^{h_5} \tilde{Q}_k \, z^2 dz$, and they are dependent on the layer thickness and material properties.

For thin films with uniform property, the surface stress loading on microcantilever can be represented by the film stress distributed uniformly across the layer surface[22]. The resultant force and moment from surface stress loading can be represented by

$$N_s = \sigma_s(h_5 - h_4) \tag{8}$$

$$M_s = \frac{1}{2}\sigma_s(h_5^2 - h_4^2) \tag{9}$$

Also,

$$\mathrm{N_i} = \int_{-h_0}^{h_5} \sigma_{i,k} dz \text{ and } \mathrm{M_i} = \int_{-h_0}^{h_5} \sigma_{i,k} z dz \tag{10}$$

Hence the system of equations obtained for deformation of the multilayered cantilever is

$$\begin{bmatrix} N \\ M \end{bmatrix} = \begin{bmatrix} A & B \\ B & D \end{bmatrix} \begin{bmatrix} \varepsilon^0 \\ \beta \end{bmatrix} + \begin{bmatrix} N_i \\ M_i \end{bmatrix} + \begin{bmatrix} N_s \\ M_s \end{bmatrix} \tag{11}$$

Under equilibrium conditions in the absence of external forces and moments, the equation (11) changes to

$$\begin{bmatrix} A & B \\ B & D \end{bmatrix} \begin{bmatrix} \varepsilon^0 \\ \beta \end{bmatrix} + \begin{bmatrix} N_i \\ M_i \end{bmatrix} + \begin{bmatrix} N_s \\ M_s \end{bmatrix} = 0 \tag{12}$$

From equation (12), the mechanical response of a microcantilever under surface stress loading is given by

$$-\begin{bmatrix} A & B \\ B & D \end{bmatrix} \begin{bmatrix} \varepsilon^0 \\ \beta \end{bmatrix} - \begin{bmatrix} N_i \\ M_i \end{bmatrix} = \begin{bmatrix} N_s \\ M_s \end{bmatrix} \tag{13}$$

From the above model, the strain field induced due to surface stress loading can then be calculated and hence vice versa.

The resistance change of the piezoresistive layer can be expressed as [21]

$$\Delta R = \frac{\partial R}{\partial L}\Delta L - \frac{\partial R}{\partial b}\Delta b + \frac{\partial R}{\partial \rho}\Delta \rho \qquad (14)$$

Where L, b and ρ are the length, width and resistivity of the piezoresistor, $\Delta L = L\varepsilon_x$, $\Delta b = b\varepsilon_y$, and $\Delta\rho = \frac{\rho E}{1-\nu^2}\left((\pi_x + \nu\pi_y)\varepsilon_x + (\pi_y + \nu\pi_x)\varepsilon_y\right)$, where π_x and π_y are longitudinal and transverse piezoresistive coefficients, which can be calculated for a (100) wafer with the longitudinal axis of the feature oriented in the (110) direction using the relations in[23]. We have used ρ_0= 60E-06 Ω.m, π_{11} = -95.04E-11 Pa^{-1}, π_{12} = 49.662E-11 Pa^{-1} and π_{44} = -12.648E-11 Pa^{-1}using [23, 24] for an n-type doping at 300K and $10^{19}cm^{-3}$. The strain in the longitudinal (ε_x) and the transverse (ε_y) direction for the piezoresistive layer can be obtained from equations (1-13). Using the above relations we can calculate the normalized response (ΔR/R).

8.3. Modeling Results

As mentioned before the different geometrical parameters that may affect the response of the cantilever are its dimensions, dimensions of the piezoresistive element, the composition of the cantilever layers, the thickness and mechanical properties of the MOF layer deposited on the cantilever. Optimization studies of these parameters on the cantilever response were done using COMSOL Multiphysics modeling software package version 3.5a. Since the focus of this paper is limited to the effect of the MOF binding layer and the various mechanical properties of the MOF on the sensor response, we shall present only these results. However optimization studies on the optimum cantilever layer composition were carried out and it was found that minimizing the thickness of the nitride layer on the support structure helped in increasing the cantilever response and the selectivity of the MOF deposition [25]. Figure 72 shows a simplified model for the layer configuration used to simulate the response for the effect of MOF binding layer on the cantilever response. The configuration used throughout in this paper is 200 nm of silicon nitride, 400 nm of silicon dioxide layer below the piezoresistive sensing layer and 200 nm of the dielectric layer above (the piezoresistive layer) coated with MOF layer. The silicon dioxide layer (as shown in Figure 72) above the piezoresistive layer can be replaced with other binding layers to improve the response.

MOF binding layer is the dielectric layer between the MOF deposition and the remaining construction of the cantilever. The importance of the binding layer stems from the role it plays during MOF deposition by Self Assembled Monolayer (SAM) deposition [25]. In order to study its effect on the sensor performance, a simulation study was carried out for SiO_2; Gold with Self assembled Monolayer (SAM), Si_3N_4 and Al_2O_3 binding layers. While the simulation with SiO_2, Si_3N_4 and Al_2O_3 are straightforward, for the dielectric with Gold - SAM, we generally add a thin layer of an insulator between the Gold and the cantilever to prevent short circuiting and the SAM layer is used to improve the MOF adhesion. The insulation layer and the SAM layer are generally <50 nm and ~1 nm respectively. Due to the limitations of computing resources we have simulated the gold layer to be the entire dielectric but electrically non-participating. The Young's Modulus (E) of gold and SiO_2 is comparable and we predict the influence of SAM layer on the response to be negligible hence we have simulated with this configuration. The results are

presented in Figure 73 for the configuration shown in Figure 72, for MOF thickness from 140 nm to 1500 nm. From the figure we see that the response for the cantilever coated with SiO_2 as the binding layer was maximum followed by the cantilever coated with Gold +SAM, then by Si_3N_4 and then by Al_2O_3. This decreasing order of response with respect to the binding layer material can be explained by considering the E and ν shown in Table 25. The Bulk Modulus of a simple elastic isotropic material is defined as K= E/3(1-2ν).The bulk modulus of a material affects its stiffness in bending. Therefore the K of the gold is slightly higher than SiO_2owing to higher Poisson's ratio of gold, and thus reduces the response. However this effect of Poisson's ratio should not be confused with the effect of Poisson's ratio of the MOF on the sensor response as in the case of the latter, the MOF undergoes a volumetric expansion. This justification can be extended to the case of $Si_3N_4$and Al_2O_3. Thus we can conclude that SiO_2coated devices are superior in response to some of the other contemporary MOF binding layer [25] from the mechanical property perspective.

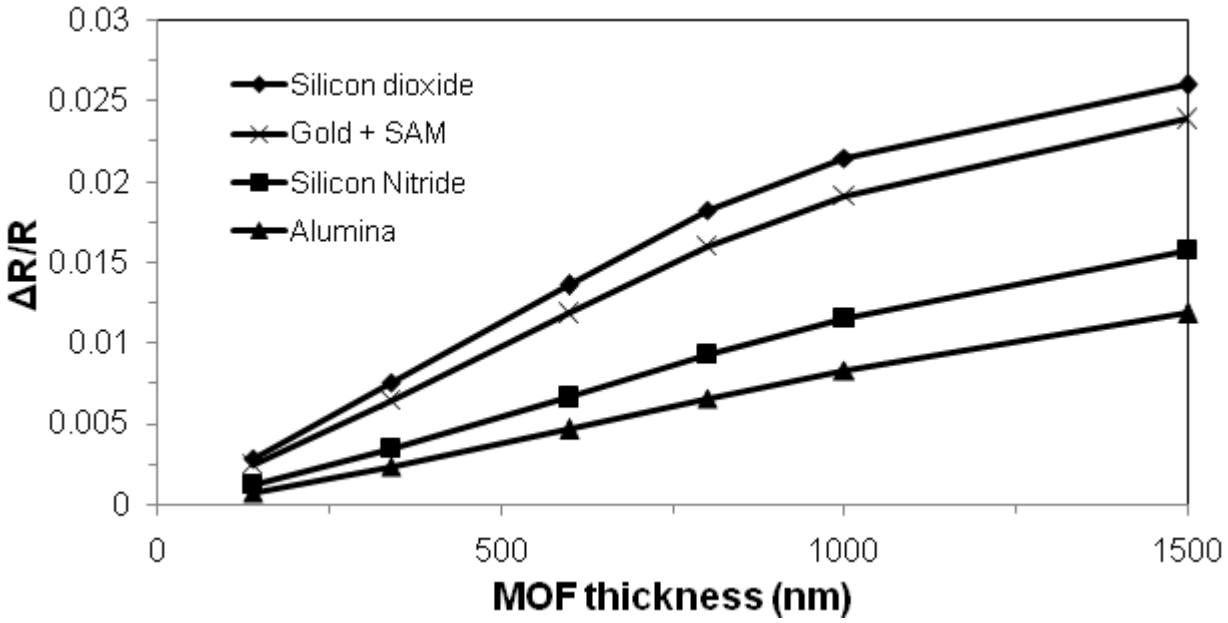

Figure 73. Response for single sided MOF deposition for different binding layers.

Up until now we have made our analysis based on single sided MOF deposition, but we can also have double sided MOF deposition. Hence the simulations were repeated for the selected configuration shown in Figure 72 with SiO_2 dielectric with MOF depositions on both sides of the cantilever and compared to the response from single sided MOF deposition. From Figure 74 we see that as the MOF thickness increases the normalized response of the cantilever increase. On comparing the response of double side MOF coated cantilever response to that of single side MOF coated cantilever for similar configuration, we observe that the normalized response for single sided MOF deposition is higher than that of double sided MOF deposition by about 30-40 %. This is to be expected due to the negation of a part of the response by the MOF on the second side. While observing the response for the double sided MOF layer it may seem that the response should be negligible because of the negation due to double MOF coating. But it is not so because of the combined effects of inherent dissimilarity in the cantilever construction and the complex

3D shape of the piezoresistor. Even in the case when similar thickness of similar dielectric is applied on either sides of the piezoresistor (not shown here), there was still appreciable response from the cantilever owing to its geometry. This analysis indicates that it would be beneficial to have preferential deposition of MOF on one side of the cantilever to have an enhanced response. The response was analyzed as a function of varying mechanical properties including Young's Modulus, Poisson ratio and density of the MOF material. We have seen from Table 25 that the Young's Modulus and density of the MOF material varied over a wide spectrum and is also shown in[19, 20, 26-29]. Though we could not obtain the Poisson's ratio of every MOF considered in this study, from what we gathered we understand that the Poisson's ratio of the MOF material changes somewhat with the chemical composition. Hence we have chosen a wide range of mechanical properties to investigate their effect on the cantilever response. Figure 75 represents the response of the cantilever for varying both the Young's Modulus and Poisson's ratio while keeping the other properties, such as thermal expansion coefficient(α) (assumed at -1.6 E-05 K^{-1}), density (ρ) (1000 kgm^{-3}) and thickness (340 nm) constant. The response was plotted for the values of the reviewed MOF's E between 0.5 Gpa and 17 Gpa and ν between 0.05 to 0.48 (consistent with the assumption of elastic isotropic behavior).For some anisotropic directions the ν can be greater than 0.5[20], however a negative Poisson's Ratio was not included. From the plot it was seen that as E and ν increases the response also increases. However on comparing the relative effect of ν and E on the sensor response, we notice that E has got a greater effect on the response.

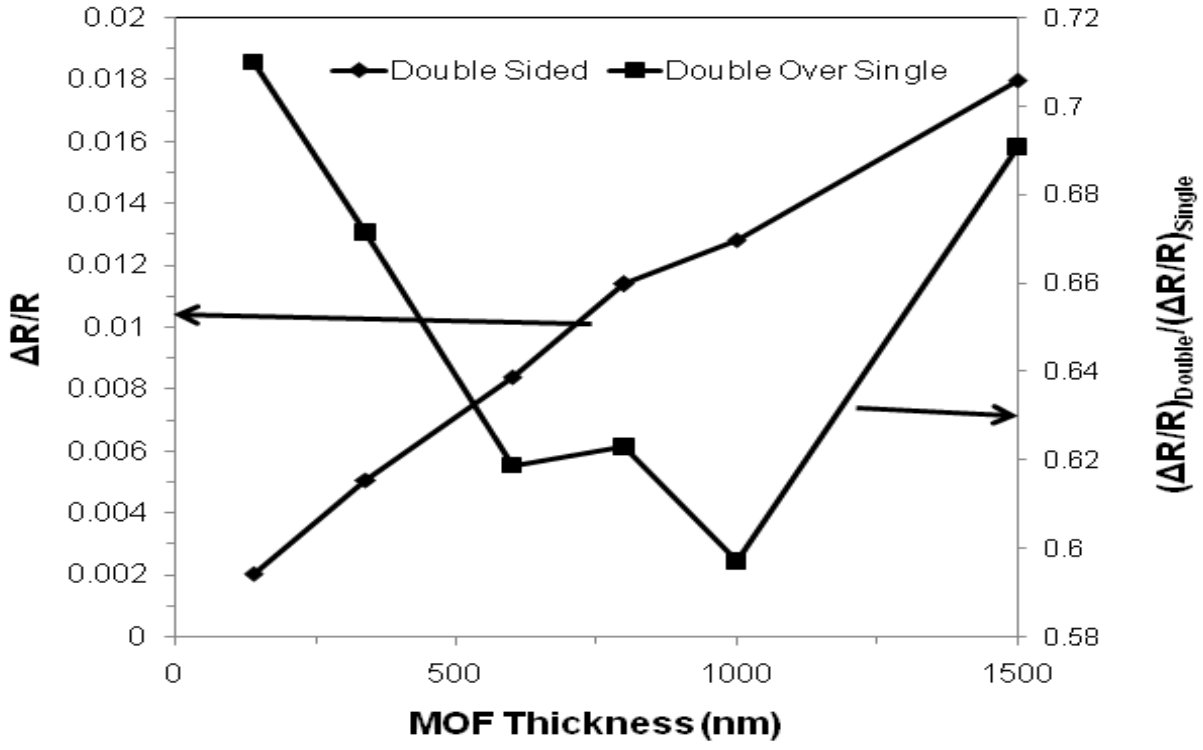

Figure 74. Response for double sided MOF coated cantilevers.

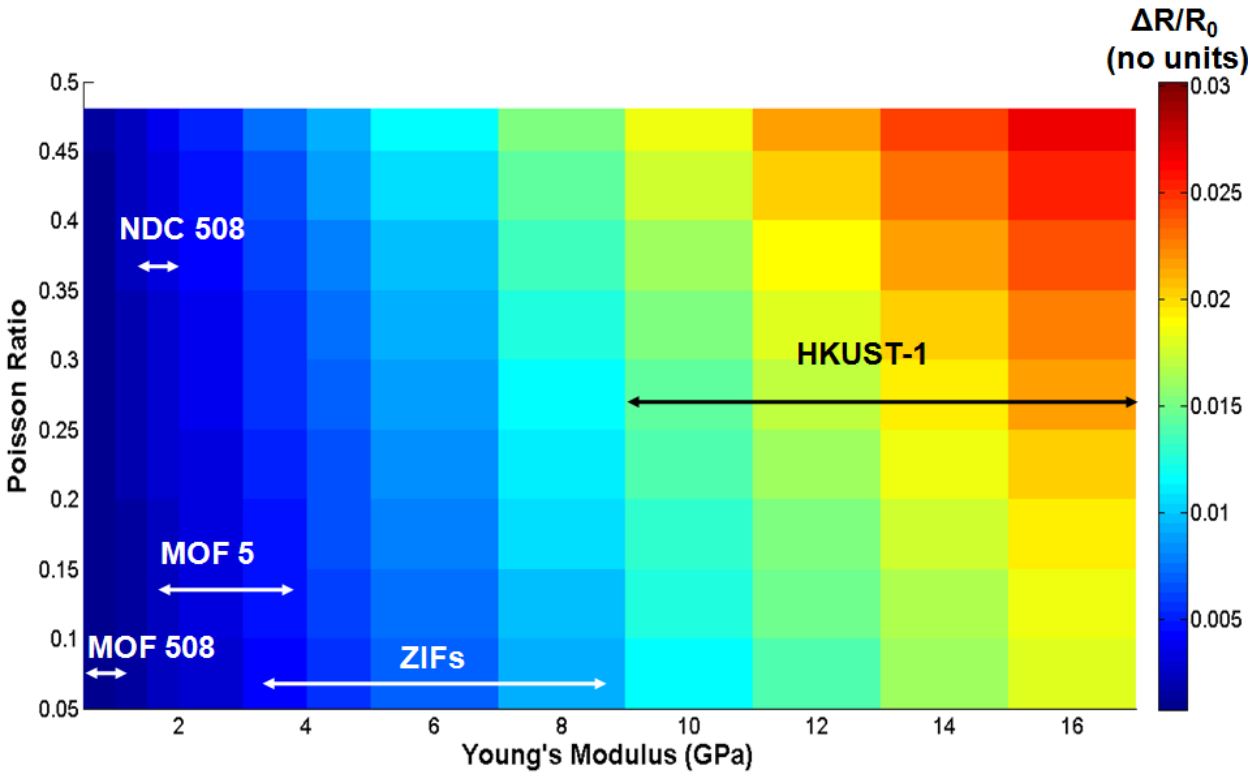

Figure 75. Response for varying Poisson ratio and Young's Modulus with labels of the range of measured Young's Modulus of each individual MOFs

A separate simulation study was performed by varying the density of the MOF material by keeping its other properties such as E(4 Gpa), ν (0.3), α (-1.6 E-05 K^{-1}) and thickness (340 nm) constant. The density was varied between 300 kgm^{-3} to 1600 kgm^{-3}. However from the plotted response it was noted that the effect of changing density had no effect on the cantilever response. This was expected due to the lack of participation of a density component in the system of equations (1-14) used to derive the response.

When a piezoresistive sensing platform is used, a voltage is applied so that parasitic heating (resistive heating of the piezoresistive material) will take place. We assessed the effect of such heating on the cantilever response by including the heat transfer module in the COMSOL Multiphysics simulation, wherein the predicted temperature rise in the microcantilever due to parasitic heating would induce stress in the cantilever layer structure in addition to that induced by simulated adsorption in the MOF layer (0.16% strain as mentioned before) and hence may produce a change in response. These simulations were performed by including thermal strain of the cantilever layers due to the resistive heating in the solid mechanics module in COMSOL Multiphysics. The thermal strain was calculated from the temperature distribution obtained from the Heat Transfer Module. The reference temperature that was chosen for the thermal strain was 300 K. The effect of resistive heating was investigated for all the MOF binding layers considered (SiO_2, Si_3N_4, Al_2O_3 and Gold-SAM), using the same configurations described above while maintaining the MOF layer thickness to be 340 nm. The temperature distribution of all the configurations at different applied voltage is presented in the supplementary section between Figures 76 and 77. Table 26 lists the range of temperatures distribution in the cantilevers for the

different configurations at each voltage. For example, the maximum temperature increase for the silica coated sensor is 2.3K at a 0.25 voltage input, increases to 40K at a voltage input of 1V. The related thermal properties such as Thermal Expansion Coefficient, α (K^{-1}), and Thermal Conductivity, k (W/m.K),of the cantilever layers are listed in Table 25. The thermal conductivity of the piezoresistive layer (Single Crystal Silicon, SCSi) is known to vary with temperature and doping level. Based on a literature review, the thermal conductivity of SC Si at the reference temperature of 300 K and for a doping level $10^{19}cm^{-3}$ was found to be between 100 to 150 W/m.K [30]. Although the temperature of the SC Si layer can rise above the reference temperature in the simulations, we assumed a constant value of the thermal conductivity of SC Si layer (120 W/m.K) and did not include the temperature coefficient of the doped silicon resistivity in the model. This allows any predicted resistance change to be associated purely with parasitic heating and will therefore not contribute to the ΔR resulting from the adsorption-induced strain in the cantilever.

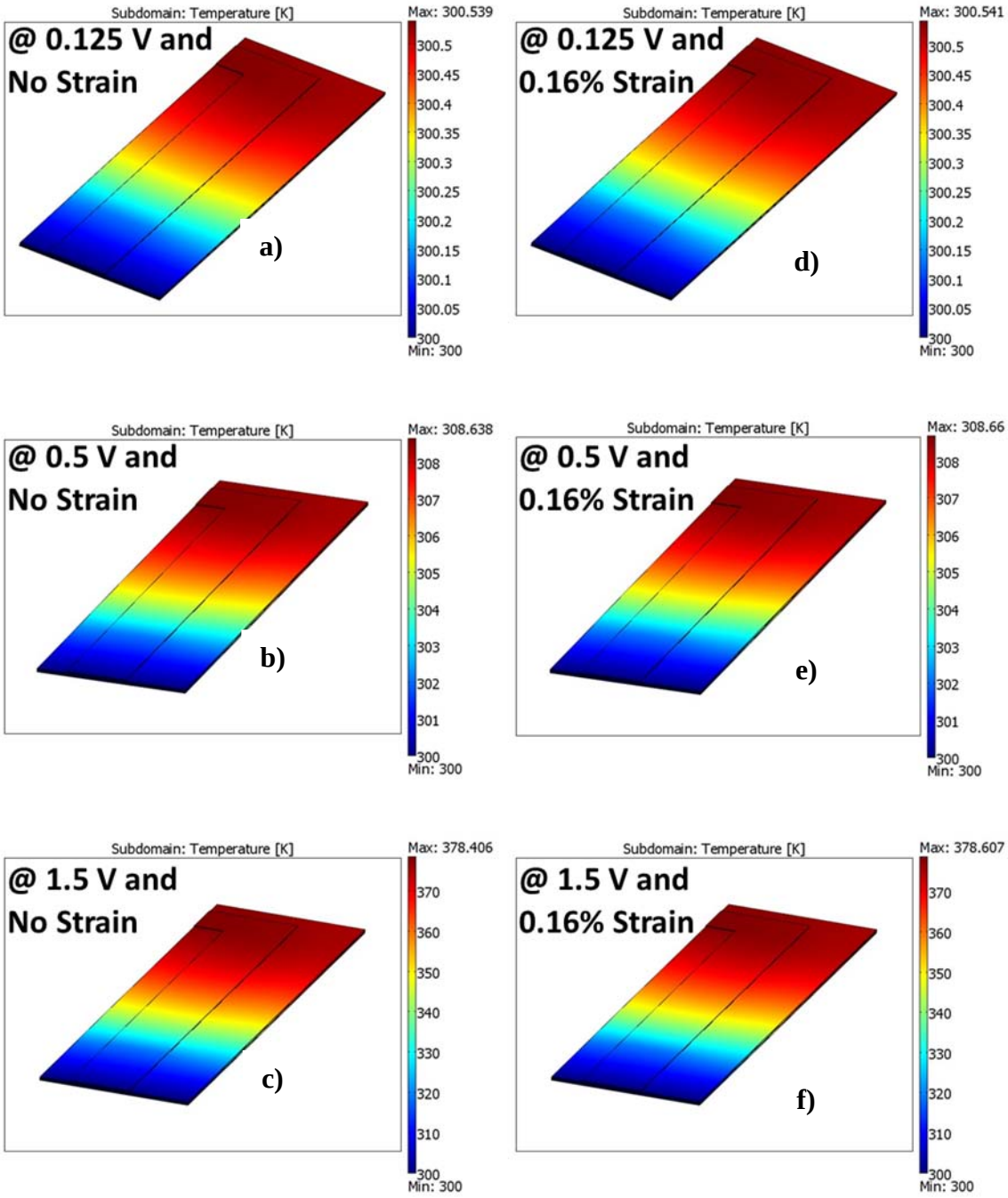

Figure 76. Temperature distribution of the half Cantilever element for different applied Voltage with Alumina as the MOF binding layer. Figures (a-c) represents the temperature distribution without applied strain while figures (d-f) represent the temperature distribution with applied strain.

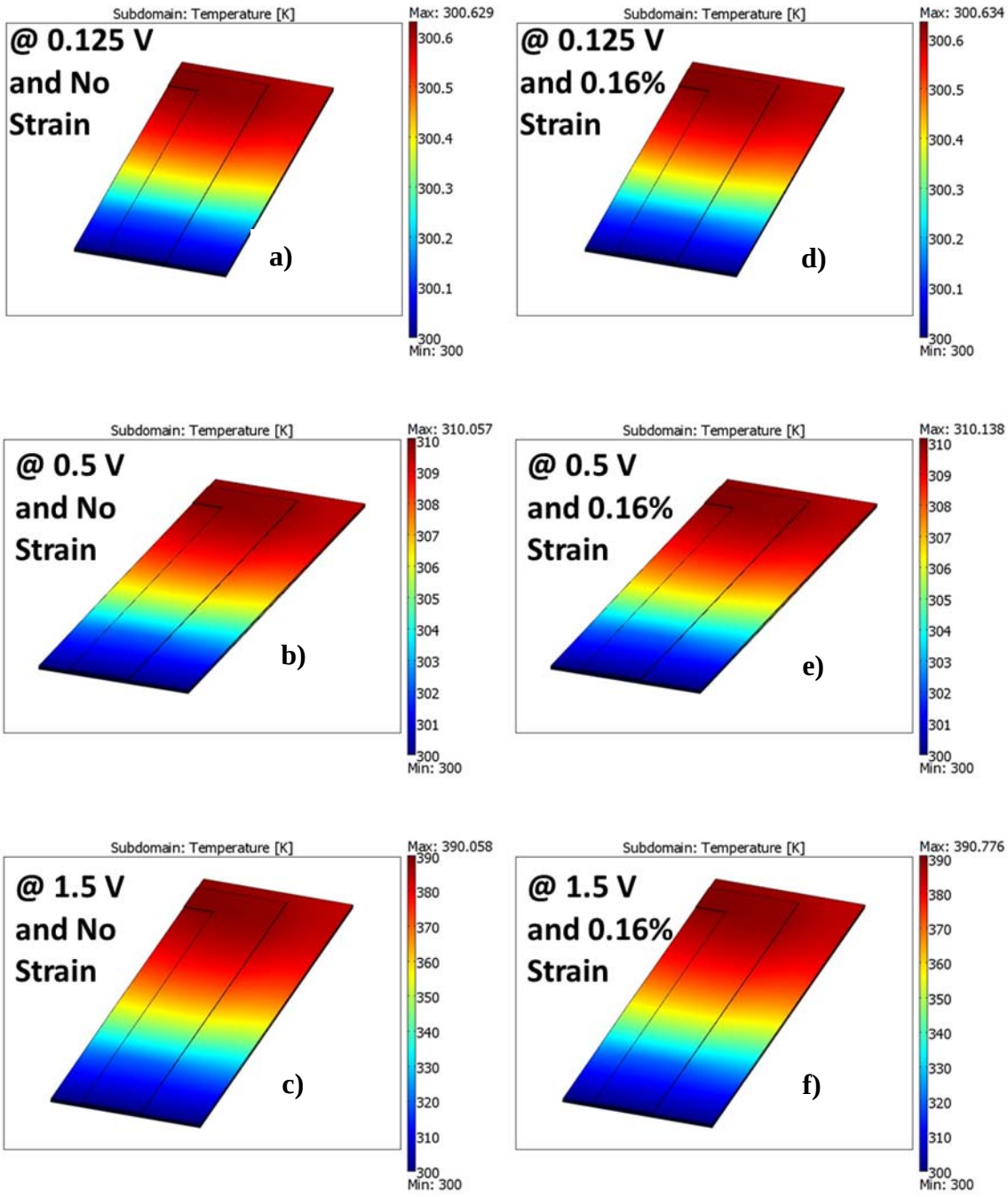

Figure 77. Temperature distribution of the half Cantilever element for different applied Voltage with Silicon dioxide as the MOF binding layer. Figures (a-c) represents the temperature distribution without applied strain while figures (d-f) represent the temperature distribution with applied strain.

Table 26. Temperature Distribution Range of the half Cantilever element for different configurations

Material → / **Applied Voltage per half sensor element ↓**		**Al_2O_3 (300 K -**	**Gold-SAM (300 K -**	**SiO_2 (300 K -**	**Si_3N_4 (300 K -**
0.125 V	No Strain	300.539 K	300.255 K	300.629 K	300.575 K
	0.16% Strain	300.541 K	300.256 K	300.634 K	300.577 K
0.25 V	No Strain	302.158 K	301.019 K	302.515 K	302.301 K
	0.16% Strain	302.163 K	301.026 K	302.535 K	302.31 K
0.5 V	No Strain	308.638 K	304.079 K	310.057 K	309.203 K
	0.16% Strain	308.66 K	304.107 K	310.138 K	309.237 K
0.75 V	No Strain	319.461 K	309.19 K	322.611 K	320.698 K
	0.16% Strain	319.51 K	309.254 K	322.792 K	320.773 K
1.0 V	No Strain	334.663 K	337.055 K	340.155 K	336.773 K
	0.16% Strain	334.751 K	337.314 K	340.476 K	336.907 K
1.5 V	No Strain	378.406 K	337.055 K	390.058 K	382.577 K
	0.16% Strain	378.607 K	337.314 K	390.776 K	382.878 K

Regarding the thermal conductivity of the MOF layer, an extensive literature search indicates that very little work has been done with regard to determining MOF thermal conductivities. The MOFs for which thermal conductivity was determined are listed in Table 25. Since such sparse literature is available for this property, we assumed a value of 0.5 W/m.K in our simulations, while keeping the remaining mechanical properties the same. With respect to the boundary conditions used in the Heat Transfer Module, we considered convection from the cantilever to be treated as a flow over a flat plate problem, with the fluid velocity equal to 1 m/s (which is equivalent to ~100 sccm of fluid flow rate for a standard 1/16" ID tube). The fluid chosen was air at 300 K and 1 atm. Based on a simple calculation, the average convection coefficient is found to be~400 $W/m^2.K$.

While simulating for the resistive heating effect, the DC voltage applied to one half of the sensing layer was varied between 0.125 V to 1.5 V, resulting in a total applied voltage of 0.25 V to 3 V per sensor element. This range covers most of the typically used applied voltages reported in the literature, which in most cases is between 0.25 V to 1 V per sensor element. The results of the simulations are presented in Figure 78. Here, the left-hand side vertical axis represents the

relative change in resistance due to parasitic heating ($\Delta R/R_{\text{With parasitic heating}}$) and the right-hand vertical axis represents the relative change in ΔR/R due to parasitic heating for the chosen configuration. The latter is defined as

$$\text{Relative Change in } \frac{\Delta R}{R} \text{ due to parasitic heating (\%)} = \left| \frac{\left(\frac{\Delta R}{R}\right)_{\text{parasitic heating}} - \left(\frac{\Delta R}{R}\right)_{\text{No parasitic heating}}}{\left(\frac{\Delta R}{R}\right)_{\text{No parasitic heating}}} \right| \times 100 \qquad (15)$$

It is clear from Figure 78 that the changes in response ($\Delta R/R_{\text{With parasitic heating}}$) due to parasitic heating are very minor. The relative change in ΔR/R due to parasitic heating plotted on the right-hand side axis indicates that a negligible effect is associated with a Si_3N_4 binding layer,while the remaining three binding layers, namely SiO_2 (0.75 V and above), gold - SAM (0.25 V and above) and alumina (0.25 V and above) exhibit a small, but perceptible change in response above a particular applied DC voltage indicating that the resistive heating affects the response slightly in these configurations. This can be traced to their physical properties such as Young's Modulus (E), thermal expansion coefficient (α) and thermal conductivity (k) for the different binding layers listed in Table 25. While the exact relationship between these properties and the cantilever response is complex [21], since the scale of variation was small (<3%), we feel that the effect of resistive heating is negligible considering the general applied DC voltage to be 0.125V to 0.5 V for half sensor element. This effort clearly reinforces our earlier conclusion that SiO_2 is the best choice of the four materials considered as the binding layer for MOF thin films because of its negligible change in response due to resistive heating.

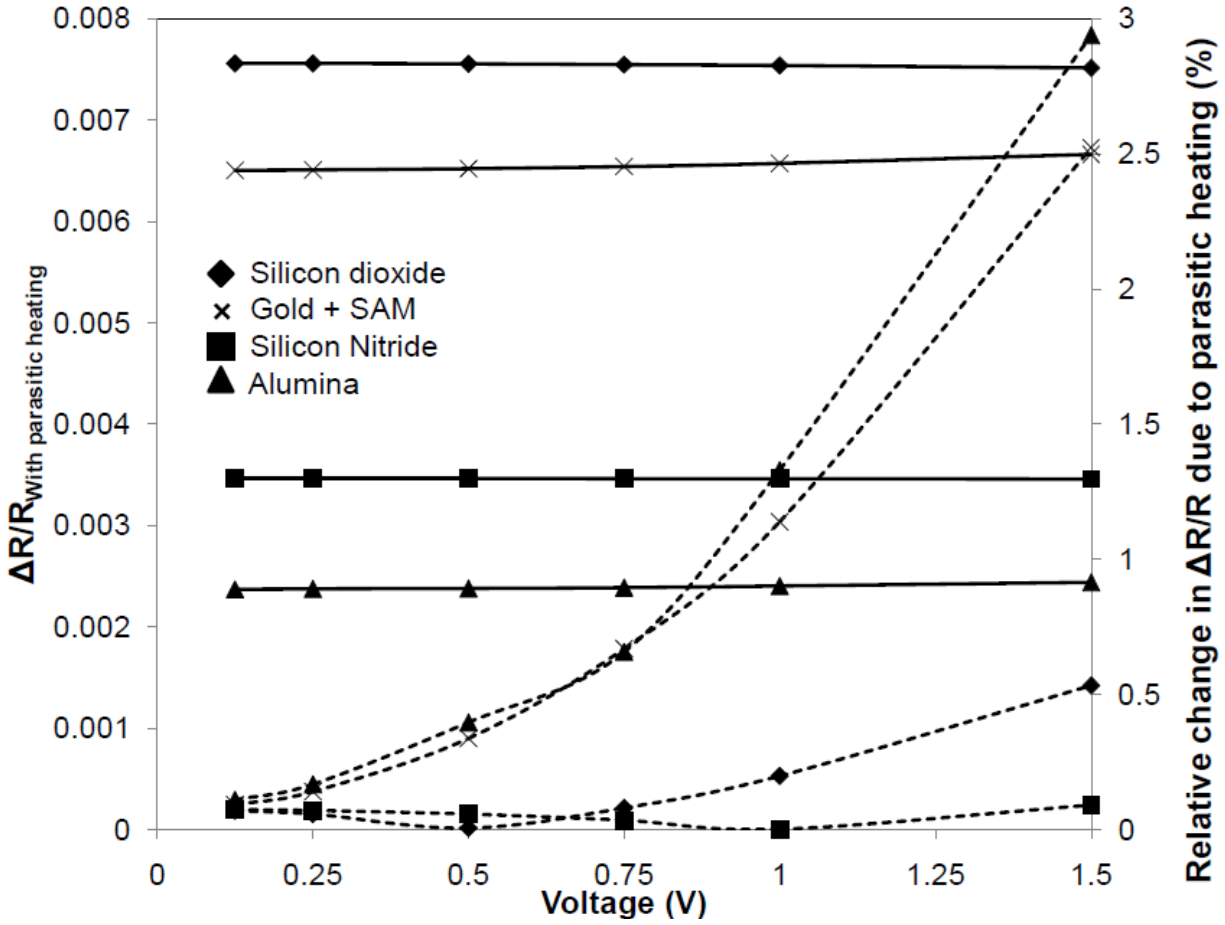

Figure 78. Effect of Resistive heating of the piezoresistive material on the Cantilever's Response. The $\Delta R/R_{\text{With parasitic heating}}$ on the left hand vertical axis is represented by solid lines (—) with appropriate markers as defined in legends. The Relative change in ΔR/R due to parasitic heating on the right hand vertical axis is represented by dashed lines (--) with appropriate markers as defined in legends

8.4. Conclusions

Metal Organic Frameworks are a rapidly developing class of materials with immense potential in the areas of molecular separation, catalysis, and sensing, among many others. While this motivates the quest to develop MOFs with high selectivity, their integration with materials used in sensor fabrication is a critical, but unexplored issue. Extensive studies on various sensors show that piezoresistive devices are attractive due to their potential for very high sensitivity, ease of instrumentation, precision, and accuracy. Strain-based detection using piezo-resistive microcantilevers combines these advantages with a compact package and minimal power consumption. However, the mechanical properties of chemical recognition layers can have a significant effect on device response, prompting our analysis of MOFs in this regard. Our analysis demonstrates that, as the Young's Modulus and Poisson's ratio are increased, the response increases as well, although the Young's Modulus has the greater effect. Interestingly, we also find that the density of the MOF layer has a negligible effect on the response. This

suggests that the presence of voids in a deposited MOF layer may not be deleterious to device sensitivity. Our modeling investigation considered materials reported in the literature for binding MOFs to surfaces (SiO_2, Al_2O_3 and Gold –SAM) as well as Si_3N_4, which is used in microcantilever fabrication. Our analysis indicates that SiO_2 binding layer was found to be most effective with regard to cantilever response. We also considered the effect of parasitic heating on the cantilever response with different MOF binding layer, but find that this has almost no influence on the resistance change predicted for various MOF surface layers. Of course, increasing the operating temperature of the device will degrade its sensitivity to some extent because the higher vapor pressure of any given analyte is a function of temperature. The magnitude of this effect will depend upon the heat of adsorption for a particular compound.

Overall, these results are encouraging, since they indicate a high tolerance for variations in MOF layer properties, including layer uniformity across the device, thickness, and density, that with present MOF growth methods are difficult to control. This bodes well for the practical use of MOFs as chemical recognition layers for a variety of sensing applications.

8.5. References

1. H. Bai, G.Q. Shi, *Sensors*, 7 (2007) 267-307.
2. G.F. Fine, L.M. Cavanagh, A. Afonja, R. Binions, *Sensors*, 10 (2010) 5469-5502.
3. S.T. Meek, J.A. Greathouse, M.D. Allendorf, *Adv. Mater.*, 23 (2011) 249-267.
4. J.R. Li, R.J. Kuppler, H.C. Zhou, *Chem. Soc. Rev.*, 38 (2009) 1477-1504.
5. D.S. Coombes, F. Cora, C. Mellot-Draznieks, R.G. Bell, *J. Phys. Chem. C*, 113 (2009) 544-552.
6. T. Devic, P. Horcajada, C. Serre, F. Salles, G. Maurin, B. Moulin, D. Heurtaux, G. Clet, A. Vimont, J.M. Greneche, B. Le Ouay, F. Moreau, E. Magnier, Y. Filinchuk, J. Marrot, J.C. Lavalley, M. Daturi, G. Ferey, *J. Am. Chem. Soc.*, 132 (2010) 1127-1136.
7. A.J. Fletcher, K.M. Thomas, M.J. Rosseinsky, *J. Solid State Chem.*, 178 (2005) 2491-2510.
8. P.K. Thallapally, *Am. Chem. Soc.*, 238 (2009).
9. K. Uemura, R. Matsuda, S. Kitagawa, *J. Solid State Chem.*, 178 (2005) 2420-2429.
10. M.D. Allendorf, R.J.T. Houk, L. Andruszkiewicz, A.A. Talin, J. Pikarsky, A. Choudhury, K.A. Gall, P.J. Hesketh, *J. Am. Chem. Soc.*, 130 (2008) 14404-+.
11. E.M. K. Arshak, G.M. Lyons, J. Harris, S. Clifford, *Sensor Review*, 24 (2004) 181-198.
12. S. Sivaramakrishnana, R. Rajamani, C.S. Smith, K.A. McGee, K.R. Mann, N. Yamashita, *Sens. Actuator B-Chem.*, 132 (2008) 296-304.
13. T. Thundat, P.I. Oden, R.J. Warmack, *Microscale Thermophys. Eng.*, 1 (1997) 185-199.
14. S.K. Vashist, *Journal of Nanotechnology Online*, (2007).
15. M.D. Allendorf, A. Schwartzberg, V. Stavila, A.A. Talin, *Chem.-Eur. J.*, 17 (2011) 11372-11388.
16. A. Choudhury, P.J. Hesketh, T. Thundat, Z.Y. Hu, *J. Micromech. Microeng.*, 17 (2007) 2065-2076.
17. E. Peeters, Process Development for 3D *Silicon Microstructures with Application to Mechanical Sensor Design*, Catholic University of Louvain, Belgium, 1994.
18. N.L. Privorotskaya, W.P. King, *Microsyst. Technol.*, 15 (2009) 333-340.
19. T.D. Bennett, A.L. Goodwin, M.T. Dove, D.A. Keen, M.G. Tucker, E.R. Barney, A.K. Soper, E.G. Bithell, J.C. Tan, A.K. Cheetham, *Phys. Rev. Lett.*, 104 (2010).
20. J.C. Tan, A.K. Cheetham, *Chem. Soc. Rev.*, 40 (2011) 1059-1080.
21. S.M. Yang, T.I. Yin, *Sens. Actuator B-Chem.*, 120 (2007) 736-744.
22. M.D.A. A. Betard, R. A. Fischer, "Growth of MOF Thin Films for Sensor Applications," in: D. Farrusseng (Ed.) *Applications of Metal-Organic Frameworks*, Wiley-VCH, Weinheim, 2010.
23. Y. Kanda, *IEEE Trans. Electron Devices*, 29 (1982) 64-70.
24. S. Sze, *VLSI Technology*, McGraw Hill, 1988.
25. D. Zacher, O. Shekhah, C. Woll, R.A. Fischer, *Chem. Soc. Rev.*, 38 (2009) 1418-1429.
26. S.S.Y. Chui, S.M.F. Lo, J.P.H. Charmant, A.G. Orpen, I.D. Williams, *Science*, 283 (1999) 1148-1150.
27. J.J. Purewal, D. Liu, J. Yang, A. Sudik, D.J. Siegel, S. Maurer, U. Müller, *International Journal of Hydrogen Energy*, 37 (2012) 2723-2727.
28. Y. Wu, A. Kobayashi, G.J. Halder, V.K. Peterson, K.W. Chapman, N. Lock, P.D. Southon, C.J. Kepert, *Angew. Chem.-Int. Edit.*, 47 (2008) 8929-8932.

29. W. Zhou, H. Wu, T. Yildirim, J.R. Simpson, A.R.H. Walker, *Phys. Rev. B,* 78 (2008).
30. M. Asheghi, K. Kurabayashi, R. Kasnavi, K.E. Goodson, *J. Appl. Phys.*, 91 (2002) 5079-5088.
31. B.L. Huang, Z. Ni, A. Millward, A.J.H. McGaughey, C. Uher, M. Kaviany, O. Yaghi, *Int. J. Heat Mass Transf.*, 50 (2007) 405-411.

[Blank page following section.]

APPENDIX A: PUBLICATIONS AND PRESENTATIONS

Reviewed journal articles

1. Robinson et al. "Ultra-sensitive Humidity Detection Using MOF-Coated Microsensors," *Anal. Chem.* **84** (2012), 7043.
2. Stavila et al. "Kinetics and mechanism of metal–organic framework thin film growth," *Chemical Science*, 2012, 3, 1531–1540
3. Venkatasubramanian et al. "MOF@MEMS: Design optimization for high sensitivity chemical detection," *Sensors & Actuators B*, **168** (2012), 256.
4. Kreno et al. "Metal-Organic Framework Materials as Chemical Sensors," invited review article, *Chem. Rev.* 2012, *112* (2), pp 1105–1125
5. Zeitler et al. "Grand Canonical Monte Carlo Simulation of Low-pressure Methane Adsorption in Nanoporous Framework Materials for Sensing Applications," *J. Phys. Chem. C* 2012, 116 (5), pp 3492–3502
6. Allendorf et al. "A Roadmap to Implementing Metal-Organic Frameworks in Electronic Devices: Challenges and Critical Directions," invited Perspective article, *Chem. Eur. J.* 17 (2011), 11372
7. Greathouse et al. "Computational Screening of Metal-Organic Frameworks for Large-Molecule Chemical Sensing," *Phys. Chem. Chem. Phys.*, 12 (2010), 12621

Book chapters

1. M. Allendorf, A. Bétard, R. A. Fischer "Growth of MOF Thin Films for Sensor Applications," invited book chapter in D. Farrusseng, Ed. *Applications of Metal-Organic Frameworks*, Wiley-VCH, Weinheim, 2011, p. 309.

Proceedings papers

1. J. H. Lee; R. T. J. Houk; R. A. Robinson; J. A. Greathouse; S. M. Thornberg; M. D. Allendorf; P. J. Hesketh, "Investigation of Microcantilever Array with Ordered Nanoporous Coatings for Selective Chemical Detection," in T. George; M. S. Islam; A. K. Dutta Eds. *Conference on Micro- and Nanotechnology Sensors, Systems, and Applications II*, Orlando, FL April 5 – 9, 2010. Micro- and Nanotechnology Sensors, Systems, and Applications II, Vol. 7679, article 767927, DOI: 10.1117/12.850217.

Invited Presentations

1. M. D. Allendorf "Connecting Structure with Function: MOFs for Chemical and Radiation Detection," MOF Schwerpunktprogramm Sensors Workshop, University of Munich, March 13, 2012.
2. M. D. Allendorf "Metal-Organic Frameworks (MOFs): Charting a course to device integration," SPIE Nanoepitaxy symposium, San Diego, CA, Aug. 24, 2011.

3. M. D. Allendorf "Chemical and Radiation Detection Using Metal-Organic Frameworks," Gordon Research Conference on Nanoporous Materials, Holderness School, Aug. 7-12, 2011.
4. V. Stavila, A. Robinson, M. D. Allendorf "Fabrication of Metal-Organic Framework Thin Films for Gas Sensing Applications," Symposium "New Horizons in Molecular Science: Design and Application of Porous Frameworks", Tampa, Florida, USA, June 20-21, 2011.
5. M. D. Allendorf "Chemical and Radiation Detection Using Metal-Organic Frameworks," GE Global Research Center June 7-8, 2011, Niskayuna, NY.
6. M. D. Allendorf "Manipulation of MOFs for Device Fabrication," UOP LLC Invitational Lecture Series (Des Plains, IL) May 4, 2011.
7. M. D. Allendorf "Integration of MOF Thin Films with Mechanical Sensors for Chemical Detection," PITTCON, March 13-17, 2011, Atlanta, GA 2.
8. Mark D. Allendorf "Manipulation of MOFs for Device Fabrication," Invited lecture at MOF2010 conference, Sept. 5-8, 2010.
9. M. D. Allendorf "Metal-Organic Frameworks: Versatile Materials for Chemical and Radiation Detection, Nanoscale Cluster Templating, and More," Dept. of Chemistry, UC San Diego, May 14, 2010.
10. M. D. Allendorf "Applications of Metal-Organic Frameworks to Chemical and Radiation Detection, Nanoscale Cluster Templating, and Beyond," Oct. 2, 2009 Inorganic Chemistry Lecture Series, UC Berkeley.

Contributed Presentations

1. Ilya Ellern, Anandram Venkatasubramanian, Peter J. Hesketh, Mark Allendorf "Characterization of Piezoresistive Microcantilever Sensors with Metal Organic Frameworks for the Detection of Volatile Organic Compounds," 222nd Meeting of the Electrochemical Society, Hawaii, Oct. 7, 2012.
2. Vitalie Stavila, Joanne Volponi, Kirsty Leong, Michael I. White, Alex L. Robinson, Jin-Hwan Lee, Anandram Venkatasubramanian, Ilya Ellern, Peter J. Hesketh, Mark D. Allendorf "Fabrication of MOF Thin Films for Chemical Sensing," presented at Spring 2012 ACS meeting, San Diego, CA.
3. Peter J. Hesketh, Ricardo Aguilar, Milad Navaei, Amber Pizzo, Ilya Ellern, Mark Allendorf, Joseph R. Stetter, Melvin Findley "Reliability of Microcantilever and Microbridge Gas Sensors for Chemical Detection," ECS Spring 2012 meeting, Seattle.
4. Ilya Ellern, Anandram Venkatasubramanian, Jin Hwan Lee, Peter J. Hesketh, Mark Allendorf "Characterization of Piezoresistive Microcantilever Sensors for the Detection of Volatile Organic Compounds Using Metal Organic Frameworks Thin Films," Student Chapter of ECS@Georgia Tech Poster Competition, Atlanta, GA, Nov. 17, 2011.
5. Ilya Ellern, Anandram Venkatasubramanian, Peter J. Hesketh, Mark Allendorf "Characterization of Piezoresistive Microcantilever Sensors with Metal Organic Frameworks for the Detection of Volatile Organic Compounds," Fall 2011 Electrochemical Society, Boston, MA, Oct. 9, 2011.
6. M. D. Allendorf, T. R. Zeitler, J. A. Greathouse "Metal-organic frameworks for greenhouse gas detection," ACS Fall 2011 meeting, Denver, CO, Aug. 29, 2011.
7. V. Stavila, A. Schwartzberg, J. Volponi, M. D. Allendorf "QCM Studies of Chemical Solution Deposition of $Cu_3(btc)_2(H_2O)_3$ Thin Films," Materials Research Society Meeting,

San Francisco, USA, Spring 2011.

8. Adam Schwartzberg, Vitalie Stavila, Mark D. Allendorf "MOFs for Device Applications: A Roadmap," Spring MRS 2011 meeting, San Francisco, April 26-28, 2011.
9. A. Venkatasubramanian, Ilya Ellern, Jin-Hwan Lee, Vitalie Stavilia, Mark D. Allendorf, Peter J. Hesketh "Design and Modeling of Microcantilever Sensors for Gas Detection using Metal Organic Frameworks," Spring MRS 2011 meeting, San Francisco, April 26-28, 2011.
10. Alex L. Robinson, Mark Allendorf, Steve M. Thornberg, Vitalie Stavila, Peter J. Hesketh "MOF Films for Microsensor Coatings," Spring MRS 2011 meeting, San Francisco, April 26-28, 2011.
11. Todd R. Zeitler, Mark D. Allendorf, Jeffery A. Greathouse "Computational Modeling of Low-pressure Gas Detection in Nanoporous Framework Materials," Spring MRS 2011 meeting, San Francisco, April 26-28, 2011.
12. R. J. T. Houk, Jin-Hwan Lee, A. Venkatasubramanian, A. Robinson, J. Skinner, S. Thornberg, J. A. Greathouse, Peter J. Hesketh, M. Meilikhov,, Kirill Yusenko, R. A. Fischer, Mark D. Allendorf "Nanoporous Framework Materials Interfaced with Mechanical Sensors for Highly-Sensitive Chemical Sensing," Spring 2010 MRS Meeting, San Francisco, CA
13. R. J. T. Houk, Jin-Hwan Lee, A. Venkatasubramanian, A. Robinson, J. Skinner, S. Thornberg, J. A. Greathouse, Peter J. Hesketh, M. Meilikhov,, Kirill Yusenko, R. A. Fischer, Mark D. Allendorf "Nanoporous Framework Materials Interfaced with Mechanical Sensors for Highly-Sensitive Chemical Sensing," Spring 2010 MRS Meeting, San Francisco, CA
14. "Microcantilever Array Sensors Using Nanoporous Metal-Organic Frameworks (MOFs) for Gas Detection," 2010 Solid-State Sensor, Actuator, and Microsystems Workshop, Hilton Head, June 2010
15. R. T. J. Houk, J. –H. Lee, S. M. Thornberg, A. Robinson, J. A. Greathouse, M. D. Allendorf, P. J. Hesketh "Ordered Nanoporous Coatings for Selective Chemical Detection," SPIE Orlando conference poster presented at "Micro- and Nanotechnology Sensors, Systems, and Applications II" SPIE Defense, Security, and Sensing, 5-9 April 2010, Orlando, FL.
16. Jin-Hwan Lee, Ronald J. T. Houk, Alex Robinson, Steven Thornberg, Mark D. Allendorf, Peter. J. Hesketh "Nanoporous Metal-Organic Framework Coated Microcantilever Sensors for Water and Methanol Detection," ECS Spring 2010 meeting, Vancouver, Canada.
17. Ronald J. T. Houk, Jin-Hwan Lee, Mark D. Allendorf, P. J. Hesketh "Microcantilever Sensors with Nanoporous Metal-Organic Films for Chemical Sensing," poster presented at Chem. and Bio. Defense Conference, Nov. 17 – 20, 2009, Dallas, TX.
18. Venkatasubramanian, Jin-Hwan Lee, Ronald J. T. Houk, Mark D. Allendorf, Sankar Nair, Peter J. Hesketh "Characterization of HKUST-1 Crystals and Their Application to MEMS Microcantilever Sensors," Fall 2010 Electrochemical Society Meeting, Oct. 10-15, 2010, Las Vegas, NV.

Patent

“Method and Apparatus for Detecting and Analyte,” M. D. Allendorf, P. J. Hesketh, U.S. Patent 8,065,904 B1, Nov. 29, 2011.

Materials, Methods and Devices to Detect and Quantify water Vapor Concentrations in an Atmosphere," A. L. Robinson and M. D. Allendorf; application filed 10/12/2011

DISTRIBUTION

1	MS0899	Technical Library	9536 (electronic copy)

For LDRD reports, add:

1	MS0359	D. Chavez, LDRD Office	1911

For CRADA reports add:

1	MS0115	OFA/NFE Agreements	10012

For Patent Caution reports, add:

1	MS0161	Legal Technology Transfer Center	11500


Sandia National Laboratories